Technische Universität München
Institut für Energietechnik

Lehrstuhl für Thermodynamik

Modeling and Analysis of High-Frequency Thermoacoustic Oscillations in Gas Turbine Combustion Chambers

Tobias Volkhard Hummel

Vollständiger Abdruck der von der Fakultät für Maschinenwesen der Technischen Universität München zur Erlangung des akademischen Grades eines

DOKTOR – INGENIEURS

genehmigten Dissertation.

Vorsitzender:
  Prof. Dr. mont. habil. Dr. rer. nat. h.c. Ewald Werner
Prüfer der Dissertation:
  1. Prof. Dr.-Ing. Thomas Sattelmayer
  2. Prof. Nicolas Noiray, Ph.D.
  3. Bruno Schuermans, Ph.D.

Die Dissertation wurde am 21.06.2018 bei der Technischen Universität München eingereicht und durch die Fakultät für Maschinenwesen am 24.10.2018 angenommen.

Acknowledgements

This dissertation summarizes the results of the research work I carried out at the Institute of Thermodynamics, Technical University of Munich (TUM) from 2013 to 2018. It was part of an extended research project on high-frequency thermoacoustic oscillations in gas turbine combustors, which was funded by TUM's Institute of Advanced Study (IAS), the Institute of Thermodynamics and the German Federal Ministry of Economic Affairs and Energy (BMWi). The administrative and financial support of these institutions is gratefully acknowledged. The scientific supervision was conducted by Dr. Bruno Schuermans in the course of his IAS Rudolf Diesel Industry Fellowship along with Prof. Dr.-Ing. Thomas Sattelmayer.

I would like to wholeheartedly thank Dr. Bruno Schuermans for his tireless and patient guidance during the course of our research project. He exemplified, and therefore taught me, the power of leading by example while his passionate attitude generated a research spirit where pushing the limits was the constant goal. My sincerest gratitude is expressed to Prof. Dr.-Ing. Thomas Sattelmayer for his interest in my topic and the scientific advisement along with respective discussions, which were always fruitful. Moreover, I am grateful that I was given the opportunity to publish at and travel to conferences around the world, which not only advanced my research but also my professional development. Thank you to Prof. Dr. Nicolas Noiray for his interest in my research and taking on the role as the second examiner of my committee. Thank you to Prof. Dr. mont. Dr. rer. nat. h.c Ewald Werner for organizing the doctoral defense as the chairman of the examination committee.

A significant portion of thankfulness has to go to my office-mate and project team-mate Frederik Berger. His composed and sharp spirit along with the dynamic collaboration during the completion of our research objectives contributed significantly towards the achievements associated with this thesis. It was an exciting ride. Thank you to Pedro Romero for the collaborations within our project. Thank you to Noah Klarmann for his help with reactive CFD simulations and Nicolai Stadlmair for the co-operation on system identification techniques. And, thank you to Michael Hertweck for his support to get started with high-frequency thermoacoustics.

I am deeply grateful for all personal friendships that have formed at the institute – most notably with Frederik Berger, Georg Fink, Nicolai Stadlmair and Noah Klarmann – along with the associated enlightening interactions during coffee breaks and activities outside of work. Thankfully acknowledged is the effort of the proof-readers of this dissertation: Frederik Berger, Nicolai Stadlmair and Thomas Hofmeister. There is no doctoral thesis without the support of hard-working students: Klaus Hammer, Thomas Hofmeister, Pedro Romeoro, Daniel Jäger, Tobias Bieniek, Johannes Rist and Joao Silva. I am happy that two students (Pedro Romero and Thomas Hofmeister) found their way to pursue doctoral ambitions in thermoacoustics themselves.

The staff of the Institute of Thermodynamics and the Institute of Advanced Study is thanked for their organizational and administrative support: Helga Bassett, Sigrid Schulz-Reichwald, Anna Kohout, Annette Sturm and Juliane Strücker.

I would like to thank my family and particularly my parents for paving the opportunity to explore the world and pursue this privileged path of education. Finally, this thesis shall be dedicated to my wife Simone (and our daughter Elea) as there are no words to describe my gratitude for her support, sacrifice and love she has shown me.

Munich, January 2019 — Tobias Hummel

Abstract

Gas turbines have been playing a key role for electrical power generation in the past decades. The importance of this role is expected to increase in the future, which is due to two main reasons. First, gas turbines are a central component within high-efficiency combined cycle power plants for electricity generation that emit considerably less carbon dioxide than e.g. coal-fired plants. Second, gas turbines are suited for compensating load fluctuations in the electric grid induced by fluctuations of renewable energy sources. This compensation role is due to gas turbines' capabilities of fast and flexible changes between operation points, fuel types and load level while maintaining a low-emission combustion process at optimal efficiencies. In order to comply with stringent emission regulations (particularly carbon monoxide and nitrogen oxides), lean premixed combustion technologies are employed. These technologies, however, cause the combustion chambers to be sensitive to develop thermoacoustic instabilities. The main focuses of this thesis is on thermoacoustic instabilities that are specifically characterized by high-frequency screech tones. In this frequency regime, thermoacoustic interactions between flame and acoustic modes are spatially variable, i.e. non-compact. As an overall research objective, a comprehensive modeling framework for analysis of high-frequency thermoacoustics in gas turbine combustors is developed. This framework is validated by conducting respective modeling and analysis tasks of a lab-scale swirl-stabilized combustor. From the results, understanding of physical mechanisms as well as system behavior of high-frequency instabilities at the first transversal mode in gas turbine combustors is deduced.

Specifically, spatially distributed, linear flame driving at the first transversal mode within this combustor is theoretically assessed and modeled. Non-compact flame transfer functions that describe the driving mechanisms are derived and employed to numerically investigate global system features that promote/inhibit the T1 mode to become unstable. Besides flame driving, damping of the first transversal modes due to acoustically induced vortex-shedding is concerned. The suitability of the Linearized Euler Equation to quantify this damping mechanism is discussed, the need for a simple model

is identified and the model is developed. The superposition of driving and damping models yields a framework to assess the thermoacoustic stability of non-compact systems that is particularly applicable to transversal modes occurring in the high-frequency regime. Results of driving and damping computations as well as the linear stability assessment are compared with experimental data readily available from 80 operation points.

Motivated by the goal to reconstruct the temporal combustor dynamics, a Reduced Order Modeling methodology is developed. This method allows to efficiently carry out time-domain simulations of the thermoacoustic dynamics that are governed by non-compact flames and multi-dimensional modes. Modal truncation as the Model Order Reduction technique is applied to large-scale state-space systems that are based on the Linearized Euler and/or Helmholtz Equations. Non-compact flame dynamics is modeled by dividing the flame into multiple compact sub-regions and forming a local feedback loop for each sub-region. The approach is capable to account for linear, non-linear and stochastic flame dynamics effects. Procedural guidelines to derive, verify and apply the Reduced Order Modeling method for non-compact systems are given. The methodology is applied to the swirl-stabilized benchmark combustor. Acoustic pressure dynamics of non-degenerate transversal mode pairs of one stable and one unstable operation point of the benchmark combustor are numerically reconstructed using respective Reduced Order Models. The results allow to infer physical insight into HF thermoacoustics from a dynamical system perspective. These investigations are extended to analytical considerations as by deriving a system of stochastic differential equations that governs the amplitude dynamics of non-degenerate transversal modes that are in a limit-cycle state. Comparing respective analytical results from a fixed point analysis to the numerical counterparts consolidates the findings of thermoacoustic time-domain behavior of non-degenerate, transversal mode in swirl-stabilized combustion systems.

The system of stochastic differential equations is utilized to derive system identification methods to extract linear growth rate from time-domain data, i.e. acoustic pressure time traces. Knowledge of this growth rate is of importance for model validation, strength ratings of an occurring instability and as an input quantity for damper design tasks. The system identification methods are verified using ROM data of which underlying growth rates are known before the methods are applied to experimentally obtained acoustic pressure amplitude time series.

Kurzfassung

Gasturbinen nehmen seit Jahrzehnten eine Schlüsselrolle bei der Stromerzeugung ein. Die Bedeutung dieser Rolle wird in Zukunft voraussichtlich weiter zunehmen, was vor allem auf zwei Gründe zurückzuführen ist. Zum einen werden Gasturbinen als eine zentrale Komponente in hocheffizienten Kombikraftwerken zur Stromerzeugung eingesetzt, welche deutlich weniger Kohlendioxid emittieren als z.B. Kohlekraftwerke. Zum anderen eignen sich Gasturbinen zur Kompensation von Lastschwankungen im Stromnetz, die durch Schwankungen von erneuerbaren Energien hervorgerufen werden. Diese Kompensationsfunktion ist darauf zurückzuführen, dass Gasturbinen schnell und flexibel zwischen Betriebspunkten, Brennstoffarten und Laststufen wechseln und gleichzeitig einen emissionsarmen Verbrennungsprozess bei optimalen Wirkungsgraden aufrecht erhalten können. Um die strengen Emissionsvorschriften (insbesondere für Kohlenmonoxid und Stickoxide) einzuhalten, werden mager vorgemischte Verbrennungstechnologien eingesetzt. Diese Technologien führen jedoch dazu, dass die Brennkammern empfindlich auf thermoakustische Instabilitäten reagieren. Der Schwerpunkt dieser Dissertation liegt auf thermoakustischen Instabilitäten, die speziell durch hochfrequente (HF) Kreischtöne charakterisiert sind. In diesem Frequenzbereich sind thermoakustische Interaktionen zwischen Flammen und akustischen Moden räumlich variabel, d.h. nicht-kompakt. Als übergeordnetes Forschungsziel wird ein umfassendes Modellierungsgerüst zur Analyse von hochfrequenter Thermoakustik in Gasturbinenbrennkammern entwickelt. Dieses Gerüst wird durch die Durchführung entsprechender Modellierungs- und Analyseaufgaben anhand einer Laborbrennkammer, welche mit drall-stabilisierter Verbrennung betrieben wird, validiert. Aus den Ergebnissen wird Verständnis über physikalische Mechanismen sowie des Systemverhaltens hochfrequenter Instabilitäten bei der ersten transversalen Mode in Gasturbinenbrennkammern abgeleitet.

Konkret wird die räumlich verteilte, lineare Flammendynamik bei der ersten transversalen (T1) akustischen Mode in dieser Brennkammer theoretisch betrachtet und anschließend modelliert. Die thermoakustischen Antriebsmechanismen werden durch nicht-kompakte Flammentransferfunk-

tionen mathematisch beschrieben, welche zuerst hergeleitet und danach verwendet werden. Die Verwendung dieser Transferfunktionen in numerische Studien führt zur Identifikation globaler Systemeigenschaften, die die die Instabilitätsneigung der T1-Mode fördern bzw. unterdrücken. Neben dem Flammenantrieb wird die Dämpfung der ersten transversalen Moden durch akustisch induzierte Wirbelablösung betrachtet. Die Eignung der linearisierten Euler-Gleichungen zur Quantifizierung dieses Dämpfungsmechanismus wird diskutiert und im Zuge dessen die Notwendigkeit eines einfachen Modells identifiziert sowie entwickelt. Die Überlagerung von Treib- und Dämpfungsmodellen liefert den Berechnungsrahmen zur Bestimmung des linearen thermoakustischen Stabilitätsverhaltens für nicht kompakte Systeme, der insbesondere für transversale Moden im Hochfrequenzbereich geeignet ist. Die Ergebnisse der Treib- und Dämpfungsberechnungen sowie der linearen Stabilitätsbewertung werden mit experimentellen Daten aus 80 verschiedenen Betriebspunkten verglichen.

Motiviert durch die Zielsetzung das zeitliche Verhalten der Modendynamik zu rekonstruieren wird eine Methodik zur Bildung von Modellen reduzierter Ordnung - sogenannten Reduced Order Models (ROM) - entwickelt. Die Methode erlaubt die effiziente Durchführung von Zeitbereichssimulationen der thermoakustischen Dynamik, die nicht-kompakte Flammeninteraktionen mit mehrdimensionale akustische Moden berücksichtigen. Konkret wird eine modale Trunkierung als Technik zur Modellreduktion auf große Zustandsraumsysteme angewendet, wobei letztere auf diskreten Formen linearisierten Euler- und/oder Helmholtz-Gleichungen basieren. Die Nichtkompaktheit der Flammendynamik wird modelliert, indem die Flamme in mehrere kompakte Teilbereiche aufgeteilt und für jeden Teilbereich eine lokale Rückkopplungsschleife gebildet wird. Der Ansatz erlaubt zudem, lineare, nichtlineare und stochastische Einflüsse auf die Flammendynamik zu berücksichtigen. Vorgehensrichtlinien zur Herleitung, Verifizierung und Anwendung der Niederordnungsmodellierung von nicht-kompakten Systemen werden erarbeitet und dargelegt. Des weiteren wird die Methodik auf die Laborbrennkammer mit drall-stabilisierter Verbrennung angewendet. Konkret wird der zeitliche Verlauf des Schalldrucks von einem nicht-degenerierten transversalem Modenpaar eines jeweils stabilen und instabilen

Betriebspunktes der Laborbrennkammer durch die Niederordnungsmodellierungsmethodik numerisch rekonstruiert. Entsprechende Interpretationen der Ergebnisse erlauben physikalisches Verständnis über die HF-Thermoakustik aus einer dynamischen Systemperspektive zu erzeugen. Analog zu den numerischen Untersuchungen wird das dynamische Systemverhalten durch analytische Betrachtungen examinieren. Dies erfolgt durch die Herleitung eines Systems stochastischer Differentialgleichungen, welches die Amplitudendynamik nicht-degenerierter transversaler Moden, die sich in einem Grenzzykluszustand befinden, beschreibt. Der Vergleich der jeweiligen analytischen Ergebnisse, also die stationären Lösungen des Gleichungssystems, mit den entsprechenden Resultaten aus den numerischen Berechnungen, führt zur Konsolidierung der Erkenntnisse des thermoakustischen Zeitbereichsverhaltens von nicht-degenerierten, transversalen Moden in drallstabilisierten Verbrennungssystemen.

Das System der stochastischen Differentialgleichungen wird des weiteren verwendet, um Systemidentifikationsmethoden zu erarbeiten. Diese Systemidentifikationsmethoden verfolgen die Zielsetzung aus Zeitbereichsdaten, d.h. Zeitreihen des akustischen Schalldrucks, lineare Wachstumsraten zu extrahieren. Die Kenntnis der Wachstumsraten ist von technisch relevanter Bedeutung für Modellvalidierungsaufgaben, die Bewertung der Intensität einer auftretenden Instabilität und als Eingangsgröße für die Auslegung von Dämpfern. Die vorgestellten Systemidentifikationsmethoden werden anhand von ROM-Daten verifiziert, deren zugrundeliegende Wachstumsraten bekannt sind. Anschließend werden die Methoden auf experimentell gewonnene Zeitreihen von akustischen Schalldruckamplituden angewendet.

Contents

List of Figures

List of Tables

Nomenclature

Latin Letters

$\mathbf{A}$	[−]	System matrix of spatial derivatives
$\mathbf{A}_{SUPG}$	[−]	Stabilization system matrix of spatial derivative
$\mathbf{A}_{LEE}$	[−]	LEE system matrix of spatial derivatives
$\mathcal{A}_G$	[kg/m^2/s]	Auxiliary variable upstream traveling wave
$\mathcal{A}_F$	[kg/m^2/s]	Auxiliary variable downstream traveling wave
$\mathbf{B}$	[−]	Source term vector/matrix
a	[−]	Series expansion coefficient
b	[−]	Azimuthal wave number
b_{1-4}	[−]	Series expansion coefficients
c	[m/s]	Speed of sound
$\mathbf{C}$	[−]	Output vector/matrix
C	[−]	Comparison function
D_Ω	[W/m^3]	Energy source due to mean flow interactions
$\mathrm{D}_{\mathbf{m}_{\mathbf{u}'}}$	[W/m^3]	Energy source due to momentum sources
$\mathrm{D}_{\dot{q}}$	[W/m^3]	Energy source due to heat release sources
$\mathbf{D}$	[kg/s/m^3]	Damping matrix
e	[J/kg]	Energy per unit mass
E	[J/m^3]	Disturbance energy density
$\mathbf{E}$	[n a]	System matrix of time derivative
$F_{\mathbf{u},\tau}$	[N/m^3]	Viscous source terms momentum equation
F	[−]	Function operator
f	[Hz]	Frequency
F	[m/s]	Downstream traveling wave
F	[Pa]	Slowly varying amplitude CCW rotating mode

$F_{p,\tau}$	[W/m^3]	Viscous source terms energy equation
G	[m/s]	Upstream traveling wave
G	[Pa]	Slowly varying amplitude CW rotating mode
h_c	[J/kg]	Heat of combustion
H	[m]	Element height
$\mathbf{H}$	[Pa]	Complex Fourier signal matrix
H_a	[Pa]	Auxiliary Fourier signal matrix
H_b	[Pa]	Auxiliary Fourier signal matrix
$\mathcal{H}$	[−]	Hilbert transform operator
i	[−]	Imaginary number
$\mathbf{I}$	[W/m^2]	Disturbance energy flux
$\bar{I}$	[−]	OH* intensity distribution
$\mathbf{I}$	[−]	Unity matrix
J_b	[−]	Bessel function of b-th order
θ	[rad/s]	Jacobian matrix
K	–	Number of series expansions
K	[W/m^3]	Proportionality factor
k	[1/m]	Wave number
k_{FF}	[−]	Autocorrelation function CCW amplitude perturbation
k_{GG}	[−]	Autocorrelation function CW amplitude perturbation
l_{tur}	[m]	Turbulent length scale
l_{per}	[m]	Periodic length scale
M	–	Number of series expansions
m_ρ	[kg/m^3/s]	Volumetric source term of mass
$\dot{m}$	[kg/s]	Mass flow rate
$\mathbf{M}_{R_T}$	[kg/m^2/s]	Auxiliary matrix reflection coefficient
$\mathcal{M}_{p'}$	[W/m^3/s]	Mean flow coupling function in wave equation
$\mathbf{m_u}$	[N/m^3]	Volumetric source term of momentum
m_p	[W/m^3]	Volumetric source term of energy
N	[−]	Number of series expansions
$\mathbf{n}$	[−]	Normal vector
N	[−]	System size
n	[W/m^3]	White noise source function
p	[Pa]	Pressure

P_{th}	[W]	Thermal power
PD	[W/m^3]	Power density
$\mathbf{P}$	[Pa]	Pressure signal matrix
q	[J/kg]	Heat transfer per unit mass
$\dot{q}$	[W/m^3]	Heat release rate per unit volume
r	[m]	Radial coordinate
R	[−]	Reflection coefficient
R	[m]	Radius
S	[m^2]	Surface
s	[m]	Bessel root
s_{cor}	[−]	Switch parameter Coriolis terms
s	[−]	Spin ratio
S_{FF}	[W/s]	Power spectral density CCW amplitude perturbation
$S_{\chi_F \chi_F}$	[W/s]	Power spectral density white noise process
$S_{\rho'}$	[kg/m^3/s]	Higher order terms perturbed mass equation
$\mathbf{S}_{\mathbf{u}'}$	[N/m^3]	Higher order terms perturbed momentum equation
$S_{p'}$	[W/m^3]	Higher order terms perturbed energy equation
t	[s]	Time variable
T	[s]	Period
τ_{tur}	[s]	Turbulent time scale
τ_{tur}	[s]	Periodic time scale
T	[K]	Temperature
T	[−]	Transmission coefficient
$\mathbf{T}$	[−]	Azimuthal probe location matrix
$\mathbf{u}$	[m/s]	Flow velocity vector
$\mathbf{u}$	[−]	Input signal matrix
u	[−]	Input signal
v	[m^3/kg]	Specific volume
V	[m^3]	Volume
$\mathbf{V}$	[−]	Right Eigenvector matrix
w	[J/kg]	Mechanical work per unit mass
$\mathbf{W}$	[−]	Left Eigenvector matrix
$\mathbf{x}$	[m]	Spatial coordinate vector
y	[−]	Output signal

$\mathbf{y}$	[−]	Output signal matrix
Z	[−]	Impedance

Greek Letters

α	[rad/s]	Acoustic damping rate
α_τ	[1/s]	Numerical stabilization strength
β	[rad/s]	Flame driving rate
χ	[Pa/s]	White noise
Δ	[−]	Difference operator
δ_{fl}	[m]	Flame thickness
Δ	[N/m^3]	Acoustic displacement vector
δ	[−]	Dirac function
η	[Pa]	Complex Fourier coefficient signal
γ	[−]	Ratio of specific heats
Γ	[W/m^3]	Noise strength
κ	[m/s/N^2]	Non-linearity coefficient
λ_{ac}	[m]	Wave length
λ	[−]	Air excess ratio
$\boldsymbol{\Lambda}$	[rad/s]	Eigenvalue matrix
λ	[rad/s]	Eigenvalue
ν	[rad/s]	Thermoacoustic growth rate
ω	[rad/s]	Angular (Eigen-)frequency
Ω	[1/s]	Vorticity
$\boldsymbol{\phi}$	[−]	Flow variable vector
Ψ	[−]	Mode shape
ϕ	[−]	Slowly varying phase
Φ	[rad]	Difference of slowly varying phases
φ	[rad]	Total phase
ρ	[kg/m^3]	Density
σ	[−]	Axial, radial mode shape function
θ	[rad]	Angular coordinate
τ	[−]	Numerical stabilization parameter

τ	[s]	Stochastic time scale
τ	[s]	Autocorrelation delay time
Ξ	[−]	Spatio-temporal white noise signal
ξ	[−]	Temporal white noise signal
ζ	[kg/s/m^3]	Loss coefficient

Superscripts

$(\dots)^I$	Case one
$(\dots)^{II}$	Case two
$(\dots)^*$	Complex conjugate
$(\dots)^c$	Continuous
$(\hat{\dots})$	Fourier coefficient/Mode
$(\tilde{\dots})$	Moving coordinate system
$(\dots)'$	Oscillation/Disturbance/Perturbation
$(\dots)^r$	Radial
$(\bar{\dots})$	Steady/Mean value
$(\dots)^T$	Transpose
$(\tilde{\dots})$	Volume integrated quantity

Subscripts

$(\dots)_a$	Acoustic
$(\dots)_{atm}$	Atmospheric
$(\dots)_A$	Standing transversal mode
$(\dots)_b$	Bloch
$(\dots)_B$	Standing transversal mode
$(\dots)_c$	Chamber
$(\dots)_D$	Deterministic
$(\dots)_d$	Downstream
$(\dots)_{el}$	Element

$(\ldots)_{ex}$	Excitation
$(\ldots)_{EXP}$	Experimental
$(\ldots)_{extr}$	Extraction
$(\ldots)_{fl}$	Flame
$(\ldots)_{f}$	Fuel
$(\ldots)_{F}$	CCW rotating transversal mode
$(\ldots)_{G}$	CW rotating transversal mode
$(\ldots)_{i}$	Imaginary
$(\ldots)_{in}$	Inlet
$(\ldots)_{j}$	Discrete azimuthal probe location
$(\ldots)_{k}$	Series expansion index
$(\ldots)_{L}$	Linear
$(\ldots)_{max}$	Maximum
$(\ldots)_{m}$	Momentum
$(\ldots)_{m}$	Series expansion index
$(\ldots)_{n}$	Mode number/type
$(\ldots)_{NL}$	Non-linear
$(\ldots)_{out}$	Outlet
$(\ldots)_{per}$	Periodic
$(\ldots)_{p}$	Probe
$(\ldots)_{q}$	Heat release
$(\ldots)_{r}$	Real
$(\ldots)_{ref}$	Reference
$(\ldots)_{ROM}$	Reduced Order Model
$(\ldots)_{r}$	Radial
$(\ldots)_{r}$	Reduced order
$(\ldots)_{S}$	Stochastic
$(\ldots)_{s}$	Sub-region
$(\ldots)_{SL}$	Shear-layer
$(\ldots)_{tur}$	Turbulent
$(\ldots)_{\tau}$	Viscous fluid shear
$(\ldots)_{th}$	Thermal
$(\ldots)_{T}$	Transversal
$(\ldots)_{\theta}$	Azimuthal

$(\dots)_u$	Upstream
$(\dots)_v$	Vortical
$(\dots)_x$	Axial

Operators

$\langle \dots \rangle$	Period averaged

Dimensionless Numbers

He	Helmholtz number
Ma	Mach number

Abbreviations

2D	Two-dimensional
3D	Three-dimensional
A^2EV	Advanced Environmental Burner
BP	Bandpass
CCW	Counterclockwise
CFD	Computational Fluid Dynamics
CPU	Central Processing Unit
CW	Clockwise
D	Damping
EXP	Experimental
FEM	Finite Element Method
FFT	Fast Fourier Transform
FP	Fixed Point
FTF	Flame Transfer Function

HE	Helmholtz Equation
HF	High-Frequency
ISZ	Intersection zone
LEE	Linearized Euler Equations
LES	Large-Eddy-Simulations
LF	Low-Frequency
LLC	Linearized Limit Cycle
MIMO	Multi-Input-Multi-Output
MMM	Multi-Microphone Method
MOR	Model Order Reduction
NSE	Navier Stokes Equations
ODE	Ordinary Differential Equation
PDE	Partial Differential Equation
PDF	Probability Density Function
PSD	Power Spectral Density
RANS	Reynolds Averaged Navier Stokes
rc	Relative contribution
rel.Err.	Relative Error
RI	Rayleigh Integral
ri	Rayleigh index
ROM	Reduced Order Model/Modeling
SDE	Stochastic Differential Equation
SUPG	Streamline-Upwind-Petrov-Galerkin
URANS	Unsteady Reynolds Averaged Navier Stokes

1 Introduction

1.1 Technical Background and Motivation

The principal measure to counteract the advancement of global climate change comprises the reduction of greenhouse gas emissions, most notably carbon dioxide CO_2 [5, 116]. Within the field of electric power generation, achieving this countermeasure implies the necessity for transformation of the current power plant landscape from dominantly fossil (e.g. coal and oil) to renewable (e.g. wind and solar) technologies. For example, Germany committed to convert its energy infrastructure so that by the year 2050 "60% percent of the gross final consumption of energy, and 80% percent of the gross electricity consumption" occurs by renewable sources [115]. Such large portions of renewable sources causes one considerable technical challenge, that is, fluctuation of the supply due to the unpredictable availability of e.g. wind or solar sources [5, 34, 117]. In order to ensure grid stability, these fluctuations need to be compensated for which the utilization of new generations of gas turbine plants – either in a standalone configuration or as part of a combined cycle plant – poses one of the most promising technical solution [5, 34, 56, 117]. The suitability of gas turbines for this task is found within the following performance potentials:

1. High operational flexibility, i.e. the capability of conducting fast and on-demand load changes. This flexibility serves to compensate the load fluctuations within the grid induced by renewable energy sources [56, 161].

2. High efficiency over a wide operational range. Thereby, CO_2 emission are minimized in compliance with climate change countermeasure strategies [5].

3. Overall low formation of pollutants, notably nitrogen oxides NO_x to meet

environmental regulations [89, 133].

Turbulent lean premixed combustion is characterized by low NO_x emission levels compared to non-premixed, i.e. diffusive combustion. The latter combustion mode is predominantly implemented in conventional gas turbine systems [80, 133]. New generations of gas turbines are operated in premixed combustion mode [80, 161], which ensures that the performance criteria of low NO_x emissions is achieved. However, lean premixed systems exhibit a sensitive susceptibility to so called self-sustained thermoacoustic oscillations [28, 37, 80, 96, 133]. As is illustrated in the next sections, these oscillations (also often referred to as thermoacoustic instabilities, pressure pulsations or combustion/combustor dynamics) are caused by constructive coupling mechanisms between the unsteady flame and the natural acoustics (i.e. eigenmodes) of the chamber. The reasons why premixed combustors are more sensitive to develop thermoacoustic instabilities than the non-premixed counterparts is due to two main reasons: (1) Combustion reactions in the former systems occur in the vicinity of the stoichiometric regions of the mixture field, which acts as a stabilizing mechanisms to thermoacoustic oscillations [133]. (2) Acoustic dissipation is lower in combustors operating with premixed flames [80, 92]. An occurrence during gas turbine operation needs to be avoided in order to prevent hardware damage, emission compliance violation and system shut downs [92, 96].

1.2 Thermoacoustic Oscillations and Rayleigh's Criterion

Self-sustained thermoacoustic oscillations in gas turbine combustors are fundamentally based on the thermoacoustic effect. This effect is explained with the help of a generic gas turbine combustion system sketched in Fig. 1.1. This system consists of an inlet and mixing section followed by a combustion chamber. Specifically, an air flow enters the inlet section (a) into which fuel is injected (c). The mixture passes through the swirler (c) to result in a swirling air-fuel flow (d) that convects into the combustion chamber. This premixed flow sustains a turbulent, aerodynamically stabilized flame (e) that releases heat due to combustion. Acoustic waves (b and c) are constantly excited due to broadband combustion noise, which propagate in up- and downstream direction through the combustor as well as reflect at walls, inlets and outlets.

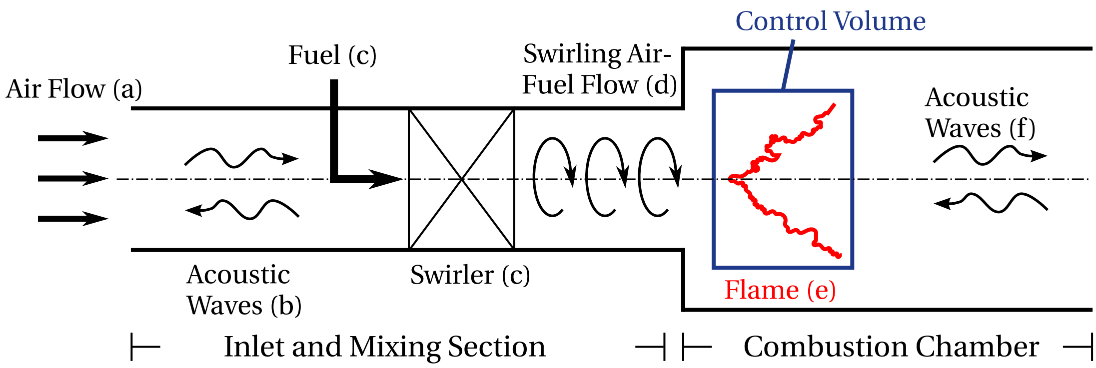

Figure 1.1: Schematic of gas turbine combustor with thermoacoustic control volume

Now, assume that the heat release rate and pressure in the control volume oscillate at a distinct frequency. For simplicity of the forthcoming explanations, the heat release rate and pressure oscillation (denoted by $\dot{q}'$ and p') is – for now – presumed spatially invariant across the control volume. Moreover, the oscillatory cycle of the latter oscillations is viewed with a thermodynamic cycle analogy. Thermodynamically, sole acoustic pressure oscillations isentropically compresses and expands the gas within the control volume. Hence, mechanical volume work is respectively done on and by the gas during the compression and expansion phases, which are of equal magnitude so that the overall net effect is zero [121, 162]. The oscillatory heat release rate can be interpreted to cause additional increases and decreases of the gas' specific volume [121]. This leads to additional volume work done by/on the gas in the control volume, which net effect can become non-zero. The energetic effect of the work processes caused by acoustic and heat release oscillations becomes clear by applying the first law of thermodynamics, i.e.

$$\Delta e = w - \underbrace{q}_{=0} \tag{1.1}$$

where Δe is the energy change of the (oscillating) gas in the control volume, w is mechanical work term and q is the heat transfer term. The latter is zero as no heat transfer occurs across the boundaries of the control volume. The mechanical work term is due to volume work that is caused by the interplay between acoustic pressure and respective changes of the gas' specific volume, which is given by [121]

$$w = \oint p' \mathrm{d}v', \tag{1.2}$$

where the closed line integration is to be carried out along the acoustic/thermodynamic cycle. The specific volume expansion v' is composed of contributions due to isentropic acoustic and heat release oscillations, i.e.

$$\mathrm{d}v' = \mathrm{d}v'^{p'} + \mathrm{d}v'^{\dot{q}'}, \tag{1.3}$$

which are reformulated to [121]

$$\mathrm{d}v'^{p'} \propto \mathrm{d}p', \tag{1.4}$$

$$\mathrm{d}v'^{\dot{q}'} = \frac{\mathrm{d}v'^{\dot{q}'}}{\mathrm{d}t}\mathrm{d}t \propto \dot{q}'\mathrm{d}t. \tag{1.5}$$

Substituting Eqns. 1.2-1.5 into Eqn. 1.1 gives

$$\Delta e \propto \underbrace{\oint p' \mathrm{d}p'}_{=0} + \oint p' \dot{q}' \mathrm{d}t. \tag{1.6}$$

The first term on the right-hand-side describes the work process due to sole isentropic oscillations – which vanishes as expected – while the value of the second work term depends on the phase difference between pressure and heat release oscillations. Equation 1.6 essentially presents Rayleigh's criterion [125,162] to describe the thermoacoustic effect, which can be formulated as: If heat release fluctuations are in-phase with pressure fluctuations of the gas in the control volume, the unsteady flame generates mechanical work in form of acoustic oscillations, which provides energy to the acoustic field and leads to an amplification of amplitude. Conversely, mechanical work is consumed by the heat release fluctuations in an out-of-phase situation, implying an extraction of energy from the acoustic field and a decline of the acoustic oscillation amplitude [121]. The integral term alone in Eqn. 1.6, i.e.

$$\oint p' \dot{q}' \mathrm{d}t, \tag{1.7}$$

is known as the Rayleigh integral, which is widely used for thermoacoustic system analysis [63, 179]. Practical understanding of Rayleigh's criterion/integral is generated by considering three different scenarios of phase relations between heat release and acoustic oscillations. These scenarios are depicted in Figs. 1.2a)-c), respectively representing in-phase, out-of-phase (180° phase shift) and 90° phase relations. As can be retrieved from the figures, the in-phase (a) and out-of-phase (b) situation emerge a positive and negative Rayleigh integral so that the flame is said to drive and damp the pressure oscillations, respectively. A zero Rayleigh integral – i.e. no driving/damping at all – occurs for a phase relation (c) of 90° between pressure and heat release oscillations. The phase relations in between these three scenarios cause corresponding energy transfer with a varying magnitude as illustrated in Fig. 1.2d).

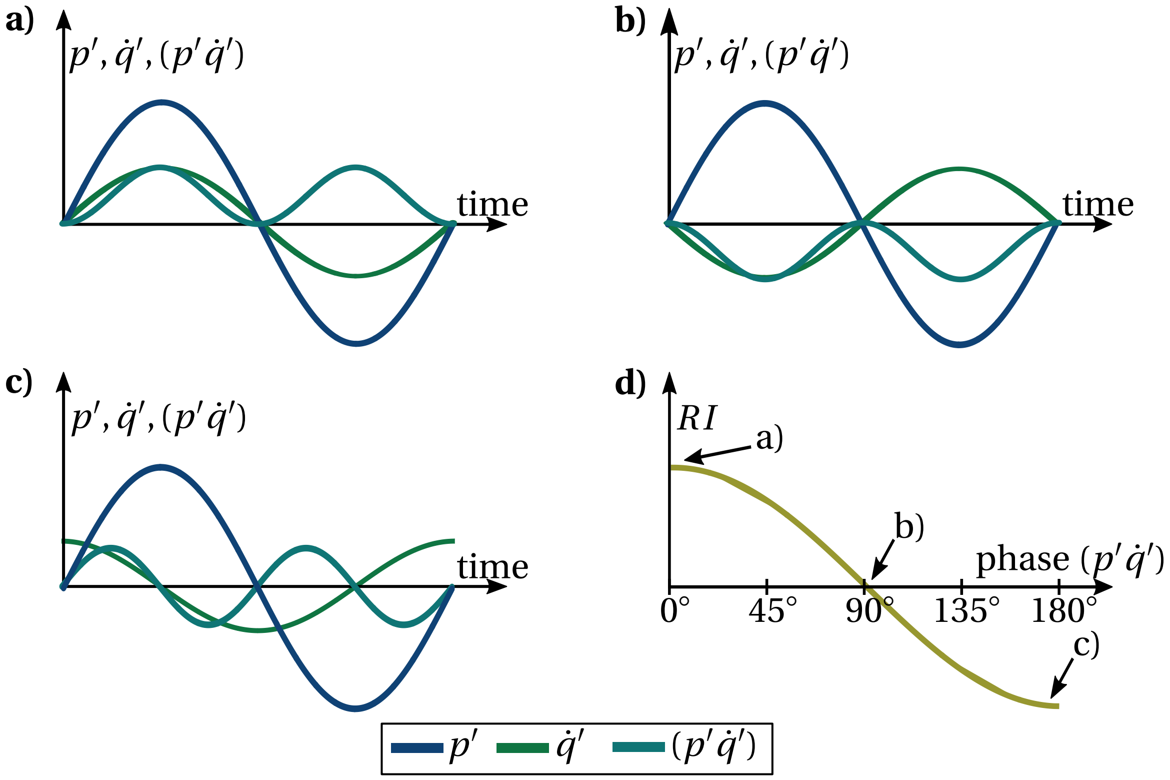

Figure 1.2: a) In-phase, b) out-of-phase, c) 90° phase shifted heat release and pressure oscillation in control volume. d) Generated acoustic energy by the flame as a function of the phase relation

In combustion systems, the acoustic oscillations at the flame are associated with the natural acoustics of the chamber geometry, i.e. eigenmodes. The presence of turbulent combustion processes causes broadband noise, which excites all modes in the chamber. Heat release oscillations at distinct frequencies are induced by modulations of the combustion process by the eigen-oscillations. The identification and understanding of how incoming acoustic perturbations physically convert into heat release oscillations represents one central objective in the field of thermoacoustic research and engineering. A fundamental mechanism that leads to heat release oscillation is illustrated with the help of an example from the field of low-frequency oscillations and Fig. 1.1. The flow is presumed to be in a perfectly premixed state after the swirler (d). Flowing into the combustion chamber, this fuel-air mixture sustains a perfectly premixed flame. The naturally present acoustic modes are non-zero in the burner tube and cause the mixture flow rate to pulsate. This pulsating mixture flow then enters the flame (e) and causes heat release oscillation upon combustion. Another prominent mechanism that occurs if the system is not perfectly-premixed, is the modulation of heat release due to convectively transported equivalence ratio fluctuations. At the fuel injector (c), acoustic oscillations of the fluid velocity induce fluctuations of equivalence ratio [96, 98, 121, 133]. These equivalence ratio fluctuations are transported with the mean flow to the flame (e) where they translate into heat release oscillations upon combustion. Thermoacoustic driving occurs at all modes/frequencies at which the heat release oscillations exhibit a phase relation between fully in-phase and 90° (Fig. 1.2d)) with respect to the pressure oscillations are driven by the flame, i.e. receive acoustic energy.

If the amount of driving energy exceeds the amount of losses (i.e. acoustic damping e.g. due to mean flow effects and/or at domain boundaries), the associated oscillations will start to grow in amplitude. The eigenmode of the combustor and the unsteady heat release are said to constructively interfere and form a positive feedback loop that leads to the amplification of each other [28, 96, 121, 133, 142]. Eventually, non-linear processes saturate this amplification, and the system settles into a constant amplitude limit cycle behavior (cf. next subsection) [36, 96, 143]. Thus, there are two necessary conditions for an instability to occur: Firstly, the in-phase relation between heat release and pressure fluctuations. Secondly, a positive energy balance between flame driving and acoustic losses due to damping for each concerned mode. Mathematically, the condition whether an instability occurs is given by

$$RI = \frac{1}{T}\int_T \int_V p'(\mathbf{x},t)\dot{q}'(\mathbf{x},t)\mathrm{d}V\mathrm{d}t > D, \tag{1.8}$$

where RI denotes the Rayleigh integral, $p'(\mathbf{x},t)$ and $\dot{q}'(\mathbf{x},t)$ are pressure and heat release rate oscillations integrated over the control/combustor volume and over one oscillation period T of the concerned frequency. The quantity D denotes all acoustic energy losses at the particular mode. Note that a spatial variability of both, heat release and pressure oscillations are admitted, which grants Eqn. 1.8 most general applicability.

1.3 Instability Evolution and Technical Implications

A mode is rendered thermoacoustically unstable, if $RI > D$. Consequently, a thermoacoustic instability occurs in the combustor, which evolves in four consecutive phases as are indicated in Fig. 1.3.

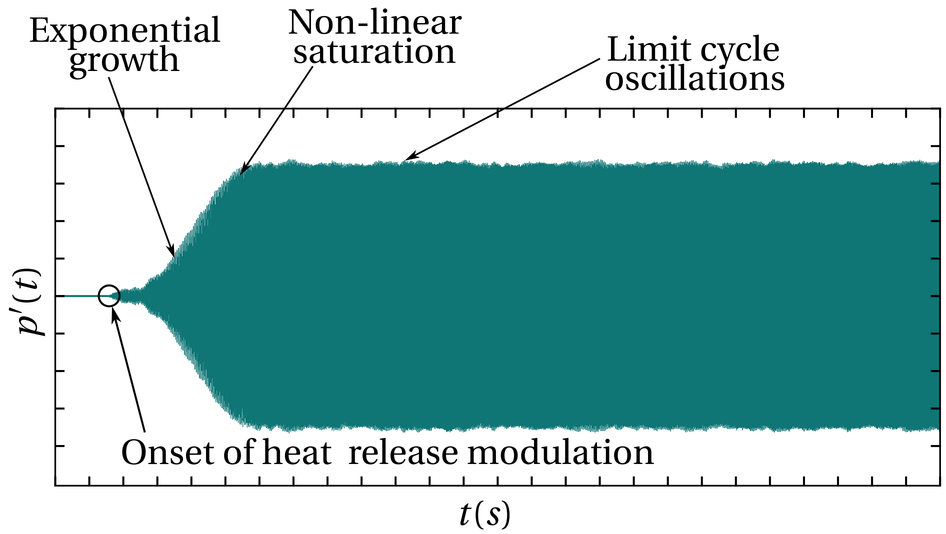

Figure 1.3: Characteristic pressure trace of a thermoacoustic instablility

Phase #1: Heat Release Modulation

At the instant of an impending instability, modulation of the heat release with the acoustic eigenmodes occurs. This implies that no growth in amplitude has yet occurred while thermoacoustic feedback mechanisms are active and the Rayleigh integral condition in Eqn. 1.8 is satisfied. Operationally, this is for example the consequence of a load change of the gas turbine away from the stable operation range as well as due to a change of the fuel composition [161].

Phase #2: Exponential Growth of Amplitude

Upon the onset of the instability, the oscillation amplitude [31, 96] starts to grow exponentially, which is due to the surplus of acoustic energy provided by the thermoacoustic interactions at the flame. The mode is said to be linearly driven by the flame.

Phase #3: Saturation of Heat Release Oscillations

While the amplitude level rises, flame modulation mechanism change, which leads to a saturation of the heat release oscillations. This saturation is caused by non-linear processes [9, 12, 36, 91, 97, 143] that are non-generalizable and depend e.g. on frequency regime, combustor as well as flame type. The (relative) reduction of heat release oscillations implies an attenuation of the thermoacoustic effect, which leads to a (relative) reduction of generated acoustic energy and acoustic oscillation amplitude.

Phase #4: Stochastically Modulated Limit Cycle Oscillations

The saturation phase continues until the thermoacoustically generated energy equates the losses due to damping such that the Rayleigh integral condition becomes $RI = D$. At this point, the eigenmode is said to have settled into a limit cycle state. Limit cycle oscillations are characterized by a constant amplitude level, which is stochastically modulated by broadband turbulent combustion noise [26, 94, 112]. It is important to point out that in gas turbine thermoacoustics the energy attenuation effects that lead to limit cycle states are solely induced by the saturation of heat release oscillations. Encountered limit cycle amplitude levels remain "small" compared to the mean pressure so that non-linear acoustics – which can cause limit cycle states in e.g. rocket combustors [31] – can be assumed as negligible in gas turbine combustors [36, 143].

Thermoacoustically Stable Oscillation Dynamics

If acoustic damping exceeds the energy generation, the mode of concern is said to be stable and the foregoing transition into limit cycle oscillations do not occur. Stable cases are characterized by the Rayleigh condition $RI < D$. While thermoacoustic coupling between heat release and acoustic eigenmodes still occurs, the net effect of energy generation remains negative. Then, the acoustic oscillations in the chamber are solely stochastically forced through broadband turbulent combustion [26, 38, 94, 113].

Operational Aspects of Thermoacoustic Instabilities

From a macroscopic perspective, thermoacoustic oscillations can be viewed as pressure pulsations that manifest in the combustion chamber. These pulsations exert thermal and mechanical stresses on the combustor hardware as well as inhibit low-emission combustion processes [96, 133]. Self-evidently, the occurrence of thermoacoustic instabilities have to be avoided across the entire load range of the gas turbine. This emerges the engineering task to design new (or retrofit existing) combustors such that these are thermoacoustically stable [161]. For this task, a thorough understanding of physical mechanism, capabilities for thermoacoustic system analysis as well as development strategies for instability suppression/mitigation is necessary. The provision of respective theoretical and mathematical fundamentals, analyses and modeling methodologies, design tools and best-practice guidelines represents one principal tasks of engineering research.

1.4 High-Frequency vs. Low-Frequency Oscillations

The general scope of this thesis comprises the investigation of thermoacoustic oscillations in gas turbine combustors in the high-frequency (HF), screech regime. All investigations are carried out using a can-type combustor setup, where one main burner tube feeds the chamber with a perfectly premixed air-fuel flow. The burner is located centrically to the chamber as can be observed in the Fig. 1.4 and as is presented in detail in Chap. 3. In order to establish a first sense of understanding of the subject, a clear characterization of HF oscillations in terms of physical features, typical frequency regimes and distinction to low-frequency (LF) instabilities is established.

Non-Compact Flames

The first feature that defines HF oscillations is found among characteristic length scale relations of flame and acoustic modes. In the case where the ratio of flame to acoustic length scale is small, the former can be considered as a thermoacoustic point source. Hence, heat release oscillations across the flame volume are spatially invariant, which renders the flame as compact and presents a characteristic situation for LF oscillations. Oppositely, the length scales in the HF regime are of equal order of magnitude so that local variation of flame-acoustic coupling effects require consideration, labeling the flame as thermoacoustically non-compact. Mathematically, this (non-)compactness is quantified by the Helmholtz number via

$$\mathrm{He} = \frac{\delta_{fl}}{\lambda_a} = \begin{cases} < HE_{\mathrm{thresh}} \rightarrow \text{compact} \\ \geq HE_{\mathrm{thresh}} \rightarrow \text{non-compact} \end{cases} \tag{1.9}$$

where δ_{fl} and λ_a refer to the characteristic flame length and the acoustic wavelength at the considered mode as indicated in Fig. 1.4. In Eqn. 1.9, the quantity HE_{thresh} presents a threshold constant that separates the compact and non-compact flame regimes. The precise value is problem-specific, i.e. depends on combustor, flame and mode of interest. As an approximate orientation, a compact flame's length scale should be much smaller than one quarter of the mode's wavelength. For example in this work, the threshold constant is found to be $HE_{\mathrm{thresh}} = 0.1$.

Multidimensional Modes

Thermoacoustically non-compact flame dynamics as given by Eqn. 1.9 usually occur in combination with multi-dimensional modes at frequencies beyond the geometrical cut-on value of the concerned chamber. Thus, as the second feature, HF oscillations manifest via transversal, radial, longitudinal (and any combinations thereof) acoustic modes, which applies to the most common types of gas turbine combustors, e.g. can, silo, annular, sequential systems. For LF oscillations, the encountered modes vary for different combustor types. Can and sequential combustors are typically governed by axial and one-dimensional modes. In silo systems, transversal, radial, longitudinal (and any combinations thereof) modes can form the basis of LF oscillations, while annular systems most often contain azimuthal modes with longitudinal components. Note that in this thesis, can-type combustors are considered so that HF and LF oscillations are distinguished by the governance of multi-dimensional and one-dimensional modes, respectively. An explicit consideration of multi-dimensional modes in LF system is not within the scope of this thesis, and thus, omitted. Representative LF and HF pressure modes in the geometry of the can-type model combustor (cf. Chap. 3) are shown in Fig. 1.4. The figure also reveals length scale relations to yield compact and non-compact thermoacoustic interactions for the LF and HF mode, respectively. The HF mode on which all investigation of this thesis are based is of first transversal (T1) type. A comprehensive overview of other transversal mode types – which are in principle equally applicable to this work's research objectives and results – can be found in [31,62,79,96,145].

Driving Mechanisms

The physical interaction mechanisms between acoustic and heat release oscillations differ between LF and HF systems, too. The former is governed by convective modulation mechanisms (e.g. mixture flow pulsations and, for the case of technically premixed systems, convectively transported equivalence ratio fluctuations entering the flame) that are converted into heat release oscillations at the flame. Whether convective modulation mechanisms also govern HF oscillations depends on two conditions: First, the mode shape needs to extent into the mixing section to be of non-zero value where the convective modulation mechanisms are initiated. Second, the frequency of the mode shape of interest needs to be within the active region of the low-pass behaviour of the flame. This low-pass behaviour depends on the length and time scales associated with the combustor setup as well as the flame

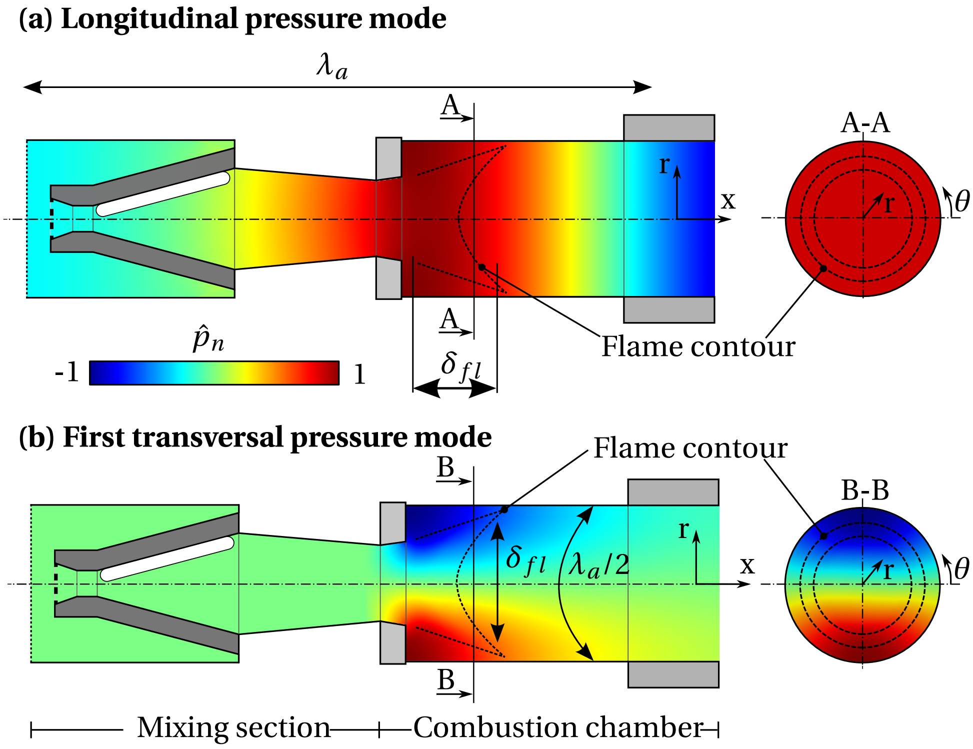

Figure 1.4: Combustion system with normalized (a) longitudinal pressure mode and compact flame (b) transversal pressure mode and non-compact flame

shape [137]. For the swirl-stabilized system concerned in this thesis (cf. Fig. 1.4), the T1 mode shape is zero. Moreover, the encountered frequencies are beyond the active zone of to flame's low-pass behaviour (cf. low-pass estimations in App. A). Thus, convective modulation effects can be disregarded for the types of swirl-stabilized configurations concerned in this thesis. However, this disregard of convective effects is not a generally applicable characteristic of HF oscillations. For example, in combustor configurations where a set of injector tubes is arranged circumferentially on the faceplate around the central burner (e.g. as in [57]), or if a sequential system with an auto-ignition flame is concerned [16], convectively driven heat release fluctuations might not be negligible. In these cases, the transversal mode in the chamber gives rise to longitudinal modes in the injector/mixing section to cause convective modulation mechanisms. To illustrate this scenario, the low-pass behaviour of the flames of a generic injector tube configuration is shown to start at higher frequencies than for a swirl-stabilized system with one central burner (cf. App. A). As is discussed in detail in Chap. 4, thermoacoustic driving at the T1 mode in this thesis is due to periodic flame shape deformations and displacement effects [148–150]. These mechanisms represent local thermoacoustic driving and are rather small compared to convective mechanisms, which explains the insignificance of the former particular in LF systems. Furthermore, the lacking presence of convective mechanisms for the concerned combustor setup explains the relevance the local driving effects in the HF regime at the T1 mode. At the same time, acoustic damping is lower for the concerned HF/T1 modes than for LF modes so that net values of Rayleigh integrals (or growth rates) are in the same area of magnitude for both frequency regimes.

Cut-on value as well as acoustic length scales depend on the individual combustor geometry. Hence, establishing a universally valid frequency value to separate LF and HF regimes is somewhat ambiguous. Rather, one can speak of HF instabilities if the foregoing features of multi-dimensional modes, non-compact flames and reduced significance of convective modulation govern the oscillations. Nevertheless, the frequencies at which HF oscillations occur in experimental and industrial gas turbine combustors are usually in the kilohertz regime, and thus labeled as "screech" instabilities [31, 119].

1.5 Literature Overview and State-of-the-Art Knowledge

High-frequency, screech tone thermoacoustic instabilities in gas turbines that are associated with non-compact interactions between heat release and acoustic oscillations have only recently entered the focus of scientific and engineering research. This is due to the increasing occurrence of these types of instabilities in industrial gas turbine combustors as a consequence of continuously expanding the systems' operational flexibility and part-load efficiency [140]. Thus, the available literature and corresponding state-of-the-art knowledge on HF instabilities sparse.

Investigations on premixed, swirl-stabilized flames in a experimental tubular combustor that exhibits limit-cycle oscillation at the first transversal mode revealed initial understanding on thermoacoustic driving mechanism. Schwing and his co-authors [151] first discovered pronounced dynamics of the outer shear-layer of the flame/flow at the frequency of the self-excited oscillations using Particle Image Velocimetry, which were thought to be responsible for the thermoacoustic feedback. However, in [149] it was found that the shear-layer response attenuates while the oscillations remain at a constant level for a change of operation parameters (e.g. the swirl intensity). Thus, the possibility of the shear-layer causing the feedback could be precluded. This is supported as the outer shear-layer in swirling flames is exposed to strong quenching effects [83] implying that total the heat release (and thus potential oscillations) is negligibly low. Although not directly causing heat release oscillations, the inspection of the shear-layer dynamics led to the finding the flame is periodically moving in-phase with the acoustic pressure and displacement field [148–150]. Based on this observation, a physical mechanism where the acoustic displacement field drives the heat release oscillation was established in [150]. A corresponding mathematical formulation of displacement driven heat release oscillations was derived for a simplified flame shape in [148].

Zellhuber [178] numerically assessed the transversal thermoacoustic performance of a generic reheat combustor using unsteady, compressible, reactive Large Eddy Simulations (LES). Zellhuber and Schwing [179] jointly confirmed the latter concept of flame displacement. They also introduced density modulations as an additional driving mechanism, although no physical connection between the former and the latter is drawn.

Ghani [50] numerically investigated HF oscillations in a bluff body gas combustor using LES, where the thermoacoustic performance is phenomenologically assessed. Any specific conclusions of mode types that govern the oscillations as well as physical driving mechanisms are not treated. Further numerical work on HF instabilities was carried out by Grimm [57]. In this work, an experimental can-type combustor with azimuthally distributed fuel injection at the faceplate was concerned. While the HF instability is reproduced by means of numerical simulations, the result interpretations remain of rather descriptive nature and a provision of conclusive physical insights is omitted.

A first analytical approach to quantify the thermoacoustic driving strength of swirl-stabilized flame interactions at the first transversal mode was taken by Hertweck [62, 63]. In this work, the Rayleigh integral was evaluated using the formulation of displacement and density modulations for a wide set of distributions of mean heat release shapes, which were obtained experimentally at different operation conditions. A dependency of the Rayleigh integral on the swirl-number was identified. Further work on analysis and modeling of HF instabilities in the field of gas turbine thermoacoustic seem non-existent in the open literature. Flame displacement is considered as a driving mechanism in [134] in which a transfer function is developed. This transfer function emerges as identical as the formulation used by Hertweck as is shown in [63].

Conversely to HF oscillations, the LF regime has been center of research projects for approximated 30 years. Thus, a vast pool of literature on fundamental mechanisms of thermoacoustics in combustion systems along with modeling approaches and analysis procedures is available. Although not directly applicable, this knowledge is certainly helpful to understand HF instabilities. A brief selection of reference found useful for this thesis is given in the following. Note that this list is certainly not complete as a respective provision of all relevant literature for LF instabilities would be far beyond the scope of the present literature overview.

Fundamental work on thermoacoustic instabilities in gas turbine combustors in terms of physics, theory and modeling approach can be found in [12, 39, 80, 96, 121, 138, 142]. Moreover, numerous literature on modeling and analysis approaches of LF oscillations is available. For example, efficient modeling methods using field methods in combinations with modal approaches in frequency domain to computationally predict a combustor's thermoacoustic stability state are provided in [27, 55, 158, 176]. Moreover, efficient computation methods on basis of the Linearized Euler/Navier-Stokes

Equations have been increasing used recently [52, 53, 82, 145, 154], which is methodologically independent whether the HF or LF regime is considered. Low-order modeling and analysis approaches for LF systems based on network concept in state-space – which enables access to frequency and time domain – are given in [13, 41, 139]. Analyzing thermoacoustic systems from a dynamical system perspective using time series either from experiments, from low-order simulations or ordinary differential equation descriptions allows to generate understanding of the system behavior [7, 21, 78, 108, 174]. Further approaches seek to model/investigate the combustor dynamics via ordinary differential equations including the effect of linear flame driving, non-linear saturation of heat release oscillations [51, 104] and stochastic effects due turbulent combustion noise is given in [26, 93, 112]. Review papers on thermoacoustic instabilities in gas turbine combustors can be found in [28, 101, 114].

Oppositely to gas turbine combustors, high-frequency thermoacoustic instabilities have been at the center of scientific attention in the field of rocket engines since the 1950s. Culick's monographic report [31] essentially presents most research results up to the year 2006 including an extensive literature database. This reference presents a useful starting point for many research tasks as it covers in principal all topics that are relevant for thermoacoustics in combustion systems such as driving and damping mechanism, modeling approaches, non-linear acoustics, dynamical and stochastic system approaches, rigorous mathematics as well as results on numerous theoretical and experimental analysis campaigns.

More recent and specific experimental work concerns high-frequency oscillations in cryogenic rocket combustors. This research focuses on exploring the physics that lead to unstable engine operation [58, 60, 61, 126, 155] at the first transversal mode. Numerical counterpart investigations on the basis of linearized conservation equations, Perturbed Non-conservative Non-linear Euler or compressible Navier-Stokes Equations are conducted in [59, 81, 136, 146, 167]. The combination of both, experimental and numerical elements aims to cross-validate experimental findings and extract theoretical explanation of the experimental observations in order to gain physical understanding of HF instabilities in rocket engines. Notably, Schulze [144, 146] developed a linear stability tool based on the Linearized Euler Equation in frequency domain applicable to non-compact rocket combustors with the focus on transversal modes. The work presents methodological details that are transferable for the development of linear stability tools of HF instabilities in gas turbine combustors.

1.6 Research Objectives and Structure of the Thesis

The central research focus of this thesis is the investigation of HF thermoacoustic oscillations in swirl-stabilized gas turbine combustors from modeling and analytical perspectives. Theoretical fundamentals, based on which the research tasks are carried out, are provided after this introduction in Chap. 2. The benchmark system, i.e. a swirl-stabilized, can-type experimental combustor that is used for all investigations conducted within this work is presented in Chap. 3. The acoustic mode of interest is the first transversal (T1) mode, although applicability of the research outcomes to other HF modes is not restricted.

The first objective of this thesis seeks to establish a comprehensive modeling and analysis framework applicable to HF and non-compact thermoacoustic oscillations in gas turbine combustors. This objective is motivated by the apparent non-existence of such a framework in the open literature (cf. Sec. 1.5). The framework is divided into two parts: The first part concerns linear thermoacoustic phenomena that can be modeled and analyzed in frequency domain. Respective details on the development, verification and application are provided in Chaps. 4-6. The specific features and research tasks associated with the development of the linear modeling framework unfold as follows:

- Provision of physical models of flame modulation, acoustic damping and mean flow interaction mechanisms in HF systems.
- Development of numerical computation methodologies for quantifica-

tion of flame driving and acoustic damping.

- Establishment of computational capabilities for linear thermoacoustic stability analyses.

For the second part of the modeling and analysis framework, non-linear phenomena in time domain are considered. Development details along with execution of corresponding analysis tasks are described in Chaps. 7-10, and specifically consists of:

- Development of a Reduced Order Modeling (ROM) approach for efficient time domain simulations of transversal HF oscillations.
- Derivation of a non-linear system of Stochastic Differential Equations (SDE) that govern amplitude dynamics of transversal HF modes in can-type chambers geometries for analytical consolidation of numerical time domain simulations.
- Development and validation of output-only system identification techniques – i.e. the extraction of thermoacoustic growth rates from time-domain data – for HF systems governed by transversal modes.

As the second objective of this thesis, the developed framework shall be applicable to industrial gas turbine combustors, which implies the necessity of the following general features:

- Time-efficient computation for system analyses to enable utilization within iterative thermoacoustic simulation practices for combustor design. [1]
- Applicability to three-dimensional geometries containing non-uniform and turbulent flow fields that are representative as encountered in industrial gas turbine combustors.
- Transferability to further types (e.g. can, silo, annular, sequential) of gas turbine combustors.

[1]For this reasons all numerical simulations and computations of this thesis are carried out on an PC with a Intel Core i7-4770K processor with 3.5 GHz and 32 GB RAM.

The third research objective of this thesis requires to generate new theoretical insights regarding HF thermoacoustic oscillations in gas turbine combustors, which presents a contribution towards the improvement of the overall understanding of the subject. The theoretical understanding is sought to be retrieved from the analyses and modeling results carried out with the framework developed for the first main objective of this thesis.

The research of this thesis is part of a research framework on HF thermoacoustics in gas turbine combustors involving two further doctoral projects with experimental (F. Berger, e.g. [15]) and numerical foci (P. Romero, e.g. [130]) at the Lehrstuhl für Thermodynamik of TU München. Respective results of these projects have been utilized for generation of a general understanding of the topic as well as for verification and validation tasks. For this thesis, whenever results from these other projects are used for any of these tasks, appropriate citations are placed. Note that these two other projects also involve the design and commissioning of a novel sequential burner test rig for investigation of HF oscillations in reheat flames [16, 129].

2 Theoretical Fundamentals

This chapter provides the theoretical background relevant for the forthcoming investigations of HF oscillations in thermoacoustically non-compact gas turbine combustors. The following topics are addressed: First, the Navier-Stokes Equations that describe gas turbine fluid flows in the most general manner are introduced in Sec. 2.1. In Sec. 2.2, flow variable decompositions are employed to derive a simplified set of conservation equations that govern only periodic flow motions, while random turbulent flow motions are absorbed within a steady mean flow description. Specific assumptions uniquely due to HF oscillations in gas turbine combustors are presented in Sec. 2.3. These assumptions are utilized in Sec. 2.4 to derive the Linearized Euler Equations, which form the mathematical starting point for all system analyses in this work. Section 2.5 presents a modal analysis approach based on Fourier Series descriptions of the unsteady flow variables, which yields the frequency domain formulation of the Linearized Euler Equations. Then, a concept to model the thermoacoustic interactions between flame dynamics and unsteady flow field by using coupling functions is outlined in Sec. 2.6. An integral description of disturbance fields in terms of total energy and respective source terms is given in Sec. 2.6, which are used to theoretically assess respective driving and damping processes occurring in thermoacoustic systems. Finally, theoretical and procedural information on numerical simulation based on the Finite Element Method as well as Computation Fluid Dynamics employed within this thesis are presented.

2.1 Navier-Stokes Equations

Thermoacoustic oscillations in gas turbine combustion chambers are allocated to the field of unsteady fluid mechanics. Thus, the governing equation are most fundamentally given by the Navier-Stokes equations as well as the energy equation. These equations are for a uni-molecular gas given by [31,96]

$$\frac{\partial \rho}{\partial t} + \mathbf{u} \cdot \nabla \rho + \rho \nabla \cdot \mathbf{u} = m_\rho, \tag{2.1}$$

$$\rho \frac{\partial \mathbf{u}}{\partial t} + \rho \mathbf{u} \cdot \nabla \mathbf{u} + \nabla p = F_{\mathbf{u},\tau} + \mathbf{m}_\mathbf{u}, \tag{2.2}$$

$$\frac{\partial p}{\partial t} + \mathbf{u} \cdot \nabla p + \gamma p \nabla \cdot \mathbf{u} = (\gamma - 1)\dot{q} + F_{p,\tau} + m_p. \tag{2.3}$$

The conservation variables $\rho(\mathbf{x}, t)$, $\mathbf{u}(\mathbf{x}, t)$, and $p(\mathbf{x}, t)$ denote density, vectorial velocity, and pressure, respectively, while γ is the ratio of specific heats. Note that temperatures and entropy can be computed using respective equations of state. The latter variables are general functions of time t and space $\mathbf{x}$ associated (for typical gas turbine combustor geometries) with Cartesian or cylindrical coordinate systems (cf. [84] for explicit formulations of these differential operators). Energy induction due to combustion is described by the volumetric source terms $\dot{q}(\mathbf{x}, t)$. In Eqns. 2.1-2.3, viscous and thermal diffusion as well as dissipation effects are absorbed in the functions $F_{\mathbf{u},\tau}(\mathbf{x}, t)$ and $F_{p,\tau}(\mathbf{x}, t)$, respectively. Explicit formulations of these diffusion functions can be found in [31]. Addition of mass, momentum and energy to the flow is described by the volumetric source terms $m_\rho(\mathbf{x}, t)$, $m_\mathbf{u}(\mathbf{x}, t)$ and $m_p(\mathbf{x}, t)$.

In principle, the unsteady flow behavior including thermoacoustic oscillations of a given combustion chamber can be retrieved by directly solving Eqns. 2.1-2.3, which has been pursued prominently by numerical approaches based on Unsteady-Reynolds-Averaged-Navier-Stokes (URANS) and Large-Eddy Simulations (LES) e.g. [142,153,172]. Although such simulations provide a precise degree level of physical results as by resolving all underlying fluid dynamic phenomena at once (e.g. turbulence, combustion reactions, periodic hydrodynamics, acoustic wave propagation and respective flame/flow interactions), required mesh sizes and computation times limit the application of such high-performance computing approaches to fundamental investigations [32]. As stated by the thesis objective in Sec. 1.6, numerical simulations carried out within this thesis are required to be fast and computationally efficient in order to ensure transferability to technically relevant combustors.

2.2 Time and Length Scale Decompositions

A simplification of the Navier-Stokes and energy equations is achieved by retaining and discarding all physical features in the equations that are respectively relevant and dispensable to the thermoacoustic performance of the concerned system. Unsteady flows at high Reynolds numbers, as occurring in gas turbine combustion chambers, can be divided into two groups, i.e.

1. Turbulent, random flow motions
2. Periodic, coherent flow motions

Periodic motions can be distinguished into acoustic and hydrodynamic flow disturbances. Acoustic disturbances can be interpreted as time-harmonic perturbations that are transported through the flow diffusively with the local speed of sound in a wave-like manner [127]. Hydrodynamic disturbances can be viewed as coherent and vortical structures within the flow, which are transported convectively with the local fluid velocity [96]. Similarly, entropy disturbances [38] can be thought of as local pockets of temperature fluctuations that convect with the local mean flow velocity, too. For thermoacoustic instabilities, only acoustic disturbances are of direct relevance as these disturbances constitute the self-sustained oscillations. Vorticity and entropy disturbances contribute only indirectly as part of acoustic damping and driving processes. Examples for an indirect impact that causes damping are vortex-shedding effects at area jumps [68] and entropy generation at flame fronts [38, 52]. Acoustic driving may be caused by whistling phenomena due to interactions between mean flow and vorticity disturbances [66, 127]. Indirect noise generation at accelerated flows through nozzle geometries due to interaction with entropy disturbances presents further possible scenario of non-flame-related acoustic driving [38]. Acoustic damping due to generation of vortical disturbances at shear layers of the mean flow is subject of Chap. 5, while entropy disturbances are neglected (cf. Sec. 2.3). Driving mechanisms due to non-flame-related effects are beyond the scope of this work. Turbulence can be viewed as stochastic motions without any recognizable pattern that lead to an increase of the flow's mixing and diffusion capabilities [123]. This description of turbulence is essentially the Reynolds-averaged interpretation [171], which is adopted in this work while it is recognized that turbulent flow physics is far more than macroscopically impacting the mean flow field as can be retrieved from the previous two references. It is important to point out that in reality the convective (vortical and entropy) disturbances – while transported by the mean flow – are exposed to turbulence, too. However, in order to achieve the desired simplification to depart from an LES framework, these coupling phenomena between turbulence and periodic motions are disregarded. This separation between turbulent and periodic motions is achieved by imposing the decomposition

$$\boldsymbol{\phi}(\mathbf{x},t) = \bar{\boldsymbol{\phi}}(\mathbf{x}) + \boldsymbol{\phi}'(\mathbf{x},t), \tag{2.4}$$

where the vector $\boldsymbol{\phi}$ represents all flow variables $\boldsymbol{\phi} = [\rho, \mathbf{u}, p]^T$ and sources $(F_{\mathbf{u},\tau}, F_{p,\tau}, m_\rho, \mathbf{m}_\mathbf{u}, m_p, \dot{q})$ associated with Eqns. 2.1-2.3. The decomposition in Eqn. 2.4 is composed of a spatially variable, steady part $\bar{\boldsymbol{\phi}}(\mathbf{x})$ and spatio-temporal unsteady part $\boldsymbol{\phi}'(\mathbf{x},t)$. All turbulence effects are absorbed within the steady fields, while all time-dependent, periodic, processes are described in the unsteady contributions. The mean flow field includes all physical effects relevant in turbulent flows occurring in gas turbine combustion chambers. These fields are separately obtained, typically by means of Computational Fluid Dynamics (CFD) of Reynolds-Averaged-Navier-Stokes (RANS) equations (cf. Sec. 2.8.2) Substituting Eqn. 2.4 into Eqns. 2.1–2.3 results in

$$\frac{\partial \rho'}{\partial t} + \bar{\mathbf{u}} \cdot \nabla \rho' + \mathbf{u}' \cdot \nabla \bar{\rho} + \bar{\rho} \nabla \cdot \mathbf{u}' + \rho' \nabla \cdot \bar{\mathbf{u}} = m_{\rho'} + S_{\rho'}, \tag{2.5}$$

$$\bar{\rho} \frac{\partial \mathbf{u}'}{\partial t} + \bar{\rho} \bar{\mathbf{u}} \cdot \nabla \mathbf{u}' + \bar{\rho} \mathbf{u}' \cdot \nabla \bar{\mathbf{u}} + \rho' \bar{\mathbf{u}} \cdot \nabla \bar{\mathbf{u}} + \nabla p' = F_{\mathbf{u}',\tau} + \mathbf{m}_{\mathbf{u}'} + \mathbf{S}_{\mathbf{u}'}, \tag{2.6}$$

$$\frac{\partial p'}{\partial t} + \bar{\mathbf{u}} \cdot \nabla p' + \mathbf{u}' \cdot \nabla \bar{p} + \gamma \bar{p} \nabla \cdot \mathbf{u}' + \gamma p' \nabla \cdot \bar{\mathbf{u}} = (\gamma - 1) \dot{q}' + F_{p',\tau} + m_{p'} + S_{p'}, \tag{2.7}$$

where $F_{\mathbf{u}',\tau}(\mathbf{x},t)$, $F_{p',\tau}(\mathbf{x},t)$, $m_{\rho'}(\mathbf{x},t)$, $\mathbf{m}_{\mathbf{u}'}(\mathbf{x},t)$, $m_{p'}(\mathbf{x},t)$ are the unsteady counterparts of the diffusion functions and volumetric source terms as defined above for Eqns. 2.1-2.3. Explicit formulation of the unsteady diffusion function can be found in [31]. In Eqns. 2.5-2.7, only first order terms are retained, while higher order terms, i.e. products of unsteady variables, are implicitly absorbed in the functions $S_{\rho'}(\mathbf{x},t), \mathbf{S}_{\mathbf{u}'}(\mathbf{x},t), S_{p'}(\mathbf{x},t)$. The explicit formulation of the higher order functions can be found in [31, 119], which physically govern non-linear interactions between the acoustic, vortical and entropy disturbances as is discussed in [31, 96].

The decomposition of the heat release source term in Eqn. 2.7 is of particular importance as the unsteady part $\dot{q}'$ represents the physical source terms of thermoacoustic oscillations. As described in Sec. 2.6, unsteady flame dynamics are generally comprised of complex mechanisms that contain linear thermoacoustic driving and non-linear saturation as well as stochastic forcing processes. Numerically resolving these processes is computationally expensive (cf. Sec. 2.2. Hence, the effect of flame dynamics is incorporated solely by using respective flame transfer functions.

Equations 2.5-2.7 represent a non-linear system of Partial Differential Equations (PDE), which carries less complex physics (due to exclusion of turbulence), but would still require considerable computational resources to produce respective numerical solutions. Hence, further simplifications of the governing equations are necessary, which are presented in the next section.

2.3 Simplifications and Assumptions

This section introduces a set of assumptions that are specific to HF thermoacoustics in gas turbine combustors, which enable the derivation the governing equations that form the basis of all modeling and analysis tasks in this thesis.

2.3.1 Isobaric Combustion at Low Mach-Numbers

Combustion in stationary gas turbines represents an (idealized) isobaric thermodynamic process, which is associated with low-Mach number mean flow fields. Hence, for simplification of the governing equations, the static pressure can be assumed as constant in the combustion chamber, implying that

$$\nabla \bar{p} = 0. \tag{2.8}$$

2.3.2 Inviscid and Adiabatic Unsteady Motions

The unsteady flow motions are assumed to occur inviscidly, which implies that $F_{\mathbf{u}',\tau} = F_{p',\tau} = 0$ in Eqns. 2.5-2.7, and presents a commonly employed assumption for thermoacoustic analyses [35,106]. Notice that turbulent dissipation processes are already excluded due to the presumed separation between periodic and turbulent flow motions as discussed in Sec. 2.2 above.

2.3.3 Isentropic Motions

The generation of entropy disturbances is neglected, which is non-intuitive in combustion systems, but physically justifiable for the T1 instabilities in swirl-stabilized combustor type used as benchmark in this thesis as follows: Entropy disturbances are caused by equivalence ratio fluctuations [132,170]. As the T1 mode does not extent into the mixing section in the concerned system (cf. Fig. 1.4), it cannot cause any fluctuation of equivalence ratio that would lead to entropy fluctuation at the flame. This isentropicity yields the relation between pressure and density [127] disturbances

$$p' = \rho' c^2, \tag{2.9}$$

which allows to reduce the number of governing equations by one as is shown below. Furthermore, imposing isentropicity in terms of the flow disturbances eliminates any ambiguity issues due to artificial generation of entropy waves [29], which are known to occur in frequency domain methods to analyze thermoacoustic systems.

2.3.4 Linearity of Disturbances

Thermoacoustic oscillations in gas turbine combustors are associated with flow disturbances (acoustic and vortical modes) that are observed to remain small compared to the mean flow [36], which implies for flow variable/sources in Eqns. 2.5-2.7

$$\boldsymbol{\phi}'(\mathbf{x}, t) \ll \bar{\boldsymbol{\phi}}(\mathbf{x}). \tag{2.10}$$

This condition holds true even in the case of an occurring thermoacoustic instability in which the system contains self-sustained acoustic limit cycle oscillations. Note that the characteristic mean quantity for linearity of the acoustic velocity is the speed of sound, i.e. requiring $\mathbf{u}'(\mathbf{x}, t) << c(\mathbf{x})$ [96]. As discussed in Sec. 1.3, a limit cycle state is caused by non-linear saturation effects that attenuate flame response strength until parity between flame driving and acoustic damping is reached. This saturation of exponential growth solely originates in the unsteady flame behavior (cf. [9, 36, 143] and Sec. 1.2), and not in any acoustic non-linearity that causes e.g. modal energy transfer as in rocket engine thermoacoustics (cf. [26,31,174,175]). Hence, the acoustic oscillations always remain "low" in amplitude, i.e. linear [36], which implies that only disturbance terms of first order are retained. Thus, higher order terms are discarded in Eqns. 2.1-2.3, i.e. $S_{\rho'}(\mathbf{x}, t) = S_{\mathbf{u}'}(\mathbf{x}, t) = S_{p'}(\mathbf{x}, t) = 0$. This linearity assumption only concerns the unsteady flow quantities, whereas the mean quantities certainly contain non-linear phenomena, e.g. turbulence and combustion.

2.4 Linearized Euler Equations

Substituting the assumptions and simplifications established in the previous section into Eqns. 2.5-2.7 yields the Linearized Euler Equations (LEE) that describe isentropic, unsteady flow disturbances in the HF regime encountered in gas turbine combustors:

$$\bar{\rho}\frac{\partial \mathbf{u}'}{\partial t} + \bar{\rho}\bar{\mathbf{u}} \cdot \nabla \mathbf{u}' + \bar{\rho}\mathbf{u}' \cdot \nabla \bar{\mathbf{u}} + \rho' \bar{\mathbf{u}} \cdot \nabla \bar{\mathbf{u}} + \nabla p' = \mathbf{m}_{\mathbf{u}'} \tag{2.11}$$

$$\frac{\partial p'}{\partial t} + \bar{\mathbf{u}} \cdot \nabla p' + \gamma \bar{p} \nabla \cdot \mathbf{u}' + \gamma p' \nabla \cdot \bar{\mathbf{u}} = (\gamma - 1)\dot{q}' + m_{p'}. \tag{2.12}$$

It is important to point out that while the higher order (i.e. non-linear) disturbance terms are canceled out, the heat release source $\dot{q}'$ itself is not restricted to be of first order. Moreover, prescribing the heat release with linear, non-linear and stochastic transfer functions (cf. Sec. 2.6) allows to model all thermoacoustic features of self-sustained limit cycles alongside the impact of combustion noise as observed during real combustor operation. These modeling tasks are carried out in the course of the time domain investigations of this thesis in Chaps. 8-9 for which Eqns. 2.11-2.12 form the mathematical starting point. Note that volumetric source terms of unsteady mass and energy are not further used in this thesis and set to zero, i.e. $m_{\rho'} = m_{p'} = 0$. Numerically determining the spatio-temporal behavior of the unsteady flow by resolving Eqns. 2.11-2.12 is time extensive, which is overcome by a Reduced Order Modeling framework developed in Chap. 7. Furthermore, if only the linear thermoacoustic behavior (e.g. for stability assessments) is of interest, a resolution of temporal evolution can be omitted by employing a modal analysis approach as presented next.

2.5 Modal Analysis in Frequency Domain

The linear nature of Eqns. 2.11-2.12 allows to describe the temporal evolution of the disturbance fields by a Fourier series, which results in a significant reduction of computational requirements to produce respective numerical solutions as the time dependency of the equations is eliminated. Hence, all linear investigations in this thesis are based on the following modal analysis approach. This approach is essentially comprised of expanding the pressure, velocity and heat release rate fluctuation fields via a complex Fourier series with a finite number of expansions, i.e.

$$p'(\mathbf{x},t) = \sum_{n=1}^{N} \frac{1}{2}\left(\hat{p}_n(\mathbf{x})\exp(i\omega_n t) + \hat{p}_n^*(\mathbf{x})\exp(-i\omega_n^* t)\right), \tag{2.13}$$

$$\mathbf{u}'(\mathbf{x},t) = \sum_{n=1}^{N} \frac{1}{2}\left(\hat{\mathbf{u}}_n(\mathbf{x})\exp(i\omega_n t) + \hat{\mathbf{u}}_n^*(\mathbf{x})\exp(-i\omega_n^* t)\right), \tag{2.14}$$

$$\rho'(\mathbf{x},t) = \sum_{n=1}^{N} \frac{1}{2}\left(\hat{\rho}_n(\mathbf{x})\exp(i\omega_n t) + \hat{\rho}_n^*(\mathbf{x})\exp(-i\omega_n^* t)\right), \tag{2.15}$$

$$\mathbf{m}_{\mathbf{u}'}(\mathbf{x},t) = \sum_{n=1}^{N} \frac{1}{2}\left(\mathbf{m}_{\hat{\mathbf{u}}_n}(\mathbf{x})\exp(i\omega_n t) + \mathbf{m}_{\hat{\mathbf{u}}_n}^*(\mathbf{x})\exp(-i\omega_n^* t)\right), \tag{2.16}$$

$$\dot{q}'(\mathbf{x},t) = \sum_{n=1}^{N} \frac{1}{2}\left(\hat{\dot{q}}_n(\mathbf{x})\exp(i\omega_n t) + \hat{\dot{q}}_n^*(\mathbf{x})\exp(-i\omega_n^* t)\right). \tag{2.17}$$

The complex valued Fourier coefficients at the n-th series expansion are denoted by $\hat{p}_n(\mathbf{x})$, $\hat{\mathbf{u}}_n(\mathbf{x})$ and $\hat{\dot{q}}_n(\mathbf{x})$, which are respectively referred to as pressure, velocity and heat release source mode shape. The mode shapes represent the spatial distribution of the acoustic oscillations associated with a distinct angular frequency ω_n. The asterisk $(*)$ denotes the complex conjugate of the modes and source terms in Eqns. 2.13-2.17. Hence, it is sufficient to compute mode shape and frequency to reconstruct the temporal oscillations. The equations that govern the respective mode shapes are derived as follows:

1. Substitution of Eqns. 2.13-2.17 into the LEE in Eqns. 2.11-2.12.
2. Dropping the summation due to linear independence of the expansion terms.
3. Multiplication with $\exp(-i\omega_n t)$ and integration over one period $\int_T(\cdot)\mathrm{d}t$ with $T = 2\pi/\omega_n$.

This yields the LEE in frequency domain, i.e.

$$\bar{\rho}\, i\omega_n \hat{\mathbf{u}}_n + \bar{\rho}\bar{\mathbf{u}}\cdot\nabla\hat{\mathbf{u}}_n + \bar{\rho}\hat{\mathbf{u}}_n\cdot\nabla\bar{\mathbf{u}} + \hat{\rho}_n\bar{\mathbf{u}}\cdot\nabla\bar{\mathbf{u}} + \nabla\hat{p}_n = \mathbf{m}_{\hat{\mathbf{u}}_n}, \tag{2.18}$$

$$i\omega\hat{p}_n + \bar{\mathbf{u}}\cdot\nabla\hat{p} + \gamma\bar{p}\nabla\cdot\hat{\mathbf{u}}_n + \gamma\hat{p}_n\nabla\cdot\bar{\mathbf{u}} = (\gamma-1)\hat{\dot{q}}_n. \tag{2.19}$$

Only linear contributions of the unsteady flame dynamics term are captured within the heat release source term $\hat{\dot{q}}_n$. Non-linear approaches in frequency domain based on flame describing functions are not considered in this thesis. Such approaches are used to computationally predict limit-cycle amplitudes [87, 97, 110, 135], which is not part of this thesis' scope.

Equations 2.18-2.19 can be solved using two different procedures, which yields two corresponding analysis types that are applied in the course of this thesis:

- Eigenfrequency analysis, i.e. synchronous solution of mode (eigenmode) and frequency (eigenfrequency) of the homogeneous version – i.e. zero external source terms – of Eqns. 2.18-2.19. The eigenfrequencies are generally complex, i.e. $\omega_n = \omega_{n,r} - i\omega_{n,i}$, where the real part describes the oscillation frequency and the imaginary part gives a measure of the energy balance of the concerned mode (cf. Sec. 2.7). Eigenfrequency analyses find particular application in this thesis for linear investigations of flame driving, acoustic damping and linear stability in Chaps. 4-6. [1]

- Response analysis, i.e. the solution of Eqns. 2.18-2.19 for a set of predefined values of oscillation frequencies ω_n. This requires setting one of the volumetric source terms ($\mathbf{m}_{\hat{\mathbf{u}}_n}$) to non-zero in specific regions in the domain or simply prescribing a wall boundary with a non-homogeneous Dirichlet boundary condition, which models e.g. external siren forcing. Pressure response analyses are utilized to compute the reflection coefficient of a thermoacoustic system as is carried out in the course of the damping quantification in Chap. 5. The concept of quantifying a thermoacoustic domain by means of a reflection coefficient is explained in [137, 144, 177] and is explicitly introduced for transversal modes in Chap. 5.

Numerous analyses in this thesis utilize Eqns. 2.18-2.19 with a zero mean velocity assumption. This eliminates any coupling terms between mean flow field and disturbance quantities. The resulting equations are then referred to as a Helmholtz Equation (HE) system, which reads

$$\bar{\rho} i\omega_n \hat{\mathbf{u}}_n + \nabla \hat{p}_n = \mathbf{m}_{\hat{\mathbf{u}}_n}, \tag{2.20}$$

$$i\omega \hat{p}_n + \gamma \bar{p} \nabla \cdot \hat{\mathbf{u}}_n = (\gamma - 1)\hat{\dot{q}}_n. \tag{2.21}$$

It is acknowledged that the "classical" Helmholtz Equation is a single, second order equation governing the acoustic pressure [127], while the HE system concerned in this work are retained in conservation form given by Eqns. 2.20-2.21. However, the computed mode solutions are identical between the "classical" Helmholtz Equation and the HE system concerned here, which justifies the terminology.

[1] Notice that the complex value of the frequency implies that the summation of Eqns. 2.13-2.17 is based on the Laplace instead of the Fourier transform [19], and an explicit distinction is omitted in this thesis for clarity.

2.6 Incorporation of Flame Dynamics

The foregoing discussions omitted any details regarding the treatment of the heat release source terms $\dot{q}'$ and $\hat{\dot{q}}$ in Eqns. 2.12-2.21. A direct numerical resolution of the unsteady flame dynamics along with the acoustic oscillation in a given combustor is unsuitable due to large computational costs as pointed out in Sec. 2.1. Instead, physical separability between the acoustic oscillations and the flame dynamics is assumed, which implies to view the former and latter as individual domains. This approach is commonly employed in LF thermoacoustic [118, 137] and adopted for the HF analyses in this work. The main idea is to establish stand-alone models (called domain) for acoustic and flame dynamics in the combustor of interest, which are then connected to yield the overall model of the thermoacoustic system performance. The physical connection between flame and acoustics is of source term nature only. Hence, only quantitative effects of the thermoacoustic interactions are captured (e.g. value of Rayleigh's integral or amplitude levels) while mode and flame shapes remain unaffected. Mean combustion $\bar{\dot{q}}$ is considered merely as a volume source of thermal energy so that an explicit discussion of combustion in gas turbine systems is not provided and one is referred to the literature [120].

2.6.1 The Acoustic Domain

The acoustic domain is geometrically and mathematically represented by the combustor volume and governing equations in time and/or frequency domain, respectively. In a stand-alone consideration of the acoustic domain, the heat release source term remains unspecified and can be viewed as "inactive". However, the effect of variable mean temperature/density/speed of sound fields due to mean combustion is accounted for.

2.6.2 The Flame Domain

Geometrically, the flame domain is given by the mean flame volume. The unsteady heat release oscillations are described by an mathematical function with acoustic quantities as the independent variables. Phenomenologically, this function is divided into

$$\dot{q}' = \dot{q}'_D + \dot{q}'_S. \tag{2.22}$$

where $\dot{q}'_D$ and $\dot{q}'_S$ denote deterministic and a stochastic contributions [21, 112, 113]. The deterministic part unfolds into

$$\dot{q}'_D = \dot{q}'_L + \dot{q}'_{NL}, \tag{2.23}$$

where $\dot{q}'_L(\mathbf{x}, t)$ and $\dot{q}'_{NL}(\mathbf{x}, t)$ describes all linear and non-linear processes related to the acoustic-flame interactions [108], respectively, Notice that the spatial dependency of the flame functions in Eqns. 2.22-2.23 automatically accounts for non-compact thermoacoustic interactions associated with HF and transversal mode oscillations encountered in this thesis.

The linear part $q'_L(\mathbf{x}, t)$ describes low amplitude modulation mechanism, i.e. how acoustic perturbations convert into heat release oscillations, and thus sources of sound. In this work, the linear part of the flame function is used for frequency domain analyses only, which is obtained by the Fourier transformation to give $\dot{q}'_L(\mathbf{x}, t) \rightarrow \hat{\dot{q}}_n(\mathbf{x})$ (cf. Eqn. 2.17).

Saturation of the exponential growth – in case of a linearly unstable situation – into a constant amplitude limit cycle is described via the non-linear flame function $q'_{NL}(\mathbf{x}, t)$. This assumption of a saturating flame is a validated approach for gas turbine combustion oscillations [36]. As explicated in Sec. 2.5, non-linear frequency domain approaches are not concerned in this thesis so that the non-linear function applies to the time domain only.

The stochastic part of the flame function $\dot{q}'_S$ in Eqn. 2.22 is used to model the effect of turbulent combustion noise, which stochastically modulates and excites the limit cycle amplitude in the unstable case and the system modes in the stable case, respectively.

The connection between the acoustic and flame domain is given by prescribing the – at this point unspecified – source term within the acoustic domain by the flame transfer function in Eqns. 2.22-2.23.

2.7 Energy Relations for Thermoacoustic Analyses

Thermoacoustic instabilities are associated with energy transformation processes, e.g. conversion of heat release oscillations into acoustic energy as explained in Chap. 1. At the same time, acoustic energy is dissipated due mean flow effects at the free shear layer of the flow. The generation and dissipation of acoustic energy is addressed in detail in Chaps. 4-5. In order to theoretically interpret and mathematically demonstrate the energy transformation processes encountered within thermoacoustic systems, an integral balance of the disturbance energy can be effectively used. Such a disturbance energy framework can be deduced from Eqns. 2.18-2.19 following Myer's work in [96, 105, 127], which gives with

$$\mathrm{E} = \frac{p'^2}{2\bar{\rho}c^2} + \frac{1}{2}\bar{\rho}(\mathbf{u}'\cdot\mathbf{u}') + \rho'(\bar{\mathbf{u}}\cdot\mathbf{u}') \tag{2.24}$$

an explicit formulation of the disturbance energy density field in the domain of interest. It can be viewed as a total energy of the unsteady flow field similar to total enthalpy of in fluid mechanics. The conservation equation for the energy density is given by

$$\frac{\mathrm{dE}}{\mathrm{d}t} + \nabla\cdot\mathbf{I} = \mathrm{D}_{\Omega'} + \mathrm{D}_{\mathbf{m}_{\mathbf{u}'}} + \mathrm{D}_{\dot{q}'}, \tag{2.25}$$

where I represents the energy flux, while $\mathrm{D}_{\Omega'}, \mathrm{D}_{\mathbf{m}_{\mathbf{u}'}}$ and $\mathrm{D}_{\dot{q}'}$ describe volumetric source terms due to mean flow effects, momentum sources and heat release oscillations, respectively. The sources expand to [96, 105, 127]

$$\mathbf{I} = (\bar{\rho}\mathbf{u}' + \rho'\bar{\mathbf{u}})(p'/\bar{\rho} + \bar{\mathbf{u}} \cdot \mathbf{u}'), \tag{2.26}$$

$$\mathrm{D}_{\Omega'} = \bar{\rho}\bar{\mathbf{u}} \cdot (\Omega' \times \mathbf{u}') + \rho'\mathbf{u}' \cdot (\bar{\Omega} \times \bar{\mathbf{u}}), \tag{2.27}$$

$$\mathrm{D}_{\mathbf{m}_{\mathbf{u}'}} = \mathbf{m}_{\mathbf{u}'} \cdot (\mathbf{u}' + \rho'\bar{\mathbf{u}}/\bar{\rho}), \tag{2.28}$$

$$\mathrm{D}_{\dot{q}'} = \frac{\gamma - 1}{\gamma \bar{p}} p' \dot{q}'. \tag{2.29}$$

The variables $\Omega' = \nabla \times \mathbf{u}'$ and $\bar{\Omega} = \nabla \times \bar{\mathbf{u}}$ in Eqn. 2.27 denote unsteady and mean vorticity of the flow field. The heat release source term $\mathrm{D}_{\dot{q}'}$ is the product of pressure and heat release rate oscillations. This product identifies as the Rayleigh integrand in Eqn. 1.7 and connects the theoretical and phenomenological energy depiction of thermoacoustic instabilities in this section and in Sec. 1.2, respectively.

An integral value of the energy equation is obtained by volume integrations over the computational domain V, which gives for the individual terms of Eqn. 2.25

$$\tilde{\mathrm{E}} = \int_V \mathrm{E} \mathrm{d}V, \tag{2.30}$$

$$\tilde{\mathrm{I}} = \int_V \nabla \cdot \mathbf{I} \mathrm{d}V = \oint_S \mathbf{I} \cdot \mathbf{n} \mathrm{dS}, \tag{2.31}$$

$$\tilde{\mathrm{D}}_{\Omega'} = \int_V \mathrm{D}_{\Omega'} \mathrm{d}V, \tag{2.32}$$

$$\tilde{\mathrm{D}}_{\mathbf{m}_{\mathbf{u}'}} = \int_V \mathrm{D}_{\mathbf{m}_{\mathbf{u}'}} \mathrm{d}V, \tag{2.33}$$

$$\tilde{\mathrm{D}}_{\dot{q}'} = \int_V \mathrm{D}_{\dot{q}'} \mathrm{d}V. \tag{2.34}$$

The oscillatory nature of these integral terms is eliminated by substituting the modal description given by Eqns. 2.13-2.17, and averaging over one period to yield

$$\left\langle \tilde{\mathrm{E}}_n \right\rangle = \frac{1}{4}\int_V [(\hat{p}_n \hat{p}_n^*)/(\bar{\rho} c^2) + \bar{\rho}(\hat{\mathbf{u}}_\mathbf{n} \cdot \hat{\mathbf{u}}_\mathbf{n}^*) + (\hat{\rho}_n^* \bar{\mathbf{u}} \cdot \hat{\mathbf{u}}_n + \hat{\rho}_n \bar{\mathbf{u}} \cdot \hat{\mathbf{u}}_n^*)]\mathrm{d}V, \tag{2.35}$$

$$\begin{aligned}\left\langle \tilde{\mathrm{I}}_n \right\rangle &= \frac{1}{4}\oint_\mathrm{S} [\hat{\mathrm{I}}_{1,n} \hat{\mathrm{I}}_{2,n}^* + \hat{\mathrm{I}}_{1,n}^* \hat{\mathrm{I}}_{2,n}]\mathrm{dS} \\ &= \frac{1}{4}\oint_\mathrm{S} [(\hat{p}_n + \bar{\rho}\bar{\mathbf{u}}_n \cdot \hat{\mathbf{u}}_n)(\hat{\mathbf{u}}_n^* + \hat{\rho}_n^* \bar{\mathbf{u}}/\bar{\rho}) + (\hat{p}_n^* + \bar{\rho}\bar{\mathbf{u}} \cdot \hat{\mathbf{u}}_n^*)(\hat{\mathbf{u}}_n + \hat{\rho}_n \bar{\mathbf{u}}/\bar{\rho})] \cdot \mathbf{n}\mathrm{dS},\end{aligned} \tag{2.36}$$

$$\left\langle \tilde{\mathrm{D}}_{\hat{\Omega},n} \right\rangle = \frac{1}{4}\int_V [\bar{\rho}\bar{\mathbf{u}} \cdot (\hat{\Omega}_n \times \hat{\mathbf{u}}_n^* + \hat{\Omega}_n^* \times \hat{\mathbf{u}}) + (\hat{\rho}_n \hat{\mathbf{u}}_n^* + \hat{\rho}_n^* \hat{\mathbf{u}}_n) \cdot (\bar{\Omega} \times \bar{\mathbf{u}})]\mathrm{d}V, \tag{2.37}$$

$$\left\langle \tilde{\mathrm{D}}_{\mathbf{m}_{\hat{\mathbf{u}}_\mathbf{n}}} \right\rangle = \frac{1}{4}\int_V [\mathbf{m}_{\hat{\mathbf{u}}_\mathbf{n}} \cdot (\hat{\mathbf{u}}_\mathbf{n}^* + \hat{\rho}_n^* \bar{\mathbf{u}}/\bar{\rho}) + \mathbf{m}_{\hat{\mathbf{u}}_\mathbf{n}^*} \cdot (\hat{\mathbf{u}} + \hat{\rho}_n \bar{\mathbf{u}}/\bar{\rho})\mathrm{d}V], \tag{2.38}$$

$$\left\langle \tilde{\mathrm{D}}_{\hat{q}_n} \right\rangle = \frac{1}{4}\int_V [(\gamma - 1)\left(\hat{q}_n \hat{p}_n^* + \hat{q}_n^* \hat{p}_n\right)/(\gamma \bar{p})]\mathrm{d}V. \tag{2.39}$$

As before, the summations are dropped due to linear independence of the expansion terms so that Eqns. 2.35-2.39 describe the respective energy relation of mode n. The flux term in Eqn. 2.36 was transformed into a surface integral using the Gaussian theorem [84], which describes the energy transfer across the system boundaries. Finally, the governing equation for the period averaged modal energy is given by

$$\frac{\mathrm{d}\left\langle \tilde{\mathrm{E}}_n \right\rangle}{\mathrm{d}t} + \left\langle \tilde{\mathrm{I}}_n \right\rangle = \left\langle \tilde{\mathrm{D}}_{\hat{\Omega},n} \right\rangle + \left\langle \tilde{\mathrm{D}}_{\mathbf{m}_{\hat{\mathbf{u}}_n}} \right\rangle + \left\langle \tilde{\mathrm{D}}_{\hat{q}_n} \right\rangle. \tag{2.40}$$

As is derived in [31], the energy change can be related to the imaginary part of the complex eigenfrequency of the mode, i.e.

$$\omega_{n,i} = \frac{1}{2}\frac{1}{\left\langle \tilde{\mathrm{E}}_n \right\rangle}\frac{\mathrm{d}\left\langle \tilde{\mathrm{E}}_n \right\rangle}{\mathrm{d}t} = \frac{1}{2}\frac{1}{\left\langle \tilde{\mathrm{E}}_n \right\rangle}[\left\langle \tilde{\mathrm{D}}_{\hat{\Omega},n} \right\rangle + \left\langle \tilde{\mathrm{D}}_{\mathbf{m}_{\hat{\mathbf{u}}_n}} \right\rangle + \left\langle \tilde{\mathrm{D}}_{\hat{q}_n} \right\rangle - \left\langle \tilde{\mathrm{I}}_n \right\rangle]. \tag{2.41}$$

Interpretatively, Eqn. 2.41 describes the total disturbance energy balance of the concerend mode that is governed by the LEE in Eqns. 2.18-2.19. Physical sources and sinks that determine this energy balance are due to mean flow interactions $\left\langle \tilde{\mathrm{D}}_{\Omega,n} \right\rangle$, volumetric momentum sources $\left\langle \tilde{\mathrm{D}}_{\mathbf{m}_{\hat{\mathbf{u}}_n}} \right\rangle$, heat release oscillation $\left\langle \tilde{\mathrm{D}}_{\hat{q}_n} \right\rangle$ and fluxes across the system boundaries $\left\langle \tilde{\mathrm{I}}_n \right\rangle$. Hence, computing the complex eigenfrequency (in particular the imaginary part) automatically provides the complete energy balance of the mode of interest.

2.8 Numerical Methods

This section provides the basics of numerical methods employed in this thesis. Specifically, an overview of the Finite Element Method (FEM) to discretize and solve thermoacoustic problems as well as Computational Fluid Dynamics (CFD) to compute steady, swirling mean flow fields is provided.

2.8.1 Finite Element Method for Thermoacoustic Problems

Numerical solutions of Eqns. 2.18-2.19 can be obtained using a stabilized FEM. The stabilization is required to avoid spurious solutions caused by the convective terms of the LEE [54, 124, 145, 165] and is based on the idea of adding artificial diffusion to the equations. The weak form of the governing equations – which presents the first step of FEM discretization procedures (cf. details in [2,44]) – is expanded with an extra term that consists of the residuum of the actual equation and a stabilization operator. For the LEE in Eqns. 2.18-2.19, this weak form formulation including the stabilization extension reads

$$\begin{aligned}\int_V [&\underbrace{(i\omega_n \mathbf{E}^c \hat{\boldsymbol{\phi}}_n^c + \mathbf{A}_{LEE}^c \hat{\boldsymbol{\phi}}_n^c - \mathbf{B}_{\mathbf{m}_{\hat{\mathbf{u}}_n}}^c - \mathbf{B}_{\hat{\dot{q}}_n}^c)}_{\text{residuum}} \mathbf{N}_{\hat{\boldsymbol{\phi}}} \\ &+ \underbrace{(i\omega_n \mathbf{E}^c \hat{\boldsymbol{\phi}}_n^c + \mathbf{A}_{LEE}^c \hat{\boldsymbol{\phi}}_n^c - \mathbf{B}_{\mathbf{m}_{\hat{\mathbf{u}}_n}}^c - \mathbf{B}_{\hat{\dot{q}}_n}^c)}_{\text{residuum}} \tau \underbrace{\mathbf{A}_{SUPG}^c \mathbf{N}_{\hat{\boldsymbol{\phi}}}}_{\text{stabilizer}}] \mathrm{d}V = 0, \end{aligned} \tag{2.42}$$

where V refers to the volume of the computational domain, and $\hat{\boldsymbol{\phi}}_n^c$ represents the solution variable, i.e. pressure $\hat{p}_n$ and velocity $\hat{\mathbf{u}}_n$ disturbances. The matrices $\mathbf{E}^c, \mathbf{A}_{LEE}^c$ and $\mathbf{A}_{SUPG}^c$ are linear operators associated with the strong form and the stabilization scheme, respectively. The vectors $\mathbf{B}_{\mathbf{m}_{\hat{\mathbf{u}}_n}}^c$ and $\mathbf{B}_{\hat{\dot{q}}_n}^c$ contain the volumetric source term of momentum and heat release ocillations, respectively. The superscript c indicates the continuous nature of the operators, which explicit forms are provided in [52, 144]. In the continuous case, the stabilization terms do not exert a quantitative impact on the solution. This becomes clear because the residuum for continuous solutions of the LEE is zero so that the stabilization term vanishes [144, 145]. However, as the solutions are produced numerically, the impact of stabilization cannot be neglected and should be assessed for each analysis individually. Throughout this thesis, the residual based Streamline Upwind Petrov Galerkin (SUPG) artificial diffusion scheme is employed, which acts only on the convection terms in the residuum (cf. [52, 124, 144, 145]). There are other schemes available, too, which can be found in the previous references. Finally, the constant parameter τ is used to control the stabilization strength as is discussed further below.

Presuming the presence of boundary conditions and a suitable mesh, i.e. a collection of nodes that span the geometry of the computational domain/combustor of interest, Eqn. 2.42 – and thereby Eqns. 2.18-2.19 – is discretized using standard FEM procedures (cf. [2,44] for FEM fundamentals). Linear shape functions are used, which emerged an optimal balance between solution robustness and computational efficiency in this work. The FEM discretization transforms the differential into an algebraic system of equation, i.e.

$$i\omega_n \mathbf{E}\hat{\boldsymbol{\phi}}_n = \underbrace{(\mathbf{A}_{LEE} + \tau\mathbf{A}_{SUPG})}_{\mathbf{A}}\hat{\boldsymbol{\phi}}_n + \mathbf{B}_{\mathbf{m}_{\hat{\mathbf{u}}n}} + \mathbf{B}_{\hat{\dot{q}}_n}, \tag{2.43}$$

where $\mathbf{E}$, $\mathbf{A}_{LEE}$ and $\mathbf{A}_{SUPG}$ denote discretization matrices associated with the time derivatives (i.e. $i\omega_n$ terms), spatial derivatives and SUPG stabilization operators, respectively. The total system matrix of Eqn. 2.43 is given by $\mathbf{A} = \mathbf{A}_{LEE} + \tau\mathbf{A}_{SUPG}$. The solution vector $\hat{\boldsymbol{\phi}}_n = [\hat{p}_n \;\; \hat{\mathbf{u}}_n]^T$ hosts the discrete solution variable at every node in the mesh. The dimension of the matrices are $N \times N$, which denotes the number of degrees of freedoms, i.e. the unknown variables at the nodes of the mesh. The vectors $\mathbf{B}_{\mathbf{m}_{\hat{\mathbf{u}}n}}$ and $\mathbf{B}_{\hat{\dot{q}}_n}$ represent the discretization of momentum and heat release source terms, respectively. Equation 2.43 can then be solved for the desired mode shapes at corresponding frequencies using readily available standard inversion methodologies as presented in detail in [2, 43]. Therefore, either an eigenvalue problem or forced field problem can be solved as described in Sec. 2.5. Expanding the heat release source term in Eqn. 2.43 with an explicit expression depending on the acoustic quantities connects the flame and acoustic domain as well as models the thermoacoustic system performance as described in Sec. 2.6. Specifically, the flame source term $\hat{\dot{q}}_n$, which is absorbed in $\mathbf{B}_{\hat{\dot{q}}_n}$, may depend on the eigenfrequency

ω_n. Then, the eigenproblem of Eqn. 2.43 is solved for the eigenvector and -frequency associated with the first transversal modes using an iterative procedure as explained in [52]. The stabilization parameter τ in Eqn. 2.43 is a field quantity, which is given by [165]

$$\tau = \alpha_\tau \max\left(\frac{\mathrm{H}_{x,el}}{|\overline{u}_{x,el}| + c_{el}}, \frac{\mathrm{H}_{y,el}}{|\overline{u}_{y,el}| + c_{el}}, \frac{\mathrm{H}_{z,el}}{|\overline{u}_{z,el}| + c_{el}}\right), \tag{2.44}$$

where the parameter α_τ is a user-defined variable to achieve the desired stability. The arguments of the maximum function are composed of the local element height in three spatial directions ($\mathrm{H}_{x,el}/\mathrm{H}_{y,el}/\mathrm{H}_{z,el}$), the local magnitude of the flow velocity vector components ($|\overline{u}_{x,el}|/|\overline{u}_{y,el}|/|\overline{u}_{z,el}|$) and the local speed of sound c_{el}. The numerical stabilization is required due to the presence of convective terms in the LEE. Hence, analyses based on a zero mean velocity assumption, i.e. HE systems, are not needed to be stabilized. The specification of boundary conditions completes the FEM discretization, which are divided into wall and inlet/outlet types.

Wall Boundary Conditions

Slip wall conditions are assumed for all velocity disturbances, i.e.

$$\hat{\mathbf{u}}_n \cdot \mathbf{n} = 0, \tag{2.45}$$

where $\mathbf{n}$ is the normal vector of the boundary pointing out of the domain. In the case of sweep analyses, an excitation device (e.g. loudspeaker) may be prescribed by assigning the wall condition in Eqn. 2.45 a finite amplitude value, i.e.

$$\hat{\mathbf{u}}_n \cdot \mathbf{n} = u_{ex}. \tag{2.46}$$

Inlet and Outlet Boundary Conditions

Inlet and outlet boundary conditions are prescribed by an impedance formulation, i.e.

$$\bar{\rho} c Z_n = \frac{\hat{p}_n}{\hat{\mathbf{u}}_\mathbf{n} \cdot \mathbf{n}}, \tag{2.47}$$

where $\bar{\rho}$ and c are the mean flow density and speed of sound at the particular boundary, respectively. Essentially, the impedance in Eqn. 2.47 relates the pressure and velocity disturbances. It may be frequency dependent e.g. if it originates from measurements to describe the acoustic volumes up- and downstream of the considered analysis domain. Details on incorporating acoustic volumes adjacent to the chamber domain by measured impedance can be found in [139, 145]. In this thesis, volumes adjacent to the analysis domain are assumed to have no impact on the modes of interest as is discussed in the results chapters. Hence, in- and outlet boundaries are prescribed with energy-neutral conditions, which are derived from the surface flux terms of disturbance energy equation in Eqn. 2.36. Specifically, the flux term is required to become zero, which yields two boundary conditions, i.e.

$$\hat{I}_{1,n} = \hat{h}_n = \hat{p}_n + \bar{\rho}\bar{\mathbf{u}} \cdot \hat{\mathbf{u}}_{\mathbf{n}} = 0, \tag{2.48}$$

$$\hat{I}_{2,n} = \hat{\dot{m}}_n = (\hat{\mathbf{u}}_n + \hat{\rho}_n \bar{\mathbf{u}}/\bar{\rho}) \cdot \mathbf{n} = 0, \tag{2.49}$$

where $\hat{I}_{1,n}$ and $\hat{I}_{2,n}$ are often referred to as fluctuating enthalpy and mass of the flow disturbance, respectively. Re-arranging these formulation in terms of a specific impedance for incorporation into the FEM discretization yields

$$\bar{\rho} c Z_n = -\bar{\rho}\bar{\mathbf{u}}, \tag{2.50}$$

$$\bar{\rho} c Z_n = -\frac{\bar{\rho} c^2}{\bar{\mathbf{u}} \cdot \mathbf{n}}. \tag{2.51}$$

Notice that Eqns. 2.50 and 2.51 respectively converge into an open and closed end termination from a classical acoustic perspective when a zero-mean velocity assumption is imposed , i.e. a HE system is concerned:

$$\bar{\rho} c Z_n = 0 \tag{2.52}$$

$$\bar{\rho} c Z_n = \infty \tag{2.53}$$

Dynamical Systems in Time Domain

For time domain simulations and analyses, Eqn. 2.43 is inversely Fourier transformed, which is permitted due to the linear nature of the equation to result in

$$\mathbf{E}\frac{\mathrm{d}\boldsymbol{\phi}'}{\mathrm{d}t} = \mathbf{A}\boldsymbol{\phi}' + \mathbf{B}_{\mathbf{m}_{\mathbf{u}'}}\mathbf{u}_m + \mathbf{B}_{\dot{q}'}\mathbf{u}_q, \tag{2.54}$$

where $\mathbf{E}$ is the descriptor matrix, $\mathbf{A}$ is the system matrix, and $\boldsymbol{\phi}' = [p' \; \mathbf{u}']^T$ is the state vector hosting the unsteady flow variable at each mesh node. The vectors (matrices) $\mathbf{B}_{\dot{q}'}$ and $\mathbf{B}_{\mathbf{m}'_{\mathbf{u}}}$ contain information on spatial location of heat release and momentum source terms, respectively. The corresponding time-domain signals are denoted by $\mathbf{u}_q$ and $\mathbf{u}_m$. Prescribing the former with a suitable flame dynamics function given by Eqn. 2.22 models linear, non-linear and stochastic thermoacoustic interactions, which is subject of Chaps. 7-8 of this thesis. Conveniently, the foregoing matrices/vectors are identical to the frequency domain versions given by Eqn. 2.43. Hence, it suffices to carry out the discretization using only the frequency domain formulations of the concerned governing equations, which yields discrete systems in both, time and frequency domain. Note this matrix equality requires the prescription of frequency independent boundary conditions for the discretization tasks. The incorporation of frequency dependent boundary conditions and flame source terms can be carried out after the discretization steps during the temporal integrations using interconnection procedures in an state-space environment [139].

Typical sizes of discretization matrices ($\mathbf{E}$ and $\mathbf{A}$) for practical thermoacoustic systems concerned in this thesis are $N = 100{,}000 - 500{,}000$. Numerical integrations of frequency domain formulations are straightforward. Time domain counterparts require extensive numerical efforts, which is sought to be avoided as by this thesis' research objectives (cf. Sec. 1.6). The reasons for this disparity is given by the steady and transient nature of the systems, where the latter is substantially more demanding in terms of computational resources. However, this disadvantage of time domain simulations is overcome in this thesis by the development (and employment) of a Reduced Order Modeling (ROM) framework. This ROM approach is applicable to LEE (or HE) systems given by Eqn. 2.54, which enables fast pace, transient simulations and is subject of Chaps. 7-8.

All FEM discretization tasks are carried out using COMSOL Multiphysics [2].

The COMSOL environment allows to prescribe weak form equations given by Eqn. 2.42 of e.g. the LEE or HE systems, corresponding boundary conditions, source terms and element types in a user-defined manner. The discretization itself is carried out in the background by the source code inaccessible to the user. The numerical solutions associated with frequency domain analyses in this work are produced within the COMSOL environment in which optimized solvers e.g. MUltifrontal Massively Parallel sparse direct Solver [2] for eigenfrequency and sweep computations are readily incorporated. Furthermore, the discretization matrices can be extracted, which presents a crucial input to the ROM framework developed in Chap. 7.

2.8.2 Mean Flow Field

The discretization of the LEE for analyses in both, time and frequency requires a steady mean flow field of the concerned combustor. The determination of these fields occurs by numerical simulations using CFD. For all mean flow simulation in this thesis, Reynolds-Averaged Navier Stokes (RANS) approach is employed using a $k-\epsilon$ turbulence model with wall functions [1, 43, 163]. Combustion models are not considered as all CFD simulations concern isothermal operations points. Temperature fields are retrieved from chemiluminescence measurements and mapped into the thermoacoustic analysis domain (cf. details in Chap. 4). Consequently, the assumption is imposed that the velocity field does not change significantly for isothermal and reactive conditions. This is justified for low Mach number flows, and implies that interactions between unsteady flow disturbances and mean velocity field is invariant between isothermal and reactive conditions (cf. Chap. 5 for details). ANSYS Fluent [1] is used to conduct all CFD simulation. As RANS CFD simulations represent a standard procedure in engineering analyses, an explicit treatment of theory, discretization and solution procedures, turbulence modeling, convergence criteria and strategies is left to the literature [1,43,163].

3 Benchmark Combustion System

This chapter presents details of the combustion system used as benchmark for the research tasks in this thesis. The system represents an atmospheric, experimental version of a can-type combustor as are commonly implemented in industrial gas turbines. A schematic of the test-rig along with a representative mean flow field is shown in Fig. 3.1. All mean flow fields used in this thesis were obtained through CFD simulations by applying a unstructured hexahedral ("cut-cell") automatic meshing procedure as outlined in [152]. The combustor system operates as follows. A preheated and perfectly-premixed gas (natural gas and air) is introduced into the plenum (a) and flows through A^2EV swirl generator (b). A swirling flow (c) in counter-clockwise direction with reference to the coordinate convention indicated in Fig. 3.1 is generated, which convect through the mixing tube (d). The flow enters a tubular quartz glass combustion chamber (e) and is consumed by a lean, turbulent, swirl-stabilized, premixed flame (f). The combustion product flow leaves the chamber through an exhaust duct (g). The following features, which are relevant for this thesis, can be varied:

- Swirl-strength (i.e. swirl number) generated in the A^2EV swirler.
- Preheated gas temperatures ranging from $\bar{T}_{in} = 293.15\,\mathrm{K} - 673.15\,\mathrm{K}$.
- Air and fuel mass flow rates to achieve different levels of thermal power (range: $P_{th} = 97\,\mathrm{kW} - 350\,\mathrm{kW}$) and air excess ratios (range: $\lambda = 1 - 2$).

In-depth information on specific designs of the entire system, components, commissioning and operation of this test-rig can be found in [100, 131]. The operation of the combustor with perfectly-premixed instead of technically-premixed combustion (as in industrial systems) is justified by the insignificance of convective modulation effects for the T1 mode in the benchmark

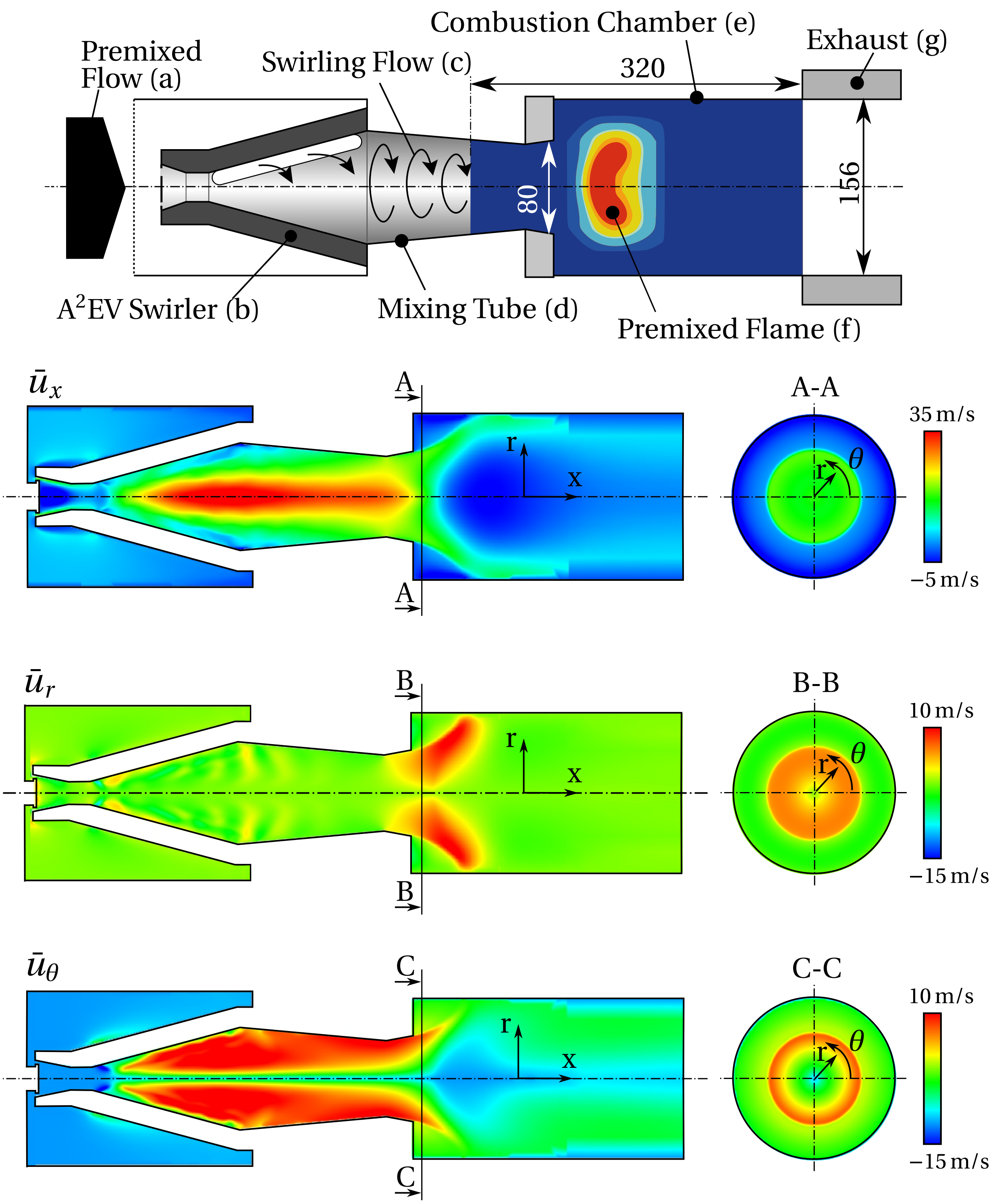

Figure 3.1: Schematic of experimental benchmark combustion system (dimensions are in mm) along with axial, radial and azimuthal mean flow velocity fields (from top to bottom)

system. This insignificance is due to on the one hand the zero value of the T1 mode in the mixing section and on the other hand due to the low-pass characteristic of the flame in the benchmark system as explained in Sec. 1.4 and App. A. The absence of these mechanisms allows to reason that thermoacoustic driving mechanisms are equal between technically- and perfectly-premixed configurations of the benchmark system at the T1 mode. At certain operation points, the T1 mode in the combustion chamber undergoes a thermoacoustic instability, which yields ideal investigation conditions for HF oscillations. Specifically, the system is utilized for the following tasks in the course of this thesis:

- Provision of geometry and operational conditions for computations.
- Test case for validation of the modeling and analysis framework.
- Research subject for analysis and investigations of HF instabilities.

For these tasks, two configurations of the benchmark system are considered: The first configuration refers to reactive operation as above-described. Analysis domain and shape of the targeted T1 mode are shown in Fig. 3.2.

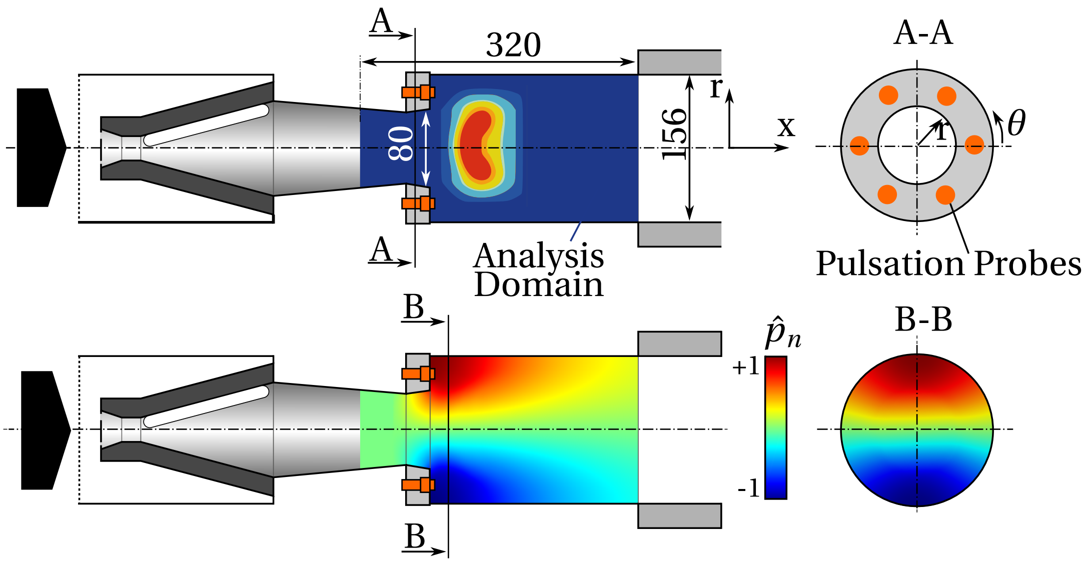

Figure 3.2: Reactive configuration of swirl-stabilized benchmark system (dimensions are in mm)

The figure indicates six pressure sensors that are azimuthally distributed at the faceplate of the chamber to provide acoustic pressure measurements. Note that broadband excitation of acoustic chamber modes occurs implicitly due to turbulent combustion for stable as well as unstable operation points. Thus, there are no external excitation devices for the reactive configuration. Information on the stability state of each considered operation points are given in a binary manner, i.e. whether a limit cycle occurs or not. Furthermore, high-speed camera diagnostics allow to record chemiluminescence radiation of the steady and unsteady combustion processes. Specific technical information on diagnostic equipment and respective operational details (pressure probe, camera systems, etc.) can be retrieved from [15, 17, 18, 62, 63, 148–150].

As the second configuration, an isothermal setup of the swirl-stabilized benchmark combustor is utilized for investigations of interactions between mean flow and acoustic oscillations at transversal modes. This setup establishes clearly defined investigation conditions of the underlying aeroacoustic processes without any superimposed impact of flame dynamics. The analysis domain along with the T1 mode shape are shown in Fig. 3.3.

A nozzle termination is attached to the chamber in order to prevent the transversal acoustic modes from propagating downstream into the exhaust duct and interact with the boundary, i.e. experience boundary damping. This converging nozzle diameter causes a local increase of the cut-on frequency so that the transversal modes attenuate in downstream direction. Equivalently, the same mode attenuates in upstream direction due to the smaller diameter (higher cut-on value) of the mixing tube so that the acoustic performance of the upstream periphery can be neglected at the considered frequencies. This creates comparable mode shapes as encountered for reactive cases, where the associated mean temperature increase in downstream direction causes the increase in cut-on frequency that leads to the axial mode attenuation.

In terms of diagnostics, the same dynamic pressure probe arrangement at the faceplate for the reactive counterpart is available as illustrated by Fig. 3.3. Turbulent flow noise is not strong enough to sufficiently excite the acoustic modes in the system. Hence, two acoustic compression drivers are

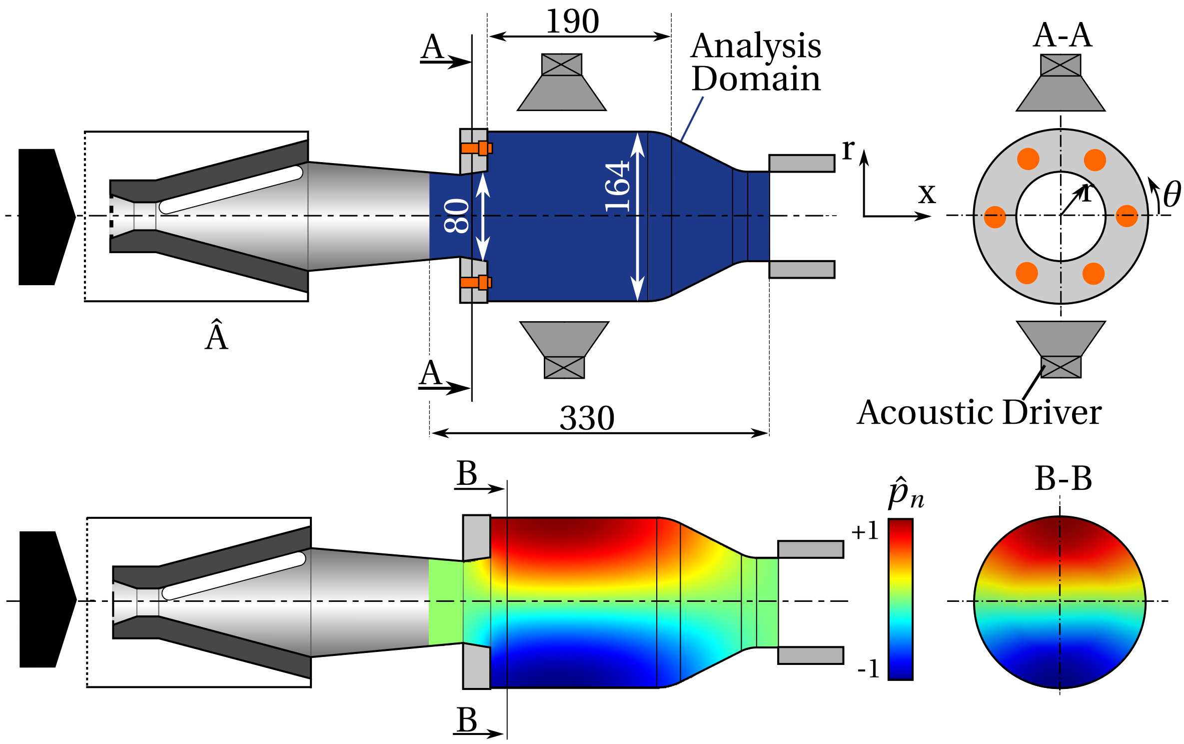

Figure 3.3: Isothermal configuration of swirl-stablilized benchmark system (dimensions are in mm)

mounted to the chamber as indicated in the figure to externally excite the transversal modes of the system.

4 Non-Compact Flame Driving

One of the most fundamental questions for theoretical understanding as well as modeling and analysis of thermoacoustic systems is how chamber acoustics and the flame physically couple at the onset of a potential instability, i.e. at very low amplitudes. Such linear coupling mechanisms in the low-frequency regime have been receiving extensive attention for the last two decades, and are thus, fairly well understood. The high-frequency counterpart however has come into focus of the gas turbine combustion community only within recent years (cf. Sec. 1.5). Hence, this chapter provides theoretical details and investigations along with flame models and a numerical analysis methodology of non-compact linear flame dynamics (i.e. flame driving or heat release modulation mechanisms) at transversal, high-frequency (HF) acoustic modes in premixed, swirl-stabilized combustors. Thereby, the chapter seeks to fulfill the following distinct objectives:

- Establishment of a numerical methodology based on Helmholtz Equation (HE) systems to compute linear driving rates of non-compact flames in the HF regime. (Sec. 4.1).
- Introduction of a rigorous theoretical framework of linear flame modulation mechanisms that drive transversal HF thermoacoustic oscillations in the benchmark combustor of this thesis (Sec. 4.2). The emerging driving mechanisms shall then be modeled and mathematically cast into corresponding non-compact flame transfer functions (Sec. 4.3).
- Utilization of these flame transfer functions for quantification of the relative contribution of density (flame deformation) and velocity (flame displacement) driven heat release oscillations (Sec. 4.5).
- Identification of specific physical features that determine a swirl-

stabilized combustion system's propensity to develop transversal HF instabilities (Sec. 4.5).

4.1 Numerical Analysis Methodology

This section introduces the specific numerical methodology with which the subsequent non-compact thermoacoustic driving computations are carried out. The modal analysis approach in frequency domain presented in Sec. 2.5 forms the basis for this analysis. Mathematically, thermoacoustic driving is modeled by energetically coupling the acoustic mode with the unsteady flame using explicit source term functions (cf. Sec. 2.6), where the latter acts as a source to the former. Also, due to the exclusive focus on flame driving in this chapter, the consideration of any acoustic damping processes is omitted and separately treated in Chap. 5. Moreover, the swirling mean flow induces a loss of degeneracy onto a transversal mode pair in the concerned system, which implies the separation of corresponding eigenfrequencies into two distinct values. This split is usually small so that it can be neglected for the purposes of the present chapter. However, the loss of degeneracy of transversal modes represents a relevant component for the phenomenological and theoretical understanding of HF thermoacoustic oscillations, and is concerned in detail in App. B.

As governing equations, the HE system given in Eqns. 2.20-2.21 is used in this chapter. For clarity reasons, the HE system is re-written and reads

$$\begin{aligned} \bar{\rho}\, i\omega_{n,a}\hat{\mathbf{u}}_{n,a} + \nabla \hat{p}_{n,a} &= \mathbf{m}_{\hat{\mathbf{u}}_n}, && (4.1)\\ i\omega_{n,a}\hat{p}_{n,a} + \bar{\rho}c^2\nabla\cdot\hat{\mathbf{u}}_{n,a} &= (\gamma-1)\,\hat{\dot{q}}_n, && (4.2) \end{aligned}$$

where only the unsteady heat release term is of concern so that $\mathbf{m}_{\hat{\mathbf{u}}_n} = 0$. In this chapter, the solution variables are the n-th acoustic eigenmode of pressure $\hat{p}_{n,a}(\mathbf{x})$, velocity $\hat{\mathbf{u}}_{n,a}(\mathbf{x})$ and unsteady heat release $\hat{\dot{q}}_n(\mathbf{x})$, which are associated with a complex angular eigenfrequency $\omega_{n,a}$. At the same time, the subscript n denotes the expansion term associated with the complex Fourier series in Eqns. 2.13-2.17. The subscript a indicates that the modes describe only acoustic disturbances of the flow, while other types of disturbances (e.g. vortical) are not captured due to the negligence of mean flow effects. Equations 4.1-4.2 account for spatial variation of the mean density $\bar{\rho}(\mathbf{x})$, ratio of specific heats $\gamma(\mathbf{x})$ and the speed of sound $c(\mathbf{x})$ due to the mean temperature $\bar{T}(\mathbf{x})$, which is caused by the combustion process. Recall that the spatial dependency of the modal heat release source term $\hat{\dot{q}}_n(\mathbf{x})$ complies with the requirement to particularly account for non-compact flames within the presented analysis framework. At this point, Eqns. 4.1-4.2 are under-determined (four equations and five unknowns), which is resolved by prescribing the heat release source term in terms of acoustic pressure $\hat{p}_{n,a}$ and velocity fluctuations $\hat{\mathbf{u}}_{n,a}$, i.e.

$$\hat{\dot{q}}_n(\mathbf{x},t) = F(\hat{p}_{n,a}(\mathbf{x}), \hat{\mathbf{u}}_{n,a}(\mathbf{x})). \tag{4.3}$$

This functional dependence formally closes Eqns. 4.1–4.2, which generally describes the linear flame response and is called flame transfer function (FTF). The analyses conducted within this chapter comprise the computation of flame driving rates, which is simply given by computing the complex eigenfrequency. Hence, Eqns. 4.1–4.2 are viewed as an eigenvalue problem, which yields the n-th eigenmode and -frequency of the concerned combustion system for a given FTF and boundary conditions. The eigenfrequencies are complex, i.e.

$$\omega_{n,a} = 2\pi f_{n,a} - i\beta_{n,a}, \tag{4.4}$$

where $f_{n,a}$ and $\beta_{n,a}$ denote oscillation frequency and flame driving rate, respectively. The driving rate describes the rate of acoustic energy change per acoustic oscillation cycle due to thermoacoustically induced heat release oscillations. This is mathematically shown by employing the assumptions (negligence of mean flow effects, negligence of any source terms except flame driving, zero losses across the system boundaries) imposed in this chapter on the conservation equation of flow disturbance energy in Eqn. 2.40, which gives

$$\frac{\mathrm{d}\langle \tilde{\mathrm{E}}_{n,a}\rangle}{\mathrm{d}t} = \left\langle \tilde{\mathrm{D}}_{\hat{\dot{q}}_n} \right\rangle - \langle \tilde{I}_{n,a}\rangle . \tag{4.5}$$

In this equation $\langle \tilde{\mathrm{E}}_{n,a}\rangle$ is the integral modal energy describing only acoustic disturbances, which is given by imposing the zero mean velocity assumption on Eqn. 2.35:

$$\left\langle \tilde{\mathrm{E}}_{n,a} \right\rangle = \frac{1}{4} \int_V \left(\frac{\hat{p}_{n,a}\hat{p}^*_{n,a}}{\gamma \bar{p}} + \bar{\rho} \hat{\mathbf{u}}_{n,a} \hat{\mathbf{u}}^*_{n,a} \right) \mathrm{d}V \tag{4.6}$$

One factor that leads to a theoretical change of acoustic energy is the flux term $\left\langle \tilde{\mathrm{I}}_{n,a} \right\rangle$ given by Eqn. 4.5, which unfolds to

$$\left\langle \tilde{\mathrm{I}}_{n,a} \right\rangle = \frac{1}{4} \int_S (\hat{p}_{n,a} \hat{\mathbf{u}}^*_{n,a} + \hat{p}^*_{n,a} \hat{\mathbf{u}}_{n,a}) \cdot \mathbf{n} \mathrm{d}S = 0, \tag{4.7}$$

where S denotes the domain surface and $\mathbf{n}$ is the corresponding outwards pointing normal vector. Due to fully-prescribed boundary conditions, any energy transfer across the system boundaries is zero as indicated. Hence, a change of the modal energy is solely governed by the source term due to heat release oscillations $\left\langle \tilde{\mathrm{D}}_{\hat{q}_n} \right\rangle$. The flame source term is given by Eqn. 2.39, which is recalled to

$$\left\langle \tilde{\mathrm{D}}_{\hat{q}_n} \right\rangle = \frac{1}{4} \int_{\mathrm{V}} \left(\frac{\gamma - 1}{\gamma \bar{p}} \left(\hat{q}_{n,a} \hat{p}^*_{n,a} + \hat{q}^*_{n,a} \hat{p}_{n,a} \right) \right) \mathrm{d}V.$$

As is shown in Sec. 2.7, the imaginary part of the complex eigenfrequency in Eqn. 2.41, i.e. here the driving rate, is proportional to the change of integral modal energy

$$\beta_{n,a} = \frac{1}{2} \frac{1}{\left\langle \tilde{\mathrm{E}}_{n,a} \right\rangle} \frac{\mathrm{d} \left\langle \tilde{\mathrm{E}}_{n,a} \right\rangle}{\mathrm{d}t} = \frac{1}{2} \frac{1}{\left\langle \tilde{\mathrm{E}}_{n,a} \right\rangle} \left\langle \tilde{\mathrm{D}}_{\hat{q}_n} \right\rangle, \tag{4.8}$$

which yields the mathematical connection between acoustic energy, heat release source term and driving rate. Hence, one crucial input for the calculation of the flame driving rates is the knowledge of an explicit formulation of the heat release source term via an appropriate FTF, which is subject of the next section.

4.2 Theoretical Discussion of Modulation Mechanisms

This section provides the theoretical basis of linear HF thermoacoustic modulation mechanisms in the swirl-stabilized benchmark combustor presented in Chap. 3. The starting point is given by the experimental observations made by [148–151]. These observations comprised a periodic flame displacement at the T1 mode. The researchers found that the heat release zone moves with the acoustic displacement field of the mode. This displacement drives the acoustic field, which in turn causes the flame displacement. In this way, a thermoacoustic feedback loop is established where heat release modulates with acoustic velocity temporally in-phase with the pressure oscillations. The computation of Helmholtz numbers by Eqn. 1.9 gives $He \approx 0.25$ and indicates non-compactness of the thermoacoustic interactions. A first model was developed on basis of a generic Dirac type flame in [148] which confirmed a driving potential due to flame displacement, but remains too generic to be applied to more "realistic" flames treated in this work. Illustrating the displacement mechanisms, the flame position always shifts towards the pressure maximum during an oscillation period T_a as schematically indicated in Fig. 4.1 for different instances in time. The figure displays a meridian cut through the tubular combustor, where the flame is sketched as a parabola. The isocontours of the instantaneous pressure mode/moving flame over half an oscillation period is shown via Figs. 4.1 a) – c).

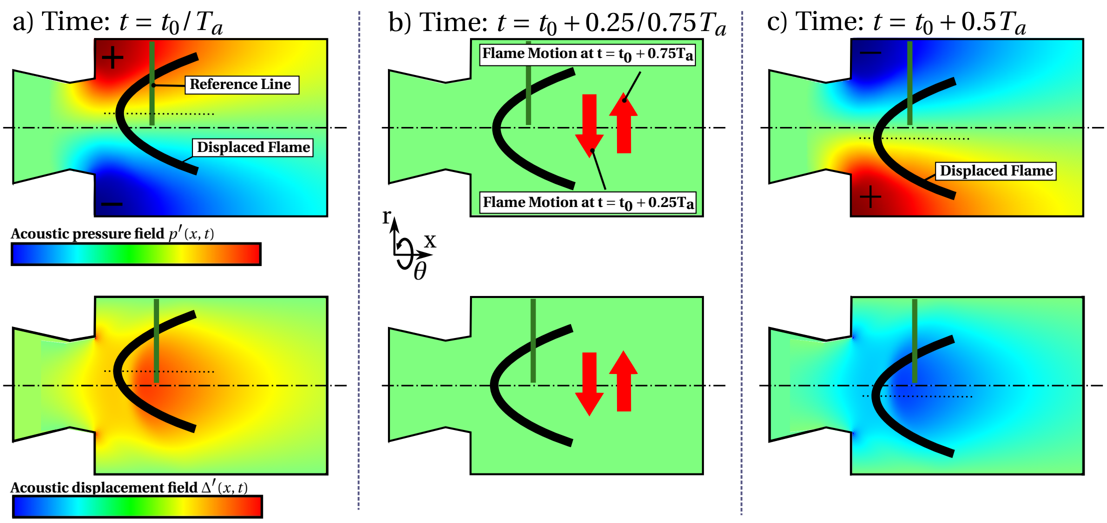

Figure 4.1: Illustration of flame displacement during one acoustic period T_a at four time instances of the oscillation cycle for the T1 pressure mode (top row) and displacement mode (bottom row)

The periodic flame displacement is the physical origin through which thermo-acoustic driving is induced into the system. This mechanism becomes apparent by decomposing the heat release into

$$q(\mathbf{x},t) = \bar{\dot{q}}(\mathbf{x}) + \dot{q}'(\mathbf{x},t), \tag{4.9}$$

which is rearranged to

$$\dot{q}'(\mathbf{x},t) = \dot{q}(\mathbf{x},t) - \bar{\dot{q}}(\mathbf{x}), \tag{4.10}$$

where $\mathbf{x}$ denotes spatial coordinates (e.g. Cartesian or cylindrical) within a fixed frame of reference. In Eqns. 4.9-4.10, $\dot{q}'(\mathbf{x},t)$ represents distributed fluctuations of heat release due to instantaneous differences between the spatial distribution of the moving $\dot{q}(\mathbf{x},t)$ and the stationary mean $\bar{\dot{q}}(\mathbf{x})$ heat release. The concept of this induction of heat release fluctuations due to flame displacement is explained in Fig. 4.2 by means of a Gaussian flame. This flame can be thought to represent the heat release rate distribution of the flame along the reference line drawn in Fig. 4.1. The red and blue areas in Fig. 4.2 display the flame in the up- and downwards displaced position as in Fig. 4.1 a) and c), respectively, whereas the bold black curve represents the time averaged heat release distribution.

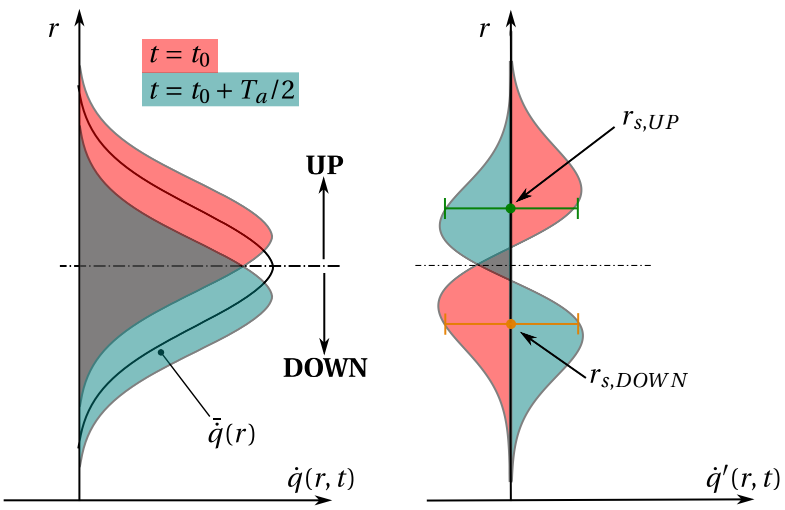

Figure 4.2: Simplified schematic of heat release fluctuations due to to flame displacement

If the flame is assumed to be of Dirac-type as in [148], it moves with one distinct value of the acoustic displacement at the Dirac position in the domain. However, this does not hold true for a general case with a "real" heat release region of finite thickness as in gas turbine combustors. As Fig. 4.1 reveals, length scales of transversal acoustics and flame shape are of the same order of magnitude. In consequence, local interactions between the former and latter must be taken into account, which presents the thermoacoustically non-compact problem. The heat release region moves with the local values of the acoustic displacement field.

The values of the acoustic displacement between positions below and above of the mean Gaussian heat release maximum (denoted by DOWN and UP in Figs. 4.2 and 4.3) differ. Consequently, local flame shape deformations as schematically shown in Fig. 4.3 are induced. Specifically, at $t = t_0$ (red

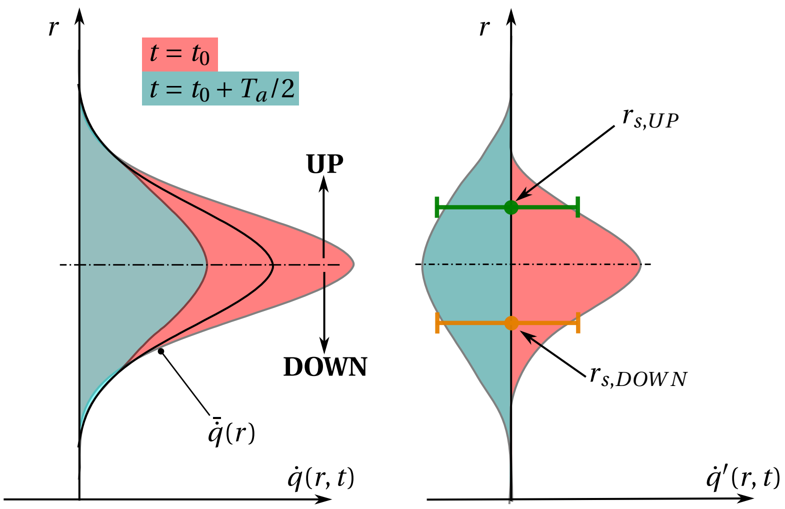

Figure 4.3: Simplified schematic of heat release fluctuations due to flame shape deformation

shaded in Fig. 4.2) the flame is exposed to a radially increasing pressure mode (cf. Fig. 4.1 a)), which implies upward flame motion with a radially decreasing (positive valued) acoustic displacement mode. Hence, the flame displacement on the DOWN side is larger than on the UP side leading to a compression of the flame region and an instantaneous increase of the maximum volumetric heat release rate. The opposite effect occurs after half of a period is elapsed at $t = t_0 + T_a/2$ (blue shaded in Fig. 4.2 c)). At this instant in time, the flame faces a radially decreasing acoustic pressure (cf. Fig. 4.1), and consequently a downward flame motion with a radially increasing (negative valued) displacement mode. Accordingly, the flame displacement is stronger on the DOWN side compared to the UP side, which causes the flame region to expand and instantaneously experience a decrease in the maximum volumetric heat release rate. These periodic compression/expansion cycles represent local oscillations of heat release as is depicted in Fig. 4.3. It is important to point out that the instantaneous distribution of displaced heat release exhibits both, positive and negative zones. Specifically, at $t = t_0$ the UP and DOWN region is respectively positive and negative, and vice versa for the time instant $t = t_0 + T_a/2$. The temporal behavior of displacing heat release and acoustic pressure at probe points $r_{s,UP}$ and $r_{s,DOWN}$ are plotted in Fig. 4.4.

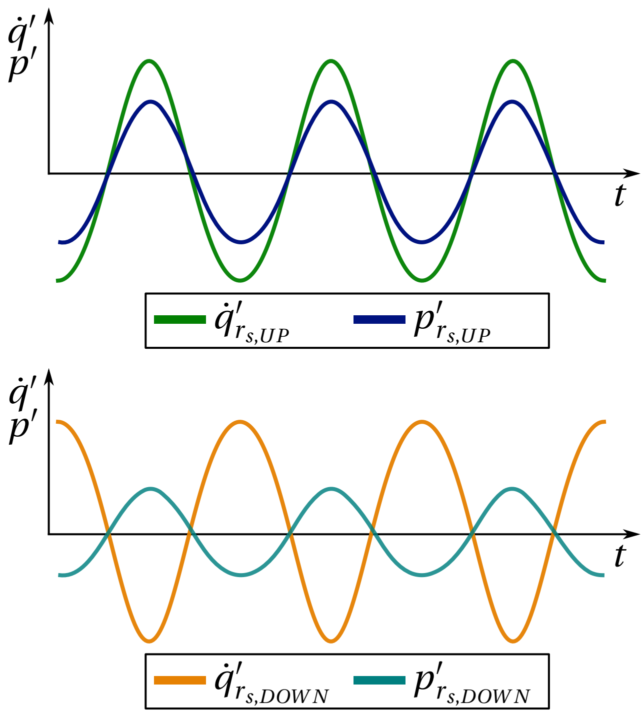

Figure 4.4: Local oscillations of heat release and pressure – flame displacement

It is revealed that oscillations between heat release and pressure are fully in-phase at the UP probe, while an out-of-phase situation is observed for the DOWN probe. According to Rayleigh's criterion (cf. Sec. 1.2), acoustic energy is generated and absorbed at the UP and DOWN probe, respectively. As the pressure amplitude is larger at UP than at DOWN – while the amplitude of the heat release oscillation is presumed as constant at both locations – the net effect of the displacing flame is positive thermoacoustic driving in the presented scenario.

The deformed heat release field in Fig. 4.3 emerges only positive and negative zones throughout the entire distribution at $t = t_0$ and $t = t_0 + T_a/2$, respectively. The temporal behavior of heat release and pressure oscillations for the deforming flame at the UP and DOWN probes is plotted in Fig. 4.5.

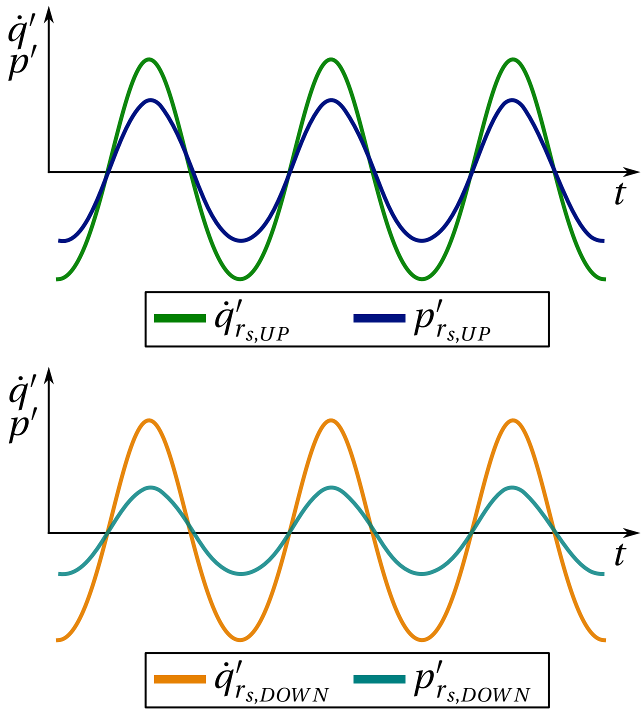

Figure 4.5: Local oscillations of heat release and pressure – flame deformation

The figure reveals that both, UP and DOWN probes record fully in-phase dynamics between heat release and pressure oscillations. Consequently, the deformation mechanism presents a source of acoustic energy at all spatial locations. Notice that all oscillation amplitudes in Figs. 4.4-4.5 are arbitrary as only qualitative relations are concerned. The discussion of positive and negative driving regions associated with flame displacement is extended to swirling flame shapes in Sec. 4.5.

It is important to emphasize that the heat release oscillations emerge locally due to the displacing and deforming flame shape. Consequently, the (combustor-)volume integrated instantaneous and fluctuating heat release distributions, which result from the superposition of the two contributing mechanisms, must respectively conserve energy and vanish at every instant in time, i.e.

$$\int_V \dot{q}(\mathbf{x}, t)\mathrm{d}V = \dot{P}_{th} \quad \forall\ t, \tag{4.11}$$

$$\int_V \dot{q}'(\mathbf{x}, t)\mathrm{d}V = 0 \quad \forall\ t. \tag{4.12}$$

Herein, $\dot{P}_{th} = \dot{m}_f h_c$ denotes the chemically available thermal power with $\dot{m}_f$ and h_c representing the fuel's mass flow rate and heat of combustion, respectively.

4.3 Derivation of Source Term Functions

The computation of the flame driving rates and the associated quantification of contributing physical mechanisms in HF thermoacoustic system requires the explicit formulation of the respective FTF, which is derived in this section. In order to model the foregoing described modulation of heat release due to the periodic flame displacement and deformation, and to derive the desired corresponding FTF, it is useful to introduce a moving reference frame. This frame is given by the coordinate transform as introduced in [179]

$$\tilde{\mathbf{x}}(\mathbf{x}, t) = \mathbf{x} - \Delta'(\mathbf{x}, t), \tag{4.13}$$

where $\tilde{\mathbf{x}} = (\tilde{x}, \tilde{y}, \tilde{z})$ denotes the moving frame's coordinates, which are linked to the fixed frame's coordinates by the acoustic displacement field $\Delta'(\mathbf{x}, t)$. The time domain versions of the oscillatory variables are used for the derivation, which appeared more effective for one's sense of imagination. Notice that

Cartesian coordinates are used for the presented derivations, which is not a necessity, and can be equally carried out within any coordinate system. Interpretatively, the moving frame can be thought of being located on the flame. Its coordinates describe the displacing and deforming flame shape. Thus, a general functional description of the heat release distribution at every instant in time is given by

$$\dot{q}(\tilde{\mathbf{x}}(\mathbf{x},t)) = \dot{q}(\mathbf{x} - \Delta'(\mathbf{x},t)), \tag{4.14}$$

where the right-hand-side provides an implicit functional description of the instantaneous heat release distribution in fixed coordinates. The next step towards developing the desired FTF is to explicitly express the displacing and deforming heat release distribution in terms of stationary mean heat release as well as unsteady acoustic quantities. The requirement of integral energy conservation is employed, which must hold true within the fixed as well as the moving frame:

$$\int_V \dot{q}(\mathbf{x},t)\mathrm{d}V = \int_{\tilde{V}} \dot{q}(\tilde{\mathbf{x}}(\mathbf{x},t))\frac{\mathrm{d}\tilde{V}}{\mathrm{d}V}\mathrm{d}V \quad \forall\ t \tag{4.15}$$

Satisfying Eqn. 4.15 is achieved by requiring

$$\dot{q}(\mathbf{x},t) = \dot{q}(\tilde{\mathbf{x}}(\mathbf{x},t))\frac{\mathrm{d}\tilde{V}}{\mathrm{d}V}, \tag{4.16}$$

with the derivative term expanding to $\frac{\mathrm{d}\tilde{V}}{\mathrm{d}V} = \frac{\mathrm{d}\tilde{x}}{\mathrm{d}x}\frac{\mathrm{d}\tilde{y}}{\mathrm{d}y}\frac{\mathrm{d}\tilde{z}}{\mathrm{d}z}$. Considering Eqns. 4.13-4.14, the desired formulation of the moving and deforming heat release distribution in the fixed coordinate frame is obtained (where only first order terms are retained):

$$\dot{q}(\mathbf{x},t) = \dot{q}(\mathbf{x} - \Delta'(\mathbf{x},t))\left(1 - \nabla\cdot\Delta'(\mathbf{x},t)\right) \tag{4.17}$$

Then, Eqn. 4.17 is further modified via a Taylor series expansion to the first order that results in

$$\dot{q}(\mathbf{x},t) = \bar{\dot{q}}(\mathbf{x}) - \nabla\bar{\dot{q}}(\mathbf{x})\cdot\Delta'(\mathbf{x},t) - \bar{\dot{q}}(\mathbf{x})\nabla\cdot\Delta'(\mathbf{x},t), \tag{4.18}$$

where $\bar{\dot{q}}(\mathbf{x})$ denotes the stationary mean heat release distribution and second-order fluctuation terms are neglected. The fluctuating field of heat release is then retrieved by combining Eqns. 4.10 and 4.18 to produce

$$\dot{q}'(\mathbf{x},t) = -\nabla(\bar{\dot{q}}(\mathbf{x})\cdot\Delta'(\mathbf{x},t)) = -\nabla\bar{\dot{q}}(\mathbf{x})\cdot\Delta'(\mathbf{x},t) - \bar{\dot{q}}(\mathbf{x})\nabla\cdot\Delta'(\mathbf{x},t). \tag{4.19}$$

The non-compact thermoacoustic analysis methodology described in Sec. 4.1 only admits FTF, which are formulated via the acoustic pressure and velocity. Thus, the acoustic displacement in Eqn. 4.19 is related to acoustic velocity via

$$\mathbf{u}' = \frac{\partial \Delta'}{\partial t}, \tag{4.20}$$

whereas the divergence of the displacement is transformed into

$$-\nabla \cdot \Delta'(\mathbf{x}, t) = \frac{\rho'}{\bar{\rho}} = \frac{p'}{\gamma \bar{p}}, \tag{4.21}$$

during which conservation of mass as well as the definition of isentropic acoustics is exploited. Substituting the frequency domain versions of Eqns. 4.20-4.21 into Eqn. 4.19 yields

$$\hat{\dot{q}}_n(\mathbf{x}) = \underbrace{-\nabla \bar{\dot{q}}(\mathbf{x}) \cdot \frac{\hat{\mathbf{u}}_{n,a}(\mathbf{x})}{i\omega_{n,a}}}_{F_{\hat{\Delta}}} + \underbrace{\bar{\dot{q}}(\mathbf{x}) \frac{\hat{p}_{n,a}(\mathbf{x})}{\gamma(\mathbf{x})\bar{p}(\mathbf{x})}}_{F_{\hat{\rho}}}, \tag{4.22}$$

which represents the required distributed FTF at mode n for the non-compact thermoacoustic analyses of this work. This FTF describes the coupling mechanisms introduced above as revealed by re-writing Eqn. 4.22 into

$$\hat{\dot{q}}_n(\mathbf{x}) = F(\hat{p}_{n,a}, \hat{\mathbf{u}}_{n,a}) = F_{\hat{\Delta}}(\hat{\mathbf{u}}_{n,a}) + F_{\hat{\rho}}(\hat{p}_{n,a}). \tag{4.23}$$

The first and second terms of Eqn. 4.23

$$\hat{\dot{q}}_{\hat{\Delta},n}(\mathbf{x}) = F_{\hat{\Delta}}(\hat{\mathbf{u}}_{n,a}) \quad = \quad -\nabla \bar{\dot{q}}(\mathbf{x}) \cdot \frac{\hat{\mathbf{u}}_{n,a}(\mathbf{x})}{i\omega_{n,a}}, \tag{4.24}$$

$$\hat{\dot{q}}_{\hat{\rho},n}(\mathbf{x}) = F_{\hat{\rho}}(\hat{p}_{n,a}) \quad = \quad \bar{\dot{q}}(\mathbf{x}) \frac{\hat{p}_{n,a}(\mathbf{x})}{\gamma(\mathbf{x})\bar{p}(\mathbf{x})}, \tag{4.25}$$

describe the thermoacoustic driving due to flame displacement and flame shape deformations. Equations 4.24 and 4.25 recover the functions postulated in [178], but the fundamental derivations presented in this work establishes the mathematical and physical interconnection between the two underlying mechanisms. Section 4.6 presents the experimental validation of these two mechanisms and the corresponding FTF. Note that the driving mechanism of flame shape deformation resembles the density modulation mechanism caused by mass flux oscillations as is encountered in the LF regime [121, 138], which are insignificant for LF modes due to the dominance of convective mechanism as explained in Sec. 1.4 and App. A.

4.4 Investigation Framework

This section provides information of the considered operation points of the experimental benchmark system used for the forthcoming investigations. Also, mean heat release and temperature distribution as well as numerical setup and analysis procedures are discussed.

4.4.1 Experimental Operation Points

The FTF derived in the previous section are used to compute respective driving rates of an entire operational window of the benchmark combustor. These driving rates form the basis for the subsequent analyses. The considered set of operation points is composed of 80 operation points associated with a low-swirl configuration. This set assembles from all combinations of the following mass flow rates, inlet temperatures, and air excess ratios:

- $\bar{\dot{m}} = 0.06, 0.08, 0.10, 0.06\,\mathrm{kg/s}$
- $\bar{T}_{\mathrm{in}} = 373.15, 473.15, 573.15, 673.15\,\mathrm{K}$
- $\lambda = 1.0, 1.2, 1.4, 1.6, 1.8$

Around half of these operation points exhibit self-sustained thermoacoustic oscillations of the T1 mode within the chamber as evaluated by assessing dynamic pressure measurements in respective experimental work (cf. [62, 63, 148–151]). Hence, the stability state (i.e. binary rating unstable or stable) of each operation point is known, and readily available.

4.4.2 Mean Heat Release and Temperature Distributions

The mean heat release distribution is a crucial parameter to the above-derived FTF in Eqn. 4.23. This distribution is approximated from time-averaged, inverse Abel transformed OH^*-chemiluminescence recordings (which are readily available, cf. Chap. 3) of the mean flame brush for each operation point.

Utilizing this approximation provides mean heat release distributions for a large variety of operation points without the need of conducting Computational Fluid Dynamics (CFD) simulations. It is assumed that the mean OH* radical intensity distribution indicates the steady heat release distribution (cf. Fig.4.6), which leads to

$$\bar{q}(\mathbf{x}) = K \cdot \bar{I}(\mathbf{x}), \tag{4.26}$$

where $\bar{I}(\mathbf{x})$ is the volumetric, time-averaged OH* intensity distribution, and K a constant proportionality factor. This factor is determined from the integral energy conservation requirement

$$\dot{P}_{th} = K \cdot \int_V \bar{I}(\mathbf{x}) \mathrm{d}V. \tag{4.27}$$

Associated mean temperature distributions are required to compute mean density and speed of sound fields for the following analyses. These fields are also derived from the averaged OH* intensity distributions (cf. Fig. 4.6) by employing certain scaling and fitting routines. Specifically, this procedure utilizes scaling and fitting rules, which are retrieved from comparisons between temperature and OH* fields of a reactive CFD simulation with the experimental OH* field of a distinct operation point. More details regarding the basic idea and procedural concepts of this fitting and scaling method can be found in [15]. The usability of OH* images to obtain mean heat release rate distribution is justified as the experiments are operated in perfectly premixed combustion mode [15, 17, 62, 63].

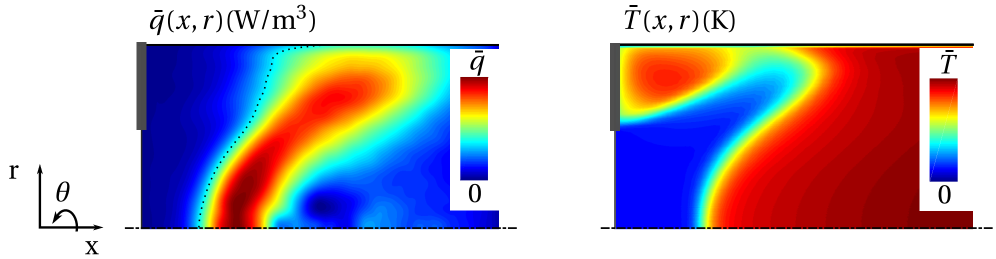

Figure 4.6: Sample mean heat release and temperature distribution

4.4.3 Numerical Setup and Analysis Procedure

The computation of driving rates $\beta_{n,a}$ of the T1 mode occurs by numerically solving Eqns. 4.1-4.2 under consideration of the respective FTF. Mean fields of heat release and mean temperature are required to prescribe the FTFs and are individually obtained for each operation point as outlined in the previous section. The computational domain involves only the three-dimensional combustor geometry as indicated in Fig. 3.2. In order to practically execute these computations, the equations are discretized and numerically solved using FEM (cf. basic theory in Sec. 2.8). Due to the absence of any convective transport terms in the governing equations in this chapter, no numerical stabilization schemes are required for discretization and system solutions. The FEM mesh and corresponding boundary conditions are illustrated in Fig. 4.7.

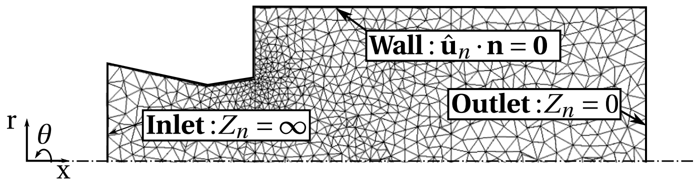

Figure 4.7: Computational domain, mesh and boundary conditions

Each node of this mesh carries a value of the conservation variables, i.e. $\hat{p}_{n,a}$ and $\hat{\mathbf{u}}_{n,a}$), which altogether presents an approximate solution to Eqns. 4.1-4.2. Specifically, the combustor domain for this work is meshed with ≈ 200,000 tetrahedral elements, and the equations are discretized using linear shape functions, which translates into ≈ 145,000 degrees of freedom to be solved for. The employed boundary conditions are also indicated in Fig. 4.7, and are slip wall conditions at all bounding walls, while the domain's in- and outlet are prescribed with an impedance, which is set to represent an acoustically hard and soft termination, i.e. $Z = \infty$ and $Z = 0$, respectively.

Due to the employed type of equations as well as the fully-reflecting (i.e. energy neutral) inlet and outlet termination, no acoustic damping is included within the analyses as desired. The resulting driving rates only contain the energetic effect of heat release oscillations as mathematically induced via the prescribed FTF. One objective of this chapter is to quantify the individual significance of the two contributing mechanisms (flame displacement and deformation) to the total modulation of heat release. This is achieved by carrying out two separate eigenvalue analyses for each operation point. These two analyses respectively utilize the FTF corresponding to flame displacement in Eqn. 4.24 and deformation in Eqn. 4.25, which yield the associated driving rates $\beta_{\hat{\Delta}}$ and $\beta_{\hat{\rho}}$. The total driving rate can be determined by superposition, i.e.

$$\beta_{tot} = \beta_{\hat{\Delta}} + \beta_{\hat{\rho}}. \tag{4.28}$$

The significance of the two coupling mechanisms is quantified by computing the relative contribution between the individual and absolute driving rate, which respectively reads

$$rc_{\hat{\Delta}} = \frac{\beta_{\hat{\Delta}}}{\beta_{tot}} \cdot 100\%, \tag{4.29}$$

$$rc_{\hat{\rho}} = \frac{\beta_{\hat{\rho}}}{\beta_{tot}} \cdot 100\%. \tag{4.30}$$

4.5 Results and Interpretations

This section presents results and interpretations of the driving analysis. First, computed driving rates of all considered operation points are provided. Then, distinct physical features that promote/inhibit non-compact flame driving are identified and discussed. Lastly, further insight in non-compact flame modulation behavior is generated by inspecting the source term function.

4.5.1 Quantification of Driving Mechanisms

The driving rates are computed by solving the HE system given by Eqns. 4.1-4.2. For each operation, the driving rate due to displacement and deformation is obtained individually by utilizing the FTF given in Eqns. 4.24 and 4.25, respectively. The calculated oscillation frequencies, which are independent of the prescribed type of modulation mechanism, are compared against readily available experimental counterparts in Fig. 4.8. The operation point number on the x-axis is only of auxiliary purpose to present and compare the frequencies. An explicit allocation to specific operation conditions is not required. The experimental frequency values result from Fast Fourier Transforms of dynamic pressure measurements that are recorded at the combustion chamber's faceplate (cf. Chap. 3 and [15, 17, 62, 63]).

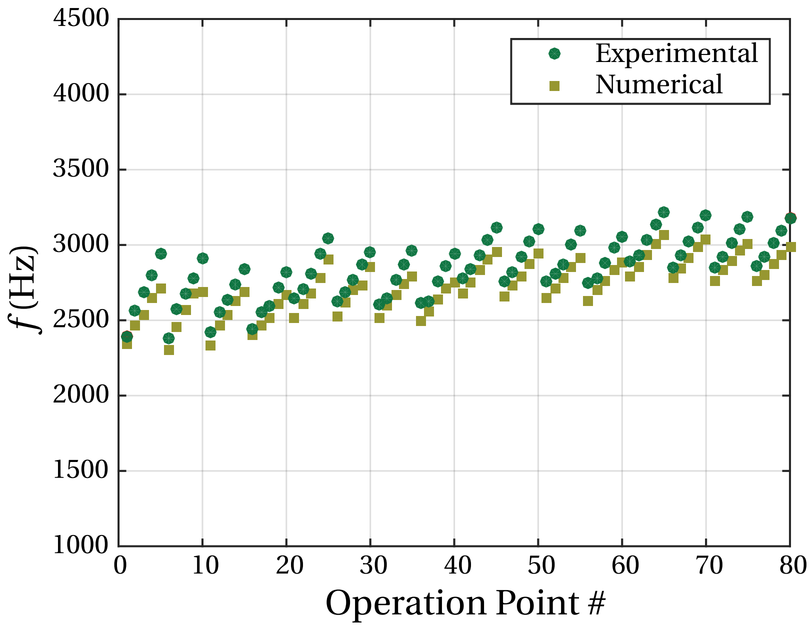

Figure 4.8: Comparison of numerical vs. experimental oscillation frequencies of all considered operation point for validation purposes

The numerical simulations accurately reproduce the experimentally measured frequencies with an average relative error of 5%. As these frequencies are sensitive to the mean temperature distribution, the employed fitting procedure to obtain this distribution that is retrieved from [15] can be viewed as implicitly validated. Thus, the results of Fig. 4.8 establish confidence that the computation method is capable of accurately reproducing the transversal acoustic eigenfrequencies as well as the mode shapes of all concerned operation points. The oscillation frequencies associated with the individual computation of the displacement and deformation FTF are identical for each operation point. The reason for this equality is due to the fully in- and out-of-phase nature of the two FTF, which does not induce a frequency shift on the modes. The experimental frequencies reflect the non-degeneracy of T1 modes due to swirling mean flow effects. However, the associated frequency differences are small (cf. Chap. 7), and are thus averaged for the comparison purpose of Fig. 4.8 to yield one distinct frequency value for each operation point. The three driving rates due to displacement, deformation and the sum of these (total driving) are plotted against the integral thermal power density and measured oscillation amplitudes [1] of all operation points in Figs. 4.9 and 4.10, respectively.This power density is given by

$$PD = \frac{\dot{P}_{th}}{V_f}, \tag{4.31}$$

where $\dot{P}_{th}$ is the thermal power as given for Eqn. 4.27 and V_f is the flame volume, which can be computed within the FEM analysis framework. Recall that the only measurement inputs – which are all readily available, cf. Chap. 3 – comprise (1) the observed (in-)stability behavior, (2) the oscillation amplitudes, and (3) the OH*-images as mean heat release indicator for each operation point.

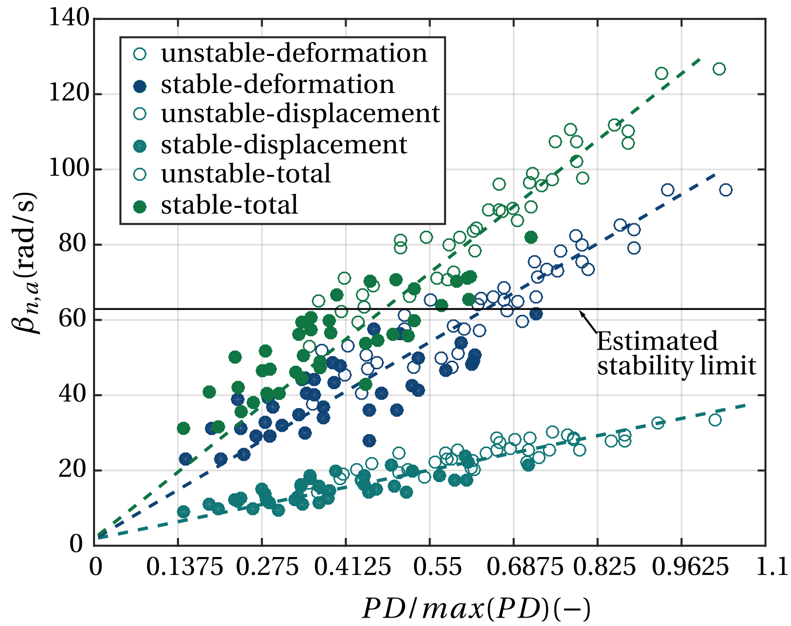

Figure 4.9: Computed driving rates vs. thermal power density

[1] given by the peak value of an Fast Fourier Transform of measured dynamic pressure time series

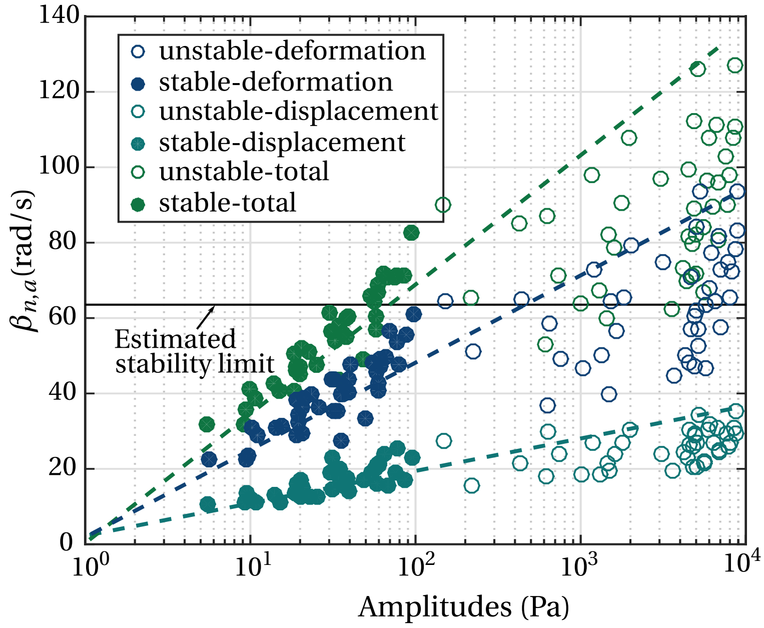

Figure 4.10: Computed driving rates vs. measured oscillation amplitudes

All driving rates and power densities provided in the respective figures are numerically computed quantities. The filled circles in the figures indicate experimentally determined stable points, whereas empty circles indicate unstable operation points. Unstable points are associated with higher computed driving rates, and vice versa for stable points, which holds true for the displacement, density and total driving rates. This trend is also evident in Fig. 4.10, where the driving rates are plotted versus the measured pressure amplitudes. The magnitude indicates the severity of the instability limit cycle. Figure 4.9 identifies a linear dependence of the driving rates on the thermal power density. This dependence can be explained by assessing the displacement and deformation FTF in Eqns. 4.24-4.25. Operation points with a large power density naturally translate into flames with high volumetric heat release rates compared to lower power densities, which explains the linear trend of the deformation driving rates.

All displacement driving rates emerge as positive for all operation points despite the theoretical possibility to yield negative values as described in Sec. 4.2. It is inferred that positive source regions outweigh the negative counterparts in the spatial distribution of the associated displacement FTF. Details on positive and negative driving regions of the displacement FTF within swirl-stabilized flames are given further below.

Overall, it is argued that higher power densities lead to higher gradients of mean heat release that are located so that the interactions with the displacement field cause positive driving and the observed linear dependence of the displacement driving rates. Thus, the propensity of a combustor to develop a HF instability at the T1 mode can be linked to the underlying thermal power density. A separation line between driving rates associated with stable and unstable operation points can be drawn in Figs. 4.9-4.10. Shifting the cloud of driving rates downwards so that the stability line coincides with the x-axes of the plots yields the image one would expect if all relevant damping effects are taken into account, too. This requires the computation of damping rates, which are then superposed with the driving rates to yield the net thermoacoustic growth rates. The computation of both, damping and growth rates are considered in Chaps. 5-6.

In order to valuate the significance of the constituting modulation mechanisms, relative contributions are computed via Eqns. 4.29-4.30, and plotted in Fig. 4.11. The figure reveals that density and velocity modulations contribute on average 75% and 25% towards the total thermoacoustic driving of the T1 mode for the concerned operation configurations, respectively. Thus, density modulation (flame shape deformations) dominates this driving, however, not as strong as to justify the principal negligence of the displacement contribution. It is important to point out that these results are not universally valid and apply only to the types of flame shapes/combustor setups considered in this thesis, i.e. swirl-stabilized systems with one central flame associated with one fuel-air mixture entering the chamber through a main burner tube. Other configuration, e.g. containing auto-ignition stabilized or jet flames would require an individual analyses in the same manner as conducted in this chapter.

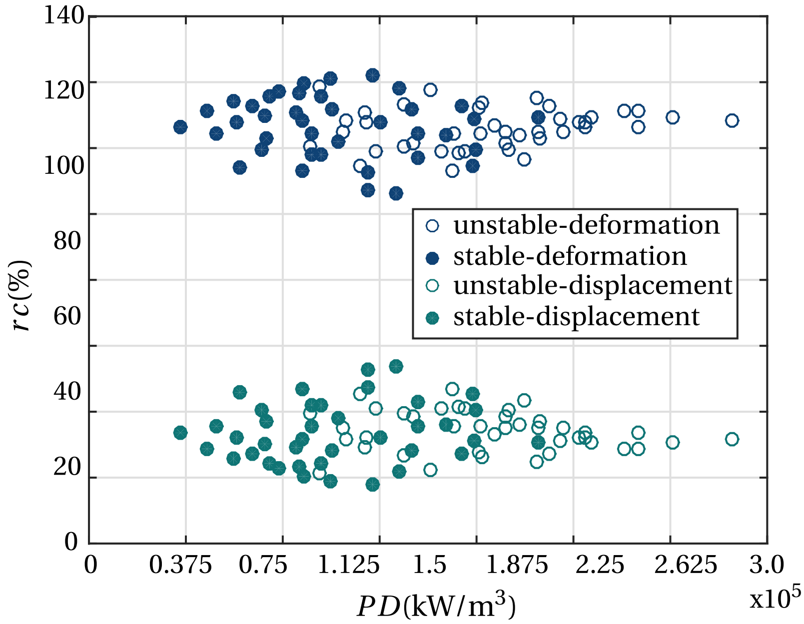

Figure 4.11: Relative contributions to total driving

4.5.2 Driving Propensity

This subsection identifies global features that determine the concerned swirl stabilized combustor's propensity to develop a HF instability at the T1 mode. For this, the magnitude of the driving rates serve as rating parameter, i.e. large values imply an amplified propensity, and vice versa. In order to identify such governing factors, a selected set of operation points is inspected in detail. All these cases are of equal thermal power, but show both, experimentally determined stable and unstable behavior. Hence, six points with a thermal power value of $\dot{P}_{th} = 194,050$ W are chosen. Three of these are respectively stable and unstable. According to the Rayleigh criterion (cf. Eqn. 1.8), thermo-acoustic driving can only occur within the spatial extent of pressure oscillations [63, 179], i.e. where the pressure mode is non-zero. Additionally, driving is solely possible within the flame region where the mean heat release is non-zero. The intersection zones (ISZ) between the pressure mode and the heat release distribution are formed for each of these six points as visualized in Fig. 4.12. The calculation of these ISZ requires to set the pressure mode to zero below a threshold value. This value is selected such that 95% of modal acoustic energy (cf. Eqn. 4.6) is maintained within the "truncated" modes for the ISZ computations.

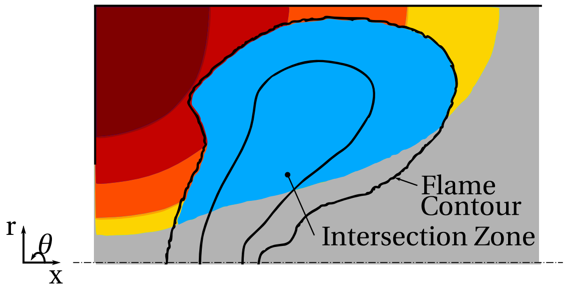

Figure 4.12: Intersection zone (blue shade) between pressure mode (rainbow) and flame contour

Then, the ratio between thermal power released within the ISZ and the total thermal power as well as between the geometrical volume of the ISZ and the total flame volume are computed. These two quantities are then assessed in terms of their role as an indicator for instability propensity. The computed values of volume and power ratio are given in Tab. 4.1.

	UNSTABLE			STABLE		
Volume Ratio (%)	52	50	56	39	40	43
Power Ratio (%)	53	52	58	41	42	48
Driving Rate (rad/s)	86	74	87	59	55	61

Table 4.1: ISZ quantites for three stable and unstable operation points at equal thermal power of a low-swirl combustor configuration

The table reveals that the thermal power released within the unstable ISZ is larger than for the stable counterpart. Hence, the available thermal power with which acoustic pressure perturbations interact to induce heat release oscillations is higher. This amplifies the thermoacoustic feedback, which ultimately leads to stronger driving with larger driving rates compared to the cases that carry less thermal power within their ISZ. Also, the volume ratios of the unstable cases are larger than these of the stable cases. Thus, a higher volumetric portion of the flame is exposed to thermoacoustic coupling for unstable cases compared to stable ones. The foregoing observations yield that large integral thermal power ratios as well as flame volume ratios associated with the swirl-stabilized combustor's underlying ISZ promote HF instabilities. This finding allows to identify the following flame/combustor features, which lead to an increase of instability propensity at the T1 mode:

- Flame location fairly close to the burner outlet within the extent of the transversal acoustic mode, which is confirmed by experimental investigations [2].
- Radially off-centered flame position towards the chamber wall.
- Compact rather than widespread flame shape.

In order to reinforce the validity of foregoing identified features, six configurations of a high-swirl setting of the combustor with the same operational parameters as the low-swirl cases are investigated in terms of ISZ and (in-) stability propensity. The respective results are shown in Tab. 4.2, which shows the same trends as established above. Larger volume and power ratios emerge for the unstable cases, which are also associated with higher driving rates, and vice versa for the stable cases. Furthermore, the increased instability severity of high-swirl cases – as experimentally identified in the work of [15] – is explainable by the above-found features, i.e. high-swirl flame shapes are more radially off-center, more compact, and are located closer to the burner outlet compared against their low-swirl counterparts.

	UNSTABLE			STABLE		
Volume Ratio (%)	65	62	64	50	48	52
Power Ratio (%)	66	61	69	53	50	54
Driving Rate (rad/s)	136	120	127	76	74	72

Table 4.2: ISZ quantities for three stable and unstable operation points at equal thermal power of a high-swirl combustor configuration

4.5.3 Assessment of Non-Compact Source Terms

Further understanding of non-compact heat release modulation in swirl-stabilized flames is generated by assessing the non-compact source terms

[2]This work was performed by F. Berger at the Lehrstuhl für Thermodynamik of TU München.

in detail. For this purpose, the integrand of the source term due to heat release oscillations in the modal energy balance (cf. Eqn. 4.8) – which links this source to the modal driving rates (cf. Eqn. 4.8) – is expanded using the FTF of displacement and deformation driving given by Eqns. 4.24-4.25. These distributed source fields are also called Rayleigh indexes [63], which respectively unfold to

$$\mathrm{ri}_{\hat{\rho}}(\mathbf{x}) = \mathrm{Re}\left(\hat{q}_{\hat{\rho},n}(\mathbf{x})\,\hat{p}_n^*(\mathbf{x})\right) = \mathrm{Re}\left(\frac{\bar{q}(\mathbf{x})}{\gamma(\mathbf{x})\,\bar{p}(\mathbf{x})}\,\hat{p}_n(\mathbf{x})\,\hat{p}_n^*(\mathbf{x})\right), \tag{4.32}$$

$$\mathrm{ri}_{\hat{\Delta}}(\mathbf{x}) = \mathrm{Re}\left(\hat{q}_{\hat{\Delta},n}(\mathbf{x})\,\hat{p}_n^*(\mathbf{x})\right) = \mathrm{Re}\left(-\frac{\nabla\bar{q}(\mathbf{x})}{\bar{\rho}(\mathbf{x})\omega_n^2}\nabla\hat{p}_n(\mathbf{x})\cdot\hat{p}_n^*(\mathbf{x})\right), \tag{4.33}$$

where the acoustic velocity of the displacement FTF is replaced by the gradient of the pressure mode using the momentum equation given by Eqn. 4.1. First, the deformation Rayleigh index in Eqn. 4.32 is always positive, which implies that the associated local heat release and pressure oscillations are (temporally) in-phase, i.e. generate acoustic energy, at all spatial positions of the source field. Conversely, heat release oscillation due to flame displacement can either be in-phase or out-of-phase with the acoustic pressure. Hence, positive and negative zones within the source field are possible, which respectively resemble generation and absorption of acoustic energy as indicated through the investigations using the generic Gaussian flame shapes in Sec. 4.2.

The reason for the presence of positive and negative zones is due to dependency of the displacement Rayleigh index on gradients of mean heat release and the pressure mode. Both quantities can exhibit positive and negative values within their respective fields. Specifically referring to Eqn. 4.33, in-phase acoustic energy generation due to flame displacement occurs (note the negative sign in the expression) at locations where a positive/negative pressure gradient meets a negative/positive mean heat release gradient. Vice versa, locations at which the pressure and mean heat release gradients are both positive/negative exhibit acoustic energy absorption due to the out-of-phase situation between heat release and pressure oscillations. The following theoretical findings related to heat release modulation due to flame deformation and displacement are established:

- Flame deformation always leads to positive driving rates, which is due to the presence of only positive zones of the Rayleigh index.
- Flame displacement can lead to either positive or negative driving rates, which depends on whether positive or negative zones dominate the Rayleigh index.

4.6 Validation of Source Term Functions

This section provides validation of the analytical FTFs given by Eqns. 4.24-4.25. All findings, interpretations and implications drawn in the foregoing sections are crucially based on the computation results of the driving rates carried out with these FTFs. Hence, the physical correctness of these results are consolidated with this experimental validation. For this purpose, the numerically obtained total Rayleigh index, i.e. the sum of individual displacement and deformation formulations $\mathrm{ri} = \mathrm{ri}_{\hat{\Delta}} + \mathrm{ri}_{\hat{\rho}}$, is compared against the experimentally obtained counterpart. One representative operation point ($\bar{\dot{m}} = 0.12\,\mathrm{kg/s}, \bar{T}_{in} = 473.15\,\mathrm{K}, \lambda = 1.4$) is selected for the comparisons. It is emphasized that the experimental determination of the FTF fields was not carried out as part of this thesis' research, and are readily retrieved from [15]. Details on measurement techniques and post-processing procedures can be found in these references. The analytical Rayleigh index fields are obtained by evaluating (and then adding) Eqns. 4.32-4.33 using the respective FTF from Eqns. 4.24-4.25 as well as numerically computed mode shapes along with the mean heat release and temperature field of the concerned operation point. The comparison of the Rayleigh indexes are shown in Fig. 4.13.

The figure reveals an excellent qualitative and quantitative agreement between the experimental and analytical Rayleigh index. An equally accurate validation between the underlying experimental and analytical FTF can be implied. More extensive validation studies using further operation points were conducted in [15, 17, 18], which emerge the same level of agreement between experiments and models. Hence, the FTF models derived and used for the analyses – as well as the associated results – in this chapter can be labeled

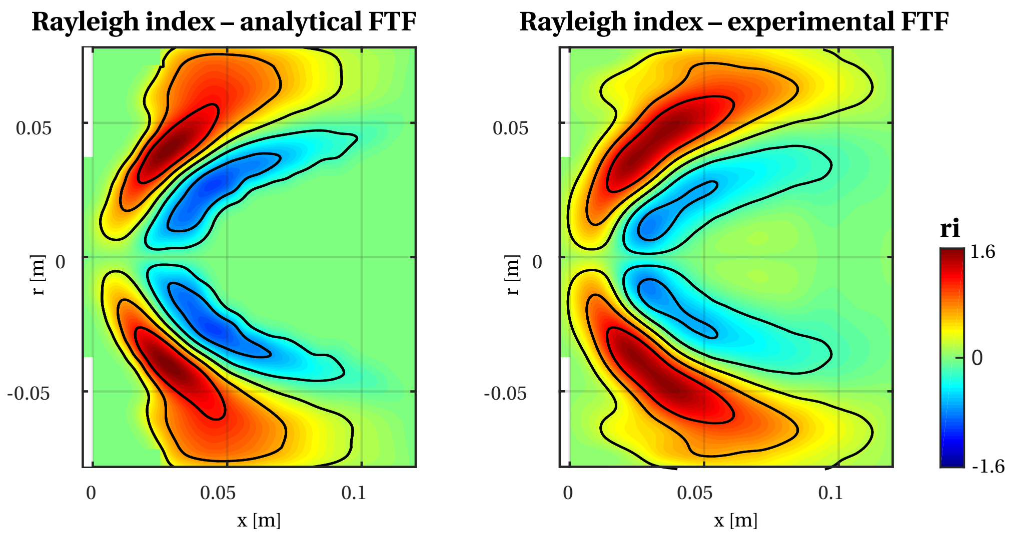

Figure 4.13: Comparison between analytical (left) and experimental (right) Rayleigh index

as experimentally validated.

4.7 Summary and Findings – Non-Compact Flame Driving

The foregoing chapter presented a theoretical and analytical treatment of HF thermoacoustic flame driving of the first transversal acoustic mode in a lab-scale swirl-stabilized gas turbine combustor, which resulted in the following findings:

- Flame displacement and deformation were confirmed as fundamental mechanism that cause HF instabilities.
- Distributed flame transfer functions of these two driving mechanisms were derived from first principles.
- Flame deformation always leads to positive driving rates.
- Flame displacement can theoretically yield positive or negative driving rates, although the latter was not observed in the presented analysis.

A non-compact modal analysis framework was established, which allowed to straightforwardly incorporate the distributed source terms to compute oscillation frequencies and driving rates of the T1 mode. Required mean temperature and heat release rate fields were obtained from OH^*-chemiluminescence measurements of the experimental benchmark combustor. A wide range of operation points of low- and high-swirl configurations of this combustor, which feature HF instabilities, were analyzed, and emerged to following results:

- Accurate reconstruction of oscillation frequencies for all operation points was achieved.
- The driving rates belonging to flame deformation and displacement driving showed consistent results with the experimental instability observation over the entire operational window.
- Driving contributions of flame shape deformations were found three times larger than flame displacement.

Additionally, the following criteria that promote a swirl-stabilized combustor's propensity to develop a HF instability were identified:

- Inclusion of large portion of mean heat release distribution within the acoustic pressure mode.
- Compact flame shape close to burner outlet and chamber walls. This criteria holds true only for the concerned T1 mode. If other modes are considered, the assessment of instability propensity needs to be re-done. Generally, compact flame shapes that are placed in regions of pressure anti-nodes of the respective mode lead to an increased instability propensity.
- High power density of flames.

Finally, note that the presented theory, methods, models and findings are in principle applicable to other transversal mode and combustor types as long as governing physical mechanisms remain the same.

5 Acoustic Damping of Transversal Modes

Dissipation of acoustic energy (i.e. damping) presents the second key factor – besides generation of acoustic energy due to flame driving – that determines whether or not a combustor undergoes a thermoacoustic instability. Acoustically induced vortex-shedding at free shear-layers of the mean flow presents one main damping mechanism in gas turbine combustors [40, 49, 67, 138]. In this thesis, the multi-dimensional nature of the concerned transversal modes in the HF regime renders this mechanism as acoustically non-compact. The application of existing methodologies to model and quantify the damping rate of the concerned modes from the field of low-frequency/compact thermoacoustics [49, 137] is not possible. Respective models that are applicable to HF modes are not existent. Furthermore, the usage of the Linearized Euler Equations to directly compute the desired damping rate is – as addressed in this chapter – not straightforwardly possible. This chapter seeks to establish a theoretical and methodological framework with which the acoustic damping of transversal modes due to shear-layer interactions can be modeled and quantified. This requires to achieve the following research objectives:

- Theoretical assessment of acoustically induced vortex-shedding for transversal modes in the HF regime (Sec. 5.1).
- Clarification of the suitability of the Linearized Euler Equations for direct numerical determination of acoustic damping rates (Sec. 5.2).
- Development of a robust methodology to model and numerically quantify the acoustic energy loss due to vortex-shedding for transversal modes (Sec. 5.3 and Sec. 5.4).
- Computation of damping rates of all 80 operations points, which were concerned for the flame driving studies in the previous chapter (Sec. 5.5).

5.1 Acoustically Induced Vortex-Shedding

Acoustically induced vortex-shedding represents one main damping mechanisms in gas turbine combustors [40, 67, 138]. A simplified explanation of this process is given in Fig. 5.1. The explanation starts by considering a mean shear-layer velocity profile at the area jump in a combustor, which causes an induction of mean vorticity into the flow field. The shear layer velocity profile is modulated by acoustic velocity oscillations, which consistently induces a fluctuation of the vorticity generation. One counter-rotating vortex pair is formed per acoustic oscillation period, which convects downstream with the local mean flow velocity. The generation of these vortices consumes acoustic energy (i.e. damping). For detailed depictions of physical mechanisms on vortex-shedding, one is referred to the literature [11, 40, 68, 103].

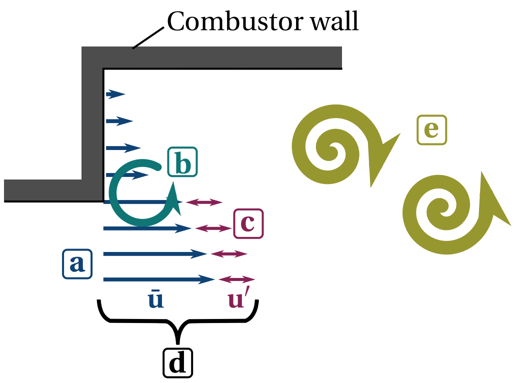

a Mean shear layer velocity profile.

b Mean vorticity caused by shear layer velocity profile.

c Acoustic velocity oscillations at shear layer.

d Modulation of mean shear layer velocity profile by acoustic velocity oscillations leads to a periodic generation of vorticity. This generation of voritcy represents damping of acoustics.

e Counter-rotating vortex pair is formed during one acoustic oscillation period, which propagates downstream with the local mean flow velocity.

Figure 5.1: Simplified concept of acoustically induced vortex-shedding

For the swirl-stabilized benchmark combustor, acoustically induced vortex-shedding is proclaimed as the only relevant damping mechanisms. The impact of other damping mechanism is assumed as negligible. Specifically, damping due to the formation of entropy disturbances is not concerned as these are irrelevant in the frequency regime encountered in this work (cf. Sec. 2.3 and [164, 170]). Damping at the domain in- and outlet can be neglected due to the attenuation of the T1 mode to zero in both, up- and downstream directions (cf. explanations and pressure mode shape plots in Chap. 3). For non-isothermal cases, the T1 mode is simply the first transversal mode appearing after the cut-on frequency of the concerned chamber. The temperature field causes this T1 mode to exhibit a natural longitudinal component. Thus, it could be labeled as T1L0, too, which is not used in this work for clarity reasons. In case of isothermal conditions and a constant diameter of the chamber, the T1 mode is also the first one after the cut-on frequency, yet, it does not attenuate naturally downstream and its shape depends on the outlet boundary condition. The mode's attenuation in up- and downstream direction is caused by the decreasing diameter and increasing temperature in downstream direction, respectively. Consequently, any interaction between the T1 mode and the inlet and outlet of the computational domain is impossible. This boundary independency applies only to the first T1 mode that are close to the cut on value. Modes with longitudinal components (i.e. T1Lx) are exposed to outlet damping. Thus, the first T1 mode (and equally first T2,T3,... modes) is more susceptible to become unstable as boundary damping effects are missing, which explains why the benchmark combustor exhibits HF instabilities at this mode and not at, e.g. the T1L2 mode. Furthermore, dissipation in the acoustic boundary layer [96, 127] is regarded as negligible in benchmark combustor. Notice that the claim of zero wall damping is of hypothetical nature, which is being investigated in the course of an ongoing research project [130].

The term "vortex-shedding" refers to the interactions between acoustic oscillations and shear-layers of a combustor's mean flow field (cf. Fig. 5.1), which causes an energy transformation chain as schematically illustrated in Fig. 5.2. The periodic formation of vortices occurs at the expense of acoustic energy. The shed vortices represent coherent structures of the flow, which propagate upon formation with the local convection speed of the mean flow. Hence, these structures can be interpreted as hydrodynamic flow disturbances, which can be considered as incompressible in low Mach number mean flows as encountered in gas turbine combustors. The hydrodynamic nature causes the vortical structures to be exposed to turbulent processes while propagating downstream [67, 123, 168]. Specifically, dissipative turbulent processes act on the kinetic vortical energy to eventually transform it into heat, which is then absorbed by the mean flow. At the point where the vortices have disappeared, the transformation chain from unsteady acoustic into unsteady

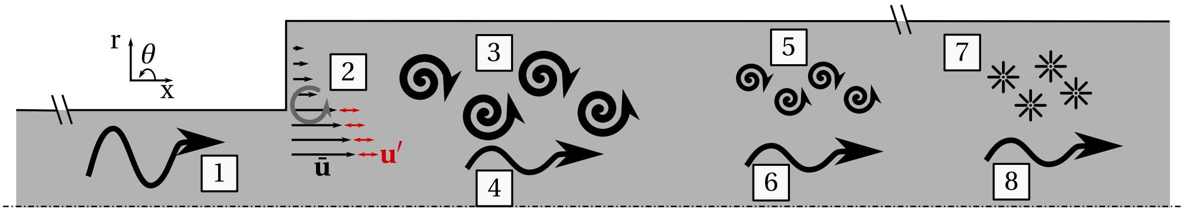

1 Acoustic disturbance (wave) , transported with local speed of sound, energy flux $I_{a,1}$

2 Mean shear layer, interactions with acoustic velocity causes periodic vortex-sheddings

3 Vortical disturbances, transported with local mean flow velocity, energy flux $I_{v,3}$

4 Acoustic wave after vortex shedding, decreased energy flux $I_{a,4} < I_{a,1}$

5 Vortical disturbances, subjected to turbulence, decreased energy flux $I_{v,5} < I_{v,3}$

6 Acoustic wave, unchanged energy flux $I_{a,6} = I_{a,4}$

7 Vortical disturbances dissipate completely into heat, zero energy flux $I_{v,7} = 0$

8 Acoustic wave, unchanged energy flux $I_{a,8} = I_{a,6}$

Figure 5.2: Energy conversion processes associated with vortex-shedding

vortical and furthermore steady thermal energy is completed as illustrated in Fig. 5.2. The energy content associated with the transformation of acoustic into vortical disturbances represents exactly the damping value relevant for the assessment of a combustor's thermoacoustic linear stability state. The discussion of in-depth details on physics and theory of vortex-shedding and accompanied turbulent dissipation processes is beyond this thesis' scope. Interactions between vortical disturbances (e.g. due to vortex-shedding) and the mean flow field that generate acoustic energy [66, 127] are governed by the LEE, too [52, 82]. However, it seems that such interaction have not (yet) appeared as relevant in HF systems. The vortex-shedding phenomenon at the T1 mode in the benchmark combustor is illustrated via Mie-Scattering images [151] in Fig. 5.3 a). Accompanied velocity and vorticity fields of the mean flow (obtained via CFD following the work of [152]) are shown in Figs. 5.3 b)-c), while unsteady counterparts are presented in Figs. 5.3 d)-e). The figures effectively indicate that the vortex-shedding process occurs along the outer shear-layer of the swirling mean flow field.

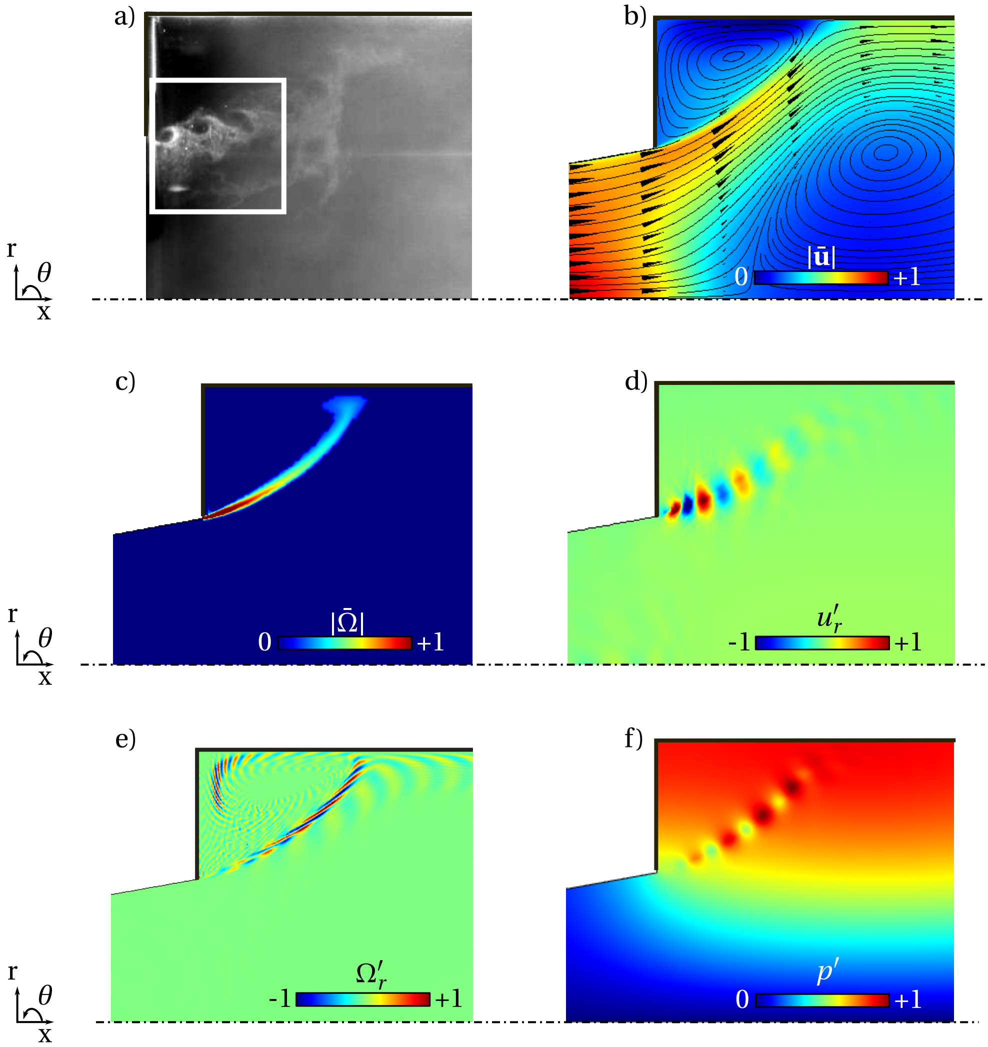

Figure 5.3: a) Mie scattering of period vortex-shedding [151] b) Normalized mean velocity field c) Normalized mean vorticity field d) Normalized instantaneous (radial) velocity disturbance field e) Normalized instantaneous (radial) vorticity disturbance field f) Normalized instantaneous pressure disturbance field

5.2 Linearized Euler Solutions for Quantification of Vortical Acoustic Damping

It has been often perceived (e.g. by the author of this thesis) that computing the eigenvalues of the LEE with an underlying mean flow field that contains a shear-layer emerges the acoustic damping rates relevant for thermoacoustic stability assessments [72]. However, as is addressed below, the LEE eigenvalues contain more physical information than acoustic damping, and a utilization for thermoacoustic stability analyses is not straightforward. Specifically, this section seeks to clarify the suitability of LEE eigenmodes for quantification of acoustic damping due to vortex-shedding from a theoretical perspective. For this purpose, LEE eigenmodes are decomposed into acoustic and vorticity disturbance modes, which are then assessed from an energy conservation perspective using the energy disturbance framework introduced in Sec. 2.7.

5.2.1 Disturbance Field Decompositions

Mathematically, the phenomenon of acoustically induced vortex-shedding is captured by the Linearized Euler Equations (LEE) in frequency domain, which are given by Eqns. 2.18-2.19. This vortex-shedding causes the presence of both, acoustic and vortical disturbances. Consequently, LEE eigenmodes contain acoustic as well as vortical disturbances that respectively propagate with the speed of sound and the mean flow velocity in a superposed manner [25, 96]. Mathematically, the unsteady velocity fields are therefore composed of acoustic and vortical contributions, i.e.

$$\hat{\mathbf{u}}_n = \hat{\mathbf{u}}_{n,a} + \hat{\mathbf{u}}_{n,v}, \tag{5.1}$$

where the former and latter vector fields are irrotational ($\nabla \times \hat{\mathbf{u}}_{n,a} = \mathbf{0}$) and solenoidal ($\nabla \cdot \hat{\mathbf{u}}_{n,v} = 0$) at mode n, respectively. Consequently, the pressure disturbance reads

$$\hat{p}_n = \hat{p}_{n,a} + \hat{p}_{n,v}. \tag{5.2}$$

In order to assess energy transformation processes, it is emphasized that LEE solutions do indeed capture the formation process of vortical disturbances at the expense of acoustic energy at the mean shear-layer. However, the absence of turbulence effects in the LEE inhibits the vortical disturbances from dissipating as it would occur in reality (cf. Sec. 5.1 and Fig. 5.2). From this perspective, the vortical disturbances remain existent upon formation and convect downstream towards the outlet of the domain. The axiomatic requirement of energy conservation leads to the statement that the unsteady flow field given by LEE modes that describe the vortex-shedding process do not experience any change of total energy, while a transformation of acoustic into vortical disturbance energy occurs at the location of vortex-shedding. Figure 5.4 illustrates this statement by presenting the energy fluxes of total, acoustic and vortical flow disturbances for a generic shear-layer that is perturbed by an upstream traveling acoustic wave. In this figure, the downstream end is presumed as infinitely long so that there are no reflections/interactions of acoustic and vortical disturbances at the outlet boundary. Note that acoustic reflection at the area expansion is neglected (i.e. assumed to be fully transmissible) for simplicity of the presented discussions.

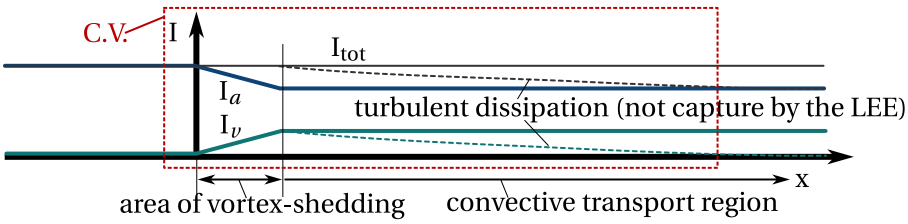

Figure 5.4: Total (I_{tot}), acoustic (I_a) and vortical (I_v) energy fluxes

Performing an energy balance of the fluxes around the control volume shown in Fig. 5.4 gives for the physics that are captured by the LEE:

$$I_{a,in} + \underbrace{I_{v,in}}_{=0} = I_{a,out} + I_{v,out} = I_{tot} \tag{5.3}$$

Employing the Linearized Navier-Stokes Equations (LNSE), i.e. the LEE with additional molecular and/or turbulent diffusion terms on the right hand side of the momentum equations would also not model the desired effects. The effect of molecular diffusion would simply model particle friction of the unsteady motions. This friction would indeed cause (quite small) losses, yet, does not describe the dissipation processes of the vortical disturbances that would yield the correct energy balance given by Eqn. 5.3. Using the turbulent viscosity as e.g. in [53] would also not model the dissipation of vortical disturbances as it acts on both, vortical and acoustic quantities. The consequence would be dissipation of both types of unsteady quantities, which contradicts the physical description that only vortical disturbances are subject to turbulent dissipation processes for a correct energy balance. Additionally, the turbulent viscosity field depends on the turbulence model used for the mean flow computations, which implies an undesirable dependency of the LNSE results on the employed turbulence model.

5.2.2 Energetic Interpretations of Eigenfrequencies

The conservation of disturbance energy (cf. Fig. 5.4) is assessed by performing an energy balance over the LEE eigenmode of interest. For this purpose, the complex eigenfrequency is used, which reads

$$\omega_n = 2\pi f_n - i\alpha_n, \tag{5.4}$$

where f_n is the oscillation frequency of mode n, and the imaginary part α_n is called LEE damping rate. It is intuitive to presume that this LEE damping rate corresponds to the damping rate required for thermoacoustic linear stability analyses [72]. This claim is investigated by relating the LEE damping rate using the conservation equation for the disturbance energy associated with an LEE mode. Referring to Eqn. 2.41, this relation is given by

$$\alpha_n = \frac{1}{2}\frac{1}{\langle \tilde{\mathrm{E}}_n \rangle}\frac{\mathrm{d}\langle \tilde{\mathrm{E}}_n \rangle}{\mathrm{d}t} = \frac{1}{2}\frac{1}{\langle \tilde{\mathrm{E}}_n \rangle}\left(\langle \tilde{\mathrm{D}}_{\hat{\Omega},n} \rangle + \langle \tilde{\mathrm{D}}_{\mathbf{m}_{\hat{\mathbf{u}}_n}} \rangle + \left\langle \tilde{\mathrm{D}}_{\hat{q}_n} \right\rangle - \langle \tilde{\mathrm{I}}_n \rangle\right), \tag{5.5}$$

were $\langle \tilde{\mathrm{E}}_n \rangle$, $\langle \tilde{\mathbf{I}}_n \rangle$ and $\langle \tilde{\mathrm{D}}_{\hat{\Omega},n} \rangle$ represent modal energy, boundary flux terms and source terms due to vortex-shedding interactions, respectively. The source term associated with heat release oscillations is set to zero $\left\langle \tilde{\mathrm{D}}_{\hat{q}_n} \right\rangle = 0$ as flame driving is not considered in this chapter. Note that explicit expressions of the foregoing terms are given by Eqns. 2.35-2.39. Moreover, the following discussions presume zero external momentum addition so that $\langle \tilde{\mathrm{D}}_{\mathbf{m}_{\hat{\mathbf{u}}_n}} \rangle = 0$ in this section, respectively.

As the unsteady velocity consists of acoustic and vortical contributions (cf. Eqn. 5.1), it is reasoned that the modal energy, flux and source term can be decomposed in an analogous manner [25, 96]:

$$\langle \tilde{\mathrm{E}}_n \rangle = \langle \tilde{\mathrm{E}}_{n,a} \rangle + \langle \tilde{\mathrm{E}}_{n,v} \rangle \tag{5.6}$$

$$\langle \tilde{\mathrm{I}}_n \rangle = \langle \tilde{\mathrm{I}}_{n,a} \rangle + \langle \tilde{\mathrm{I}}_{n,v} \rangle \tag{5.7}$$

$$\langle \tilde{\mathrm{D}}_{\hat{\Omega},n} \rangle = \langle \tilde{\mathrm{D}}_{\hat{\Omega},n,a} \rangle + \langle \tilde{\mathrm{D}}_{\hat{\Omega},n,v} \rangle \tag{5.8}$$

It is pointed out that theoretically, the substitution of the decomposed velocity and pressure disturbance into the energy, flux and source expressions emerges mixed terms, i.e. $\mathrm{E}_{n,a,v}, \mathrm{I}_{n,a,v}$ and $\mathrm{D}_{\hat{\Omega},n,a,v}$. A definite physical interpretation of these terms is not yet clarified and poses an open research question [96]. However, the length scale relation between vortical and acoustic disturbances (cf. Fig. 5.3) allows to reason that the mixed terms can be considered small so that upon volume integration

$$\langle \tilde{\mathrm{E}}_{n,a,v} \rangle \ll \langle \tilde{\mathrm{E}}_{n,v} \rangle \,/\, \langle \tilde{\mathrm{E}}_{n,a} \rangle, \tag{5.9}$$

$$\langle \tilde{\mathrm{I}}_{n,a,v} \rangle \ll \langle \tilde{\mathrm{I}}_{n,v} \rangle \,/\, \langle \tilde{\mathrm{I}}_{n,a} \rangle, \tag{5.10}$$

$$\langle \tilde{\mathrm{D}}_{n,a,v} \rangle \ll \langle \tilde{\mathrm{D}}_{n,v} \rangle \,/\, \langle \tilde{\mathrm{D}}_{n,a} \rangle, \tag{5.11}$$

and are thus not further considered in the forthcoming discussions. The LEE modes describe the total flow disturbance, i.e. the superposition of acoustic and vortical contributions. Practically, a respective decomposition is not straightforwardly possible, and thus, not available for this thesis work. Consequently, the individual modal energies, fluxes and source terms in Eqns. 5.6-5.8 cannot be explicitly obtained. Nevertheless, the decomposition mindset presents a crucial component to shed light into the energy transformation processes and the accompanied role of the LEE damping rate.

The proportionality relation between LEE damping rate and change of modal energy of Eqn. 5.5 along with the decomposition in Eqn. 5.6 leads to

$$\alpha_n = \frac{1}{2}\frac{1}{\langle \tilde{\mathrm{E}}_n \rangle}\frac{\mathrm{d}\langle \tilde{\mathrm{E}}_n \rangle}{\mathrm{d}t} = \underbrace{\frac{1}{2}\frac{1}{\langle \tilde{\mathrm{E}}_{n,a} \rangle}\frac{\mathrm{d}\langle \tilde{\mathrm{E}}_{n,a} \rangle}{\mathrm{d}t}}_{=\alpha_{n,a}} + \underbrace{\frac{1}{2}\frac{1}{\langle \tilde{\mathrm{E}}_{n,v} \rangle}\frac{\mathrm{d}\langle \tilde{\mathrm{E}}_{n,v} \rangle}{\mathrm{d}t}}_{=\alpha_{n,v}}, \tag{5.12}$$

where $\frac{1}{2}\frac{1}{\langle\tilde{\mathrm{E}}_{n,a}\rangle}\frac{\mathrm{d}\langle\tilde{\mathrm{E}}_{n,a}\rangle}{\mathrm{d}t} = \alpha_{n,a}$ and $\frac{1}{2}\frac{1}{\langle\tilde{\mathrm{E}}_{n,v}\rangle}\frac{\mathrm{d}\langle\tilde{\mathrm{E}}_{n,v}\rangle}{\mathrm{d}t} = \alpha_{n,v}$ denote energy changes associated with the acoustic and vortical disturbance modes, respectively. It directly follows that

$$\alpha_n = \alpha_{n,a} + \alpha_{n,v}, \tag{5.13}$$

which shows that the LEE damping rate is composed of individual damping rates associated with the acoustic $\alpha_{n,a}$ and vortical $\alpha_{n,v}$ disturbances. Physically, the origins of the individual damping rates are retrieved from the decompositions in Eqns. 5.6-5.8, which yield

$$\alpha_{n,a} = \frac{1}{2}\frac{1}{\langle\tilde{\mathrm{E}}_{n,a}\rangle}\frac{\mathrm{d}\langle\tilde{\mathrm{E}}_{n,a}\rangle}{\mathrm{d}t} = \frac{1}{2}\frac{1}{\langle\tilde{\mathrm{E}}_{n,a}\rangle}\left(\langle\tilde{\mathrm{D}}_{\hat{\Omega},n,a}\rangle - \langle\tilde{\mathrm{I}}_{n,a}\rangle\right), \tag{5.14}$$

$$\alpha_{n,v} = \frac{1}{2}\frac{1}{\langle\tilde{\mathrm{E}}_{n,v}\rangle}\frac{\mathrm{d}\langle\tilde{\mathrm{E}}_{n,v}\rangle}{\mathrm{d}t} = \frac{1}{2}\frac{1}{\langle\tilde{\mathrm{E}}_{n,v}\rangle}\left(\langle\tilde{\mathrm{D}}_{\hat{\Omega},n,v}\rangle - \langle\tilde{\mathrm{I}}_{n,v}\rangle\right). \tag{5.15}$$

These equations reveal that the governing factors that cause a change of individual modal energy (i.e. non-zero individual damping rates) are due to respective flux terms $\langle\tilde{\mathrm{I}}_{n,a}\rangle$ and $\langle\tilde{\mathrm{I}}_{n,v}\rangle$ as well as source terms $\langle\tilde{\mathrm{D}}_{\hat{\Omega},n,a}\rangle$ and $\langle\tilde{\mathrm{D}}_{\hat{\Omega},n,v}\rangle$. Thus, a physical interpretation of the three available damping rates given in Eqn. 5.13 can now be established:

- Acoustic damping rate $\alpha_{n,a}$ describes the modal change of energy associated with the acoustic disturbance.
- Vortical damping rate $\alpha_{n,v}$ describes the modal change of energy associated with the vortical disturbance.
- LEE damping rate α_n describes the net effect the modal change of energy associated with total disturbance, i.e. the superposition of the acoustic and vortical disturbances.

The assessment of thermoacoustic stability – which represents one central objective of this thesis – relies only on the acoustic damping rate $\alpha_{n,a}$, while the vortical damping rate $\alpha_{n,v}$ is irrelevant for this task. Hence, a direct use of the LEE damping rates α_n is not straightforward, which is subsequently discussed in more detail by assessing the relations between the acoustic and vortical source as well as flux terms in the context of overall energy conservation.

Source Term Relations

The first step towards revealing the inapplicability of LEE damping rates for thermoacoustic stability analysis is comprised of establishing a physical connection between the individual source terms $\langle \tilde{\mathrm{D}}_{\hat{\Omega},n,a} \rangle$ and $\langle \tilde{D}_{\hat{\Omega},n,v} \rangle$ that causes a change of modal energy/damping rates associated with the acoustic and vortical modes. The event of vortex-shedding triggers the formation of vortices at the mean flow's shear-layer at the expense of acoustic energy (cf. Sec. 5.1). Conservation of energy and absence of any dissipation effects in the LEE requires that the source term due to mean flow interaction, i.e. the vortex-shedding process, vanishes to give

$$\langle \tilde{\mathrm{D}}_{\hat{\Omega},n} \rangle = 0, \tag{5.16}$$

which gives for the individual source terms

$$\langle \tilde{\mathrm{D}}_{\hat{\Omega},n,a} \rangle = -\langle \tilde{\mathrm{D}}_{\hat{\Omega},n,v} \rangle . \tag{5.17}$$

The remaining factor that leads to a non-zero LEE damping rate in Eqn. 5.5 is the flux term $\langle \tilde{\mathrm{I}}_n \rangle$, which describes the transfer of disturbance energy across the system boundaries. If one uses LES instead of LEE, the source term would be non-zero as turbulent dissipation of vortical disturbances is accounted for (cf. [168]). The impact of the scenarios of zero and non-zero flux boundaries on the LEE damping rate is addressed next.

LEE Damping Rates for Zero Energy Flux at System Boundaries $\langle \tilde{\mathbf{I}}_n \rangle = 0$

The case of zero flux term $\langle \tilde{\mathrm{I}}_n \rangle = \langle \tilde{\mathrm{I}}_{n,a} \rangle = \langle \tilde{\mathrm{I}}_{n,v} \rangle = 0$, implies that there is no energy transfer across the system boundaries. From an energy balance perspective where the control volume is given by the combustor domain, disturbance energy can neither enter nor leave at the inlet and outlet, respectively. There is transformation of acoustic to vortical energy at shear-layer due to vortex-shedding (cf. Eqns. 5.16-5.17). The total disturbance energy of the concerned (LEE) mode is thus constant, which yields

$$\frac{\mathrm{d}\langle \tilde{\mathrm{E}}_n \rangle}{\mathrm{d}t} = 0 \rightarrow \alpha_n = 0, \tag{5.18}$$

and leads to the statement that LEE damping rates are zero for zero flux boundary conditions.

LEE Damping Rates for Non-Zero Energy Flux at System Boundaries $\langle \tilde{\mathrm{I}}_n \rangle \neq 0$

If the vortical disturbances that convect downstream were simply allowed to exit the domain/control volume, the LEE damping rate would reflect the "correct" and desired energy balance. This scenario is achieved by setting the vortical flux at the domain outlet equal to the vortical dissipation term. Also, all of the acoustic energy needs to remain within the domain, i.e.

$$\langle \tilde{\mathrm{I}}_{n,v} \rangle_{out} = \langle \tilde{D}_{n,v} \rangle, \tag{5.19}$$

$$\langle \tilde{\mathrm{I}}_{n,a} \rangle_{out} = 0. \tag{5.20}$$

Substituting Eqn. 5.19 into Eqn. 5.15 reveals that the net change of vortical energy is zero, i.e.

$$\frac{\mathrm{d}\langle \tilde{\mathrm{E}}_{n,v} \rangle}{\mathrm{d}t} = 0 \rightarrow \alpha_{n,v} = 0. \tag{5.21}$$

Substituting Eqn. 5.21 into Eqn. 5.13 mathematically reveals that the LEE damping rate is equal to the acoustic damping rate, i.e.

$$\alpha_n = \alpha_{n,a}, \tag{5.22}$$

for the present case of full transmission of vortical energy at the domain outlet. Unfortunately, prescribing the flux boundary condition in Eqns. 5.19-5.20 is not possible in practice, i.e. there is no formulation that transmits all vortical energy and retains all acoustic energy at the outlet. Moreover, the value of vortical dissipation is not available either, which is due to the inseparability of the LEE solution variable. Thus, the computation of the desired acoustic damping rate – although theoretically possible – by directly solving for LEE eigenmodes is, at this point, denied.

Conclusively, the only boundary condition that can be confidentially applied for numerical simulation of LEE systems is the prescription of zero flux, i.e. $\langle \tilde{\mathrm{I}}_n \rangle = 0$ as given by Eqns. 2.48-2.49. These zero flux boundary conditions can be interpreted as a fully reflecting (in an energy sense) boundary condition for LEE modes that contain both, acoustic and vortical contributions. Even the prescription of measured impedance boundary conditions should be handled with care if the LEE are solved. Specifically, these impedances presume the presence of sole acoustics. Hence, prescribing such an impedance (which is valid for acoustic disturbances only) at boundaries (e.g. domain outlets) which are exposed to vortical disturbances, non-physical interactions in form of incorrect reflections and transmissions are induced. Conveniently, all LEE eigenfrequency simulations in this work are conducted with zero flux boundary conditions so that the previous issues are not applicable and need no further consideration.

5.3 Quantification Methodology for Vortical Acoustic Damping of Transversal Modes

In this section, a methodology to determine acoustic damping rates due to vortex-shedding processes is developed. Specifically, governing equations, modeling details and solution procedures are subsequently presented in the following subsections.

5.3.1 Governing Equations

The methodology proposed to model and quantify vortical damping of transversal modes is based on the HE as for the driving rate computations in Chap. 4, i.e.

$$\bar{\rho} i\omega_{n,a}\hat{\mathbf{u}}_{n,a} + \nabla \hat{p}_{n,a} = \mathbf{m}_{\hat{\mathbf{u}},n,a}, \tag{5.23}$$

$$i\omega_{n,a}\hat{p}_{n,a} + \gamma \bar{p}\nabla \cdot \hat{\mathbf{u}}_{n,a} = \underbrace{(\gamma - 1)\hat{\dot{q}}_n}_{=0}, \tag{5.24}$$

which are identical to Eqns. 4.1-4.2 except that a source term to the momentum equation is retained while the energy counterpart due to heat release oscillations is set to zero. The solutions of Eqns. 5.23-5.24 yield irrotational velocity disturbance fields driven by pressure gradients as the potential, i.e. purely acoustic modes. This irrationality implies that the damping rates describe pure acoustics, i.e. $\alpha_{n,a}$. Recall that the negligence of mean flow denies the capturing of interaction effects that induce a loss of degeneracy, i.e. split of eigenfrequencies, associated with transversal mode pairs, which is acceptable for the purpose of computing driving/damping rates as explained in Sec. 4.1.

5.3.2 Absorption Model

Acoustic dissipation due to vortex-shedding is modeled as a sink of momentum while capturing any hydrodynamic effects is disregarded. Mathematically, this sink of momentum is modeled by linearly expanding the volumetric source term in Eqn. 5.23 to the first order, i.e.

$$\mathbf{m}_{\hat{\mathbf{u}},n,a} = -\mathbf{D} \cdot \hat{\mathbf{u}}_{n,a} \cdot \delta(\mathbf{x} - \mathbf{x}_D). \tag{5.25}$$

The matrix $\mathbf{D}$ is assumed to unfold into a 3×3 diagonal matrix with entries $\mathbf{D}(1,1) = \zeta_x$, $\mathbf{D}(2,2) = \zeta_r$, and $\mathbf{D}(3,3) = \zeta_\theta$. These quantities can be interpreted as acoustic loss coefficients in an analogous manner as occurring in vortical damping models [49, 138] for low-frequency instabilities. The Dirac function in Eqn. 5.25 indicates that the damping term is only defined in the region $\mathbf{x}_D$ where dissipation physically occurs. This region is given by the shear-layer of the mean flow, i.e. the mean vorticity field $\bar{\Omega}$ as illustrated in Fig. 5.3.

In order to model the damping effect of vortex-shedding, it is assumed that dissipation of acoustics occurs isotropically along the shear-layer of the mean flow allow. This assumptions allows to imply equality between the three loss coefficients, i.e. $\zeta_x = \zeta_r = \zeta_\theta = \zeta$, and leads to a reduction of the three unknown coefficients in Eqn. 5.25 from three to one. The loss matrix becomes

$$\mathbf{D} = \zeta \cdot \mathbf{I}, \tag{5.26}$$

where $\mathbf{I}$ is the 3×3 identity matrix and ζ is the unknown loss coefficient. In order to demonstrate that the proposed methodology induces damping on the concerned modes, the relation between the damping rate and change of modal energy is again applied. Employing the assumptions associated with Eqns. 5.23-5.24 on the Eqns. 5.12 yields

$$\alpha_{n,a} = \frac{1}{2}\frac{1}{\langle \tilde{\mathrm{E}}_{n,a}\rangle}\frac{\mathrm{d}\langle \tilde{\mathrm{E}}_{n,a}\rangle}{\mathrm{d}t} = -\frac{1}{8}\frac{1}{\langle \tilde{\mathrm{E}}_{n,a}\rangle}\int_V [\mathbf{D}\cdot\hat{\mathbf{u}}_{n,a}\cdot\hat{\mathbf{u}}^*_{n,a}\cdot\delta(\mathbf{x}-\mathbf{x}_D)]\,\mathrm{d}V \tag{5.27}$$

which reveals that the proposed loss model in Eqn. 5.26 acts indeed dissipatively (i.e. negative change of energy) for $\zeta > 0$. Hence, the remaining task before the damping rate can be computed is the determination of the loss coefficient ζ, which is presented next.

5.3.3 Determination of Loss Coefficient

The determination of the loss coefficient ζ in Eqn. 5.26 occurs by imposing an equality requirement between the reflection coefficient of the concerned configuration obtained from respective simulations of the full LEE (which includes the physics) and the HE system (which includes the damping model). This reflection coefficient is defined as

$$\mathrm{R}_T = \frac{\hat{\mathrm{F}}_T}{\hat{\mathrm{G}}_T} \tag{5.28}$$

where $\hat{\mathrm{F}}_T$ and $\hat{\mathrm{G}}_T$ are frequency dependent down- and upstream traveling acoustic wave amplitudes as indicated in Fig. 5.5. The subscript T denotes that the traveling wave amplitudes are associated with transversal mode shapes.

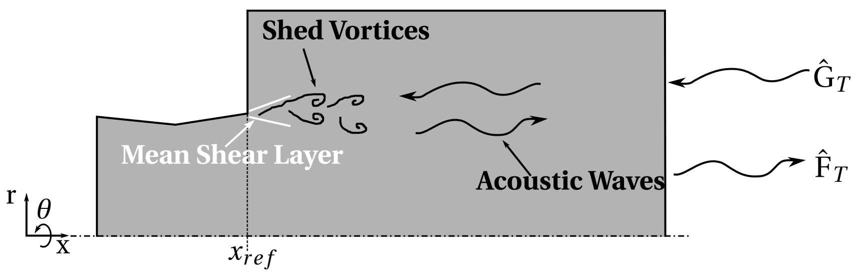

Figure 5.5: Characterization of an acoustic domain (shaded in grey) by reflection coefficients with the reference location at the burner exit

Using the Multi-Microphone-Method (MMM) [3, 45, 55, 147] to retrieve this reflection coefficient filters out any vortical disturbances present in the LEE solutions [54, 82], and represents a unambiguous quantification of the pure acoustic damping due to the vortex-shedding . Essentially, the MMM fits the numerically simulated pressure field to an analytical counterpart expression that governs the traveling wave amplitudes. This expression is given by the solution of the convective Helmholtz equation [96, 127] for a uniform axial mean velocity in a pipe with constant cross section, which reads for cylindrical coordinates

$$\hat{p}_{MMM}(\mathbf{x},\omega) = \mathcal{A}_F(\mathbf{x},\omega)\hat{\mathrm{F}}_T + \mathcal{A}_G(\mathbf{x},\omega)\hat{\mathrm{G}}_T. \tag{5.29}$$

The auxiliary functions $\mathcal{A}_F$ and $\mathcal{A}_G$ expand to

$$\mathcal{A}_F(\mathbf{x},\omega) = \bar{\rho} c J_b(r k^r_{T1}) \exp(-i k^{x+}(x - x_{ref})) \exp(\pm i b(\theta - \theta_{ref})), \tag{5.30}$$

$$\mathcal{A}_G(\mathbf{x},\omega) = \bar{\rho} c J_b(r k^r_{T1}) \exp(-i k^{x-}(x - x_{ref})) \exp(\pm i b(\theta - \theta_{ref})), \tag{5.31}$$

where J_b is the Bessel function of b-th order while x_{ref} and θ_{ref} are reference values (which are set to zero in this work) of axial and azimuthal coordinate, respectively. In Eqns. 5.29-5.31, b is the azimuthal wave number (which is for T1 modes $b = 1$) while the axial wave numbers $k^{x\pm}$ are given by

$$k^{x\pm} = \frac{k}{1-\bar{M}^2}\left(-\bar{M} \pm \sqrt{1-\left(\frac{k^r_{T1}}{k}\right)^2 (1-\bar{M}^2)}\right), \tag{5.32}$$

where $\bar{M}$ represents the axial Mach number of a presumed uniform mean flow field. The total wave number is defined as $k = \omega/c$ with ω being the angular (real) frequency and c the speed of sound. The radial wave number in Eqns. 5.29-5.32 is $k^r_{T1} = s_{T1}/R_c$, where $s_{T1} = 1.8412$ is the Bessel root associated with the T1 mode solution of the convective wave equation [96], and R_c is the chamber radius. The employment of Bloch symmetry simplifications – as is explained in Sec. 5.4.1 – implies the sole presence of one specific mode type (here: T1 modes with arbitrary longitudinal components). Hence, other mode types such as pure L modes, which naturally occur in the investigated frequency regimes along with the T1 modes in a superposed manner if three-dimensional computational domains are used, can be omitted in the pressure field description of Eqn. 5.29. Detailed theory and determination procedures of reflection coefficients for systems with several multi-dimensional modes of various types can be found in [79, 144].

The complex wave amplitudes $\hat{\mathrm{F}}_T$ and $\hat{\mathrm{G}}_T$ are obtained by fitting Eqn. 5.29 to the numerically computed pressure fields at the (real) frequencies of interest. Specifically, these pressure modes are given by numerical solutions of the LEE/HE model, which represent response fields to an external excitation (cf. details below). The fitting procedure starts by re-writing Eqn. 5.29 in matrix-vector notation, i.e.

$$\hat{\mathbf{p}} = \mathbf{M}_{R_T} \cdot [\hat{F}_T \;\; \hat{G}_T]^T \tag{5.33}$$

where $\hat{\mathbf{p}}(\mathbf{x}_p) = [\hat{p}(x_{p,1}, r_{p,1}, \theta_{p,1}) \;\; \hat{p}(x_{p,2}, r_{p,2}, \theta_{p,2}) \;\; \ldots \;\; \hat{p}(x_{p,N_p}, r_{p,N_p}, \theta_{p,N_p})]^T$ is a row vector containing complex pressure values retrieved from N_p discrete probes $\mathbf{x}_p$ within the computational domain. This probe array is required to be located within a region of the domain, which satisfies the underlying assumption (i.e. constant mean velocity and cross section) of the objective function in Eqn. 5.29 for the fit. The matrix

$$\mathbf{M}_{R_T} = \begin{bmatrix} \mathcal{A}_F(x_{p,1}, r_{p,1}, \theta_{p,1}) & \mathcal{A}_G(x_{p,1}, r_{p,1}, \theta_{p,1}) \\ \mathcal{A}_F(x_{p,2}, r_{p,2}, \theta_{p,2}) & \mathcal{A}_G(x_{p,2}, r_{p,2}, \theta_{p,2}) \\ \cdot & \cdot \\ \cdot & \cdot \\ \cdot & \cdot \\ \mathcal{A}_F(x_{p,N_p}, r_{p,N_p}, \theta_{p,N_p}) & \mathcal{A}_G(x_{p,N_p}, r_{p,N_p}, \theta_{p,N_p}) \end{bmatrix} \tag{5.34}$$

is composed of two row vectors carrying the discrete values of the mode shape function evaluated at the probe locations. Finally, the overdetermined system in Eqn. 5.33 ist solved for the unknown amplitudes in a least square sense, which is achieved by pseudo-inversion, i.e.

$$[\hat{F}_T \;\; \hat{G}_T]^T = (\mathbf{M}_{R_T}^T \cdot \mathbf{M}_{R_T})^{-1} \mathbf{M}_{R_T}^T \cdot \hat{\mathbf{p}}, \tag{5.35}$$

The value for ζ – which is in general frequency dependent – that equates reflection coefficients of the LEE with the HE model yields a quantitative correct description of the vortical acoustic losses at the respective frequency. The main steps to setup the HE damping model and obtain the loss coefficient are summarized as follows:

1. Visualization of the mean shear-layer $\bar{\Omega}$ and identification of the sink location $\mathbf{x}_D$ (cf. Fig. 5.3c).

2. Computation of the reflection coefficients R_T over the frequency range of interest from LEE solutions.

3. Determination of ζ values such that the reflection coefficient from 2. is reproduced by the HE model.

Once the values of ζ are known across the concerned frequency band, Eqns. 5.23-5.24 can be solved for the eigenmodes of interest, which yields the desired acoustic damping rate.

5.4 Validation Test Cases

This section seeks to validate the conservation of disturbance energy statement in Sec. 5.2 and the quantification approach of Sec. 5.3. All validation studies are carried out using the isothermal configuration of the swirl-stabilized combustion system presented in Chap. 3 as benchmark test case. The reason for selecting this isothermal configuration is to provide optimal conditions to investigate acoustically induced vortex-shedding and accompanied acoustic damping processes. The absence of combustion implies the absence of any thermoacoustic processes, leaving vortex-shedding processes as the sole mechanisms that govern the damping rate value without any superposed presence of flame driving effects. It can be expected that the mean temperature/density gradients impacts the vortex-shedding processes (cf. vorticity equation and discussion of corresponding terms in [96]). Thus, a respective assessment of theory, quantitative impact on damping rates and inclusion in the loss model is required for an advancement of the approach and is assigned to future work.

All upcoming analyses are executed using the same operation point, which is defined by an air mass flow rate of $\bar{\dot{m}} = 120\,\mathrm{g/s}$ at $\bar{T}_{in} = 293.15\,\mathrm{K}$. Details on design, experimental setup and computation domain is provided in Fig. 3.3. The simulated velocity field is presented in Fig. 5.6 and is representative of the turbulent flow conditions occurring in industrial (e.g. can type) gas turbine combustors. The velocity field is shown in Fig. 5.6 in 3D form to illustrate the swirling and multidimensional as well as rotationally symmetric character, whereas the following simulations are executed in 2D as explained next.

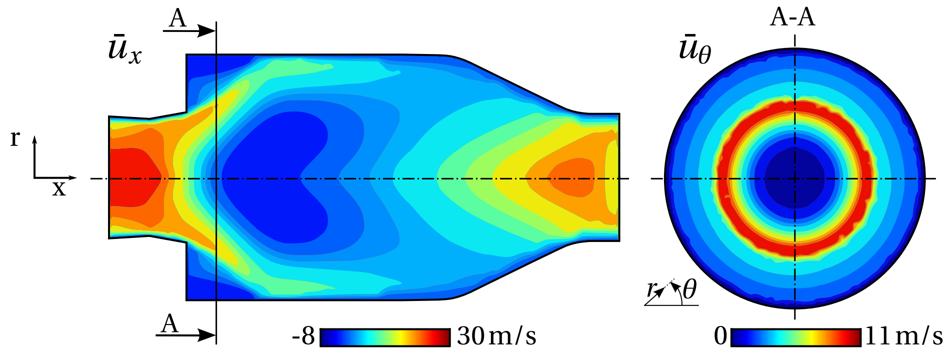

Figure 5.6: Swirling mean flow field combustion chamber with nozzle outlet

5.4.1 Bloch Symmetry Framework

The mean flow field of the swirl-stabilized benchmark combustor can be assumed as axisymmetric (cf. Fig. 5.6). This circumstance allows for the application of Bloch symmetry simplifications [102] to transform the computational domain from 3D into 2D. Thereby, a substantial increase of mesh resolution capabilities is achieved, which enables to accurately resolve the vortex-shedding processes. Bloch symmetry exploits the azimuthal periodicity associated with transversal modes, which motivates to separate the solution variables, i.e.

$$\hat{p}_n(x,r,\theta) = \hat{p}_{n,b}(x,r)\exp(\pm ib\theta), \tag{5.36}$$

$$\hat{\mathbf{u}}_n(x,r,\theta) = \hat{\mathbf{u}}_{n,b}(x,r)\exp(\pm ib\theta), \tag{5.37}$$

$$\mathbf{m}_{\hat{\mathbf{u}},n}(x,r,\theta) = \mathbf{m}_{\hat{\mathbf{u}},n,b}(x,r)\exp(\pm ib\theta), \tag{5.38}$$

$$\hat{q}_n(x,r,\theta) = \hat{q}_{n,b}(x,r)\exp(\pm ib\theta), \tag{5.39}$$

where $\hat{p}_b(x,r)$, $\hat{\mathbf{u}}_b(x,r)$, $\mathbf{m}_{\hat{\mathbf{u}},n,b}(x,r)$ and $\hat{q}_{n,b}(x,r)$ are axisymmetric (Bloch) mode shapes/sources associated with the azimuthal variability of $\exp(\pm ib\theta)$. This azimuthal shape function describes a rotating mode where $\pm$ denotes the direction of rotation, i.e $+$ = clockwise (CCW) and $-$ = counterclockwise (CW) with respect to the reference frame given in Fig. 5.6). If T1 modes are concerned, the azimuthal wave number for first transversal modes is $b = +1$ while the consideration of e.g. longitudinal or second transversal modes implies that $b = 0$ and $b = 2$, respectively. Equations 5.36-5.39 are substituted into the three-dimensional LEE given by Eqns. 2.18-2.19. Division by $\exp(\pm i b\theta)$ yields a modified version of the LEE, i.e. Bloch LEE, that governs the Bloch mode shapes, which are axisymmetric and thus allow for the solution on 2D domain as is indicated in Fig. 5.7.

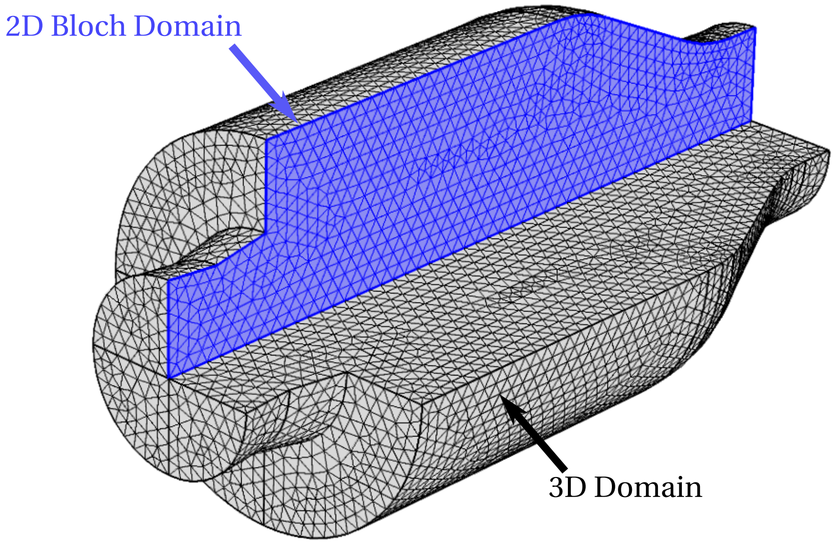

Figure 5.7: Numerical setup of LEE eigenfrequency simulations: a) domain and boundary conditions b) coarse mesh c) fine mesh

The reconstruction of the corresponding "true" three-dimensional transversal mode shapes is given by Eqns. 5.36-5.39. Numerical discretization and solution procedures as well as prescription of boundary conditions associated with 2D Bloch LEE simulations are identical as for the 3D counterparts (cf. Sec. 2.8). One shortcoming of the Bloch methodology is the in advance definition of the rotation direction via the azimuthal wave number b. Hence, in order to compute the Bloch solution associated with CW and CCW rotating modes, which is required if the loss of non-degeneracy of transversal mode pairs in swirling mean flows is investigated (cf. App. B), two respective simulations with $b = +1$ and $b = -1$ need to be carried out. However, due to the substantial increase in computational efficiency by utilizing the Bloch framework, the additional effort required to compute these two solutions separately can be neglected.

5.4.2 Results – Energy Conservation of LEE Modes

The conservation of total disturbance energy within LEE eigenmodes (cf. Sec. 5.2) is assessed by computing the LEE damping rate α_n for energy neutral boundary conditions (cf. Fig. 5.8a)). In accordance with Eqns. 5.17-5.18, a zero valued damping rate would then verify this conservation of energy statement. Also, the impact of numerical stabilization is inspected. The assessments are carried out using the T1 as well as the T1L1 eigenmode of the isothermal nozzle test case. The decreasing cross sectional area of the nozzle causes an axially increasing cut-on frequency (as the increasing temperature causes in the reactive case), and thus detaches both modes from the outlet boundary condition. The Bloch LEE is solved to produce the desired eigensolutions, which implies the utilization of a 2D mesh configuration for the discretizations. In order to assess the impact of the mesh on the damping rates , two different degrees of fineness, i.e. coarse and fine (Fig. 5.8b)-c)), are used. The coarse and fine mesh are composed of approximately 12,000 and 230,000 linear elements to give $N \approx 24{,}000$ and $N \approx 455{,}000$ degrees of freedom to be solved, respectively.

The resulting mode shapes (CCW mode, $b = -1$) of pressure and velocity of the fine mesh are presented in Fig. 5.9, which reveal two relevant observations:

- Formation of vortices along the mean shear-layer, which confirms that the vortex-shedding is captured within LEE solutions.
- Containment of vortical disturbances in the domain, where a portion is circulating along with the outer recirculation zone of the swirling mean flow field while another portion is convected downstream. The image indicates a vanishing character of the vortical disturbances towards the outlet. The reason for this seemingly dissipating behavior is the advection of the vortical disturbance with the local mean velocity, which decelerates, spreads out downstream of the swirl zone (cf. Fig. 5.8) and retains

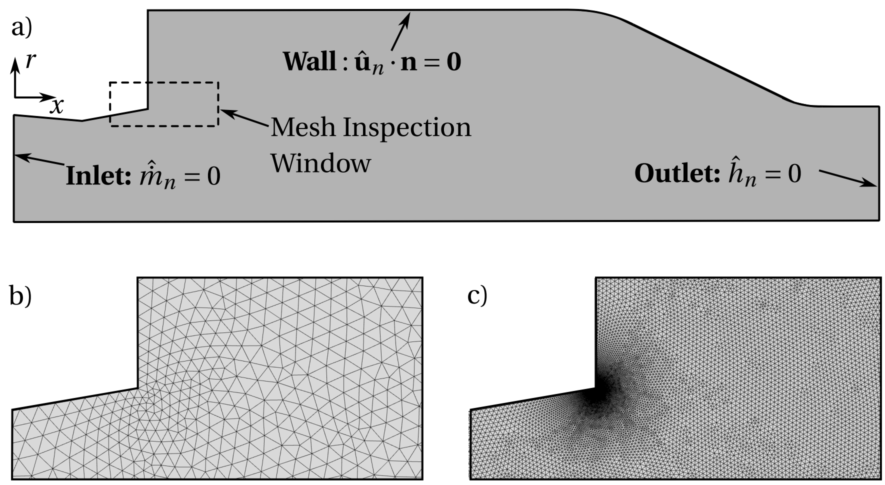

Figure 5.8: Numerical setup of LEE eigenfrequency simulations: a) domain and boundary conditions b) coarse mesh c) fine mesh

within the domain.

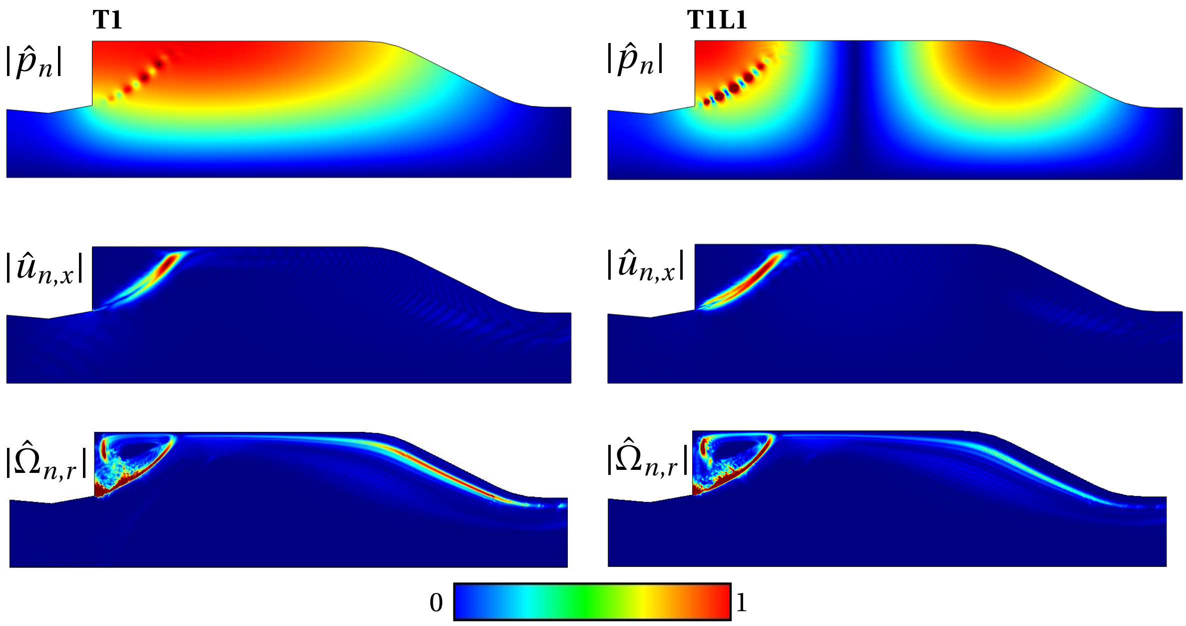

Figure 5.9: Normalized pressure and velocity mode shapes

The LEE damping rates and oscillation frequencies computed for varying stabilization parameter α_τ of the T1 and T1L1 modes are shown in Fig. 5.10 for the two mesh configurations. The plots show the results for the CW mode ($b = +1$) while equivalent computations using the CCW setting ($b = -1$) yields the same behavior, which is not shown to avoid unnecessary repetitions.

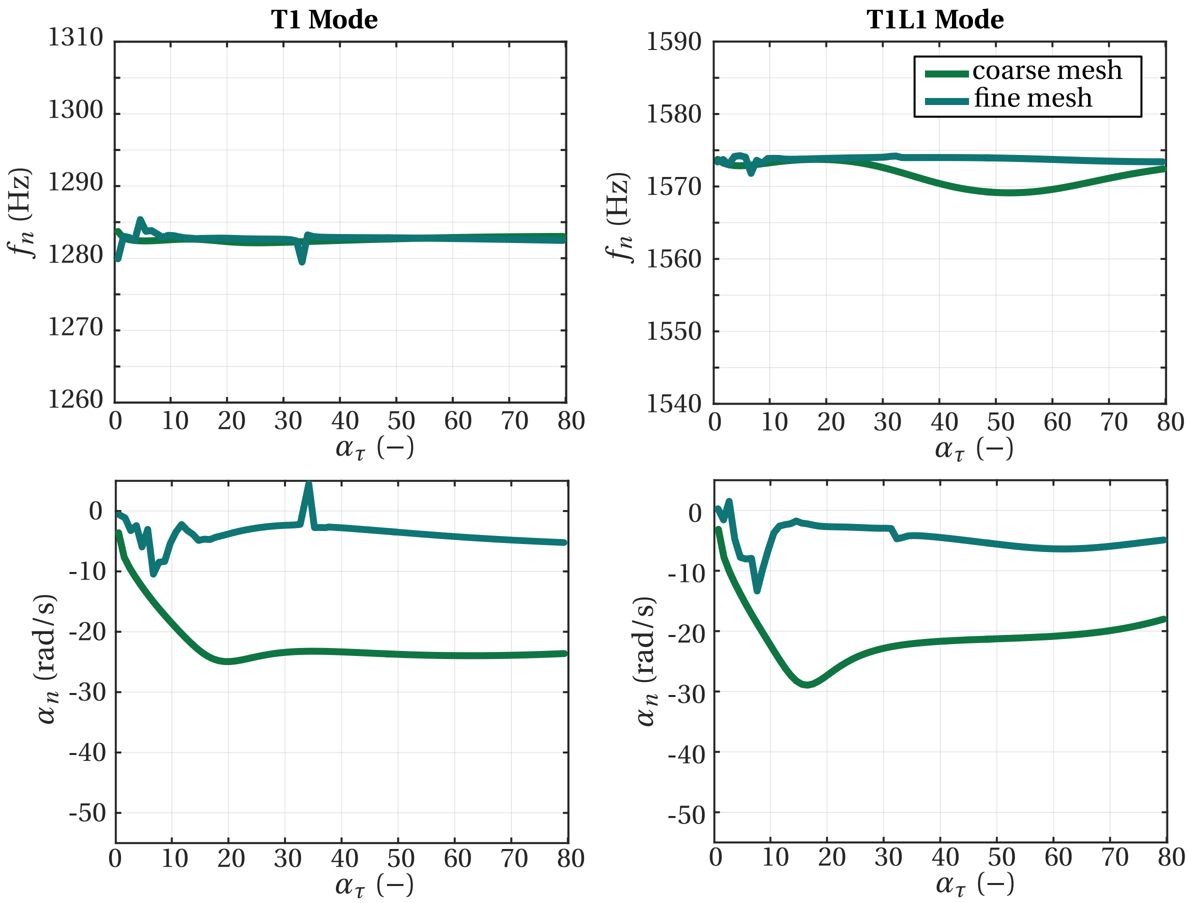

Figure 5.10: LEE eigenfrequency vs. numerical stabilization parameter for the CW mode ($b = +1$)

The plot emerges the following findings:

- Variations of oscillation frequencies with increasing stabilization strength are negligibly small.
- Smallest value of the stabilization parameter that yields fully non-spurious/numerically stable mode shape solutions emerged as $\alpha_\tau = 1$. Mode shape solutions below this value represents non-negligible spurious features and should not be considered for further analyses.

- LEE damping rates over the considered range of stabilization parameters for the fine mesh are fairly constant and near-zero. The finite values of the damping rate is allocated to numerical diffusion effects induced by the FEM mesh. Hence, the energy conservation statement for LEE eigensolution established in Sec. 5.2 and given by Eqn. 5.18 can be confirmed. Furthermore, the constancy of the damping rate with increasing values of α_τ indicates that numerical stabilization schemes are negligible, if the mesh resolution is sufficiently fine as theoretically expected. An elegant methodology, e.g. based on a modified set of LEE equations, would be to use the stabilization parameter – since it is mathematically a diffusion term – in a way that it would act on the convectively transported vortical disturbances in a dissipative manner. Thereby, real world turbulent diffusion could be modeled/mimicked by the stabilization term. However, the development of such a method is beyond the scope of this thesis and left for future research work.
- Nearly linear decrease of the LEE damping rates from $\alpha_\tau = 1$ to $\alpha_\tau = 10$ for both eigenmodes of the coarse mesh simulations. For further increasing values of the stabilization parameter, the evolution saturates and becomes rather arbitrary for the T1 and T1L1 damping rate, respectively. Hence, the impact of numerical stabilization for the coarse mesh is found as non-negligible.
- Overall, accurately resolving all vortex-shedding processes along with the associated conservation of total disturbance energy within LEE eigenmodes requires a considerably fine mesh resolution. A sufficient degree of mesh fineness is achieved, if stabilization independence as well as near zero values of the damping rates emerges.

As pointed out above, using the LNSE [54, 82] instead of the LEE would add molecular/turbulent diffusion terms to the equation. The molecular diffusion term models viscous dissipation within the flow motions. The turbulent diffusion term acts dissipatively on both, acoustic and vortical disturbances in the regions of the domain defined by the turbulent viscosity field that is a result of CFD simulations (cf. comments above in Sec. 5.1). Essentially, these two dissipation effects do not represent the turbulent dissipation of vortical disturbance as would be required for the desired energy balance. The observation of the linear decrease of the damping rates with increasing stabilization parameter (range 0-10 in Fig. 5.10) for the coarse mesh cases motivates to use such a configuration to model the dissipation of vortical disturbances in a qualitative manner. The coarse mesh induces numerical diffusion, which is sensitive to the stabilization parameter. For increasing mesh refinement, this connection between stabilization parameter and mesh diffusion vanishes. The stabilization parameter can then be used as a tuning variable to establish the desired damping rates. Such qualitative reproductions are important e.g. for time domain investigations, which are based on the discrete LEE systems/eigenmodes as is concerned in Chaps. 7-8. The shortcoming of this approach is clearly the lack of predictive capabilities, i.e. an in advance determination of the α_τ value that yields the correct damping rate/amount of dissipation is not possible. It is emphasized that there are no guidelines to determine the most suitable mesh "coarseness" to induce the linear dependence between stabilization parameter and LEE damping rate. Moreover, purposefully inducing such numerical errors into the solution of differential equations might not seem like a robust and advanced engineering/science practice. Hence, this "coarsened" mesh approach to model acoustic damping through adjusting the stabilization strength should be used with great care and strong awareness of the underlying circumstances.

Finally, it is important to point out that the degree of mesh resolution to achieve the solution accuracy is a consequence of the Bloch framework, and the associated 2D computational domain. Carrying out equivalent simulations with the same (fine) mesh resolution on a 3D domain would translate into discrete system sizes of $N \approx 10,000,000$. Producing numerical solutions of systems with these sizes is unattainable with standard (i.e. non-high performance computing) computational resources as are used for the numerical simulations of this thesis. Hence, the implementation of the Bloch framework for LEE solutions presents the essential component to accurately resolve vortex-shedding processes within swirling mean flows. The domain transformation from 3D to 2D using the Bloch approach is only possible if the combustor is rotationally symmetric in terms of geometry and mean flow field. For industrial configurations, such a symmetry condition is rarely satisfied. Nevertheless, the Bloch approach can be applied to reduce the computational domain size of industrial combustors, too. For example for the analysis of annular system, only a particular segment can be used as the computational domain instead of the entire ring. Thereby, an improvement of the computational efficiency (cf. [102]) is achieved, too, although not to a degree as encountered for 2D-Bloch domains of the benchmark test case in this thesis. However, the application to simple geometry test cases allows to carry out investigations, develop and verify models that are transferable to industrial settings.

5.4.3 Results – Damping Rate Quantification

This section provides the validation results of the damping rate quantification method. Specifically, vortical damping of transversal modes within the test case configuration/operation point is modeled and quantified applying the procedure proposed in Sec. 5.3. The first step of this methodology is the visualization of the dissipation/momentum sink region $\mathbf{x}_D$, which is simply given by the locations at the outer shear-layer, where the mean flow vorticity is non-zero (cf. Fig. 5.11 a)).

Next, the reflection coefficient is computed for a frequency band of $\omega_n = [1200, 1795] \cdot 2\pi$ rad/s with increments of $\Delta\omega_n = 35 \cdot 2\pi$ rad/s, which includes the eigenfrequencies of the T1 and T1L1 modes in the test case combustor. The domain used to compute the pressure response modes to further obtain the reflection coefficients differs to the nozzle chamber that constitutes the validation test case. Specifically, the nozzle termination is removed and the chamber tube is elongated in downstream direction to yield the computational domain for the determination of the reflection coefficients. The elongation is justified as long as the swirling mean flow field – and thus the vortex-shedding interactions – in the vicinity of the faceplate remains identical between the nozzle and the straight domain. This equality is affirmed by comparing the respective velocity fields given by Figs. 5.6 and 5.11b). The reason for this elongation is due to the necessity to establish

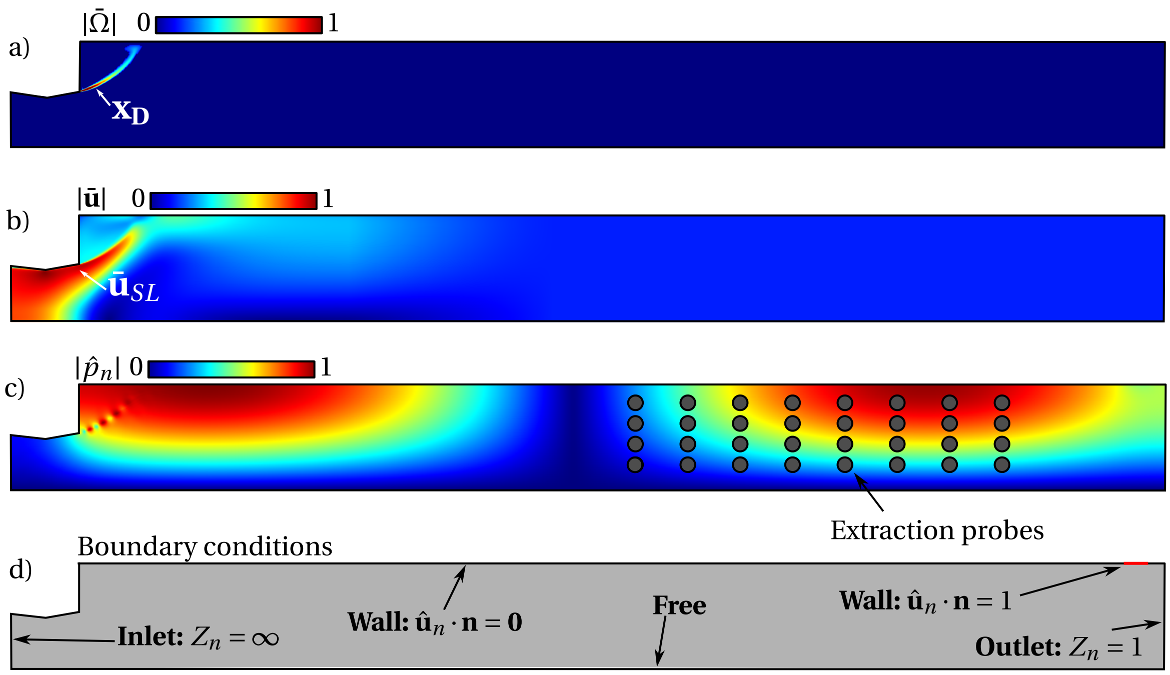

Figure 5.11: a) Mean shear-layer (normalized) b) mean velocity field (normalized) c) pressure response mode with extraction probes (normalized) d) boundary conditions

mean flow conditions (i.e. constant mean velocity and cross sectional area) that agree with the underlying assumptions of the objective function in Eqn. 5.29. Hence, extraction probes are located in this downstream region to yield pressure values required to perform the least square operation given by Eqn. 5.35 to determine the desired wave amplitudes. The probe array along with a representative pressure response mode is shown in Fig. 5.11 c). Figure. 5.11 d) provides information on boundary conditions and excitation sources for LEE/HE simulation to obtain the reflection coefficients. For the inlet, a hard wall boundary was chosen, which is presumed to exert not impact on the reflection coefficient results. The reason for this assumption is due to the cut-on frequency value within the burner tube (cf. Chap. 3), which prevents any transversal modes from existing - and interactions with the boundary - within the investigated frequency regime.

The magnitude of the resulting reflection coefficients for the CW and

CCW Bloch setup are displayed in Fig. 5.12, which reveals an almost constant behavior across the concerned frequency range with a slight increase (less damping) for increasing frequencies. The reflection coefficient of the CCW mode setup, i.e. $b = -1$, of the Bloch framework yielded nearly identical results as the CW counterpart for $b = +1$. The plots also show the reflection coefficients for different values of the numerical stabilization parameter α_τ, which are nearly identical. Hence, the impact of numerical stabilization can be rated as negligible, which indicates sufficient mesh fineness.

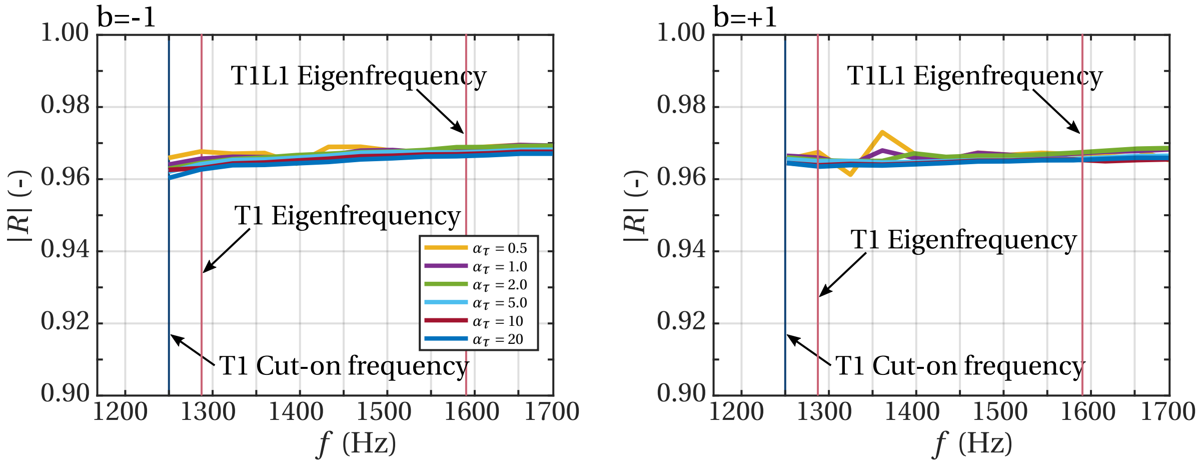

Figure 5.12: Reflection coefficient of LEE simulations for CCW ($b = -1$, left) and CW mode ($b = +1$, right) Bloch description and varying stabilization parameter

The reflection coefficient distribution required to carry out the damping model procedure is obtained by taking the mean of the CW and CCW results at the stabilization parameter $\alpha_\tau = 1$, and is shown in Fig. 5.13. The loss-coefficient ζ of Eqn. 5.26, which yields the identical distribution of the reflection coefficient through analogous simulation using the HE model given by Eqns. 5.23-5.24 is shown in Fig. 5.13b). The mesh used for the simulations features the same refinement at the edge of the chamber inlet in the vicinity of the mean shear-layer as the fine case configuration of LEE eigenmode analysis shown in Fig. 5.8. At the downstream end of the elongated domain, the mesh is composed of the same element size as in the downstream end of the nozzle domain. The resulting number of element emerged to approximately 180,000, which gives by using linear shape functions for the discretization of the Bloch

LEE $N \approx 350,000$ degrees of freedoms to be solved.

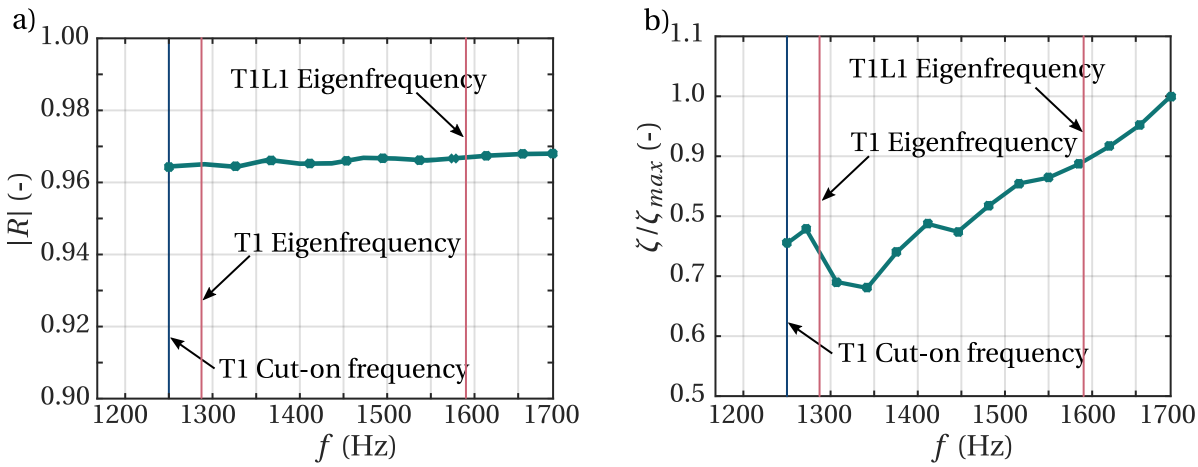

Figure 5.13: a) Reflection coefficient b) Matched loss coefficient

Finally, the complex eigenfrequencies of Eqns. 5.23-5.24 are computed for the T1 and T1L1 mode of the nozzle domain under consideration of the ζ distribution in Fig. 5.13b). The Bloch framework is applied in an analogous fashion as for the LEE eigenfrequency simulations above using the fine mesh and boundary conditions as well as assuming $\bar{\mathbf{u}} = \mathbf{0}$ as shown in Fig. 5.8. Notice that the accurate solution of the HE system would not require this level of mesh resolution and even allow for the employment of three-dimensional domains as for the driving rate computations in Chap. 4. The present computations of the damping rates are nevertheless carried out using the 2D Bloch framework, which is simply due to maintain consistency with the accompanied LEE simulations in this chapter. Also, the lacking mean flow yields degenerate transversal mode pairs, i.e. equal frequencies and damping rates. The resulting damping rate values describe the pure acoustic damping due to vortex-shedding as desired, and are provided in Tab. 5.1. The table contains the measured counterparts of damping rates and oscillation frequencies (cf. Chap. 3 for information and references on the raw data acquisition), and reveals an accurate reproduction of the measurement benchmarks by the model. Note, the experimental damping rates were obtained by fitting the pressure signal after sudden shut off of the excitation to an exponential function (cf. method details in [159, 169]). The damping rate is found to be robust to the frequency value, i.e. evaluating the loss coefficient (and thus the damping rate) at the experimental frequency value $f_{n,EXP}$ (which is the average of the two non-degenerate frequency values) instead of the computed value of the HE system f_n yields no considerable differences as for the computed value. The experimental frequencies were determined by with the help of the Fast Fourier Transform.

	$\bar{\alpha}_{n,a,EXP}(rad/s)$	$\alpha_{n,a}(rad/s)$	$\bar{f}_{n,EXP}(Hz)$	$f_n(Hz)$
T1	-15 ± 2	-16	1283	1275
T1L1	-25 ± 3	-24	1577	1562

Table 5.1: Measured and calculated damping rates and oscillation frequencies

5.5 Damping Rate Computations of Reactive Configuration

The quantification methodology is applied to the reactive configuration of the swirl-stabilized benchmark combustor. Specifically, the damping rates due to vortex-shedding of the same 80 operation points concerned in the previous chapter for the flame driving investigations are computed. Thereby, three goals are sought to be achieved:

- Demonstration of the quantification method's applicability to reactive configurations.
- Provision of damping rates for the stability assessments of the benchmark combustor that carried out subsequently in Chap. 6.
- Identification of physical features that promote vortical damping of transversal modes in swirling mean flows.

It is important to point out that the reflection coefficients extracted from LEE/HE model simulations are obtained with an underlying mean flow field that is isothermal, i.e. without combustion. The temperature for these simulation is set to the preheat value of the concerned operation point. The negligence of combustion implies equality of vortical damping in both, isothermal and reactive flow situations, which is a common assumption for thermoacoustic analyses (e.g. burner and flame matrix approaches for LF systems [118]). However, a thorough assessment of the validity of this invariance assumptions for non-compact, HF modes remains open for future work.

Notice that a parameter variation of only air mass flow rates and preheat temperatures among the 80 reactive operations points in Sec. 4.4 need to be considered as air-excess ratios are irrelevant due to the concerned isothermal flow fields. Hence, the isothermal flow fields are obtained for all combinations of

- $\bar{\dot{m}} = 0.06, 0.08, 0.10, 0.06\,\mathrm{kg/s}$
- $\bar{T}_{\mathrm{in}} = 373.15, 473.15, 573.15, 673.15\,\mathrm{K}$

which implies a total of 16 CFD computations. Then, the reflection coefficient distribution is computed for each isothermal operation point. For this, the same mesh, numerical stabilization setup and probe locations that yielded robust results for the validation test case in Sec. 5.4 are used. From each distribution, five different loss-coefficients ζ corresponding to the different air excess ratio variations (and thus adiabatic temperatures and ultimately eigenfrequencies) in the reactive case are determined as above-described. Recall that the range of air excess ratios is $\lambda = 1.0 - 1.8$ which translates for the different combination of air mass flow rates into a range of $T_{ad} = 1550\,\mathrm{K} - 2314\,\mathrm{K}$ for the adiabatic flame temperatures. All 80 T1 eigenfrequencies, which implicitly contain the effect of an active temperature distribution, are readily available from the driving rate computations of the previous chapter (cf. Fig. 4.8). The damping rates are then computed for the 80 operation points by solving the HE model with the respective loss coefficient and mean temperature distributions. The sensitivity of these target frequencies on the corresponding damping rate results is robust, i.e. a variations of the frequency within a $\pm 10\%$ range yielded no significant deviation ($< 5\%$) of the resulting damping rate, which establishes confidence in the of results.

Figure 5.14 shows the resulting damping rates, which are plotted against the power density (cf. Eqn. 4.31) of the operation point. The reasons for using the power density as independent variable is to ensure comparability with the driving rate analysis in Sec. 4.5. There is no direct connection between combustion properties and damping. As before, the filled and open circles in Fig. 5.14 indicate whether an operation point is stable and unstable based on experiential observations, respectively. The figure allows to establish the following observations:

- All damping rates are negative, which confirms that a loss/dissipation of energy is captured as desired.
- Linear increase of damping strength (decrease of negative damping rate) with power density.
- Stable operation points exhibit weaker damping compared to the unstable counterparts.

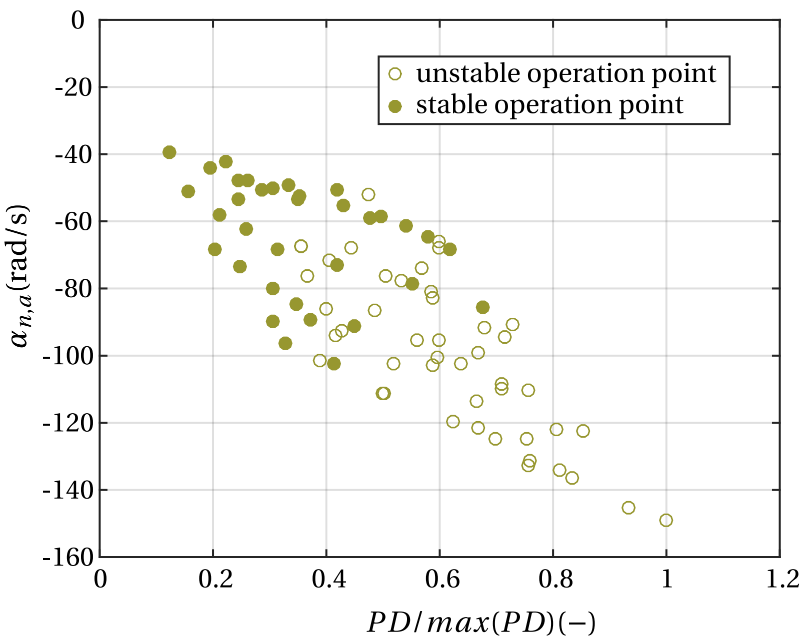

Figure 5.14: Damping rates vs. (normalized) thermal power density

In order to establish a physical explanation of these observations, preheat temperature, velocity magnitude at the burner edge (indicated in Fig. 5.11b)) and temperature jump are plotted against the damping rate. These plots are provided in Figs. 5.15-5.17. The finding extracted from Fig. 5.15 is the dependency of the damping rates on the velocity magnitude of the mean shear-layer. Physically, a higher flow velocity at the burner edge induces stronger mean vorticity associated with the shear-layer, which then causes – upon acoustic perturbation – enhancement of vortex-shedding, and thus acoustic damping. This explanation coincides with vortical damping models for LF systems [138], which reveal an dependency of an increasing damping rate with increasing burner mean velocity, too.

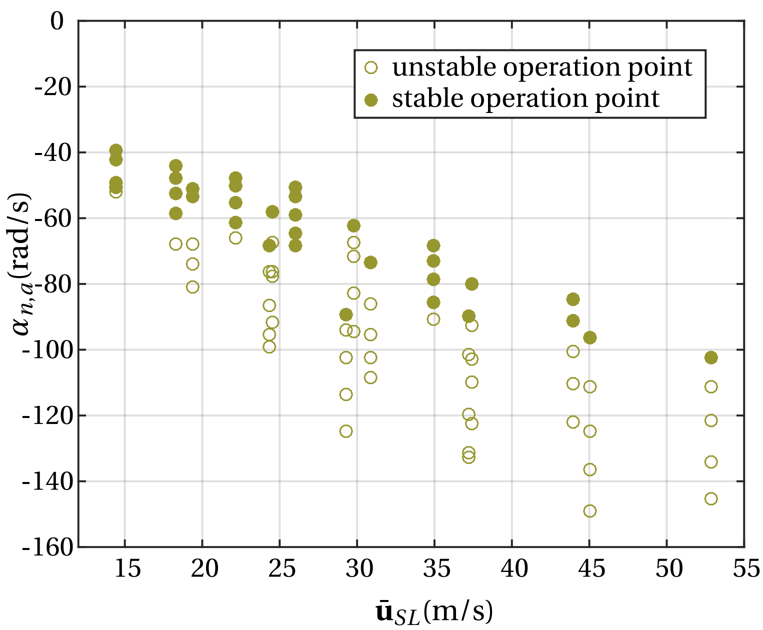

Figure 5.15: Damping rates vs. shear-layer velocity magnitude

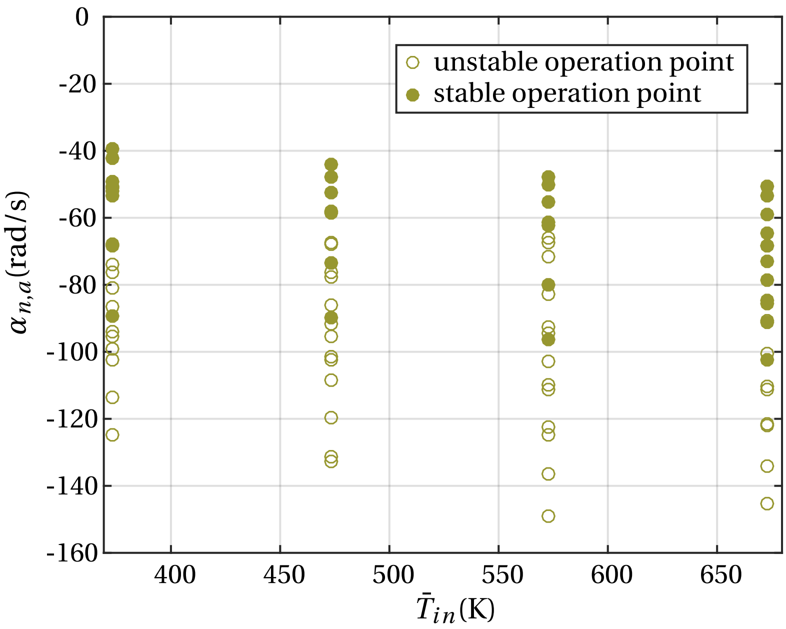

Figure 5.16: Damping rates vs. preheat temperatures

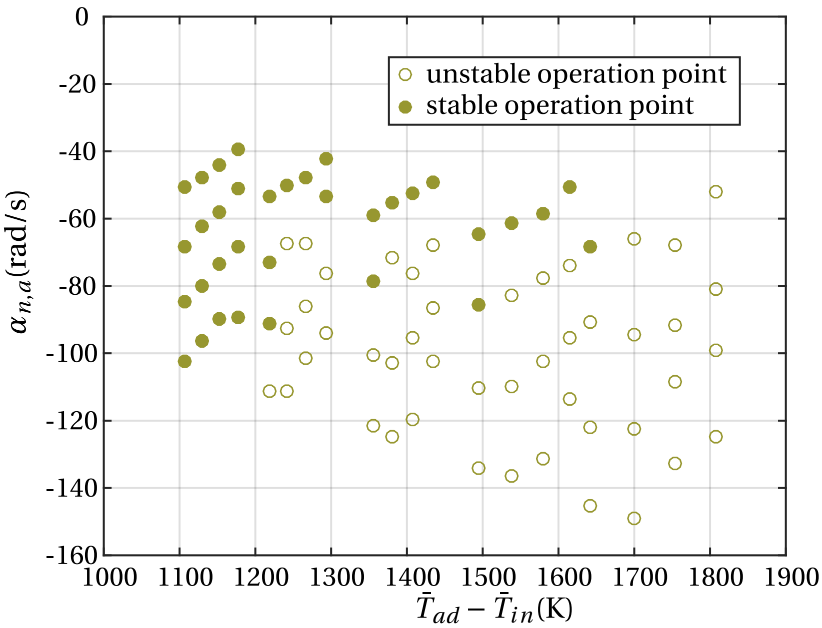

Figure 5.17: Damping rates vs. Temperature jump temperatures

Inspecting Fig. 5.16 emerges a more or less constant dependency of damping rates on the preheat temperature. The variation of damping rates at a fixed preheat temperature is again due to the underlying mean velocities at the shear-layer. The impact of the inlet temperature is not completely negligible as for a given inlet mass flow rate, the higher preheat levels lead to lower densities and further to higher flow velocities due to mass conservation. It can be stated that higher inlet temperatures ultimately increase damping for a fixed mass flow rate. Figure 5.17 reveals somewhat of a trend of the damping rate magnitude for an increasing temperature jump, although a clear dependency as well as a physical explanation cannot be recognized.

The previous plots give some insight into the impact of single parameters on the damping rate. However, a clear dependency of the damping strength along with a physical explanation could not be established. In order to establish such an explanation, an analytical expression that describes vortical damping from 1D, LF systems is utilized and can be written as [138]

$$\alpha_{n,a,LF} \propto \zeta_{LF} \bar{\dot{m}} \hat{u}_x \tag{5.40}$$

where ζ_{LF} is the loss coefficient, $\bar{\dot{m}}$ is the mean mass flow rate in the burner tube and $\hat{u}_x$ is the acoustic velocity at the burner outlet/chamber inlet. This expression is now conceptually transferred to the modeling approach for T1 modes introduced above, which gives

$$\alpha_{n,a} \propto \zeta \bar{\dot{m}} \hat{u}_{sl} \tag{5.41}$$

where ζ is the loss coefficient of Eqn. 5.26, $\bar{\dot{m}}$ is the mean mass flow rate in the burner tube and $\hat{u}_{sl}$ denotes the acoustic velocity at the shear-layer where the absorption zone is non-zero. It is postulated that the acoustic velocity at the shear layer is proportional to the mean temperature jump, i.e. $\hat{u}_{sl} \propto \bar{T}_{ad} - \bar{T}_{in}$, which is justified as follows: For a fixed axial flame (as is the case for the considered operation points), a large temperature jump leads to a higher disparity between the cut-on frequency in the hot downstream region and the actual oscillation frequency than for lower temperature jumps. As the consequence, the mode attenuation caused by the axially increasing cut on frequency (cf. Sec. 5.1) is stronger. The mode shape is axially shorter, and thus, exhibits larger acoustic velocities in the region of the shear layer relative to modes that are axially longer and are associated with a smaller temperature jump. This reasoning agrees with the work and findings in [62], where axially shorter T1 mode shapes are shown to exhibit higher damping rates than axially longer ones for T1 modes in a tube. Hence, the presumed dependence of the damping rate of the T1 mode in this chapter is written as

$$\alpha_{n,a} \propto \zeta \bar{\dot{m}}(\bar{T}_{ad} - \bar{T}_{in}). \tag{5.42}$$

This relation merges the dependency of the damping rate on global hydrodynamic (i.e. via the mass flow rate and the loss coefficient) and thermal (i.e. via the temperature jump) parameters. The damping rates are plotted against the product of loss coefficient, mass flow rate and temperature jump in Fig. 5.18. A clear linear dependence of the growth rate to this product can be observed. Thus, high damping occurs for large mass flow rates and loss coefficients as well as large temperature jumps. Particularly the combination of large mass flow rates and large temperature jumps (which is associated to an air excess ratio close to one) explains the increasing damping rates for operation points with higher power density as shown in Fig. 5.14.

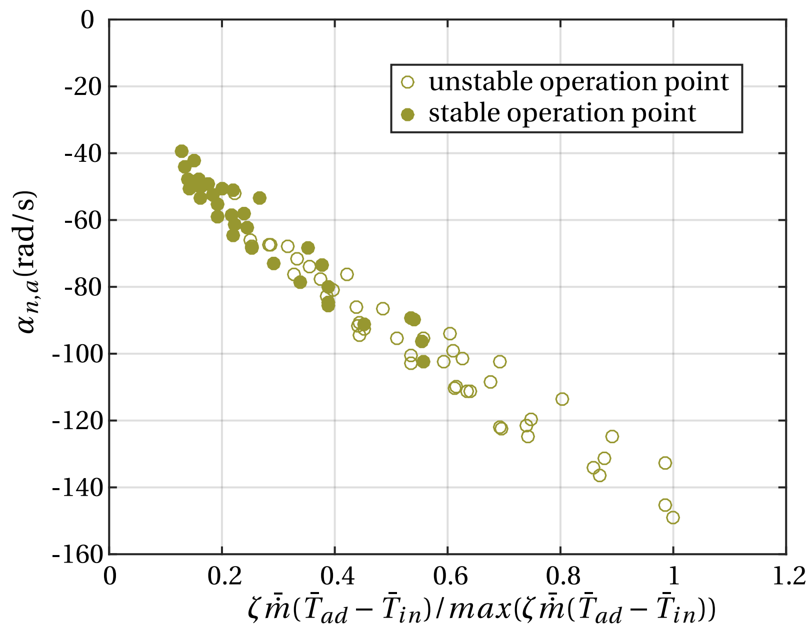

Figure 5.18: Damping rates vs. $\zeta \bar{\dot{m}}(\bar{T}_{ad} - \bar{T}_{in})$

5.6 Summary and Findings – Damping of Transversal Acoustic Modes

The first part of the foregoing chapter provided a theoretical discussion regarding physical processes associated with vortex-shedding induced by transversal acoustic modes. Particular emphasis was placed on discussing the nature of eigenmodes obtained by LEE simulations in terms of physical mechanisms and energy conservation captured within the solutions. These theoretical assessments revealed the following findings:

- LEE eigenmodes adequately reproduce the acoustically induced vortex-shedding for transversal modes in swirling mean flow environments. These interactions lead to the superposed presence of both, acoustic and vortical modes within the LEE solutions.

- The absence of turbulent dissipation in the LEE leads to a theoretical energy conservation of acoustic and vortical disturbances associated with vortex-shedding processes within the eigenmodes. The impact of further interactions between vortical disturbances and non-uniform mean flow was assumed as negligible and was thus not considered. Respective investigations of this assumption and the phenomena itself are left for future work.

- A straightforward utilization of LEE damping rates for mean flows with strong shear-layers present for linear thermoacoustic stability assessment tasks is generally not possible. This inapplicability is due to the absence of turbulent dissipation as well as the unavailability (the point of the compilation of this thesis) of respective dissipation models as well as suitable outlet boundary conditions that would allow vortical disturbances to convect out of the domain.

- A rather heuristic approach was identified that allows to qualitatively model vortical acoustic damping by adjusting the numerical stabilization parameter as well as exploiting numerical diffusion induced by a "coarsened" mesh. As there is no theoretical basis for this approach, universal utilization guidelines cannot be established so that the employment should be carried out with great care.

The energy conservation hypothesis as well as the suitability of LEE eigenmodes to compute acoustic damping rates were verified using the isothermal configuration of the swirl-stabilized benchmark system of this thesis. In order to ensure accurate numerical resolution of the interactions between shear-layer and acoustic disturbances, a Bloch symmetry framework was adopted to the LEE. This framework allows to transform the numerical domain from 3D into 2D, which implies a substantial increase of numerical resolution capabilities for non-high performance computing approaches. Moreover, this increase allowed to resolve the LEE to sufficient degree so that independency of mesh and numerical stabilization parameter is achieved, which would not be possible, if 3D domains are concerned.

In order to unambiguously determine the damping rates of transversal modes due to vortex-shedding, a quantification methodology based on a local loss model in Helmholtz type of governing equations was developed. Mean flow effects were neglected for this approach. The nature of the Helmholtz type of equations yields modes of acoustic disturbance type only so that the computed eigenfrequencies contain the acoustic damping rates relevant for thermoacoustic stability analyses. The loss model is facilitated in the momentum equation, which assumes that loss of acoustic energy occurs at the shear-layer of the swirling flow. The model contains one loss coefficient, which is obtained by imposing an equality condition between reflection coefficient computed by the LEE and the HE model. An isothermal nozzle configuration of the benchmark combustor is used to validate the method. The impact of a variable mean temperature distribution on the vortex-shedding processes remains an open task for future work. Experimentally obtained damping rates of the T1 and T1L1 mode were reproduced by the methodology and found applicable to compute damping rates for stability assessments of reactive configuration of can type combustors.

Then, the methodology was employed to 80 operations points of the reactive configuration of the benchmark system. The damping rates due to vortex-shedding at the first transversal mode were computed, which serve as input to the thermoacoustic stability assessment carried out in the next chapter. Interpretations of results emerged the following findings regarding damping of transversal modes due to vortex-shedding in swirling mean flow environments:

- Observation of a linear dependency of damping rates with thermal power density.
- Combustion parameters (e.g. power value) do not directly impact damping. Rather, the physical origin of this linear dependence is found within the mean flow velocity magnitude at the burner edge.
- Inlet temperatures exert an indirect impact on the damping rates as higher levels lead to higher flow velocity if the mass flow rate is fixed.
- Linear dependence of the damping rate on the product of loss coefficient, mean mass flow rate and temperature jump was revealed.

Overall, the developed methodology for quantification of acoustic damping rates of multi-dimensional HF modes in swirl-stabilized gas turbine combustors yielded reasonable results. Future work tasks should comprise further (parametric) investigations on vortical damping of HF modes to increase the physical understanding as well as to derive design for stability guidelines can be carried out. For example, the sensitivity of swirl intensity as well as the axial position of inner recirculation zone on the acoustic damping rate of transversal modes poses potential subjects for such studies. Also, quantitative comparison between computed and experimentally obtained damping rates should be considered to strengthen the validation of the methodology.

6 Linear Stability Assessment

This chapter combines the outcomes of the two previous chapters to establish a theoretical and practical framework for linear thermoacoustics stability assessments of gas turbine combustors that feature HF oscillations as well as non-compact flame dynamics. This stability assessment comprises the following research objectives:

- Establishment of the theoretical background for numerical linear stability assessments of non-compact thermoacoustic oscillations governed by transversal modes (Sec. 6.1).
- Executing the linear stability assessment on the swirl stabilized benchmark combustor (Sec. 6.2).
- Interpretation of the results in terms of physical correctness and technical applicability of the methodology (Sec. 6.2).

6.1 Theoretical Background

The terminology "linear stability analysis" in the context of thermoacoustic oscillations generally implies the computational prediction whether an operation point of a given combustors will undergo an instability. Employing a modal analysis approach, this task is achieved by considering all energetic contributions – i.e. flame driving as well as acoustic damping – in the governing equations, i.e.

$$\bar{\rho} i\omega_{n,a}\hat{\mathbf{u}}_{n,a} + \nabla \hat{p}_{n,a} = \mathbf{m}_{\hat{\mathbf{u}}_{n,a}}, \tag{6.1}$$

$$i\omega_{n,a}\hat{p}_{n,a} + \gamma \bar{p}\nabla \cdot \hat{\mathbf{u}}_{n,a} = (\gamma - 1)\hat{q}_n. \tag{6.2}$$

where $\hat{p}_{n,a}(\mathbf{x})$ and $\hat{\mathbf{u}}_{n,a}(\mathbf{x})$ represent the acoustic pressure and velocity eigenmodes. Equations 6.1-6.2 resemble a HE type system as used for the individual driving and damping analyses in Chaps. 4-5 in which source/sink terms to model flame driving $\hat{q}_n(\mathbf{x})$ and acoustic damping $\mathbf{m}_{\hat{\mathbf{u}}_{n,a}}(\mathbf{x})$ are retained. Hence, the same assumptions of a zero-mean flow, fully reflecting in- and outlet boundary conditions, handling of non-compactness, explicit expansion of source/sink models, and numerical FEM procedures to compute the desired eigensolution as discussed in the previous two chapters equally apply here, too. The linear stability of the mode n is simply evaluated by solving Eqns. 6.1-6.2 for the respective complex eigenfrequency, which unfolds to

$$\omega_{n,a} = 2\pi f_n - i\nu_{n,a} \tag{6.3}$$

where $f_{n,a}$ is the oscillation frequency, and $\nu_{n,a}$ is called net thermoacoustic growth rate. This growth rate is composed of the superposition

$$\nu_{n,a} = \beta_{n,a} + \alpha_{n,a}, \tag{6.4}$$

where $\beta_{n,a}$ and $\alpha_{n,a}$ denote the total flame driving and acoustic damping rate of mode n. Recall that the damping rate is per convention in this work negative $\alpha_{n,a} < 0$. As explained in Chap. 4, the driving rate is composed of two mechanisms, i.e. flame displacement and deformation which gives

$$\beta_{n,a} = \beta_{\hat{\Delta},n,a} + \beta_{\hat{\rho},n,a}. \tag{6.5}$$

For the damping rate, the only mechanism considered as relevant is due to acoustically induced vortex-shedding (cf. Chap. 5). However, if further damping processes are present in the considered combustor, the total acoustic damping rate is obtained by the superposition of the individual damping rates.

The sign of the growth rate essentially defines the linear stability state of mode n, and thus, of the thermoacoustic system [31]:

$$\nu_{n,a} > 0 \quad \rightarrow \quad \text{unstable} \tag{6.6}$$

$$\nu_{n,a} = 0 \quad \rightarrow \quad \text{asymptotically stable} \tag{6.7}$$

$$\nu_{n,a} < 0 \quad \rightarrow \quad \text{stable} \tag{6.8}$$

The sufficiency of using the growth rate as the rating parameter for linear stability of a particular mode can be demonstrated in two ways:

- Mathematically, i.e. substituting growth rate into the Fourier series formulation of the underlying the modal approach.
- Energetically, i.e. performing an energy balance on the acoustic mode.

6.1.1 Illustration of Linear Stability via Fourier Series

Mathematically, the modal analysis approach employed in this thesis (cf. Sec. 2.5) is fundamentally based on the description of thermoacoustic oscillations of the chamber of interest via a discrete Fourier series in Eqns. 2.13-2.17. The Fourier series directly reveals the linear stability of the system, and is recalled to

$$\boldsymbol{\phi}'(\mathbf{x},t) = \sum_{n=1}^{N} \frac{1}{2}(\hat{\boldsymbol{\phi}}_n(\mathbf{x}) \exp(i\omega_n t) + \hat{\boldsymbol{\phi}}_n^*(\mathbf{x}) \exp(-i\omega_n^* t)), \tag{6.9}$$

where $\boldsymbol{\phi}$ represents the spatially dependent unsteady quantities (i.e. pressure p, vectorial velocity $\mathbf{u}$ and heat release rate q). The prime ($'$) denotes oscillations in time, while the N eigenmodes – which constitute the summation expansion – are indicated by the hat (ˆ). The asterisks $*$ denotes the complex conjugate of the respective quantity. Substituting the complex eigenfrequency given in Eqn. 6.4 into Eqn. 6.9 yields

$$\boldsymbol{\phi}'(\mathbf{x},t) = \sum_{n=1}^{N} \frac{1}{2}(\hat{\boldsymbol{\phi}}_n(\mathbf{x}) \exp(i2\pi f_{n,a} t) + \hat{\boldsymbol{\phi}}_n^*(\mathbf{x}) \exp(-i2\pi f_{n,a} t)) \exp(\nu_{n,a} t), \tag{6.10}$$

which effectively reveals that the modal contribution to the temporal oscillation is an exponential amplitude growth and decay if $\nu_{n,a} > 0$ and $\nu_{n,a} < 0$, respectively. In the former case, the mode n is labelled linearly unstable and in the latter linearly stable, which is in agreement with Eqns. 6.7-6.8.

6.1.2 Illustration of Linear Stability via Modal Energy

An energetic illustration of linear stability of a thermoacoustic mode is provided by performing an energy balance on the acoustic mode of interest. This energy balance is carried out in an analogous manner as for the driving and damping investigations in Secs. 4.1 and 5.3, respectively, and is given by

$$\frac{\mathrm{d}\langle \tilde{\mathrm{E}}_{n,a}\rangle}{\mathrm{d}t} = \left\langle \tilde{\mathrm{D}}_{\hat{q}_n} \right\rangle + \left\langle \tilde{\mathrm{D}}_{\mathbf{m}_{\hat{\mathbf{u}}_{n,a}}} \right\rangle . \tag{6.11}$$

Recall that $\langle \tilde{\mathrm{E}}_{n,a}\rangle$ in Eqn. 6.11 governs only acoustic disturbances as the imposed zero mean flow assumption eliminates all vorticity source terms. The prescription of fully-reflecting boundary conditions causes all flux terms to vanish. Hence, the only sources that govern the change of modal acoustic energy are due to flame driving $\left\langle \tilde{\mathrm{D}}_{\hat{q}_n} \right\rangle$ and acoustic dissipation $\langle \tilde{\mathrm{D}}_{\mathbf{m}_{\hat{\mathbf{u}}_n}} \rangle$. Explicit formulations of these sources are given by is retrieved from Eqn. 4.8 and Eqn. 5.27. The question whether a given combustor undergoes a thermoacoustic instability is answered by the sign of the temporal change of modal energy, i.e.:

$$\frac{\mathrm{d}\langle \tilde{\mathrm{E}}_{n,a}\rangle}{\mathrm{d}t} > 0 \quad \rightarrow \quad \text{mode receives energy} \rightarrow \text{unstable} \tag{6.12}$$

$$\frac{\mathrm{d}\langle \tilde{\mathrm{E}}_{n,a}\rangle}{\mathrm{d}t} < 0 \quad \rightarrow \quad \text{energy is removed from the mode} \rightarrow \text{stable} \tag{6.13}$$

A connection between the growth rate definition of linear stability in Eqn. 6.4 is established by decomposing the change of modal energy in driving and damping contribution, i.e.

$$\underbrace{\frac{1}{2}\frac{1}{\langle \tilde{\mathrm{E}}_a\rangle}\frac{\mathrm{d}\langle \tilde{\mathrm{E}}_a\rangle\big|_{net}}{\mathrm{d}t}}_{=\nu_{n,a}} = \underbrace{\frac{1}{2}\frac{1}{\langle \tilde{\mathrm{E}}_a\rangle}\frac{\mathrm{d}\langle \tilde{\mathrm{E}}_a\rangle\big|_{\hat{q}}}{\mathrm{d}t}}_{=\beta_{n,a}} + \underbrace{\frac{1}{2}\frac{1}{\langle \tilde{\mathrm{E}}_a\rangle}\frac{\mathrm{d}\langle \tilde{\mathrm{E}}_a\rangle\big|_{\mathbf{m}_{\hat{\mathbf{u}}_{n,a}}}}{\mathrm{d}t}}_{=\alpha_{n,a}} . \tag{6.14}$$

The individual modal energy changes represent the driving and damping rates given by Eqns. 4.8 and 5.27 so that the growth rate relation of Eqn. 6.4 is reproduced from an energy balance perspective.

6.2 Results, Findings and Conclusions

The linear stability analysis of the 80 operation points concerned in the previous two chapters is simply executed by evaluating Eqn. 6.4 with the driving and damping rates that are readily available from Chaps. 4-5. The results are shown in Fig. 6.1, where all three relevant quantities, i.e. driving, damping and net growth rates are plotted. As before, a filled and open circle declares an operation point stable and unstable, respectively, which solely results from experimental observations.

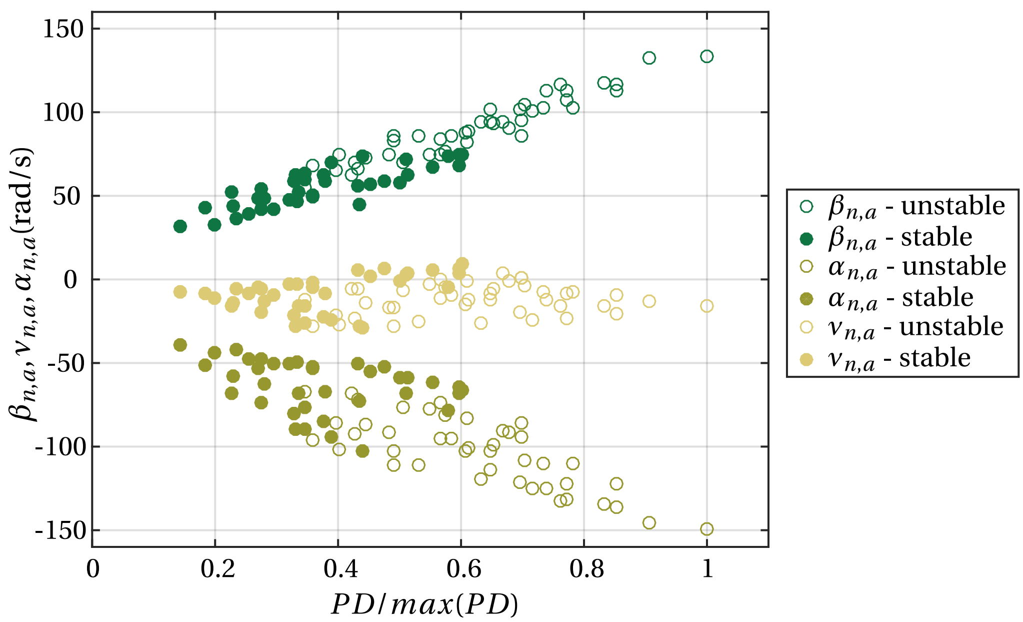

Figure 6.1: Net growth, driving and damping rates

Generally, the computed growth rates are within realistic orders of magnitudes. The specific result interpretations occur in the following by inspecting the stable and unstable operation points separately.

6.2.1 Stable Operation Points

Inspecting the growth rates of the stable operations points (filled circles) allows to identify two distinct observations:

- All operation points in the low power density regime ($PD/max(PD) < 0.4$) are computed as stable, i.e. $\nu_{n,a} < 0$.
- In the intermediate power density region ($0.4 < PD/max(PD) < 0.6$), the operation points are (wrongly) computed as unstable, i.e. $\nu_{n,a} > 0$, although the growth rates are small and close to the stability border $\nu_{n,a} = 0$.

It can be stated that the presented methodology is usable to qualitatively reproduce the stability state of the stable operation points. The reasons for the few operation points that exhibit a marginally unstable growth rate can be explained by the sole consideration of only vortex-shedding as acoustic damping mechanism. As argued in Chap. 5, vortex-shedding can be assumed as the most dominant damping mechanism for transversal modes in the tubular benchmark combustor. However, acoustic losses due to dissipation in the boundary layer and at the domain in-/outlets are certainly non-zero. Consequently, some additional damping due to these foregoing mechanism would suffice to shift the respective growth rates downwards towards negative values, which would then reflect the stable observation, too.

6.2.2 Unstable Operation Points

The assessment of the computed growth rates associated with the unstable operations points (open circles) yields the following observations:

- All growth rates are in the same order of magnitude and approximately constant with increasing power density.
- Computationally, the growth rates emerge as stable, i.e. $\nu_{n,a} < 0$, which contradicts the experimental observations for which positive growth rates, i.e. $\nu_{n,a} > 0$ are expected.

The observed stability behavior for unstable configurations of the benchmark systems is not reproduced by the linear stability analysis, which presents a dissatisfying result. However, the negative magnitudes of the growth rates are quite close to zero, and thus, not far away from the expected results, i.e. positive magnitudes. An in-depth assessment for identifying the reasons that would yield positive growth rates along with implementing respective improvements to the methodology/models is left for future work. As a suggested path, the driving and damping mechanism and modeling methodologies should be revisited in a systematic manner. For the damping rates, confidence in the correctness is established as the scattering behaviour observable in Fig. 6.1 could be explained by the interplay of the influencing factors loss coefficient, temperature jump and mass flow rate (cf. Sec. 5.5 and Fig. 5.18). Of course, numerical inaccuracies associated with the absorption modeling approach introduced in Chap. 5 remains a possibility, too. Furthermore, additional damping mechanisms should be taken into consideration, e.g. dissipation in the wall boundary layer [130], which shifts down both, the damping and growth rate cloud, and thereby, the unstable points further away from the "correct" boundary.

Then, it could be inferred that some additional driving is missing in order to lift the unstable operation points above the zero line. One approach could be to raise the question whether there is a further driving mechanism in addition to the displacement and deformation effects – which remains a rather speculative suggestion. Another approach would be to re-assess the correctness of the computed driving rates. These rates were approximated from OH^* measurements recorded during unstable limit cycle operation. In order to be theoretically correct, a linear stability consideration requires mean flame shapes that correspond to a "zero" acoustic oscillations amplitude. Hence, the effect of "truly" linear flame images on the computed driving rates should be assessed by using OH^* measurements that are retrieved from stable operation (i.e. requiring to stabilize the limit-cycle oscillations by employing suitable damping devises in the experiment). Moreover, obtaining the mean heat release distribution via reactive CFD simulations should be taken into consideration, too. However, investigations of amplitude dependent flame response in [17] revealed that for increasing amplitudes the effect of displacement and deformation equally increases and decreases, respectively. The total driving rates remain at the same value regardless of the pulsation amplitude.

This constancy represents an argument that the driving rates in Fig. 6.1 are – despite being retrieved from mean flame images recorded during limit cycle operation – suitable for a linear stability assessment.

All in all, it has to be admitted that the results are not as desired, but can nevertheless be labeled as promising as the order of magnitude were found as realistic and routes of finding possible causes of the inconsistencies were outlined. Thus, open work tasks are to pursue these routes and conduct further research. The overall goal should be to establish a robust linear stability analysis framework applicable to non-compact gas turbine combustors.

7 Reduced Order Modeling Framework

The previous chapters of this thesis considered linear modeling and analyses of non-compact thermoacoustic systems in frequency domain. These analyses are effectively used to investigate physical behavior regarding flame driving, acoustic damping and thermoacoustic stability at the onset of a thermoacoustic instability, i.e. at small (linear) oscillations amplitudes. Ultimately, these efforts established the basis to carry out linear thermoacoustic stability analyses of HF oscillation in gas turbine combustors.

However, the frequency domain framework exhibits the following limitations:

- Impossibility of reconstructing the thermoacoustic dynamics, i.e. simulating the temporal evolution of a thermoacoustic instability from linear modulation to non-linear saturation into a constant amplitude limit cycle.
- Inability of modeling and analyzing the impact of stochastic forcing effects due to turbulent combustion noise on the thermoacoustic oscillations.
- Impracticality of capturing modal interactions caused by non-linear flame dynamics.

Modeling and carrying out these tasks requires a time domain framework. Corresponding analyses can be used to generate theoretical understanding of thermoacoustic oscillations from a dynamical system perspective [7,21,78,94, 113]. In practice, time domain simulations are used for designing active and passive instability mitigation techniques [30, 111, 139] as well as for developing system identification techniques based on acoustic pressure data [21] and

Chap. 10. For LF systems, such a time domain framework is given by a state-space description of the combustion system in conjunction with a network modeling approach [13, 20, 41, 139]. However, these LF approaches are constrained by the thermoacoustic compactness assumption (cf. Sec. 1.4), and are therefore not applicable to non-compact systems in the HF regime. In theory, utilizing the 3D LEE (or even an HE system) in time domain along with respective non-compact flame models would satisfy the desired tasks and present a suitable framework. Unfortunately, typical discrete system sizes of the benchmark combustor in Chap. 3 are too large for efficient numerical integrations, and are thus impractical for application in this thesis. In order to enable fast and efficient time domain simulations, a Reduced Order Modeling (ROM) methodology of 3D LEE/HE systems, which is capable of accounting for non-compact flames as well as multidimensional modes in the HF regime, is developed in this chapter. The development tasks unfold into the following specific objectives:

- Introducing a methodology to derive Reduced Order Models (ROM) of 3D LEE/HE systems, which forms the central component to establish the non-linear analysis framework for HF thermoacoustic oscillations (Sec. 7.1 and Sec. 7.2).
- Development of capabilities to model and simulate non-compact thermoacoustic feedback that allows to account for linear, non-linear and stochastic flame dynamics (Sec. 7.3).
- Establishing procedural guidelines to setup and verify the ROM and accompanied non-compact feedback framework a-priory to carrying out time domain analyses (Sec. 7.4).

7.1 Model Order Reduction Methodology

The starting point for the derivation of the desired ROM is given by the discretized form of the LEE in time domain, which is given by Eqn. 2.54 and is re-written as

$$\mathbf{E}\frac{\mathrm{d}\boldsymbol{\phi}'}{\mathrm{d}t} = \mathbf{A}\boldsymbol{\phi}' + \mathbf{B}_{\mathbf{m_{u'}}}\mathbf{u}_m + \mathbf{B}_{\dot{q}'}\mathbf{u}_q, \tag{7.1}$$

which represents a dynamical system in state-space form of size N. Recall that in Eqn. 7.1, $\mathbf{E}$ is the descriptor matrix, $\mathbf{A}$ is the system matrix, and $\boldsymbol{\phi}' = [p'\ \mathbf{u}']^T$ is the state vector hosting the unsteady flow variable at each mesh node. The source term vectors $\mathbf{B}_{\dot{q}'}$ and $\mathbf{B}_{\mathbf{m}'_{\mathbf{u}}}$ carry information on the spatial location of the sources, and are used to insert input signals of heat release oscillations $\mathbf{u}_q$ and momentum addition $\mathbf{u}_m$ into the system, respectively. Multiple inputs, which are e.g. associated with spatially distributed sources across the computational domain can be facilitated by simply assembling an input matrix of corresponding source term vectors. Output signals of acoustics/flow disturbances are retrieved by

$$\mathbf{y} = \mathbf{C}\boldsymbol{\phi}', \tag{7.2}$$

where $\mathbf{C}$ is the output matrix, which is assembled from several row vectors, each carrying an unity entry at the position of the desired output variable and location within the FEM mesh, and zero elsewhere.

The state-space system given by Eqns. 7.1 and 7.2 is of the same order N as the corresponding linear system in frequency domain given by the FEM discretization in Eq. 2.43. Recall that time and frequency domain formulations of the discrete systems are simply connected by the Fourier transform as explained in Sec. 2.8. The dynamical systems treated within this work are of order $N \approx 300{,}000 - 500{,}000$, which can be labeled for the computational resources considered in this thesis as large-scale. Temporal integrations of such large systems are vastly expensive in terms of computational resources, and are impractical for efficient thermoacoustic system simulations. For this reason, the system of Eqns. 7.1 and 7.2 is subjected to a Model Order Reduction (MOR) technique, which aims to significantly reduce the system's order, while retaining the capability of accurately reproducing the large-scale system's solutions. The employed MOR technique is referred to as modal truncation [8, 14]. At first, matrix $\mathbf{A}$ is re-written by means of an generalized eigenvalue decomposition, which is given by

$$\mathbf{E}\frac{\mathrm{d}\boldsymbol{\phi}'}{\mathrm{d}t} = \mathbf{E}\mathbf{V}\boldsymbol{\Lambda}\mathbf{W}\boldsymbol{\phi}' + \mathbf{B}_{\mathbf{m}_{\mathbf{u}'}}\mathbf{u}_m + \mathbf{B}_{\dot{q}'}\mathbf{u}_q, \tag{7.3}$$

where $\mathbf{V}$ and $\mathbf{W} = \mathbf{V}^{-1}$ is the right and left eigenvector matrix, respectively, and $\boldsymbol{\Lambda}$ a diagonal matrix with the corresponding eigenvalues. Subsequently premultiplying Eqn. 7.3 by $\mathbf{E}^{-1}$ and $\mathbf{W}$ gives

$$\mathbf{W}\frac{\mathrm{d}\boldsymbol{\phi}'}{\mathrm{d}t} = \boldsymbol{\Lambda}\mathbf{W}\boldsymbol{\phi}' + \mathbf{W}\mathbf{E}^{-1}(\mathbf{B}_{\mathbf{m}_{\mathbf{u}'}}\mathbf{u}_m + \mathbf{B}_{\dot{q}'}\mathbf{u}_q), \tag{7.4}$$

where

$$\mathbf{W}\mathbf{V} = \mathbf{V}^{-1}\mathbf{V} = \mathbf{I} \tag{7.5}$$

is exploited. This unity condition is used to manipulate the output relation given by Eqn. 7.2 as follows:

$$\mathbf{y} = \mathbf{C}\mathbf{V}\mathbf{W}\boldsymbol{\phi}' \tag{7.6}$$

The eigenvalue matrix $\boldsymbol{\Lambda}$ contains the complex eigenfrequencies of the system's eigenmodes. Isolating these eigenfrequencies according to the frequency range of interest for the sought investigations/simulations – e.g. for the HF systems in this thesis the first five longitudinal modes and the first five transversal modes – along with the corresponding right and left eigenvectors in $\mathbf{V}$ and $\mathbf{W}$ allows to significantly reduce the system order ($N \to N_r$):

$$\boldsymbol{\Lambda}(NxN) \Rightarrow \boldsymbol{\Lambda}_r(N_r x N_r) \tag{7.7}$$
$$\mathbf{V}(NxN) \Rightarrow \mathbf{V}_r(NxN_r) \tag{7.8}$$
$$\mathbf{W}(NxN) \Rightarrow \mathbf{W}_r(N_r xN) \tag{7.9}$$

Substituting the expressions 7.7 – 7.9 into Eqns. 7.4 - 7.6 derives the desired ROM:

$$\frac{\mathrm{d}\boldsymbol{\phi}_r'}{\mathrm{d}t} = \mathbf{A}_r\boldsymbol{\phi}_r' + \mathbf{B}_{\mathbf{m}_{\mathbf{u}'},r}\mathbf{u}_m + \mathbf{B}_{\dot{q}',r}\mathbf{u}_q, \tag{7.10}$$
$$\mathbf{y} = \mathbf{C}_r\boldsymbol{\phi}_r', \tag{7.11}$$

In this equation, $\mathbf{A}_r = \boldsymbol{\Lambda}_r$ and the order of the system is N_r, where $N_r \ll N$. The

ROM's state-variable, in- and output-matrices respectively expand to

$$\boldsymbol{\phi}'_r = \mathbf{W}_r\boldsymbol{\phi}', \tag{7.12}$$

$$\mathbf{B}_{\mathbf{m}_{\mathbf{u}'},r} = \mathbf{W}\mathbf{E}^{-1}\mathbf{B}_{\mathbf{m}_{\mathbf{u}'}}, \tag{7.13}$$

$$\mathbf{B}_{\dot{q}',r} = \mathbf{W}\mathbf{E}^{-1}\mathbf{B}_{\dot{q}'}, \tag{7.14}$$

$$\mathbf{C}_r = \mathbf{C}\mathbf{V}_r. \tag{7.15}$$

The inversion of the descriptor matrix in Eqns. 7.13-7.14 can be circumvented by exploiting the unity conditions of the left and right eigenmodes in Eqn. 7.5, which is shown in detail in App. C. The inputs $\mathbf{u}_m$ and $\mathbf{u}_q$ as well as the output y are not affected by the reduction procedure. Mathematically, the foregoing modal reduction is essentially the projection of the high-order system into a subspace, which is spanned by its truncated left eigenspace. The main computational challenge of the ROM derivation is the one-time determination of the left and right eigenmodes. Details on computation times and specific mesh sizes of the eigenmodes of the system concerned in this chapter are given in the respective sections below. The 2D Bloch methodology could be also employed to obtain the 3D eigenmodes (cf. Sec. 5.4), which is however not pursued for the ROM derivation and analyses in this thesis. The reasons for using a 3D domain to obtain the eigenmodes are on the one hand to demonstrate the applicability to true 3D geometries as encountered for industrial gas turbine combustors, and on the other hand due to the non-availability of the 2D Bloch framework at the time of the ROM developments.

The quality of the ROM – i.e. how well it reconstructs the benchmarks given by the corresponding high-order system – is evaluated in the frequency domain by computing a relative error given by

$$\text{rel.Err.}(i\omega) = \frac{||\hat{p}_{n,r}(\mathbf{x}_{extr}, i\omega) - \hat{p}_n(\mathbf{x}_{extr}, i\omega)||_2}{||\hat{p}_n(\mathbf{x}_{extr}, i\omega)||_2}, \tag{7.16}$$

where $||..||_2$ denotes the H_2-norm[1], $\hat{p}_{n,r}(\mathbf{x}_{extr}, i\omega)$ and $\hat{p}_{n,r}(\mathbf{x}_{extr}, i\omega)$ are the pressure responses at the position $\mathbf{x}_{extr}$ due to an external excitation of the original and reduced system over a certain band of angular frequencies ω, respectively.

[1]For a row vector $\mathbf{a}$ with complex entries: $||\mathbf{a}||_2 = \sqrt{\mathbf{a}\mathbf{a}^H}$

7.2 Validation Test Case

In this section, the ROM capability to describe complex acoustic systems is validated. A test case consisting of a combustor-like configuration, i.e. an orifice-tube, is set up, and the aeroacoustic performance reconstructed by the ROM. An orifice-tube is a commonly used configuration to study acoustic/unsteady flow problems that are similar as occurring in real gas turbine combustors, and is hence ideally suitable to validate the ROM approach. Strong mean flow gradients at the orifice lead to vortex-shedding that is induced due to interaction between acoustic oscillations and shear-layer of the mean flow as is addressed in detail in Chap. 5. Validation is achieved by comparing the ROM results against LEE simulation results and measurements, the latter of which is readily retrieved from [147]. Note that the orifice test case contains only longitudinal acoustics, i.e. represents LF features. The purpose of this test case is to provide a first assessment of the suitability of the MOR approach to model real world systems. The omission of HF features is justified in order to maintain simplicity of the test case in terms of physical behavior and post-processing methods. The application of the ROM approach to HF systems with multidimensional modes is subject of Secs. 7.3-7.4.

7.2.1 Orifice Tube

The geometry and dimensions (in mm) of the orifice configuration are shown in Fig. 7.1.

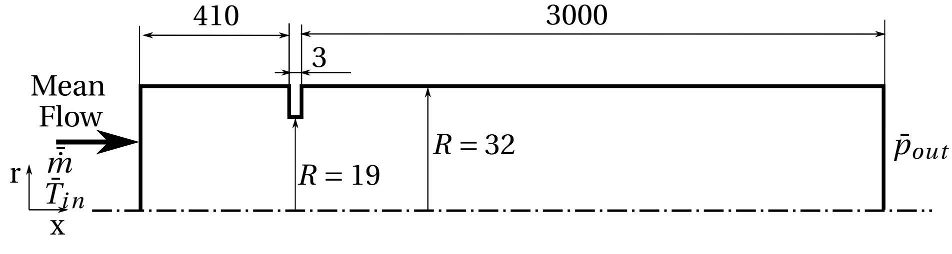

Figure 7.1: Orifice tube configuration

An operation point is selected that leads to similar mean velocity fields as found in real combustors, which yields a mass flow rate of $\bar{\dot{m}} = 160.8\,\mathrm{g/s}$ of air at ambient conditions ($\bar{T}_{\mathrm{in}} = 288.15\,\mathrm{K}$, $\bar{p}_{\mathrm{out}} = 1\,\mathrm{atm}$). The mean Mach number in the orifice is $Ma = 0.4$.

7.2.2 Numerical Setup

The acoustic behavior of the orifice is mathematically described by the isentropic LEE [2] in frequency domain given by Eqns. 2.18-2.19. The required linearization point, i.e. the mean flow field, is provided by RANS CFD simulations of the above-mentioned operation point. The mean flow field is retrieved from [147]. The geometry is meshed with approximately 110,000 tetrahedral elements. Fig. 7.2 shows the particular refinement in the vicinity of the orifice, which is required to accurately capture the complex interactions between acoustic fluctuations and mean flow gradients. Azimuthal and radial symmetry is exploited due to the experimentally considered span of frequencies being below the cut-on value for higher, non-longitudinal modes.

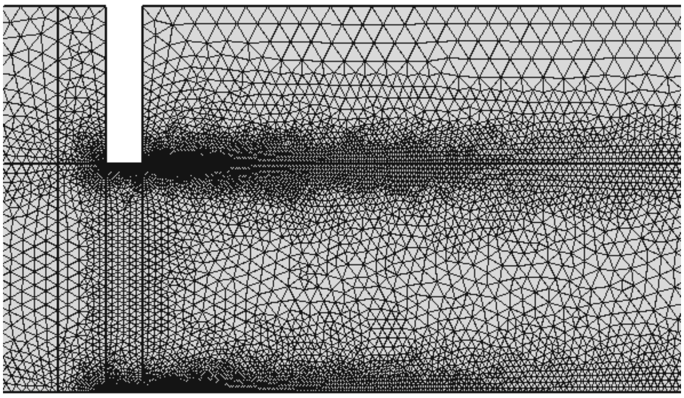

Figure 7.2: FEM mesh at orifice

As indicated in Fig. 7.3, and contrary to [147], fully reflecting boundary conditions are chosen at the in- and outlet in order to unambiguously identify the eigenmodes required for the MOR procedure. As for the damping analyses of the swirl stabilized benchmark combustor in Chap. 5, the governing equations

[2]Note that in the publication associated with this chapter of this thesis' author, the Linearized Navier-Stokes Equations were used. In this work, the terminology LEE is employed for consistency with the other chapters. ROM reproduction results do not differ between the two types of equations.

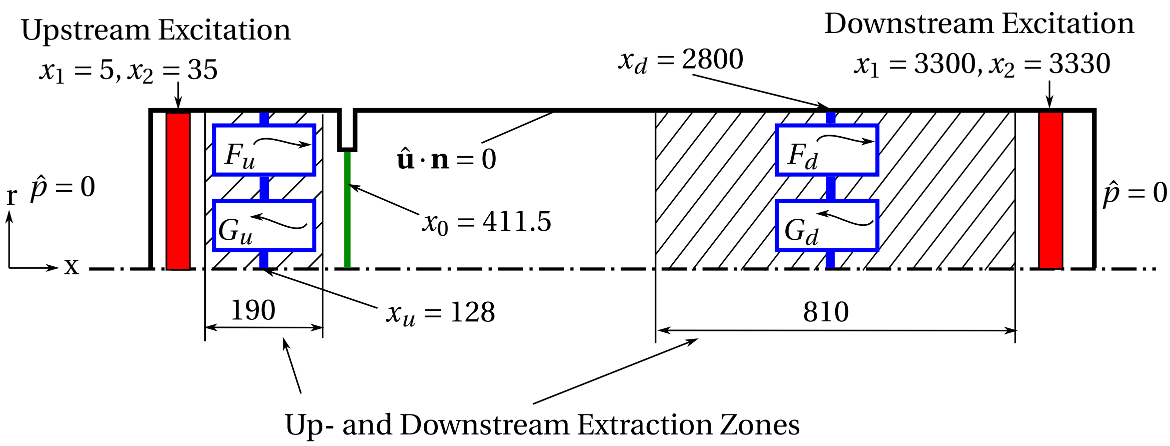

Figure 7.3: Numerical setup of the orifice tube

are stabilized by the SUPG (Streamline Upwind Petrov-Galerkin) method (cf. details in Sec. 2.8) in order to avoid numerical instabilities. Acoustic excitation to produce non-trivial solutions upon frequency sweep analyses is achieved by prescribing the source term of the x-directional momentum equation with an excitation function. For this, a piecewise cosine function is chosen to ensure a smooth embedding of the source term regions into the mesh:

$$m_{\hat{\mathbf{u}}_\mathbf{n},x} = \begin{cases} 0.5(-\cos(2\pi(x-x_1)/(x_2-x_1))+1), \\ \qquad \text{if } x_1 < x < \frac{x_1+x_2}{2} \\ 0.5(\cos(2\pi(x-(\frac{x_1+x_2}{2}))/(x_2-x_1))+1), \\ \qquad \text{if } \frac{x_1+x_2}{2} < x < x_2 \\ 0 \quad \text{elsewhere,} \end{cases} \tag{7.17}$$

These source terms are located either up- or downstream of the orifice near the boundaries as illustrated in Fig. 7.3. The LEE are discretized on the foregoing described mesh applying linear shape functions. The associated linear system has around 170,000 degrees of freedom.

7.2.3 Scattering Matrix

Acoustic elements such as the orifice tube are effectively characterized by a scattering matrix S. This matrix relates incoming and outgoing waves (cf. Fig.

7.4) traveling at a certain frequency ω in terms of transmission and reflection coefficients by the linear relation

$$\begin{bmatrix} \hat{F}_d \\ \hat{G}_u \end{bmatrix} = \underbrace{\begin{bmatrix} T_d & R_u \\ R_d & T_u \end{bmatrix}}_{S(\omega)} \begin{bmatrix} \hat{F}_u \\ \hat{G}_d \end{bmatrix}. \tag{7.18}$$

Herein, $\hat{F}_u/\hat{F}_d$ and $\hat{G}_u/\hat{G}_d$ are the respectively right- and leftward traveling waves – which are complex quantities – evaluated at reference planes up- and downstream (x_u and x_d in Fig. 7.3) of the element. The scattering coefficients of transmission T_u/T_d and reflection R_u/R_d – which are subject to be identified – describe physical events (e.g. damping at the orifice's shear-layer) within the acoustic element in a black-box manner.

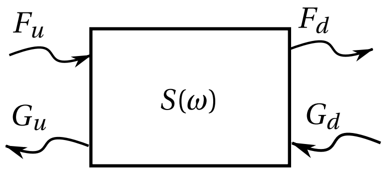

Figure 7.4: Scattering matrix

The traveling waves (Riemann invariants) are related to the acoustic pressure and velocity by

$$\hat{F} = \frac{1}{2}\left(\frac{\hat{p}}{\bar{\rho}c} + \hat{u}_x\right), \tag{7.19}$$

$$\hat{G} = \frac{1}{2}\left(\frac{\hat{p}}{\bar{\rho}c} - \hat{u}_x\right), \tag{7.20}$$

where $\hat{u}_x$ is the axial component of the velocity mode. The scattering coefficients of the experimental benchmarks of the orifice tube in [147] were obtained by the Multi-Microphone Method in accordance with the procedure outlined in [3, 4, 45, 54, 137]. Two independent acoustic fields are respectively computed by applying acoustic excitation at a distinct frequency up- (case I) and downstream (case II) of the orifice as shown on Fig. 7.3. Then, four equations are available to solve the four unknown scattering coefficients for each considered excitation frequency by

$$\begin{pmatrix} \hat{T}_d & \hat{R}_u \\ \hat{R}_d & \hat{T}_u \end{pmatrix} = \begin{pmatrix} \hat{F}_d^I & \hat{F}_d^{II} \\ \hat{G}_u^I & \hat{G}_u^{II} \end{pmatrix} \begin{pmatrix} \hat{F}_u^I & \hat{F}_u^{II} \\ \hat{G}_d^I & \hat{G}_d^{II} \end{pmatrix}^{-1}, \tag{7.21}$$

requiring the respective Riemann invariants at the denoted locations. Unfortunately, the acoustic field is polluted with vorticity disturbances due to the vortex-shedding processes in the vicinity of the orifice. For this reason, a direct assembly of the Riemann invariants as per Eqs. 7.19 and 7.20 would yield incorrect results [147, 166]. Analogous as for the determination of the reflection coefficient in the swirl-stabilized benchmark combustor in Chap. 5, the invariants are retrieved from a reconstruction of the analytical solution for plane wave propagation with uniform mean flow, which is given by

$$\hat{p}^I_{(u/d)}(x) = \bar{\rho}_{u/d} c_{u/d} [\hat{F}^I_{u/d} \exp(-i k^{x+}_{u/d} x) + \hat{G}^I_{u/d} \exp(-i k^{x-}_{u/d} x)], \tag{7.22}$$
$$\hat{p}^{II}_{(u/d)}(x) = \bar{\rho}_{u/d} c_{u/d} [\hat{F}^{II}_{u/d} \exp(-i k^{x+}_{u/d} x) + \hat{G}^{II}_{u/d} \exp(-i k^{x-}_{u/d} x)], \tag{7.23}$$

where the wave numbers $k^{x\pm}_{u/d}$ expand to

$$k^{x\pm}_{u/d} = \pm \frac{\omega}{c_{u/d} \pm \bar{u}_{x,u/d}}. \tag{7.24}$$

The reconstruction is carried out using a finite number ($\sim 50-120$) of extracted (cross section-averaged) pressure values at distinct locations within certain zones up- and downstream (cf. Fig. 7.3) of the orifice for both excitation cases. Mathematically, this overdetermines Eqns. 7.22-7.23, which requires the determination of the Riemann invariants via the method of least squares (cf. Sec. 5.3 and [141, 147, 166]).

ROM Creation and Verification

The MOR of the high-order LEE system of the orifice configuration is carried out described in Sec. 7.1. Covering the frequency range of interest – i.e. $500\,\text{Hz} \leq f \leq 1500\,\text{Hz}$ – yields a ROM order of $N_r = 84$, which is a magnificent order reduction compared to the LEE system with an order of $N \approx 170,000$. The two independent excitation cases are conveniently merged into the ROM, unfolding two column vectors to form the $\mathbf{B}_{\mathbf{m}_{\mathbf{u}'}}$-matrix. CPU-times and relative errors (cf. Eqn. 7.16) for the considered frequency range at the up- and downstream reference locations for both excitation cases are given in Table 7.1. The one-time computation of the left and right eigenmodes to carry out the MOR required around 20 min. The corresponding plots of the pressure responses are presented in Figs. 7.5, and illustrate excellent agreement between ROM and high-order LEE results. All in all, accepting a small loss in accuracy (while gaining magnificent CPU-speed) infers that the ROM reconstructs the LEE reference acceptably well.

	Upstr. Excit.	Downstr. Excit.
rel.Err at x_u	4.16 %	1.75 %
rel.Err at x_d	1.26 %	1.11 %
Δt_{LEE}	20 min	20 min
Δt_{ROM}	10^{-8}sec	

Table 7.1: CPU-times & relative errors

7.2.4 Validation Results

The scattering coefficients are evaluated for a frequency spectrum between 500 Hz and 1500 Hz in 50 Hz steps with results from the high-order LEE system and the ROM. The resulting amplitudes and phases are plotted in Figs. 7.6 and 7.7. The reference location for the phase angles is at x_0 (cf. Fig. 7.3), which is in the center of the orifice.

The figures reveal an excellent agreement between the ROM results and the high-order LEE as well as the experimental benchmarks. The occurring deviations are found negligible, especially when considering the CPU-time required to produce the ROM results compared to the high-order LEE simulations. The CPU times are the same as in Table 7.1, but one has to consider that the two independent sets for high-order LEE results need to be obtained by two simulation runs, whereas the ROM results require only a single simulation due to its MIMO system nature. All in all, the reconstruction results infer that the proposed MOR approach can be employed to produce ROMs that accurately describe real-world aeroacoustic systems. Consequently, such ROMs are granted full eligibility to be used as the main building block for modeling non-compact thermoacoustic system and flame dynamics.

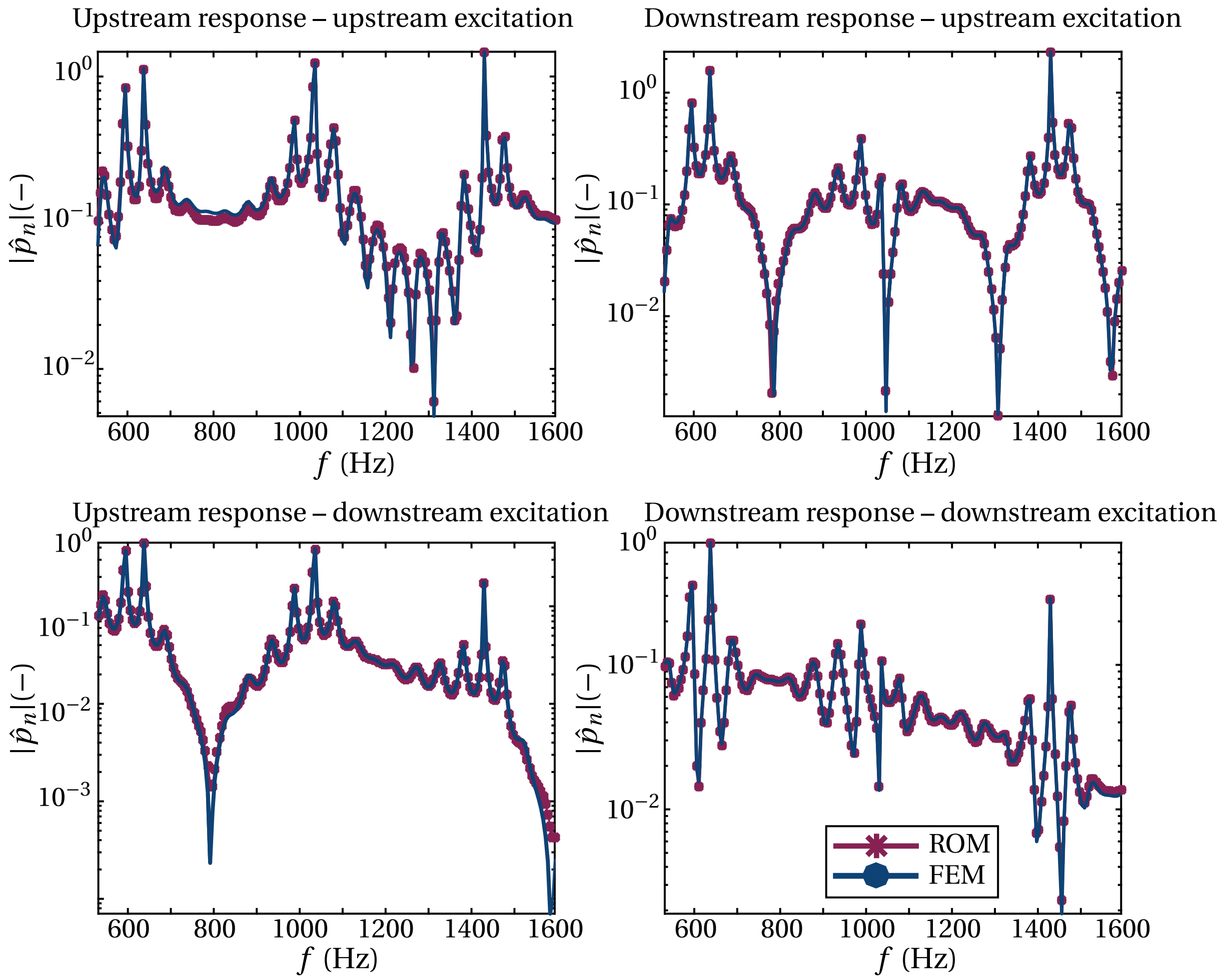

Figure 7.5: Pressure responses – orifice tube

7.3 Reduced Order Model of Non-Compact Thermoacoustic Systems

In this section, a modeling framework – which is centrally based on the above-presented ROM methodology – for the analyses of non-compact thermo-acoustic systems is introduced. For this purpose, a novel method to incorporate non-compact flame dynamics is presented, which is then applied to the benchmark combustor to demonstrate the work flow in the subsequent section. The general idea of incorporating non-compact flame dynamics within a ROM description of a given combustor is presented in Fig. 7.8.

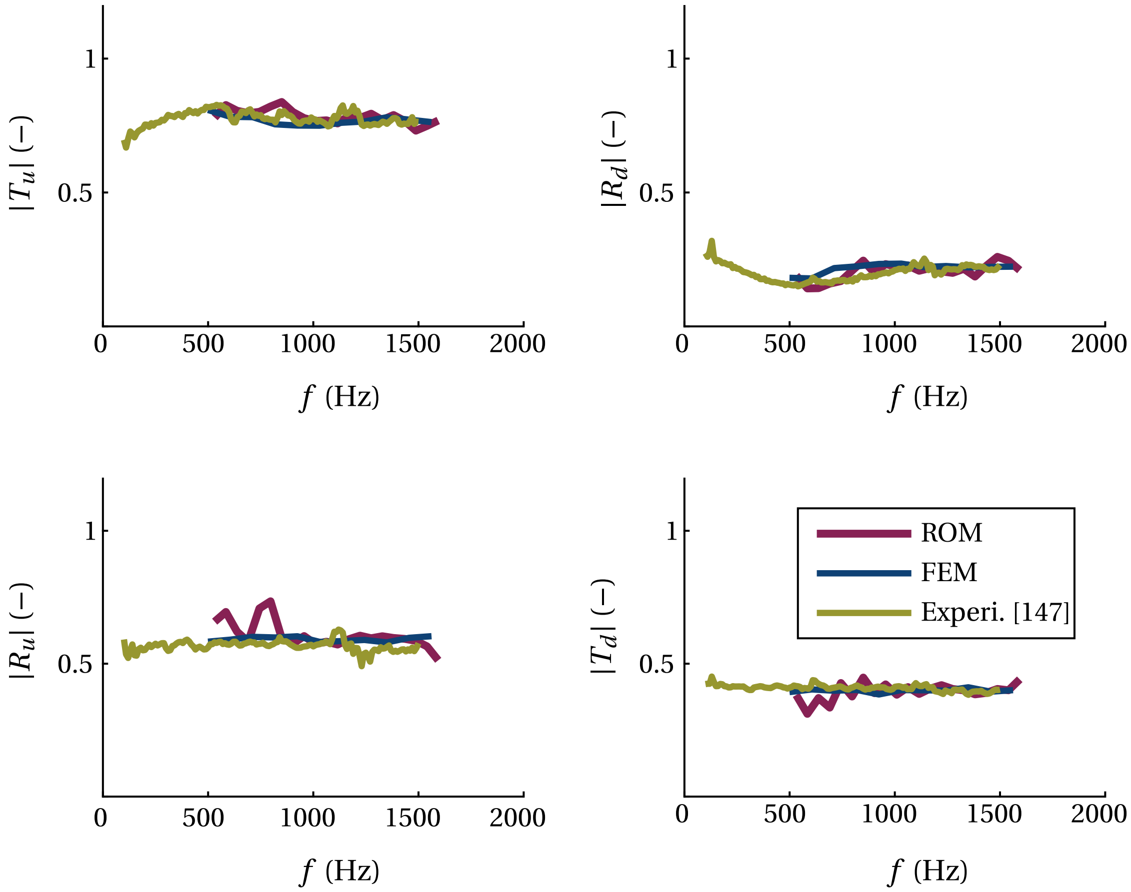

Figure 7.6: Amplitudes of scattering coefficients

This figure shows a characteristic flame shape as encountered in the swirl-stabilized benchmark combustor (cf. Chap. 3) along with the first transversal pressure mode shape. It is revealed that length scales of the former and latter are of the same order of magnitude, which confirms the non-compactness of the system. The non-compact thermoacoustic interactions are modeled by dividing the flame shape into multiple compact sub-regions (cf. Fig. 7.8) and forming a local feedback loop for each sub-region. Each sub-region's reference signal is extracted at the center of each concerned sub-region by a corresponding output vector. This output signal is converted into a heat release signal using the general transfer function given by Eqns. 2.22-2.23 in Sec. 2.6

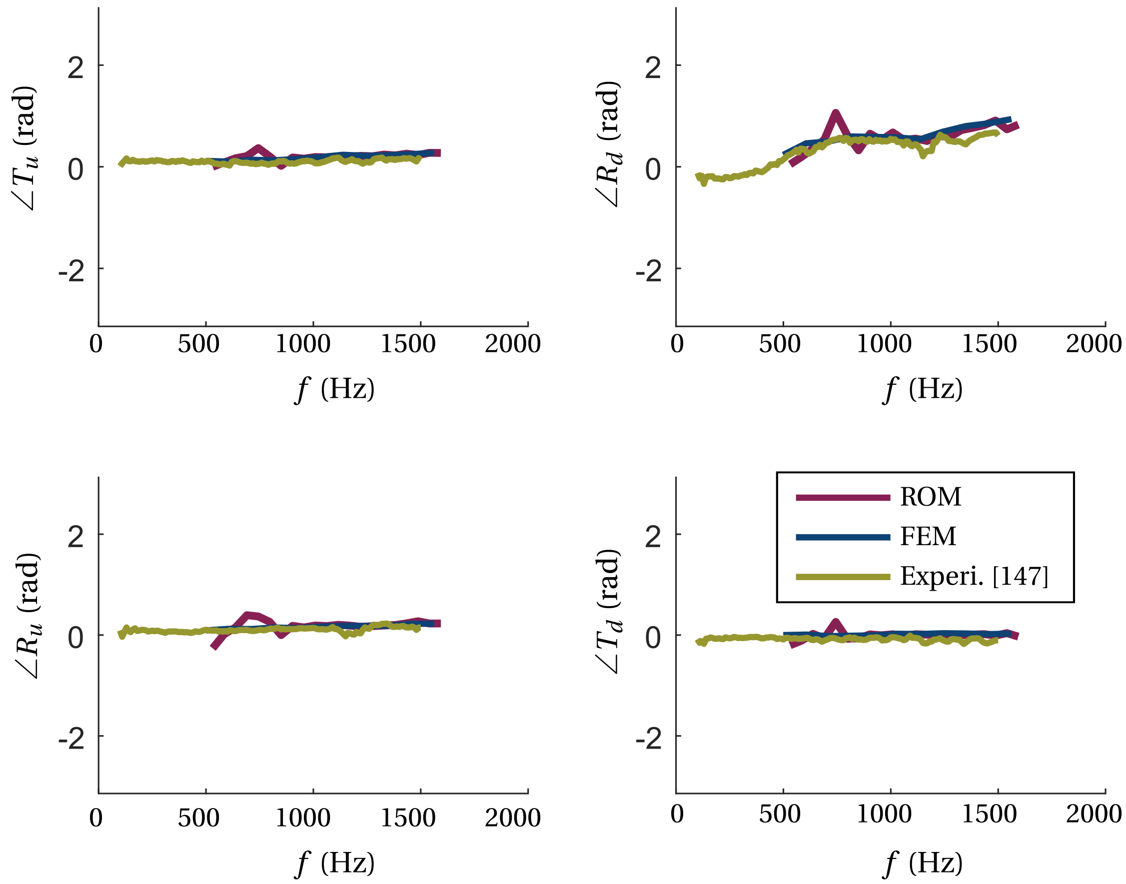

Figure 7.7: Phase angles of scattering coefficients

formulated on sub-region level (denoted by the subscript s), i.e.

$$q'_s = F_{L,s}(p'_s) + F_{NL,s}(p'_s) + F_{S,s}, \tag{7.25}$$

where $F_{L,s}$ and $F_{NL,s}$ implicitly describe linear and non-linear thermoacoustic coupling processes, respectively. The term $F_{S,s}$ denotes the function that models the stochastic effects on the oscillations due to turbulent combustion noise as explained in Sec. 2.6. Notice that retaining only the linear part of the transfer function in Eqn. 7.25 allows to carry out linear stability assessments in frequency domain. Such analyses are essentially analogous to linear driving, damping and stability assessments presented in Chaps. 4-6, and can be effectively used for verification of the ROM feedback connections. The entire transfer function, i.e. considering the linear, non-linear as well as stochas-

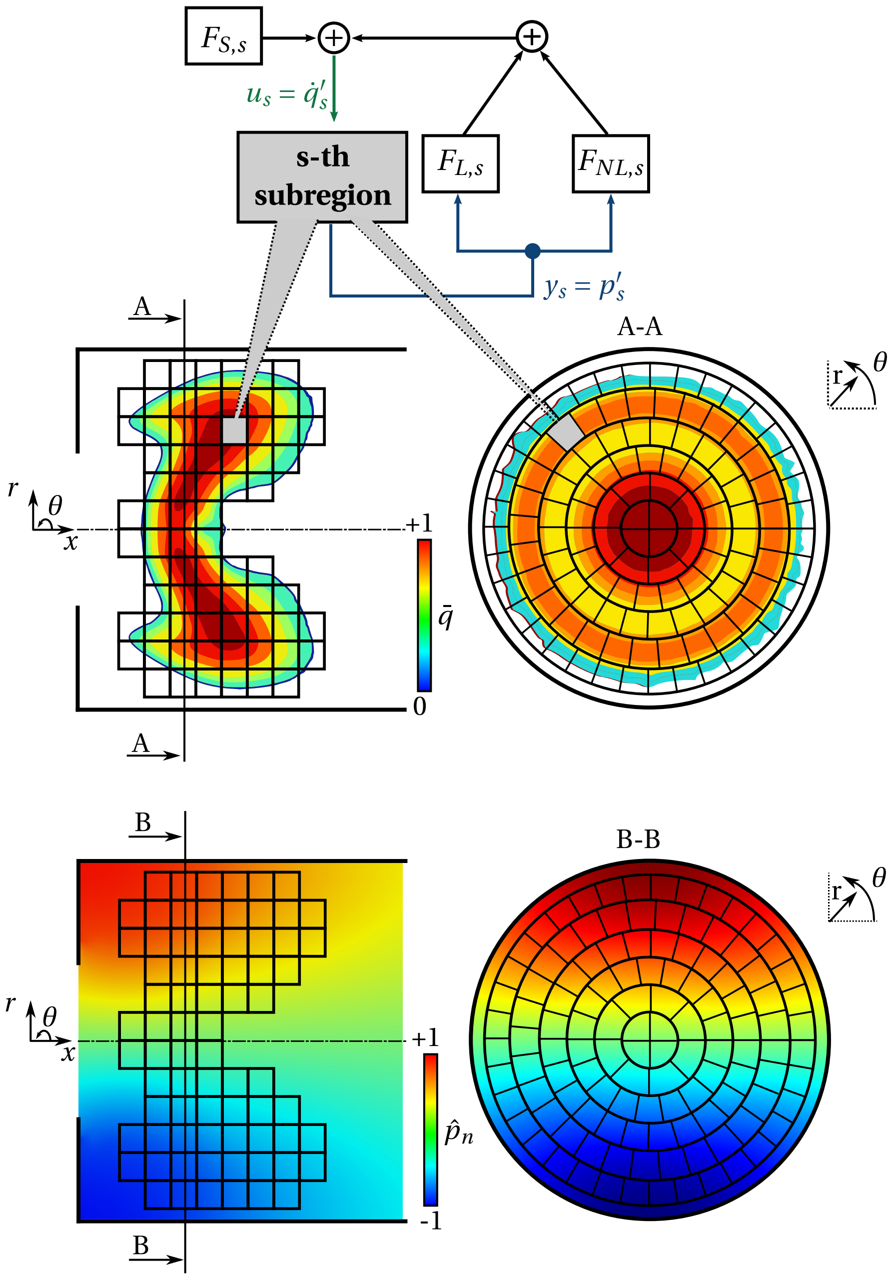

Figure 7.8: Non-compact flame segmentation, mean heat release distribution, and Multi-Input-Multi-Output (MIMO) feedback connections for Reduced Order Modeling framework

tic part in Eqn. 7.25, is employed for time domain simulations carried out in Chap. 8. Regardless of the specific form of the transfer function used, the resulting heat release oscillations are fed into the ROM by an appropriate input vector. This input vector is created from a FEM load vector for which each sub-region is flagged by setting the heat release fluctuation amplitude of the source term in the energy equation to unity at all grid nodes associated with the respective region, and zero elsewhere. Setting this fluctuation amplitude to unity neutralizes the – at this point open-loop – input term to ensure an unbiased feedback modeling, i.e. it is ensured that the heat release input that is converted by transfer functions is magnitude-wise correct. Finally, the non-compact thermoacoustic interactions are modeled by forming the feedback loop for each sub-region via multiple in- and output signal routes, i.e. establishing a Multi-Input Multi-Output (MIMO) feedback system.

7.4 Derivation of MIMO Reduced Order Model

The creation and verification of the MIMO-ROM system that describes the non-compact thermoacoustic performance of a given combustor is divided into the following steps:

1. Problem setup, i.e. definition of governing equations and boundary conditions of the concerned combustor.
2. FEM discretization to retrieve the large-scale system matrices.
3. Creation of the open loop ROM and verification via comparisons of pressure response functions.
4. Flame segmentation and set up of MIMO feedback framework along with the formulation of local transfer functions.
5. MIMO feedback closure and verification via comparison of complex eigenfrequencies.

In the following, these steps are employed on two operation points of the swirl-stabilized benchmark combustion system. Thereby, explicit handling guidelines of the non-compact thermoacoustic modeling concept are provided. At the same time, the MIMO-ROM framework for the time domain simulations conducted in Chap. 8 below is produced, too.

Step #1: Problem Setup of Concerned Combustor

The thermoacoustic performance of two distinct operation points (cf. Tab. 7.2) of the reactive configuration benchmark combustor is modeled and analyzed with the MIMO-ROM methodology. One operation point exhibits self-sustained, first transversal oscillations, i.e. is thermoacoustically unstable, while the other one is stable as indicated by the dynamic pressure amplitude values in Tab. 7.2.

Parameter	**Stable**	**Unstable**	**Units**
Normalized pressure amplitude	0.012	1.0	-
Air excess ratio	1.8	1.1	-
Air mass flow	120	120	g/s
Fuel mass flow	3.9	7.0	g/s
Inlet temperature	673	673	K
Thermal power	195,000	350,000	W

Table 7.2: Operation points of the unstable/stable case

The open-loop thermoacoustic performance of these two operation points are modeled via the LEE given by Eqns. 2.18-2.19. Theoretically, the computation of the acoustic damping due to non-uniform mean flow effects, i.e. vortex-shedding, is not straightforward with these equations (cf. Chap. 5). However, due to the 3D nature of the computation domain the grid resolution is rather coarse compared to the fine resolution that resolved all vortex-shedding processes adequately (cf. Fig. 5.8c). As is explained in Sec. 5.4, this coarseness induces a sufficient level of numerical diffusion, which allows to model vortical damping using the numerical stabilization parameter as a tuning variable. This allows to adapt the damping/growth rates of the eigenmodes for the ROM creation as desired. Of course, this "coarsened" mesh approach eliminates any capabilities of damping predictions that are quantitatively correct. However, a quantitative prediction is not necessary as the main purpose of the ROM is to conduct time-domain simulation of the temporal behaviour of the thermoacoustic modes. Thus, the growth rates are required to be only binarily correct, i.e. positive or negative to respectively investigate the dynamics of stable an unstable modes. Note that the phrase "coarse mesh" refers to the resolution of the vortex-shedding processes and the associated vorticity mode. Rating the mesh regarding the resolution of the acoustic mode and respective flame-acoustic interactions – which are of predominant interest for the following analyses – is found as adequately fine. The inclusion of quantitatively correct damping rates within the ROM would be achieved if the HE modeling approach introduced in Sec. 5.3 is used instead of the LEE as underlying governing equation/large scale system. Nevertheless, the LEE is used over the HE model, which is justified by the following reasons:

- The LEE capture mean flow effects that cause the loss of degeneracy of the transversal mode pairs, which is an essential feature of the non-linear system dynamics as is addressed in Chap. 8.
- The LEE in conjunction with numerical stabilization parameters and a coarsened mesh automatically acts on all concerned modes of the ROM. This approach circumvents the need to obtain the damping rate for each mode individually (as would be required if the HE damping modeling approach is employed).

The required mean velocity and pressure fields are retrieved from isothermal CFD simulations of the two operation points as for the linear damping quantification in Chap. 5. Mean heat release and temperature distributions are obtained from time-averaged, inverse Abel transformed OH^* intensity images of the "real" flame in the combustor facility, results and details of which can be retrieved from [15]. The flame is rotationally symmetric (cf. Fig. 7.8). Hence, the inverse Abel transformed OH^* chemiluminescence 2D cut-plane images are used to construct the flame volume within the computational domain by an azimuthal revolution of 360 degrees of the respective image. The separation of thermal and velocity mean fields essentially assumes that acoustic damping is solely a result of interaction processes between acoustic and non-uniform mean flow velocity, i.e. due to acoustically induced vortex-shedding. This separation approach was already applied and justified in the course of the damping modeling in Chap. 5. Finally, acoustic boundary conditions at the combustor's bounding surfaces need to be prescribed (cf. Fig. 7.9). At the inlet, an energetically neutral condition $\hat{m} = 0$ is imposed, while a pressure node $\hat{p} = 0$ and slip conditions $\hat{\mathbf{u}} \cdot \mathbf{n} = 0$ are imposed at the outlet and the walls, respectively. Thus, the only source of damping is acoustically induced vortex-shedding and the subsequent absorption of vortical disturbances by the artificial diffusion scheme/coarsened mesh approach.

Step #2: Discretization of Governing Equations

The LEE description in frequency domain of the open-loop aeroacoustics performance of the two operation points is transformed into large-scale systems via a Streamline Upwind Petrov Galerkin (SUPG) stabilized FEM scheme. Details on the SUPG theory and implementation can be retrieved from Sec. 2.8. The unstructured mesh of the 3D combustor domain on which the FEM discretization is conducted consists of around $435,000$ tetrahedral elements for both cases, and displays in Fig. 7.9. This mesh translates into a resolution of minimum 15 elements per wavelength in the coarsest region at the outlet, and 90 elements per wavelength in the finest region around the flame with respect to the T1 modes. Using linear elements, the resulting final size of the FEM system amounts to $N \approx 300,000$ degrees of freedom.

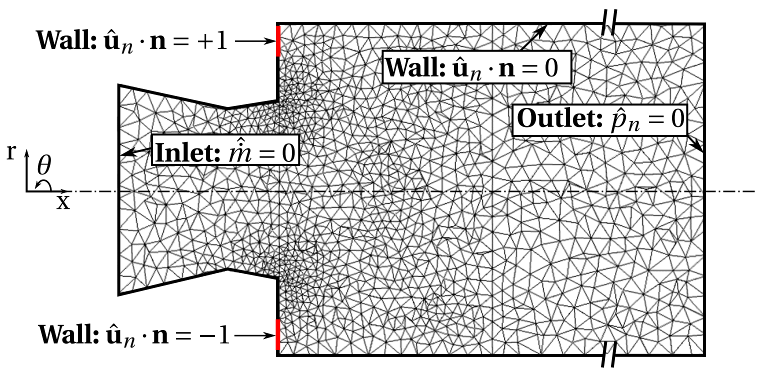

Figure 7.9: Mesh, excitation sources and boundary conditions

Step #3: ROM Creation and Frequency Response Verification

The ROM of the two considered cases (stable and unstable) are created and validated within this section. For this purpose, the subspace into which the respective large-scale LEE system is projected needs to be defined. The subspace is spanned by a collection of eigenvectors of the associated LEE system, which are associated with the eigenfrequencies across the frequency range and includes the targeted T1 mode:

$$2000\,\mathrm{Hz} \leq f_{MOR} \leq \; 5000\,\mathrm{Hz} \tag{7.26}$$

Specifically, seven longitudinal, ten first transversal, and two second transversal modes comprise the subspace. Execution of the MOR procedure (cf. Sec. 7.1 above) produces the ROM with a final dimension – considering the complex conjugate nature of the eigenmodes – of $N_r = 2 \times 19 = 38$ for both cases. Hence, a substantial order reduction over five orders of magnitude for both cases is achieved. Thermoacoustic driving is not yet considered, but will be in the next step. At this point, the ROM's reproduction capabilities are assessed by means of frequency swept pressure responses to external excitations. For this purpose, two wall sections at the faceplate of the combustor are prescribed with an excitation wall boundary conditions as is indicated in Fig. 7.9 to predominantly excite first transversal modes.

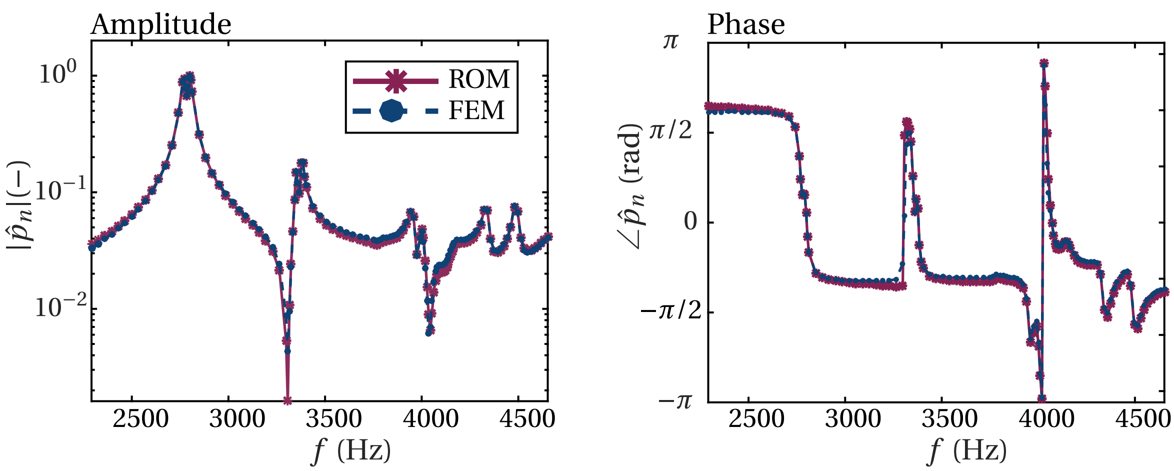

Figure 7.10: Frequency pressure responses of stable case's open loop systems

The responses of the ROM and LEE systems are computed for both cases over the range given by Eqn. 7.26 with $N_f = 120$ discrete frequencies. The resulting amplitudes and phases of the open-loop stable and unstable case are shown in Figs. 7.10-7.11, which indicate adequate agreement between ROM and LEE results. Table 7.3 provides the relative error (cf. Eqn. 7.16) for both cases. The errors remain below 2%, which reveals an accurate reproduction capability of large-scale system performance by the respective ROM. Computation times of the ROM response occur basically instantaneous ($7x10^{-3}$sec), while the LEE sweeps lasted 11 hours for each case. A one-time obtainment of the eigenmodes of the derived the ROM is required and lasted 1 hour for each case. Conclusively, substantially small ROM dimensions with associated vanishingly short computational times are achieved, while large-scale system benchmarks results are accurately reproduced.

-	STABLE	UNSTABLE
REL.ERR.	1.6%	0.9%

Table 7.3: Relative errors of the stable and unstable open-loop ROM

Step #4: Flame Segmentation and MIMO Feedback Framework

The flame segmentation is carried out as shown in Fig. 7.8, which yields a three-dimensional structure composed of individual volumes. For each of these volumes, an in- and output vector is created, which are then assembled to yield the respective in- and output matrices. The transfer function needed to convert (local) pressure signals to heat release oscillations consists – due to

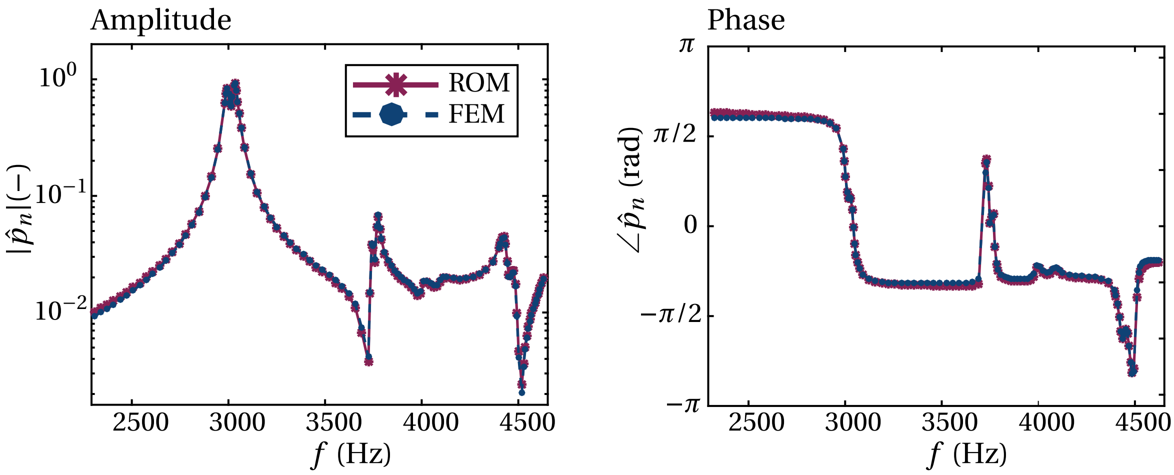

Figure 7.11: Frequency pressure responses of unstable case's open loop systems

the frequency domain verification task via eigenfrequencies in the next step – only of the linear part of Eqn. 7.25, and explicitly unfolds into

$$q'_s = F_L(p'_s) = q'_{\rho',s} + q'_{\Delta',s} = \frac{\bar{q}_s}{\gamma_s \bar{p}_s} p'_s - \frac{\nabla \bar{q}_s}{\bar{\rho}\omega^2_{n,a}} \nabla p'_s \tag{7.27}$$

where the mean values of heat release rate $\bar{q}_s$, pressure $\bar{p}_s$, density $\bar{\rho}_s$ and ratio of specific heats γ_s as well as the acoustic pressure signal p'_s are space averaged values for each sub-region s. The two parts of the linear transfer function represent the driving mechanisms due to flame deformation and displacement as presented in Chap. 4. Notice that the displacement transfer function is modified to yield a functional dependence on the pressure oscillation, which is achieved by using the acoustic momentum equation (cf. homogeneous form of Eqn. 2.20) to replace the velocity. To be specific, the pressure dependence is given by means of the spatial gradient. The pressure gradient signal at a particular sub-region is generated – and thus incorporated within the MIMO-ROM computations – by the pressure signals of the adjacent sub-region using standard finite difference approaches [43]. The reason for using the pressure gradient instead of the velocity in Eqn. 7.27 is given by the requirement that input variables to thermoacoustic transfer functions are required to be of pure acoustic nature. For LEE modes, which provide the mathematical basis of the MIMO-ROM in this work, only the pressure mode satisfies this pure acoustic feature (cf. Eqn. 5.2), whereas the velocity contains acoustic and hydrodynamic contributions (cf. Eqn. 5.1).

Step #5: MIMO Feedback Closure and Eigenfrequency Verification

This section verifies the MIMO-ROM feedback approach by assessing the linear thermoacoustic stability of the two subjected cases. For this purpose, the linear, distributed transfer function in Eqn. 7.27 is used to close the MIMO-ROM feedback loop. The eigenfrequencies of this closed system are straightforwardly computed using standard linear algebra techniques, i.e. linear fractional transforms as shown in [137]. These eigenfrequencies are complex, i.e.

$$\omega_{n,a} = 2\pi f_{n,a} - i\nu_{n,a}, \tag{7.28}$$

where $f_{n,a}$ and $\nu_{n,a}$ denote oscillation frequency and growth rate of the acoustic mode n, respectively. The sign of the growth rate determines linear stability, i.e. mode n is rendered thermoacoustically stable/unstable for $\nu_{n,a} < 0/ > 0$ (cf. Chap. 6). The resulting MIMO-ROM eigenfrequencies are presented in Fig. 7.12 along with corresponding eigenfrequency benchmarks of the large-scale LEE system. These LEE solutions are obtained by prescribing the heat release source term $\hat{\hat{q}}_n$ in Eqn. 2.19 with the source term given in Eqn. 8.21, and then solving this closed system for the desired eigenmodes/frequencies. Figure 7.12 reveals three main outcomes:

- Binarily correct reproduction of experimentally observed T1 stability – i.e. positive and negative growth rates for the unstable and stable operation point – is achieved by tuning the numerical stabilization parameter as required. This is justified as the time-domain simulations in the next chapter only require these binarily adjusted growth rate values of the considered thermoacoustic modes for the associated analyses.
- Identification of deviating oscillation frequencies and growth rates between the T1 mode pairs for each case. This loss of T1 degeneracy is caused by mean flow interactions between acoustic oscillations and swirling velocity field (cf. App. B).
- Accurate eigenfrequency results of the MIMO-ROM compared against the LEE verification results in respective relative errors of growth rates that remain below 5% for the T1 modes, which is certainly acceptable in the light of the significant order reduction achieved. The oscillation frequencies of the ROM and FEM results match exactly, which is due to the underlying MOR procedure.

It is important to point out that if one's primary interest is in linear thermoacoustic analyses, there is no need to conduct the MIMO-ROM modeling approach as the field methods in frequency domain presented in Chaps. 4–6 are more suitable for such tasks. The purpose of employing linear analyses in this chapter is primarily to verify the reproduction capabilities of the MIMO-ROM approach of the high-order reference setup to ensure suitability for the desired time-domain simulations in the next chapter.

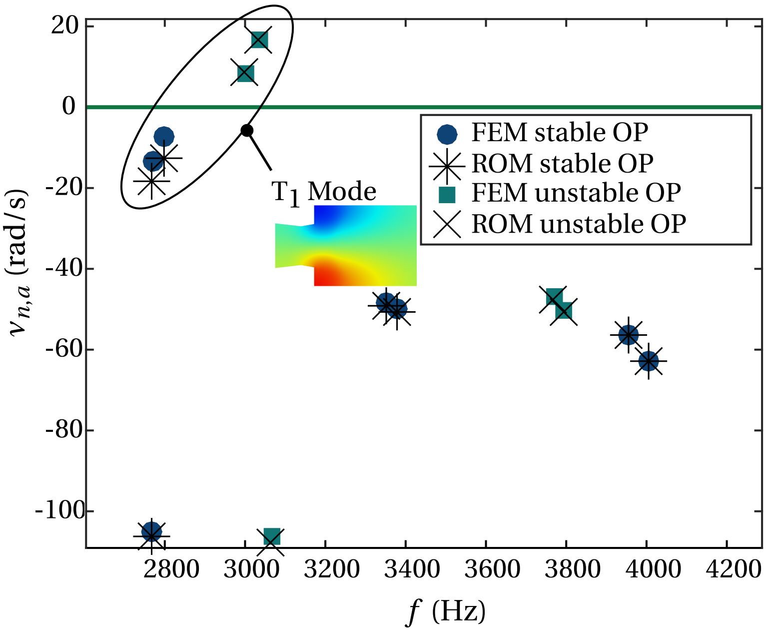

Figure 7.12: Complex eigenfrequencies of closed loop for both operation points

A comparison of the T1 oscillation frequencies of the ROM/high-order LEE systems against the experimentally measured counterparts is given in Tabs. 7.4 and 7.5 for the stable and unstable case, respectively. The tables show the deviating frequencies as a consequence of the loss of degeneracy, which are allocated to two counter-rotating T1 modes. The higher and lower frequency mode (labeled T1$_F$ and T1$_G$ mode) rotates counterclockwise (CCW) and clockwise (CW), which is the same and opposite direction as the swirling mean flow, respectively (cf. App. B for details on the origin of this loss of degeneracy).

	EXPERIMENT	**MIMO-ROM**	**REL.ERR.**
f_F	2,870 Hz	2,801 Hz	2.5%
f_G	2,840 Hz	2,776 Hz	2.25%

Table 7.4: Comparison of oscillation frequencies – stable case

	EXPERIMENT	**MIMO-ROM**	**REL.ERR.**
f_F	3,150 Hz	3,038 Hz	3.5%
f_G	3,100 Hz	3,003 Hz	3.2%

Table 7.5: Comparison of oscillation frequencies – unstable case

Relative errors (cf. Tabs. 7.4-7.5) between calculated and measured frequencies remain below 4%, which is an accurate agreement. It can be concluded that the MIMO-ROM approach accurately reproduces the high-order LEE verification baseline as well as the applicable experimental observation in the linear regime. Hence, the respective MIMO-ROM systems can be confidentially employed for time domain simulations in Chap. 8 as well as for verification tasks of the growth rate extraction methods developed in Chap. 10.

7.5 Summary and Findings – ROM Development

The foregoing chapter presented the development of a Reduced Order Modeling (ROM) methodology that is particularly applicable to model HF thermoacoustic oscillations governed by transversal modes in gas turbine combustors. Specifically, the methodology exhibits the following modeling capabilities:

- Consideration of 3D domains and multi-dimensional acoustic modes.
- Incorporation of non-compact flame dynamics using a Multi-Input-Multi-Output (MIMO) feedback modeling approach.
- Formulation of the ROM in state-space to enable both, frequency and time domain analyses.

Theoretically, the methodology is based on modal reduction of large-scale LEE systems, i.e. the projection of this system into a subspace that is spanned by a selected set of eigenmodes. The range of eigenmodes is determined by the range of frequency in which the thermoacoustic dynamics of the combustor is investigated. Applicability of the ROM methodology to combustor-like configurations was validated by computing the aeroacoustic scattering behavior of an orifice tube. Experimental as well as LEE reference results were accurately reproduced, while a considerable increase of computational efficiency of the ROM computations was achieved.

Then, the ROM methodology was applied to the swirl-stabilized benchmark combustor, which included the consideration of non-compact flame dynamics via the MIMO feedback approach. The procedural derivations steps of the methodology for thermoacoustically active HF systems were demonstrated. At the same time, the required ROM framework for the time-domain simulations and analyses carried out in the next chapter was established. Specifically, ROM of one stable and one unstable operation point were derived and verified. The verification occurred in frequency domain by means of comparing pressure response and complex eigenfrequencies obtained by large-scale LEE and ROM computations. Additionally, a substantial order reduction was achieved as desired, which rendered the ROM eligible for further usage.

The ROM framework forms a comprehensive tool for time domain analyses, which can be readily applied to gas turbine combustors of industrial scale. Often these tasks include the incorporation of damping devices at distinct locations of the combustor wall to test the effect on the system dynamics [111]. Moreover, assessing the impact of up-and downstream periphery on the acoustic modes – especially when interactions between mode and in-/outlet boundaries of the chamber are non-negligible – is frequently of interest, too. Procedurally, the incorporation of both (damping devices and up-/downstream periphery) occurs by interconnecting the combustor domain with transfer functions [13]. This interconnection is achieved in an analogues manner as the connection of the non-compact feedback, and can thus be considered as a readily available capability within the ROM framework. An explicit demonstration of such analyses was beyond the scope of this thesis and remains open for future work.

8 Combustor Dynamics – Numerical Analysis

This chapter applies the previously developed MIMO-ROM methodology to conduct time domain simulations and corresponding analyses of HF thermoacoustic dynamics in the swirl-stabilized benchmark combustor. The references [21, 78, 94, 113] are used as overall sources for these tasks. The same operation points (1x unstable, 1x stable) used to demonstrate the derivation and verification procedure in Sec. 7.4 of the ROM framework are used for this tasks. Hence, the required MIMO-ROM systems are readily available for the simulations in this chapter. The specific objectives of this chapter are then:

- Reconstruction of experimentally observed combustor dynamics constituted by non-degenerate T1 mode pairs by ROM simulations.
- Characterization of HF thermoacoustic oscillations from a dynamical system perspective.
- Identification of distinct physical features that govern HF thermoacoustic limit cycle dynamics.
- Demonstrating the suitability of the non-compact MIMO-ROM approach for time domain analyses/simulations of technically relevant combustors.

8.1 Preparations of Time Domain Analyses

This section presents preliminary information relevant for time domain analyses in this chapter. First, a post-processing procedure to classify and describe the dynamical behavior of transversal modes in tubular combustor geometries is presented. Second, non-compact transfer function that are suitable to model time domain flame dynamics are introduced.

8.1.1 Transversal Mode Dynamics

Possible scenarios of transversal mode dynamics, i.e. how the particular mode behaves in time domain, are as follows:

1. Rotating mode dynamics in either clockwise (CW) or counterclockwise (CCW) direction.
2. Standing mode dynamics.
3. Mix of rotating and standing mode features.

Identifying the dynamical scenario from acoustic pressure time series allows for efficient interpretation of the experimental and simulation results. This task is achieved by employing a post-processing methodology. This methodology is based on the assumption that transversal mode dynamics are described by a superposition of two, in opposite direction traveling first transversal modes. This is achieved by expanding the spatial acoustic pressure oscillation by a two-fold Fourier series given by [24, 42]

$$p'(\mathbf{x},t) = \overbrace{\eta_F(t)\Psi_F(\mathbf{x})}^{p'_F} + \overbrace{\eta_G(t)\Psi_G(\mathbf{x})}^{p'_G} + p'^{*}_F + p'^{*}_G, \tag{8.1}$$

where the shape functions $\Psi_F(\mathbf{x})$ and $\Psi_G(\mathbf{x})$ are associated with a counterclockwise (CCW, p'_F) and clockwise (CW, p'_G) rotating transversal mode, respectively. The complex Fourier coefficients $\eta_F(t)$ and $\eta_G(t)$ are time-dependent signals associated with each rotating mode. Theoretically, the pressure oscillations are governed by an infinite Fourier series. In practice, bandpass-filtering of the time signals around the resonance frequency needs to be carried out to eliminate contributions to the time series by other modes than the T1 pair. The mode shapes are given by

$$\Psi_F(\mathbf{x}) = \Psi_G^*(\mathbf{x}) = \sigma(x,r)\exp(-i\theta) \tag{8.2}$$

$$\Psi_G(\mathbf{x}) = \Psi_F^*(\mathbf{x}) = \sigma(x,r)\exp(i\theta) \tag{8.3}$$

where $\exp(-i\theta)$ and $\exp(i\theta)$ imply CCW and CW direction of rotation, respectively. Any axial and radial variability of the mode shapes is absorbed in $\sigma(x,r)$, which is a real expression. Higher transversal modes (e.g. T2) can be treated analogously as shown herein for the T1 mode. In Eqns. 8.2-8.3, the asterisk (*) indicates the complex conjugate of the concerned function.

Employing the counter-rotating description of the mode dynamics as given by Eqn. 8.1 poses one dominant advantages over using the approach that is based on two standing modes (cf. [21, 108, 112]). This advantage is the ability to capture the non-degeneracy feature at the first transversal mode (cf. App. B) that is encountered in swirling, non-uniform mean flow environments, which is not possible using the standing mode approach. This non-degeneracy manifests in different oscillation eigenfrequencies of the constituting rotating modes p'_F and p'_G. Consequently, the oscillations of the complex Fourier coefficient $\eta_F(t)$ and $\eta_G(t)$ are not restricted to be equal.

The next step to extract information about the mode dynamics from a given time series is to identify the Fourier coefficient signals $\eta_F(t)$ and $\eta_G(t)$. Practically, time traces of acoustic pressure signals (N_t samples) are recorded through probes at N_θ azimuthal positions, which are mounted at the faceplate of the benchmark combustor as indicated in Figs. 3.2.

$$p'(\theta,t) = (\eta_F + \eta_G^*)\sigma(x_p,r_p)\exp(-i\theta) + (\eta_F^* + \eta_G)\sigma(x_p,r_p)\exp(i\theta). \tag{8.4}$$

The value of the axial-radial mode shape function is set to one, which avoids any impact on the amplitude values of the Fourier coefficients, i.e. $\sigma(x_p,r_p) = 1$. Then, Eqn. 8.4 is re-written as an overdetermined linear system, i.e.

$$\mathbf{P}(\theta_j,t) = \mathbf{H}(t)\cdot\mathbf{T}(\theta_j), \tag{8.5}$$

where $\mathbf{T}(\theta_j) = [\exp(-i\theta_j)\ \ \exp(i\theta_j)]^T$. The pressure time signals of the azimuthal probes at θ_j with $j = 1,2,\ldots N_\theta$ are collected in the $N_t \times N_\theta$ matrix

$\mathbf{P}(\theta_j, t)$. The matrix $\mathbf{H} = [H_a \quad H_b]$ dimension $N_t \times 2$, where the first and second column represent complex time traces composed of Fourier amplitudes $H_a = \eta_F + \eta_G^*$ and $H_b = \eta_F^* + \eta_G$, respectively. These time traces are obtained in a least-square sense, i.e. pseudo-inverting Eqn. 8.5

$$\mathbf{H} = \mathbf{P} \cdot \mathbf{T}^T \cdot (\mathbf{T} \cdot \mathbf{T}^T)^{-1}. \tag{8.6}$$

Assuming that the temporal change of the amplitude traces of these wave signals is slow compared to the time scale of the associated acoustic oscillation allows the following polar decomposition

$$\eta_F(t) = F(t) \exp[i(\omega_F t + \phi_F(t))], \tag{8.7}$$

$$\eta_G(t) = G(t) \exp[i(\omega_G t + \phi_G(t))], \tag{8.8}$$

where $F(t)/G(t)$ and $\phi_F(t)/\phi_G(t)$ represent slowly varying, time-dependent amplitudes and phases, respectively. The traces $\eta_F(t)/F(t)/\phi_F(t)$ are associated with the CCW rotating mode while $\eta_G(t)/G(t)/\phi_G(t)$ corresponds to the mode rotating in CW direction. The oscillation frequencies ω_F/ω_G are not restricted to be equal. The amplitude and phase traces are obtained by Hilbert transforming the time signals of Eqn. 8.6, which yields

$$H_F = \mathcal{H}(H_a) = H_{a,r}(t) + i H_{a,i}(t), \tag{8.9}$$

$$H_G = \mathcal{H}(H_b) = H_{b,r}(t) + i H_{b,i}(t). \tag{8.10}$$

The Fourier amplitudes are then given by

$$F(t) = |H_F|, \tag{8.11}$$

$$G(t) = |H_G|, \tag{8.12}$$

while the corresponding total phase evolutions are obtained using the Hilbert transform via

$$\varphi_F(t) = \omega_F t + \phi_F(t) = \angle\mathcal{H}(Real(H_F(t))/F(t)), \tag{8.13}$$

$$\varphi_G(t) = \omega_G t + \phi_G(t) = \angle\mathcal{H}(Real(H_G(t))/G(t)). \tag{8.14}$$

Then, the oscillatory signals of the decomposition are determined by evaluating Eqns. 8.7–8.8 using the amplitude and total phase traces given by Eqns.

8.9–8.14. The eigenfrequencies ω_F and ω_G are then retrieved e.g. from spectrum plots that are obtained by taking the Fast Fourier Transform (FFT) of the respective signals. Knowing these eigenfrequencies allows to determine the slowly varying phase evolutions by rearranging Eqns. 8.13–8.14, i.e.

$$\phi_F(t) = \varphi_F(t) - \omega_F t, \tag{8.15}$$

$$\phi_G(t) = \varphi_G(t) - \omega_G t. \tag{8.16}$$

The correctness of the foregoing decomposition procedure is ensured by respective application to dynamic pressure traces given at the $N_\theta = 5$ azimuthal probes of the swirl-stabilized benchmark combustor. Specifically, the methodology is applied to pressure measurements associated with the isothermal test case used for the damping model and mean flow investigation in Chap. 5 and App. B. The spectra of the decomposed mode signals η_F and η_G are plotted in Fig. 8.1. The figure effectively reveals two distinct peaks that indicate the frequencies associated with the CCW and CW mode, which correctly originate from the signals η_F and η_G, respectively. Hence, the non-degeneracy features of transversal modes is correctly captured, which grants the decomposition approach suitability for usage of time series analysis in this chapter.

Furthermore, the decomposition approach is applied to the pressure traces retrieved from the unstable operation point of the reactive configuration concerned in this work. The spectra are shown in Fig. 8.2, which reveal the deviating eigenfrequencies (indicated by the dashed vertical lines) of the CCW and CW signals, too. The amplitude peak of the CW signal is much smaller than the CCW counterpart, which is caused by the suppression of the former by the latter mode due to mode interactions during the limit-cycle oscillations as is explained in the upcoming sections. As for the isothermal data, non-degeneracy of the transversal mode pairs is captured by the decomposition, and thus, confirms the suitability of the approach for further usage.

The instantaneous values of slowly varying amplitudes $F(t)/G(t)$ reveal the mode dynamics, which specifically unfold into a CCW and a CW rotating mode if $F(t) = 0$ and $G(t) = 0$, respectively. The situation $F(t) = G(t)$ denotes a standing mode, and $F(t) \neq G(t) \neq 0$ mixed-type behavior. These dynamic

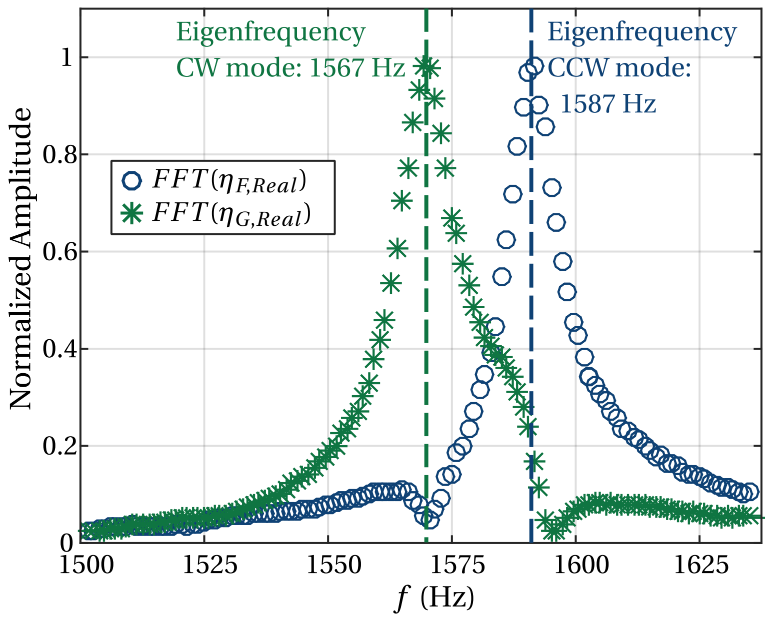

Figure 8.1: Pressure spectrum of the CCW and CW signals (η_F and η_G) – isothermal benchmark configuration (normalized with maximum amplitude of η_F)

scenarios are effectively illustrated by a spin ratio [24] given by

$$s(t) = \frac{F(t) - G(t)}{F(t) + G(t)}, \tag{8.17}$$

which translates into $s = \pm 1$ for a CCW and CW rotating mode, respectively. A spin ratio of $s = 0$ indicates a standing mode, while values in between these extrema represent mixed-type behavior.

8.1.2 Time-Domain Flame Dynamics Function

In order to execute time-domain simulations, the linear, non-linear and stochastic parts of the non-compact transfer function given in Eqn. 7.25 need to be explicitly formulated for the MIMO-ROM feedback connections. The linear part is simply retained as for the linear verification analysis in Eqn. 7.27,

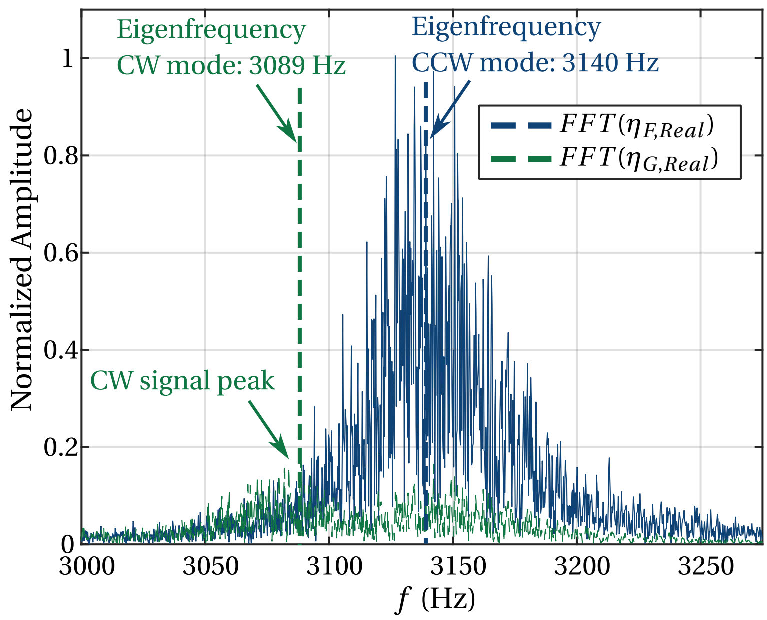

Figure 8.2: Pressure spectrum of the CCW and CW signals (η_F and η_G) – reactive configuration (normalized with maximum amplitude of η_F)

which is recalled here for clarity to

$$F_{L,s}(p'_s) = q'_{\rho',s} + q'_{\Delta',s} = \frac{\bar{q}_s}{\gamma_s \bar{p}_s} p'_s - \frac{\nabla \bar{q}_s}{\bar{\rho}\bar{\omega}^2_{n,a}} \nabla p'_s \tag{8.18}$$

where $\bar{\rho}_s$ γ_s, $\bar{q}_s$, and $\bar{p}_s$ denote the mean density, isentropicity coefficient value, mean volumetric heat release rate, and static pressure averaged over the concerned compact sub-region, respectively. The frequency $\bar{\omega}_{n,a}$ in Eqns. 8.18 is the mean value of the CCW and CW modes' eigenfrequencies. Eqn. 8.18 describes modulation of heat release with acoustic pressure oscillations, and is derived and discussed in detail in Chap. 4.[1] The results, i.e. growth rates and acoustic pressure time traces, are identical between both approaches to account for linear flame displacement. Saturation of heat release is described by a static non-linear function given by

$$F_{NL,s}(p') = -\kappa p'^3_s, \tag{8.19}$$

[1]Note that in the publication [72] associated with this chapter, the displacement part of the linear transfer function in Eqn. 8.18 was not explicitly considered for the time-domain feedback. Instead, the effect of flame displacement at the T1 mode was implicitly included within the eigenmodes to perform the MOR to obtain the open-loop ROM, which is simply due to the lacking implementation of considering spatial gradients of pressure oscillations in the MIMO-ROM framework at the time of the publication.

which presents an empirical function that is based on observations from experiments (cf. [112, 113]). The saturation function represents a power series expansion to the fourth order. However, the even terms (second p'^2 and fourth order p'^4) have no impact on the amplitude dynamics as is shown by the analytical averaging procedures in the next chapter and in [112]. The quantity $\kappa > 0$ is called non-linearity coefficient to model the flame's saturation strength, and is presumed a global constant independent of the particular sub-region of the flame. Equation 8.19 essentially models the saturation of the oscillating heat release rate with increasing amplitudes to yield self-sustained limit cycle oscillations of the mode of interest. The stochastic source terms expands to

$$F_{S,s} = \Gamma \Xi_s. \tag{8.20}$$

where Γ is the noise strength of and (spatially and temporally) uncorrelated white noise Ξ_s where the former is a constant while the latter represents and individual Gaussian signal for each sub-region. Spatial correlation between different sub-regions are thus neglected. Considering inter-spatial coherence of the source terms – which might be relevant in reality – is assigned to future work. There is no dependency of the stochastic source term in Eqn. 8.20 on the acoustic pressure oscillations, which reflects the additive noise assumption employed in this work. An explicit formulation of the non-compact heat release source term at sub-region level is produced by substituting Eqns. 8.18-8.20 into Eqn. 7.25 to give

$$q'_s = \frac{\bar{q}_s}{\gamma_s \bar{p}_s} p'_s - \frac{\nabla \bar{q}_s}{\bar{\rho} \bar{\omega}_{n,a}^{2}} \nabla p'_s - \kappa p'^3_s + \Gamma \Xi_s. \tag{8.21}$$

8.2 Results and Interpretations

This section presents the results of the time-domain simulations. Specifically, the thermoacoustic dynamics of the concerned stable and unstable operation point are reconstructed. For this, the non-compact feedback loops are closed via Eqn. 8.21 for which the MIMO-ROM state-space systems are readily available from Sec. 7.4. The additive white noise sources constantly excite the system dynamics throughout the simulations, which eliminates the need of any external excitation sources. Both systems are integrated in time using a Runge-Kutta-Dormand-Prince algorithm of 5^{th} order over a time span of 4 seconds. The required CPU time is approximately 2 minutes for each case. This span captures around 12,000 oscillation periods of the T1 mode at a sampling time of $\mathrm{d}t = 10^{-5}$seconds. The acoustic pressure time traces are recorded at $N_\theta = 5$ azimuthal probe locations at the benchmark combustor's faceplate, which is the same number of pressure sensors as in the experiment (cf. Chap. 3). Stable and unstable system simulations are adjusted to match the experimental observations by means of the non-linearity coefficient κ and the intensity Γ associated with the noise term Ξ_s in Eqn. 8.21, which represents the procedure established in [21]. The final values for κ and Γ are $30,000$ and 0.25 for both cases, respectively. MIMO-ROM simulation results are then compared against experimental data in order to retrieved physical insight of the subjected thermoacoustic system.

8.2.1 Stable Case

At first, the simulated pressure traces at the azimuthal probe locations are band-passed filtered around the two T1 frequencies (cf. Tab. 7.4). In a subsequent step, the above-introduced methodology of decomposing these band-limited signals (cf. Eqn. 8.5) into time-dependent Fourier coefficients $\eta_F(t)$ and $\eta_G(t)$ of the respectively CCW and CW spinning waves is employed to the experimental and ROM data. Recall that the experimental traces are readily available for this work as discussed and referenced in Chap. 3. The resulting signals are comparatively shown in Fig. 8.3 over a representative time span of 0.3 seconds. The plots yield fairly equal amplitude levels for the experimental and ROM signals, which is achieved by adjusting the noise strength Γ for the simulations. Generally, the figures reveal a successful reproduction of the signal produced by MIMO-ROM simulations as experimentally benchmarked, in which qualitative oscillatory character of the acoustic pressure, caused by stochastic forcing effects, is recovered. In the stable case, no deterministic limit cycle is established as the underlying mode is thermoacoustically stable. The oscillations are driven by broadband combustion noise [94], which causes the random amplitude evolution as can be observed in Fig. 8.3.

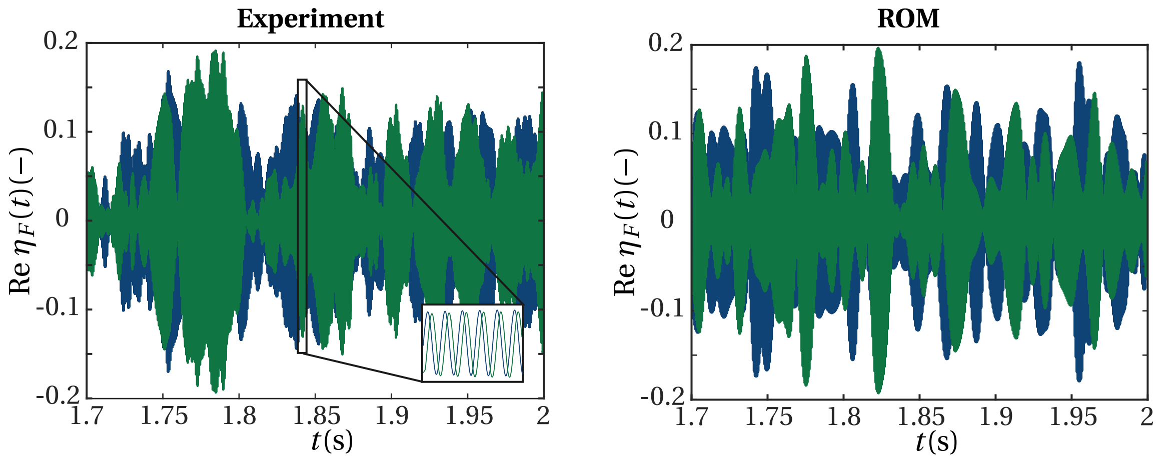

Figure 8.3: Stable case: temporal oscillations of Fourier coefficients (left column: experimental results, right column: ROM results)

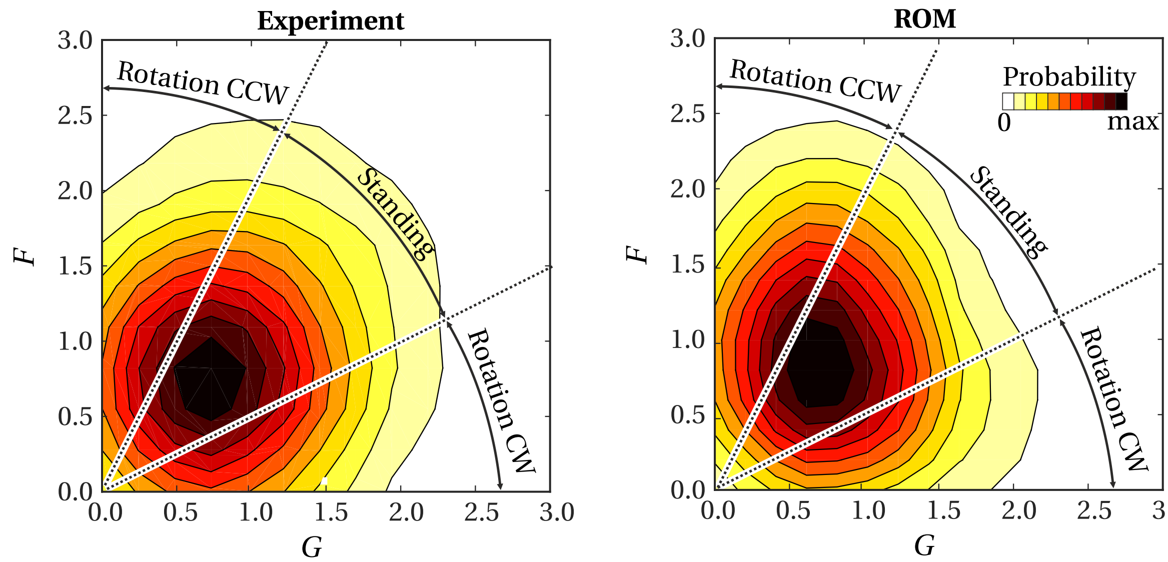

Figure 8.4: Stable case: Probability Density Distributions

Then, the corresponding slowly varying amplitudes of Eqns. 8.7-8.8 are obtained as shown in Sec. 8.1 above for simulated and measured pressure signal sets, and normalized. The normalized amplitudes are plotted as a joint probability density function (PDF) in Fig. 8.4[2], and corresponding spin-ratios s (cf. Eqn. 8.17) are displayed via histograms in Fig. 8.5.

[2]layout and colormap of the PDF plot adapted from the work in [173]

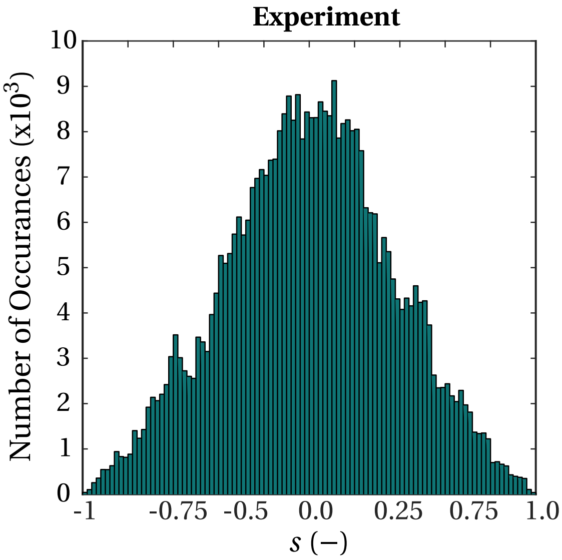

Figure 8.5: Stable case: spin-ratio histograms

Both figure types reveal predominantly standing mode dynamics for both, ROM and experimental results. The bell-shaped spread in Fig. 8.5 is caused by stochastic forcing due to turbulent combustion noise, which yields the possibility of instantaneous mixed type or even purely rotating mode behavior. The presented results/observations effectively serve to demonstrate the ROM's capability to identify and explain physical situations: Closely inspecting the PDF diagrams yields the maximum probability of the ROM's two waves' amplitudes at $F_{\mathrm{m}ax,ROM} = 0.80$ and $G_{\mathrm{m}ax,ROM} = 0.70$, while the experimental counterparts valuate at $F_{\mathrm{m}ax,EXP} = 0.78$ and $G_{\mathrm{m}ax,EXP} = 0.72$. The slight difference of these values implicates a dominantly standing T1 mode, which slowly rotates CCW, which is the direction of the swirling mean flow. This slow rotation in CCW direction is also revealed by the histogram plots in Fig. 8.5, which yield a mean spin-ratio of $s_{mean,ROM} = 0.0024$ and $s_{mean,EXP} = 0.0021$ for the ROM and experimental data sets, respectively. The interpretation of this small rotational feature is due to stochastic forcing, which constantly excites both rotating T1 modes. Specifically, the (stochastically excited) $\mathrm{T1}_F$ and $\mathrm{T1}_G$ modes spin in CCW and CW direction, respectively. The spinning speed (i.e. the eigenfrequency) of the former $\mathrm{T1}_F$ mode is larger than of the latter $\mathrm{T1}_G$ mode. Superposing these two individual mode behaviors yields a standing mode that slowly rotates as overall pressure dynamics. The angular speed of this slow rotation is given by the difference between the eigenfrequencies of the $T1_F$ and $T1_G$ modes.

8.2.2 Unstable Case

The dynamic pressure simulation data produced by the non-linear MIMO-ROM of the unstable case feature an initial exponential growth stage, which settles into the limit cycle oscillation stage due to non-linear saturation – as is theoretically expected. Analogously to the stable case, CCW and CW spinning Fourier amplitude signals $\eta_F(t)$ and $\eta_G(t)$ as well as corresponding slowly varying amplitudes $F(t)$ and $G(t)$ are computed from limit cycle data. Limit cycle oscillation amplitude levels, which additionally feature a distinct low-frequency modulation/beating are reproduced against the experimental benchmarks as shown in Fig. 8.6 with less pronounced beating amplitudes for the ROM signal. The CCW spinning wave $\eta_F(t)$ exhibits approximately two to three times the amplitude of the CW wave $\eta_G(t)$, which implies mixed type T1 mode dynamics. The envelope beating is revealed by the FFT of the signals' slowly varying amplitudes. The spectra show a low-frequency peak, which is the beating frequency. Corresponding plots are given in Fig. D.1 in App. D.

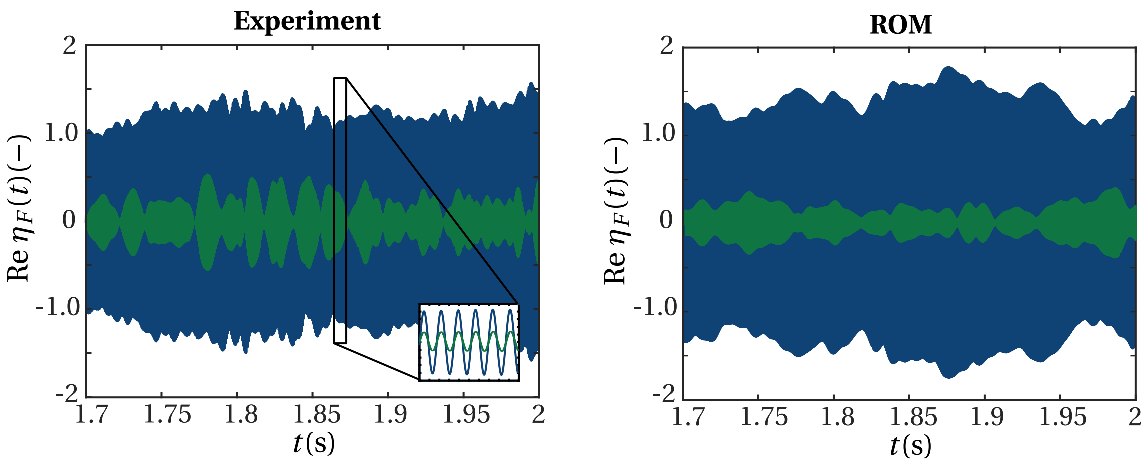

Figure 8.6: Unstable case: temporal oscillations of Fourier coefficients (left column: experimental results, right column: ROM results)

The PDF plots in Fig. 8.7 confirm these T1 dynamics, and additionally reveal that the direction of the rotations is CCW. This direction is – as for the slow rotation of the stable case – the same direction as the mean swirl of the combustor, and is associated with the higher frequency $T1_F$ mode (cf. Tab. 7.5). The mixed-type dynamics can be characterized as divided between a standing and rotating mode with an elevated tendency to the latter. This result emerges with an approximate mean spin-ratio of $s_{mean,ROM} = 0.71$ and $s_{mean,EXP} = 0.69$ from the histogram plots in Fig. 8.8, too. Again good agreement between the experimental and simulated data is found. The impact of stochastic forcing is smaller compared to the stable results as retrievable from the narrower Gaussian spin-ratio histograms, and the more compact shape of the PDF contours. This reduced presence of noise is due to the immensely elevated amplitude level of the limit cycle relative to the stable oscillations, which is three orders of magnitudes larger (cf. Figs. 8.3 and 8.6), while the noise strength is kept constant between the simulations of the stable and unstable case.

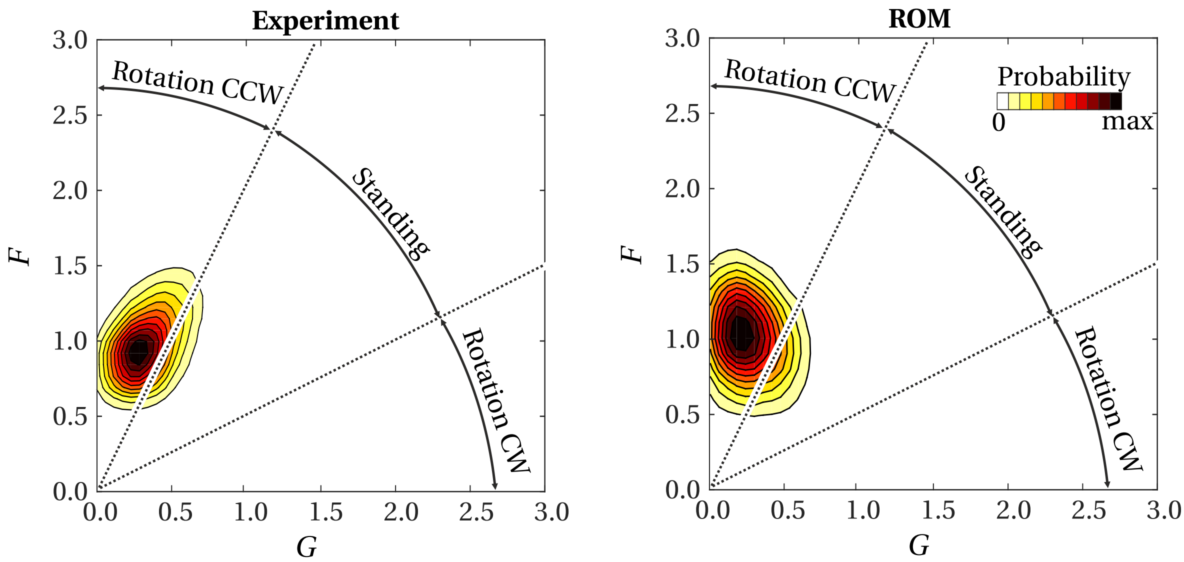

Figure 8.7: Unstable case: Probability Density Distributions

The reason for the rotational part of the mixed-type T1 mode to occur CCW is found by inspecting the linear growth rates of the two modes $T1_F$ (CCW, higher frequency) and $T1_G$ (CW, lower frequency). The respective growth rates valuate at $\nu_F = 17 rad/s > \nu_G = 9 rad/s$. Thus, the preferred mode direction is linked to the constituent mode with the larger growth rate. Artificially swapping the $T1_F$ and $T1_G$ growth rate, which is straightforwardly doable within the ROM derivation so that $\nu_F = 9 rad/s < \nu_G = 17 rad/s$ confirms the forego-

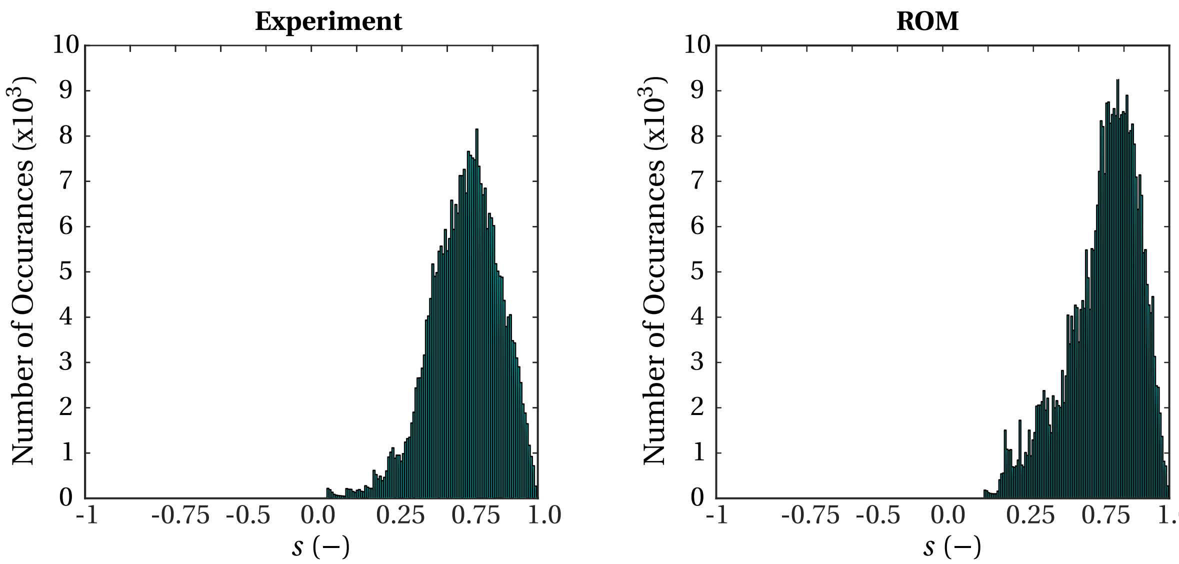

Figure 8.8: Unstable case: spin-ratio histograms

ing explanation. Corresponding time domain simulation results disclose the same mixed-type T1 mode dynamics, but with the rotational part occurring CW as is shown in Fig. 8.9. Notice that this swapping is physically meaningless, but is justified as it serves to demonstrate the decisive role of the growth rate for direction of the limit-cycle mode, whereas the oscillation frequency is not of any relevance for this matter.

More physical insight regarding the evolution of the instability in terms of its progression through the exponential growth into the limit cycle is generated by executing the MIMO-ROM simulations with a vanishingly low noise strength. Consequently, the results are unpolluted by stochastic effects, and solely reflect the deterministic thermoacoustic system performance. The temporal behavior of the deterministic amplitudes are plotted along with the noise-containing counterparts in Fig. 8.10. It can be observed that the CCW amplitude's $F(t)$ deterministic signal, which provides the rotational direction of the mixed-mode dynamics smoothly grows in an exponential manner, and then settles into a limit cycle. Thereby, the deterministic level reflects an approximate mean value of the noise-containing amplitude levels. The deterministic CW amplitude $G(t)$ also enters a growth period, reaches a maximum at a much lower amplitude than the CCW signal, and then descends to nearly

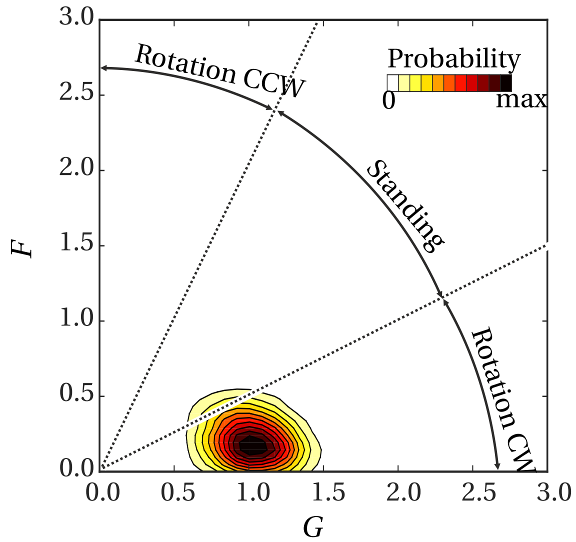

Figure 8.9: PDF of swapped growth rate simulations

zero amplitude instead of remaining in a constant limit cycle - even though the mode is linearly unstable. Thus the deterministic case resembles purely rotating T1 dynamics.

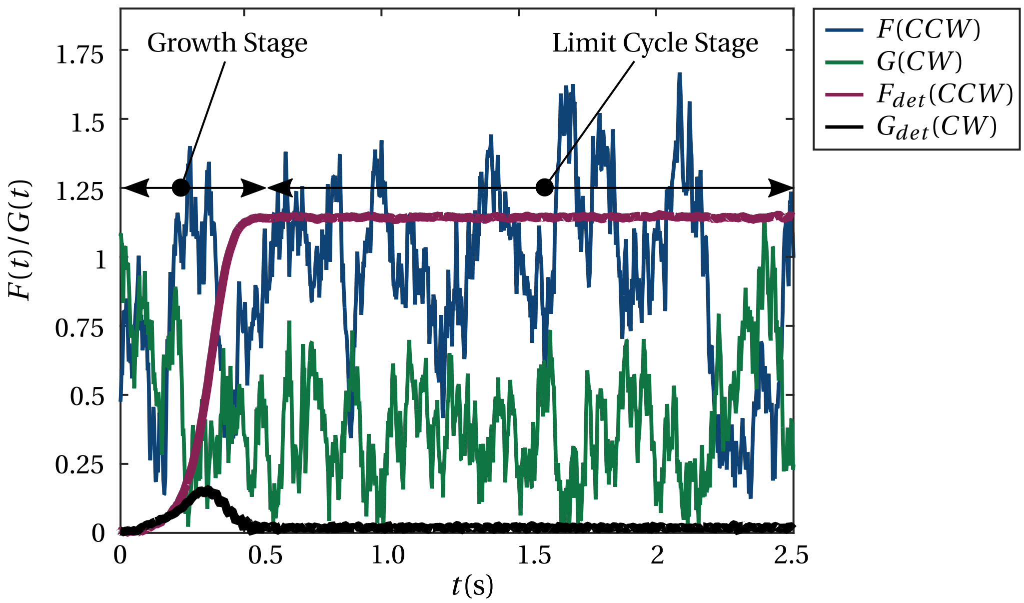

Figure 8.10: Simulated amplitude evolutions

Consequently, the real system dynamics – i.e. MIMO-ROM results that match the experimental benchmarks – can be explained as follows: The qualitative behavior of the deterministic performance is retained, which yields a limit cycle rotation of the higher growth rate mode ($T1_F$), while the lower growth rate mode ($T1_G$) vanishes. The presence of stochastic forcing on the one hand randomly modulates the limit cycle amplitudes of the rotating $T1_F$ mode, and on the other hand causes the $T1_G$ mode oscillations to be non-zero. Hence, the existence of the mixed-type dynamics originates at one rotating T1 mode, which spins in a thermoacoustically self-sustained manner. Conversely, the oppositely rotating mode $T1_G$ is purely stochastically driven. Superposition between the former and the latter constituent modes ultimately reproduces – and thereby explains – the physical process observed within the subjected experimental combustor. Furthermore, the cubic saturation formulation of heat release oscillations (cf. Eqn.8.21) can be validated to sufficiently describe the non-linear flame dynamics in the concerned combustor. This validation is retrieved due to the agreement between MIMO-ROM and measurement results, where the former implicitly depends on the transfer function's saturation term. It is important to point out that this non-linear function actually represents a fourth order Taylor series expansion (cf. next chapter and [112]), which implies an increased accuracy of the saturation mechanism the function seeks to reconstruct. Although universal applicability to all thermoacoustic problems is not possible, the positive results of this work along with the positive application in [109] establishes confidence in using the presented cubic saturation function to describe super-critical bifurcations of thermoacoustic modes, i.e. limit cycle resulting from linearly unstable stability state. If one seeks to capture sub-critical bifurcations, i.e. a triggered limit cycle associated with a linearly stable mode, a fifth-order series expansion to describe flame dynamics should be employed [107].

8.3 Summary and Findings – Numerical Analysis of Combustor Dynamics

This chapter presented the time domain analysis of HF, transversal thermoacoustic oscillations in swirl-stabilized gas turbine combustors. For this purpose, the previously introduced ROM approach, which presents a low-order state-space system that describes the given combustor thermoacoustic performance including non-compact flame dynamics was employed. These ROM relied on the LEE as mathematical basis, which ensured that non-degeneracy of transversal modes in mean flow environments is adequately captured within the time domain analysis. Specifically, two operation points (1x stable and 1x unstable) were utilized for the analyses for which the respective ROM setup was readily available from the previous chapter. The analysis was comprised of time-domain simulations by means of numerically integrating respective ROM, and yielded corresponding acoustic pressure time traces of both operation points. The numerically obtained traces were then compared to experimental counterpart traces for result interpretations.

For the stable case, the following dynamic features were identified:

- Dynamics of the transversal mode pair behaves as a damped linear coupled oscillator system driven by white noise (cf. next chapter for explicit details).
- Predominantly standing first transversal mode.
- Slow rotation of this standing mode in direction of the swirling mean velocity.
- Slow rotation due to loss of degeneracy of transversal mode pair.
- Slow rotation speed is associated to the CCW and CW modes' frequency difference, which is considerably smaller than the speed of sound.

The non-linear part of the flame transfer function produced limit cycle oscillation within the unstable case simulations. An acceptable agreement between the simulation and experimental results was achieved, which rendered the usage of a cubic saturation function to describe the non-linear heat release saturation suitable for swirl-stabilized premixed flames in cylindrical combustion chamber geometries. Also, a low-frequency modulation of limit-cycle oscillation – i.e. an amplitude beating – was experimentally revealed, numerically reproduced, and allocated to the non-degeneracy of the T1 mode pair. The following physical characteristics associated with the unstable case were retrieved:

- Dynamics of the transversal mode pair behaves as a non-linear coupled oscillator system driven by thermoacoustic effect and white noise (cf. next chapter for explicit details).
- Mixed-type mode dynamics, i.e. partly standing and rotating first transversal mode.
- Deterministic evolution of limit cycle only features one of the transversal mode pair; the other mode vanishes.
- Limit cycle mode with lower growth rate vanishes, while mode with larger growth rates dominates the limit cycle and hence the direction of rotation.
- Stochastic forcing effects randomly modulate the limit cycle mode.
- Stochastic forcing effects randomly excite the vanished mode.
- Superposition of these two (stochastically forced limit cycle and vanished mode) causes the observed mixed-mode dynamics.

Besides the generation of insight and understanding of HF oscillations, carrying out the analyses on the swirl-stabilized benchmark combustor demonstrate the ROM methodology's applicability to technically relevant system. It can be stated that the methodology can be confidentially used for time domain analyses of other combustor types that contain non-compact flame dynamics and HF modes.

For future work, modeling non-linear and stochastic dynamics of non-compact flames should be further explored, ideally using other combustor configurations. For this purpose, mathematically more advanced saturation functions (cf. [90, 112]) as well as spatially and temporally correlated noise sources could be used and assessed in terms of reproduction capability of experimental baseline to increase generality of the methodology.

9 Combustor Dynamics – Theoretical Analysis

This chapter presents the theoretical extension to the time series analyses conducted in the previous chapter. For this reasons, the limit-cycle dynamics constituted by a non-degenerate T1 mode pair in the swirl-stabilized benchmark combustor is modeled via a coupled, first order system of non-linear Stochastic Differential Equations (SDE). This system of SDE is sought to govern the amplitude-phase dynamics of the oscillations including the impact of linear, non-linear and stochastic effects of an unsteady and non-compact flame. The procedure to derive the SDE is based on spatial and temporal averaging operations as conceptually provided by [31, 112, 113]. Utilizing the amplitude-phase pair as solution variables (instead of the oscillatory variables) allows to employ analysis techniques from the field of non-linear dynamics to yield insight into the thermoacoustic dynamics from a theoretical perspective. Furthermore, the amplitude-phase description gives rise to derive respective solution expressions, which form the mathematical basis for the development of output-only system identification techniques in Chap. 10. The content of the present chapter is given by the following objectives:

- Derivation of a system of SDE that governs the amplitude-phase dynamics of non-degenerate transversal modes (Sec. 9.1)
- Execution of a fixed point analysis for comparison against experimental/numerical findings of the previous chapter and respective interpretation (Sec. 9.2).

9.1 Derivation of Stochastic Differential Equations

This section presents the derivation steps of the SDE, which govern the amplitude phase dynamics of transversal modes in the benchmark combustor. For this, the starting point is given by a wave equation form of the Linearized Euler Equations (cf. [31] for explicit derivation steps), i.e.

$$\frac{\partial^2 p'}{\partial t^2} - \bar{\rho}\bar{c}^2 \nabla \cdot \left(\frac{1}{\bar{\rho}} \nabla p' \right) + \mathcal{M}_{p'} = (\gamma - 1) \frac{\partial \dot{q}'}{\partial t}, \tag{9.1}$$

which is a partial differential equation governing the scalar field of spatio-temporal acoustic pressure oscillations $p' = p'(\mathbf{x}, t)$ that are thermoacoustically driven by the heat release source term $\dot{q}' = \dot{q}'(\mathbf{x_{fl}}, t)$. The spatial variable is a vector $\mathbf{x}$, which describes in this chapter cylindrical $\mathbf{x} = [x, r, \theta]^T$ coordinates while the subscript **fl** denotes that the function is only non-zero in the flame region and zero elsewhere. The reasons for using a wave equation formulation instead of LEE form is as follows. The wave equation is only one scalar differential equations, whereas the LEE consists of four coupled equations. The analytical techniques for the forthcoming derivations can only be employed to the scalar equations. In Eqn. 9.1, $\mathcal{M}_{p'}$ contains all coupling terms between mean and oscillatory flow quantities (cf. explicit formulations in [31]).

In order to include linear, non-linear and stochastic flame dynamics, the heat release source term is described by a power series as well as an additive noise term as in [90, 112]. As in these references, the heat release source term in Eqn. 9.1 formulated as

$$\dot{q}' = \sum_{\substack{m=0 \\ k=0}}^{M,K} a_{mk} p'^m \dot{p}'^k + \Gamma \Xi, \tag{9.2}$$

where $a_{mk}(\mathbf{x_{fl}})$ are spatially variable (across the flame volume $\mathbf{x_{fl}}$) series coefficient. The first expansion term for $m = k = 0$ is time-independent, and can be interpreted as the time-average of the heat release oscillations implying that $a_{00} = 0$. The time derivative pressure terms $\dot{p}'^k$ act on the phase/frequency of the acoustic modes [112] that are driven by the source term in Eqn. 9.2. These terms are not further considered in the forthcoming derivation of the SDE as reasoned in [112], and an explicit consideration is left for future work. The number of corresponding series expansions is set to zero, i.e. $K = 0$. Expanding the series to the fourth order yields

$$\dot{q}' = b_1 p' + b_2 p'^2 + b_3 p'^3 + b_4 p'^4 + \Gamma\Xi, \tag{9.3}$$

where the first order coefficient $b_1(\mathbf{x_{fl}})$ describes the distributed linear thermoacoustic coupling, while the coefficients $b_2(\mathbf{x_{fl}}) - b_4(\mathbf{x_{fl}})$ are allocated to describe non-linear saturation effects. Additive stochastic forcing is modeled – as for the MIMO-ROM simulations in Chap. 8 – by $\Gamma\Xi(\mathbf{x_{fl}}, t)$, which denotes distributed, spatially uncorrelated white noise signals that are emitted by the turbulent flame. Coefficients, acoustic pressure variables, and the stochastic forcing term in Eqn. 9.3 are most generally formulated via a spatial dependency across the flame volume, i.e. capable of accounting for the non-compact flame dynamics as required in this thesis.

The procedure to derive the SDE is presented in the following subsections. This first step is to transform the wave equation in Eqn. 9.1 into a second order coupled oscillator system using spatial averaging methods. From this second order system, the SDE is deduced by employing temporal averaging procedures.

9.1.1 Complex Coupled Stochastic Oscillator

The derivation of the coupled oscillator starts by rewriting the acoustic pressure oscillations by the superposition of the combustor's natural modes, i.e.

$$p' = \sum_{n=0}^{\infty} \frac{1}{2} \left(p'_{n,a} + p'^{*}_{n,a} \right), \tag{9.4}$$

where $p'_{n,a}$ denotes the spatial-temporal pressure oscillations of the eigenmode n, while p'^{*}_{n} is the complex conjugate counterpart. The addition of the complex conjugate of the mode ensures that the pressure signal is real valued, where the factor $\frac{1}{2}$ is required to conserve the amplitude of the oscillations, i.e. $p' = \mathrm{Real}(p'_{n,a})$. The (natural) eigenmodes are described by the Helmholtz equation, i.e.

$$\omega_{n,a}^2 p'_{n,a} = -\bar{\rho}\bar{c}^2 \nabla \cdot \left(\frac{1}{\bar{\rho}} \nabla p'_{n,a}\right), \tag{9.5}$$

$$\omega_{n,a}^2 p'^{*}_{n,a} = -\bar{\rho}\bar{c}^2 \nabla \cdot \left(\frac{1}{\bar{\rho}} \nabla p'^{*}_{n,a}\right), \tag{9.6}$$

where $\omega_{n,a}$ is the (real) oscillation frequency of the mode n.

Only the impact of acoustic damping due to mean flow effects is of interest, which allows to expand respective interaction terms in Eqn. 9.1 by an absorption model, i.e.

$$\mathcal{M}_{p'} = \sum_{n=0}^{\infty} 2\alpha_{n,a} \left(\frac{\partial p'_{n,a}}{\partial t} + \frac{\partial p'^{*}_{n,a}}{\partial t}\right), \tag{9.7}$$

where $\alpha_{n,a}$ is the pure acoustic damping rate for the particular mode. Moreover, the absorption description of Eqn. 9.7 precludes any occurrence of vortical disturbances in the acoustic velocity as are present for general LEE solutions. The acoustic velocity can then be deduced using the acoustic pressure formulation in Eqn. 9.4 along with the momentum equation (assuming zero mean flow $\bar{\mathbf{u}} = \mathbf{0}$) given by Eqn. 2.11. Now, the wave equation is transformed from a partial differential equation into an ordinary differential equation, which occurs by substituting Eqns. 9.3- 9.7 into Eqn. 9.1 to give

$$\begin{aligned} &\sum_{n=0}^{\infty} \ddot{p}'_{n,a} + \ddot{p}'^{*}_{n,a} + 2\alpha_{n,a}(\dot{p}'_{n,a} + \dot{p}'^{*}_{n,a}) + \omega_{n,a}^2(p'_{n,a} + p'^{*}_{n,a}) \\ &= \sum_{n=0}^{\infty} \dot{q}'(p'_{n,a}, p'^{*}_{n,a}, \dot{p}'_{n,a}, \dot{p}'^{*}_{n,a}), \end{aligned} \tag{9.8}$$

where the second and first time derivatives are respectively denoted by $(\ddot{\ })$ and $(\dot{\ })$ for simplicity.

The focus of this work concerns the thermoacoustic oscillations governed by the (non-degenerate) T1 modes in cylindrical combustion chambers. Hence, the pressure field is formulated using the two-fold Fourier series analogous as for the decomposition methodology for the identification of mode dynamics in Sec. 8.1. Consequently, the number of expansion terms in Eqn. 9.4 amounts to two, i.e. $n = 1,2$, which give for the individual pressure terms:

$$p_1 = p'_F = \eta_F(t)\Psi_F(\mathbf{x}) \tag{9.9}$$
$$p_1^* = p_F^* = \eta_F^*(t)\Psi_F^*(\mathbf{x}) \tag{9.10}$$
$$p_2 = p'_G = \eta_G(t)\Psi_G(\mathbf{x}) \tag{9.11}$$
$$p_2^* = p_G^* = \eta_G^*(t)\Psi_G^*(\mathbf{x}) \tag{9.12}$$

In these equations, $\eta_F(t)$ and $\eta_G(t)$ represent complex, time-dependent Fourier coefficients of the counter-clockwise (CCW) and clockwise (CW) rotating mode. The mode shape functions can be obtained solving a Helmholtz equation, which are however, not explicitly needed for the forthcoming derivations. Rather, the derivations are based on the orthonormality of the mode shape functions, which implies the following condition

$$\int_V \Psi_n \Psi_m^* dV = \begin{cases} 1 \rightarrow n = m, \\ 0 \rightarrow n \neq m, \end{cases} \tag{9.13}$$

where V is the combustor volume. In case one considers LEE modes for the shape functions it needs to be considered that these are not orthogonal due to the captured mean flow effects. However, these effects are weak so that the loss of orthogonality is weak and thus negligible, too. The complex eigenfrequencies associated with $\eta_F(t) \rightarrow (\omega_F - i\nu_F)$ and $\eta_G(t) \rightarrow (\omega_G - i\nu_G)$ are not restricted to be equal, which fully accounts for loss of degeneracy associated with the CCW and CW modes in the concerned benchmark combustor (cf. App. B). Specifically, the difference between the angular oscillation frequencies is small, which gives the condition:

$$\begin{aligned} &\Delta\omega = \omega_F - \omega_G \\ &\rightarrow \omega_{n,a} = (\omega_F + \omega_G)/2 \\ &\rightarrow \omega_{n,a} \gg \Delta\omega \end{aligned} \tag{9.14}$$

Moreover, the loss of degeneracy induces a deviation of the modes' damping rates, i.e.

$$\nu_F \neq \nu_G, \tag{9.15}$$

which difference is not restricted to be small as for the oscillation frequencies. Modeling the present modal dynamics of two non-degenerate counter-rotating modes cannot be captured by the state-of-the art approaches based on two standing modes as e.g. in [108, 113], and requires the approach introduced in this chapter. The desired oscillator system is derived by substituting Eqns. 9.9-9.12 into Eqn. 9.8 and a subsequent Galerkin projection. Specifically, this Galerkin projection is comprised of multiplying the equation with $\Psi_F^*(\mathbf{x}) = \Psi_G(\mathbf{x})$ and $\Psi_G^*(\mathbf{x}) = \Psi_F(\mathbf{x})$, followed by a volume integration, i.e. $\int_V$ (Eqn. 9.8)$\cdot\Psi_F/\Psi_G dV$. This gives

$$\ddot{\eta}_F + \ddot{\eta}_G^* + 2\alpha_F\dot{\eta}_F + 2\alpha_G\dot{\eta}_G^* + \omega_F^2\eta_F + \omega_G^2\eta_G^* = \dot{q}_1, \tag{9.16}$$

$$\ddot{\eta}_F^* + \ddot{\eta}_G + 2\alpha_F\dot{\eta}_F^* + 2\alpha_G\dot{\eta}_G + \omega_F^2\eta_F^* + \omega_G^2\eta_G = \dot{q}_2, \tag{9.17}$$

where the right-hand-side of the flame dynamics function unfolds to

$$\dot{q}_1 = 2\beta_F(\dot{\eta}_F + \dot{\eta}_G^*) - 3\kappa(\eta_F + \eta_G^*)^2(\dot{\eta}_F^* + \dot{\eta}_G) - 6\kappa(\eta_F + \eta_G^*)(\eta_F^* + \eta_G)(\dot{\eta}_F + \dot{\eta}_G^*) + \Gamma\xi, \tag{9.18}$$

$$\dot{q}_2 = 2\beta_G(\dot{\eta}_F^* + \dot{\eta}_G) - 3\kappa(\eta_F^* + \eta_G)^2(\dot{\eta}_F + \dot{\eta}_G^*) - 6\kappa(\eta_F^* + \eta_G)(\eta_F + \eta_G^*)(\dot{\eta}_F^* + \dot{\eta}_G) + \Gamma\xi. \tag{9.19}$$

Interestingly, the even coefficients of the generalized flame function in Eqn. 9.3 cancel out during the spatial averaging operations, and thus can be revealed as non-contributing to the flame's saturation dynamics. The space dependency of the series coefficients emerges as constant during the Galerkin projections. The first and third coefficient result in the linear driving rate and the non-linear saturation constant, i.e. $b_1(\mathbf{x}) \to 2\beta_{F/G}$ and $b_3(\mathbf{x}) \to -\kappa$, respectively. Notice that the cancellation of the even terms in the transfer function reproduces the presumed cubic saturation assumption made in Sec. 8.1 for the MIMO-ROM numerical simulations. Similarly, the noise term in Eqn. 9.3 is assumed to loose its space dependency during the Galerkin projection to converge into a delta-correlated white noise source $\Xi(\mathbf{x}, t) \to \xi(t)$ given by [112]

$$\langle\xi(t)\xi(t+\tau)\rangle = \lim_{T\to\infty}\frac{1}{T}\int_0^T \xi(t)\xi(t+\tau)dt = \frac{\Gamma_\xi}{2}\delta(\tau), \tag{9.20}$$

where $\frac{\Gamma_\xi}{2}$ denotes the intensity and τ represents the characteristic time scale of the noise process.

9.1.2 Deterministic Amplitude-Phase Equations

The desired SDE is obtained by transforming the second order oscillator system in Eqns. 9.16-9.17 into a first order system of differential equations. The respective operations are based on integral averaging methods as for the Galerkin projections above, which are of temporal instead of spatial nature. Specifically, a complex time averaging method as presented in [33, 99], which resembles an extension to the Krylov-Bogoliubov approach [85], is employed. This method crucially relies on a weak non-linearity assumption [51], which implies that the qualitative acoustic oscillations are given by the normal solution – i.e. $\dot{q}_1 = \dot{q}_2 = 0$, $\alpha_F = \alpha_G = 0$, $\Delta\omega = 0$ – of Eqns. 9.16 - 9.17. Hence, the shape of the temporal Fourier coefficients is given by

$$\eta_F(t) = F(t)\exp(i\omega t)\exp(i\phi_F(t)), \tag{9.21}$$

$$\eta_F^*(t) = F(t)\exp(-i\omega t)\exp(-i\phi_F(t)), \tag{9.22}$$

$$\eta_G(t) = G(t)\exp(i\omega t)\exp(i\phi_G(t)), \tag{9.23}$$

$$\eta_G^*(t) = G(t)\exp(-i\omega t)\exp(-i\phi_G(t)), \tag{9.24}$$

where the integration constants – i.e. amplitudes (F, G) and phases (ϕ_F, ϕ_G) of the respective mode – are presumed as time dependent with the constraint that the characteristic time scales vary much slower than the oscillatory time scale. Hence, these amplitude and phases are labeled slowly varying in time and can be assumed constant over one acoustic period. Substitution of Eqns. 9.21 - 9.24 into Eqns. 9.16 - 9.17, employing the complex averaging procedure over one period of oscillation $T = 2\pi/\omega$, while considering the condition given by Eqn. 9.14 produces the following first order system for the slowly varying amplitudes and phase dynamics:

$$\dot{F} = \nu_F F - 3\kappa\left(\frac{1}{2}F^3 + FG^2\right) + n_F, \tag{9.25}$$

$$\dot{G} = \nu_G G - 3\kappa\left(\frac{1}{2}G^3 + GF^2\right) + n_G, \tag{9.26}$$

$$\dot{\Phi} = 2\Delta\omega + n_\Phi. \tag{9.27}$$

In the last equation, $\Phi = \phi_F - \phi_G$, and n_F, n_G, n_Φ contain the white noise source terms, the treatment of which in terms of temporal averaging is shown in the next subsection. The quantities $\nu_F = \beta_F - \alpha_F$ and $\nu_G = \beta_G - \alpha_G$ denote the net growth rate between flame driving and acoustic damping of the respective mode, which are not restricted to be equal as in Eqn. 9.15. This inequality successfully represents the non-degenerate situation of transversal modes in swirling mean flow environments as found in the benchmark combustor of this thesis.

9.1.3 Stochastic Amplitude-Phase Equations

The stochastic averaging of the noise terms in Eqns. 9.25-9.27 are performed as outlined in [107, 128, 128, 156] which centrally rely on the whiteness assumption given in Eqn. 9.20. Finally, the system of SDE derives to

$$\dot{F} = \nu_F F - 3\kappa\left(\frac{1}{2}F^3 + FG^2\right) + \frac{\Gamma_\xi}{4\omega_{n,a}^2 F} + \chi_F, \tag{9.28}$$

$$\dot{G} = \nu_G G - 3\kappa\left(\frac{1}{2}G^3 + GF^2\right) + \frac{\Gamma_\xi}{4\omega_{n,a}^2 G} + \chi_G, \tag{9.29}$$

$$\dot{\Phi} = 2\Delta\omega + \left(\frac{1}{F} + \frac{1}{G}\right)\chi_\Phi, \tag{9.30}$$

where $\chi_F, \chi_G, \chi_\Phi$ are delta-correlated white noises of intensity $\Gamma_\xi/(2\omega_{n,a}^2)$. Equations 9.28-9.30 govern the joint process of stochastic and deterministic dynamics related to the amplitudes and phases of the second order oscillator equations in Eqns. 9.16 - 9.17. The following sections focus on the theoretical analysis of the deterministic behavior. The impact of stochastic forcing is only considered from a phenomenological perspective as per additively perturbing the deterministic results. Furthermore, Eqns. 9.28-9.30 represent the mathematical basis for the growth rate extraction methods developed in Chap. 10 below.

9.2 Fixed Point Analysis

The term fixed point (FP) analysis refers to a classical approach from the field of non-linear systems that allows to analytically identify the long-term behaviour of a dynamical system (cf. fundamentals in [160]). Such a FP analysis is applied to the SDE system in order to gain analytical insight into the thermoacoustic dynamics associated with the counter-rotating T1 modes. Specifically, the analysis is composed of three steps. First, the identification of the FPs, i.e. the long-time solution of the dynamical system, is conducted. Second, the physical feasibility of each FP is evaluated by inspecting the linear stability of the solution at the respective FP. Third, the analytical results of the previous two steps are graphically illustrated for further interpretations.

9.2.1 Determination of Fixed Points

In order to compute the FP of the SDE given by Eqns. 9.28-9.29, the derivatives are set to zero ($\dot{F} = \dot{G} = 0$). Stochastic forcing is neglected, i.e. $\Gamma_\xi = 0$, which implies that only the deterministic parts of the SDE is considered. Per convention, the term deterministic refers to the terms that originate from thermoacoustic interactions. The noise intensity term in Eqns. 9.28-9.29, i.e. $-\frac{\Gamma_\xi}{4\omega_{n,a}^2 F}$ and $\frac{\Gamma_\xi}{4\omega_{n,a}^2 G}$ – originate from stochastic noise effects, and are thus are not considered as deterministic in this thesis. The additive noise assumption simply leads to a stochastic perturbation of the FP solution. Physically feasible FP solutions are:

$$\text{FP \#1:} \bar{F} = \sqrt{2\nu_F/3\kappa}, \bar{G} = 0 \rightarrow \text{CCW-rot. mode} \tag{9.31}$$

$$\text{FP \#2:} \bar{F} = 0, \bar{G} = \sqrt{2\nu_G/3\kappa} \rightarrow \text{CW-rot. mode} \tag{9.32}$$

$$\text{FP \#3:} \bar{F} = \sqrt{(4\nu_G - 2\nu_F)/(9\kappa)}, \tag{9.33}$$

$$\bar{G} = \sqrt{(4\nu_F - 2\nu_G)/(9\kappa)} \rightarrow \text{Mixed Mode} \tag{9.34}$$

$$\text{FP \#4:} \bar{F} = 0, \bar{G} = 0 \rightarrow \text{Zero amplitude mode} \tag{9.35}$$

In the case of equal growth rates ($\nu_F = \nu_G$), Eqns. 10.5-9.35 reproduce the results of a similar analysis based on a standing mode approach carried out in [108] for azimuthal systems, where FP #3 converges to a standing mode solution.

9.2.2 Stability of Fixed Points

In order to assess the physical realizability of each solution, the linear stability of each FP is determined. Therefore, the deterministic part of 9.28-9.29 is linearized around each FP by respectively substituting:

$$F(t) = \bar{F} + F'(t) \rightarrow F' \ll \bar{F} \tag{9.36}$$

$$G(t) = \bar{G} + G'(t) \rightarrow G' \ll \bar{G} \tag{9.37}$$

The resulting linear system reads

$$\begin{bmatrix} \dot{F}' \\ \dot{G}' \end{bmatrix} = \mathbf{J} \begin{bmatrix} F' \\ G' \end{bmatrix} \tag{9.38}$$

where the so called Jacobian matrix **J** is given by

$$\mathbf{J} = \begin{bmatrix} \nu_F - 3\kappa(\bar{G}^2 + 3/2\bar{F}^2) & -3\kappa\bar{F}\bar{G} \\ -3\kappa\bar{F}\bar{G} & \nu_G - 3\kappa(\bar{F}^2 + 3/2\bar{G}^2) \end{bmatrix},$$

which yields the following eigenvalue pairs:

$$\text{FP \#1:} \lambda_1 = -2\nu_F, \lambda_2 = \nu_G - 2\nu_F \tag{9.39}$$

$$\text{FP \#2:} \lambda_1 = -2\nu_G, \lambda_2 = \nu_F - 2\nu_G \tag{9.40}$$

$$\text{FP \#3:} \lambda_1/\lambda_1 \rightarrow \text{Eqns. } E.1/E.2 \text{ in App. } E \tag{9.41}$$

$$\text{FP \#4:} \lambda_1 = \nu_G, \lambda_2 = \nu_F \tag{9.42}$$

These eigenvalue pairs indicate the stability of each FP. Physically, this stability informs about the dynamical behavior of the system – which is presumed to be steadily at rest at the fixed point of concern – upon a small perturbation. Beware that the term "stability" of the fixed points of the non-linear system in this chapter is unrelated to linear stability of thermoacoustic modes concerned in Chap. 6. Specifically, possible scenarios are revealed by writing the general solution of the amplitude perturbations of Eqns. 9.36-9.37, i.e.

$$F' \approx \exp(\lambda_1 t) + \exp(\lambda_2 t), \tag{9.43}$$

$$G' \approx \exp(\lambda_1 t) + \exp(\lambda_2 t). \tag{9.44}$$

These equations indicate that an amplitude perturbation exponentially returns to and departs from the underlying FP, if both eigenvalues are negative and at least one eigenvalue is positive, respectively. Consequently, the former scenario labels the FP as stable (attractor), while the latter case is called unstable. Unstable FPs are further distinguished between repellers and saddle points, which are characterized by both and only one eigenvalue being positive, respectively. Notice that there are more types of FP [160], which are however not relevant for the thermoacoustic systems considered in this thesis. Generally, stable FPs represent solutions that are physically possible to represent real combustor dynamics, whereas unstable FPs are rather unattainable. For the concerned system in this chapter, the physical realizabilites of the FPs unfold as:

- FP#1 → stable for: $\nu_F > 0$ & $\nu_G < 2\nu_F$ (attractor)
- FP#2 → stable for: $\nu_G > 0$ & $\nu_F < 2\nu_G$ (attractor)
- FP#3 → unstable for: $\nu_F > 0$ & $\nu_G > 0$ (saddle)
- FP#4 → unstable for: $\nu_F > 0$ & $\nu_G > 0$ (repeller)

For gas turbine combustors subjected in this work, the growth rates are within the range to render FP#1 and FP#2 stable attractors. An explicit consideration of unconstrained growth rate relations is left open for future work. Solutions of FP#4 (zero amplitude) and FP#3 (mixed mode) are physically impossible to exist, where the theoretically possible existence of the latter is ruled out due to the additive noise presence. Hence, the CCW and CW rotating modes remain the only two physically feasible solutions, which agrees with the findings of Chap. 8 as well as [17, 104]. For $\nu_F > \nu_G$, the limit-cycle is governed by a CCW rotating mode. This theoretical finding of of the rotation direction of the limit cycle mode agrees with the numerical outcomes in Chap. 8. Interestingly, the case of a thermoacoustically stable T1 mode, i.e. $\nu_F < 0$ & $\nu_G < 0$, is governed by the foregoing FP analysis, too. Then, the zero amplitude FP#4 becomes the stable attractor while the limit cycle solutions of FP#1/FP#2 change into unstable repellers. The foregoing results hold only true if the concerned combustors exhibits a rotationally symmetric mean flame shape and geometry as well as no externally mounted devises (e.g. dampers) that induce asymmetries into the system.

9.2.3 Graphical Illustration

In order to deepen the insight regarding which of the two stable FP prevail in the concerned thermoacoustic system, a phase portrait of the deterministic part of the SDE in Eqns. 9.28-9.29 is computed (cf. Fig. 9.1). This phase portrait represents the solution trajectories from several initial condition pairs to the associated (normalized with $\bar{F}$) steady state. Representative values for $\nu_F = 22\,\mathrm{rad/s}, \nu_G = 18\,\mathrm{rad/s}$ were selected.

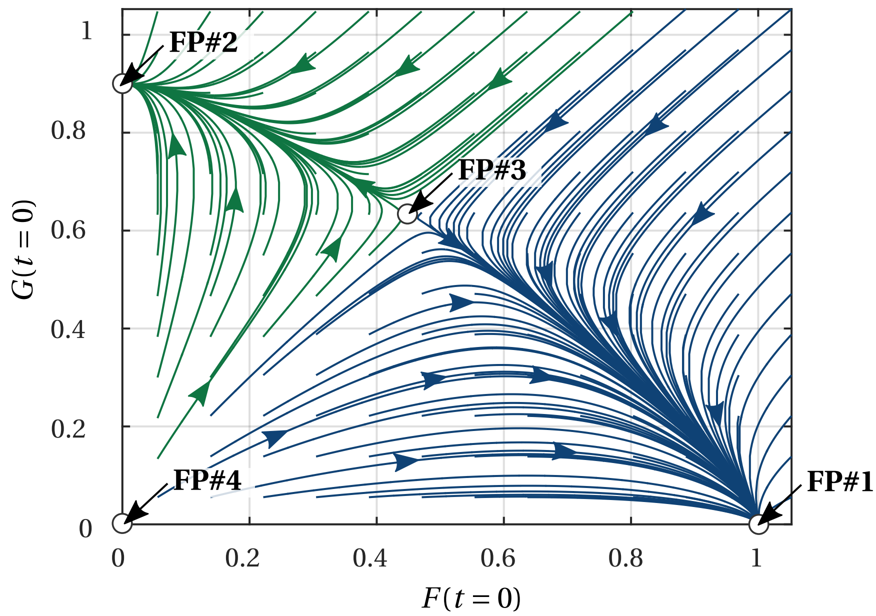

Figure 9.1: Phase portrait of deterministic system with basins of attraction (FP#1 = blue, FP#2 = green)

The phase portrait confirms the nature of the FPs as discussed in the previous subsection by effectively revealing the basins (blue for F, green for G) of the two rotating mode solutions. The location of the initial condition, that is whether it lies within the F or G basin, determines which rotation direction prevails. Assuming that the onset of an instability in real systems elapses from a linearly stable (regarding the thermoacoustic mode of concern) state (i.e. $F(t=0) = G(t=0) \approx 0$, cf. Fig. 9.1), the limit cycle dynamics will be governed by the rotating mode associated with the larger growth rate, which is in the present case the $\mathrm{T1}_F$ mode in CCW direction. For swirling mean flow environments, this mode – as is shown in Chap. 8 – always coincides with the swirl direction. Hence, the results of the FP analysis in this and the previous subsection theoretically confirm findings based on numerical MIMO-ROM simulations of Chap. 8. This finding is consolidated experimentally in [17], where the limit cycles of several operation points are revealed to be constituted by a rotating T1 modes in the same direction as the mean flow swirl.

Considering the impact of noise, the random perturbations could cause a jump (if the noise strength is sufficiently strong and/or the growth rate gap is sufficiently small) from one basin into the other. Such an event would imply a sudden change of rotation dynamics that is especially prone to occur in the initial phase of the limit cycle development. The corresponding solution then converges to the opposite solution as deterministically expected, although the occurrence has not yet been observed in any operation point of the swirl-stabilized experimental benchmark system [17]. The special case for equal growth rates exhibits equally sized basins of attraction for the CCW and CW rotating mode solution so that the likelihood of occurrence of each of the latter in a noise containing system is equal (cf. [143] for similar findings), respectively.

Note that the phase is not concerned in previous FP investigation as it is decoupled from the amplitude dynamics in Eqns. 9.28 - 9.30. The phase is only needed to reconstruct the non-degeneracy of the oscillatory dynamics by integrating Eqn. 9.30, i.e.

$$\begin{aligned} &\Phi = 2\Delta w t + \Phi_{ref}, \\ &\rightarrow \phi_F = \Delta w t + \phi_{F,ref}, \\ &\rightarrow \phi_G = -\Delta w t + \phi_{G,ref}, \end{aligned} \tag{9.45}$$

and respective substitutions into Eqns. 9.21-9.24 as well as Eqn. 9.4. The reference phase is typically set to zero $\Phi_{ref} = \phi_{F,ref} = \phi_{G,ref} = 0$. The impact of noise perturbs the phase solution in Eqn. 9.45 – analogously to the amplitude solutions – in a Gaussian manner. Notice that the phases are irrelevant to the FP solutions of the amplitude, and are not required to determine the direction of rotation as it is for the standing mode method in [108].

9.3 Summary and Findings – Theoretical Analysis of Combustor Dynamics

In the current chapter, HF limit cycle oscillations constituted by non-degenerate transversal modes in thermoacoustically non-compact swirl-stabilized combustors are theoretically analyzed. For this analysis, a non-linear system of Stochastic Differential Equations (SDE) that govern the amplitude-phase dynamics of the oscillations was derived. The derivation of this SDE started with the inhomogeneous wave equation and utilized complex spatial and temporal averaging operations similar to Galerkin projections in conjunction with the Krylov-Bogoliubov method. The spatio-temporal pressure oscillation were described by a superposition of two counter-rotating T1 modes. Oscillation frequencies and growth rates of these modes were set to deviate, which reflects – and hence incorporates – the physical features of non-degeneracy within the SDE. The deterministic-stochastic flame dynamics were mathematically described by a pressure dependent Taylor series formulation and additive white noise sources.

A fixed point analysis of the deterministic part of the SDE revealed the rotating mode limit cycle behavior as the only stable FP solution, where the rotation direction is linked to the mode with a larger growth rate. This finding agrees with the numerical and experimental observations of the swirl-stabilized benchmark combustor, and provides a respective theoretical explanation from a dynamical system perspective. Specifically, the core findings of the fixed point analysis are given by:

- Predictability of limit cycle modal rotation direction in swirl stabilized systems is possible by solely inspecting the linear growth rates.

- Applicability of cubic saturation description for non-linear flame dynamics within the considered benchmark combustor was revealed due to agreement between modeled and observed fixed point behaviors.

Furthermore, the system of SDE represents the mathematical basis for the development of system identification methodologies applicable to HF oscillations in the next chapter.

Future work associated with this chapter was identified as to extent the SDE derivations to account for modes with largely space frequencies, e.g. T1 and T2 modes. In alignment with the future work task identified for the ROM analyses in the previous chapter, the impact of multiplicative noise as well as consideration of more advanced series expansions to describe non-linear flame dynamics to increase the generality of the method pose topics for future investigations.

10 Growth Rate Identification from Time-Domain Data

This chapter presents the development and verification of an output-only system identification methodology that is applicable to non-compact thermoacoustic systems governed by transversal mode pairs. The concept of output-only system identification is fundamentally treated in [46, 47, 64, 86], and was recently introduced for low-frequency, compact thermoacoustic systems in [22, 23, 107, 112]. These references serve as starting point of the work presented in this chapter. Note that the term system identification is widely used in many different engineering disciplines, and generally refers to the task of obtaining a mathematical model from a certain set of observations/data (e.g. determination of flame transfer functions from LES numerical data [122]). The main goal of the output-only system identification methodologies in this thesis/foregoing mentioned references is to extract linear thermoacoustic growth rates $\nu_{n,a}$ of the mode of interest from time domain data. Knowledge of the growth rate is of high technical relevance as it assumes a crucial role e.g. within the following tasks:

1. Quantitative characterization of the stability of acoustics modes and the sensitivity to different operation parameter [109].
2. Design of damping devices [111].
3. Validation of computational prediction tools including flame driving and acoustic damping models [21].

The term "output-only" implies that the time domain data is retrieved from an autonomously operating system, where the system is naturally excited by turbulent combustion noise. The consideration of any external excitation device such as a siren is not required. Hence, the methods are in principle applicable to dynamic pressure measurements retrieved from industrial gas turbine combustors that are in operation.

This chapter is structured based on the following research objectives:

- Execution of verification test cases using numerically generated reference data to test the methodologies (Sec. 10.3).
- Demonstration of the methodologies' principal applicability to measured data by carrying out respective experimental test cases (Sec. 10.3).

Moreover, the methodologies are required to be applicable to linearly stable and unstable thermoacoustic oscillations that are governed by transversal modes in gas turbine chambers. Verification and experimental test case configuration is given by the swirl-stabilized benchmark system, where numerical and experimental acoustic pressure time traces are readily available from the previous chapters.

10.1 Purpose and Conceptual Approach

The main purpose of output-only system identification in the field of thermoacoustics is to extract linear growth rates from time domain data. Acoustic pressure time series are utilized, which are the most commonly available form of measurements from experimental and industrial combustors. The conceptual approach of the identification is depicted in Fig. 10.1.

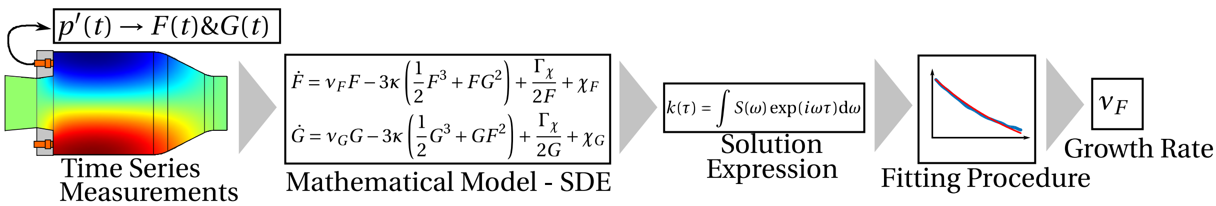

Figure 10.1: Conceptual approach of output-only system identification methodologies

First, a suitable model that describes the thermoacoustic system dynamics of the respective acoustic pressure time series via stochastic differential equations (SDE) needs to be established. For transversal modes, this model is given by the system of SDE derived in the previous chapter. These SDE govern the modal amplitude dynamics of the pressure oscillations. The non-degenerate nature of transversal mode pairs due to swirling mean flow effects (cf. App. B) are accounted for, which implies that unequal growth rates ν_F and ν_G are the target quantities of the identification efforts. In order to establish equivalence between model and data, the amplitude traces of oscillatory pressure signals need to be obtained by employing the decomposition techniques described in Sec. 8.1. Then, respective solution expressions of the SDE, which include the growth rates as model constants, are derived. Due to the presence of stochastic elements in the model, these solution expressions are given in the form of an auto-correlation function of the amplitude dynamics. Finally, the desired growth rates are extracted by fitting corresponding measurement data to these expressions. This fitting task represents one main component of the entire system identification work flow.

10.2 Theoretical Basis

In this section, the theoretical basis of the identification methodology is presented. Specifically, the approach "Linearized Limit Cycle (LLC)" is employed. The origin of this methodology can be found in [107], where details on theory and derivation steps for LF systems are provided. The SDE governing the amplitude dynamics as given by Eqns. 9.28-9.29 presents the starting point for the LLC method. These equations are recalled for clarity to

$$\dot{F} = \nu_F F - 3\kappa\left(\frac{1}{2}F^3 + FG^2\right) + \frac{\Gamma_\xi}{4\omega_{n,a}^2 F} + \chi_F, \tag{10.1}$$

$$\dot{G} = \nu_G G - 3\kappa\left(\frac{1}{2}G^3 + GF^2\right) + \frac{\Gamma_\xi}{4\omega_{n,a}^2 F} + \chi_G. \tag{10.2}$$

The assumption that stochastic perturbations of the deterministic amplitude due to combustion noise are small is imposed. Hence, the amplitudes can be described by a linear expansion, i.e.

$$F = \bar{F} + F'(t) \rightarrow F' \ll \bar{F} \tag{10.3}$$

$$G = \bar{G} + G'(t) \rightarrow G' \ll \bar{G} \tag{10.4}$$

where $\bar{F}/\bar{G}$ and F'/G' represent mean and perturbation amplitude of the CCW and CW running mode, respectively. The mean amplitudes are given by a fixed point analysis of the deterministic part of the SDE. As stated in Sec. 9.2, the noise intensity term is not viewed as a deterministic part of the SDE. Thus, the FP used for the forthcoming derivations are unaffected by the noise intensity term. As is shown in Sec. 9.2, rotating modes are the only two physically feasible, i.e. stable, fixed point (FP) solutions for the concerned benchmark combustor. Recalling Eqns. 10.5-10.6, these FP solutions unfold to

$$\text{FP \#1:} \quad \bar{F} = \sqrt{2\nu_F/3\kappa}, \bar{G} = 0 \rightarrow \text{CCW-rot. mode,} \tag{10.5}$$

$$\text{FP \#2:} \quad \bar{F} = 0, \bar{G} = \sqrt{2\nu_G/3\kappa} \rightarrow \text{CW-rot. mode.} \tag{10.6}$$

As found in the previous chapters, for practical swirl-stabilized combustion systems the direction of rotation (of the T1 modes) follows the direction of the swirling mean flow. For the benchmark system in this work, CCW rotation prevails, although the procedure is analogous, if a CW rotating mode constitutes the limit cycle. The SDE are linearized by substitution of Eqns. 10.3-10.4 into Eqns. 10.1-10.2. Additionally substituting Eqn. 10.6 into Eqns. 10.1-10.2 allows to obtain a linear first order equation for the CCW mode's amplitude perturbation, i.e.

$$\dot{F}' = \left(-2\nu_F + \frac{\Gamma_\xi}{4\omega_{n,a}^2 \bar{F}^2}\right) F' + \chi_F, \tag{10.7}$$

where the presumed low noise intensity leads to $\Gamma_\xi / 4\omega_{n,a}^2 \bar{F}^2 \ll 1 \rightarrow \Gamma_\xi \approx 0$. The CW mode's counterpart equation for G' results in a trivial expression due to the zero mean amplitude of the fixed point. Thus, the growth rate of the zero amplitude mode is not accessible for the LLC identification approach. The linearity allows to Fourier transform Eqn. 10.7 and formulate the power spectral density of the amplitude perturbation [48, 107], i.e.

$$S_{FF} = \frac{S_{\chi_F \chi_F}}{\omega^2 + 4\nu_F^2}, \tag{10.8}$$

where $S_{\chi_F \chi_F}$ is the power spectral density of the noise process associated χ_F, and ω is the independent variable angular frequency. The Wiener-Khinchin-theorem relates a time signal's power spectral density to the auto-correlation of the signal [48, 95], i.e.

$$k_{FF}(\tau) = \int_{-\infty}^{+\infty} S_{FF} \exp(i\omega\tau) \mathrm{d}\omega. \tag{10.9}$$

The integral can be solved analytically using the Residue-theorem [6,65,84,95] to yield the following auto-correlation function of the amplitude perturbation:

$$k_{FF}(\tau) = \exp(-2\nu_F \tau) \tag{10.10}$$

This equation is normalized such that $k_{FF}(0) = 1$, while τ is the time delay vector. The relation in Eqn. 10.10 is used to extract the growth rate of an unstable $\mathrm{T1}_F$ mode by fitting the right hand side against the auto-correlation obtained from time traces of the CCW mode's amplitude perturbation F'. The first order nature of the underlying differential equation yields exponential decay only. Utilizing standard least-square techniques for the fitting tasks suffices and are used for the test cases further below.

The previous explanations presume linearly unstable scenarios, i.e. $\nu_G > 0$ and $\nu_F > 0$, where the underlying modal oscillations are in a limit cycle state. In order to derive an expression for the identification of stable growth rates, i.e. $\nu_G < 0$ and $\nu_F < 0$, the non-linearity coefficient in the system of SDE is set to zero $\kappa = 0$. This is justified by the small levels of amplitudes in the stable case, where no non-linear saturation mechanisms are active. Thus, the term in the equations that models non-linear saturation of heat release oscillations is eliminated. In this case, the amplitude dynamics is solely governed by stochastic forcing as expected. The resulting equations read

$$\dot{F} = \nu_F F + \frac{\Gamma_\xi}{4\omega_{n,a}^2 F} + \chi_F, \tag{10.11}$$

$$\dot{G} = \nu_G G + \frac{\Gamma_\xi}{4\omega_{n,a}^2 G} + \chi_G. \tag{10.12}$$

Due to the elimination of the non-linear terms, the modal amplitudes of the CCW and CW mode are no longer coupled in Eqns. 10.11-10.12. Conversely to the unstable cases, both amplitudes – and thus growth rates – are accessible for the extraction procedures. The equations are linear due to the absence of non-linear flame dynamics in the stable case. For this reason, the decomposition of the amplitudes into the mean and time-dependent part as well as the noise strength are not restricted to the smallness assumption (cf. Eqns. 10.3-10.4). Substituting the amplitude decomposition of Eqns. 10.3-10.4 into Eqns. 10.1-10.2 gives

$$\dot{F}' = \nu_F \bar{F} + \frac{\Gamma_\xi}{4\omega_{n,a}^2 \bar{F}} + \nu_F F' - \frac{F'\Gamma_\xi}{4\omega_{n,a}^2 \bar{F}^2} + \chi_F, \tag{10.13}$$

$$\dot{G}' = \nu_G \bar{G} + \frac{\Gamma_\xi}{4\omega_{n,a}^2 \bar{G}} + \nu_G G' - \frac{G'\Gamma_\xi}{4\omega_{n,a}^2 \bar{G}^2} + \chi_G, \tag{10.14}$$

The first two terms that contain only mean quantities on the right hand side of each equation represent the steady state expression of the system including the impact of the noise strength Γ_ξ. Hence, respective expressions for the mean amplitude value of the stochastically forced oscillations are given by

$$\bar{F}_s = \left(-\frac{\Gamma_\xi}{4\omega_{n,a}^2 \nu_F} \right)^{1/2}, \tag{10.15}$$

$$\bar{G}_s = \left(-\frac{\Gamma_\xi}{4\omega_{n,a}^2 \nu_G} \right)^{1/2}, \tag{10.16}$$

which leads by insertion into Eqns. 10.13-10.14 to the following equations that govern the amplitude perturbations for linearly stable cases:

$$\dot{F}_s' = 2\nu_F F_s' + \chi_F \tag{10.17}$$

$$\dot{G}_s' = 2\nu_G G_s' + \chi_G \tag{10.18}$$

Interestingly, these equations are identical to the counterpart equation in Eqn. 10.7 for the unstable cases except the different sign of the growth rate term. A generalization of the stable and unstable regime can be carried out by identifying the absolute value of the growth rate $|\nu_{n,a}|$. This result aligns with the outcomes in [88, 107] for single oscillator models. Proceeding as outlined above, Eqns. 10.17-10.18 are transformed into the auto-correlation function

$$k_{FF} = \exp(2\nu_F \tau), \tag{10.19}$$

$$k_{GG} = \exp(2\nu_G \tau), \tag{10.20}$$

based on which the fits to extract the desired growth rates from measured data are performed. The auto-correlation of amplitude dynamics from linearly stable cases are exponentially decaying. Thus, according to Eqns. 10.19-10.20, the identified growth rates are – as expected – smaller than zero $\nu_F < 0$ and $\nu_G < 0$.

10.3 Verification and Validation Test Cases

The two operation points (1x stable and 1x unstable) already used for the ROM dynamical system analysis in Chap. 8 are used for verification and validation of the LLC identification methodology. The Fourier signals $\eta_F(t)$ and $\eta_G(t)$ associated with the CCW and CW mode given in Figs. 8.3 and 8.6 of both, the ROM and measurement data are re-shown for clarity in Figs. 10.2-10.3.

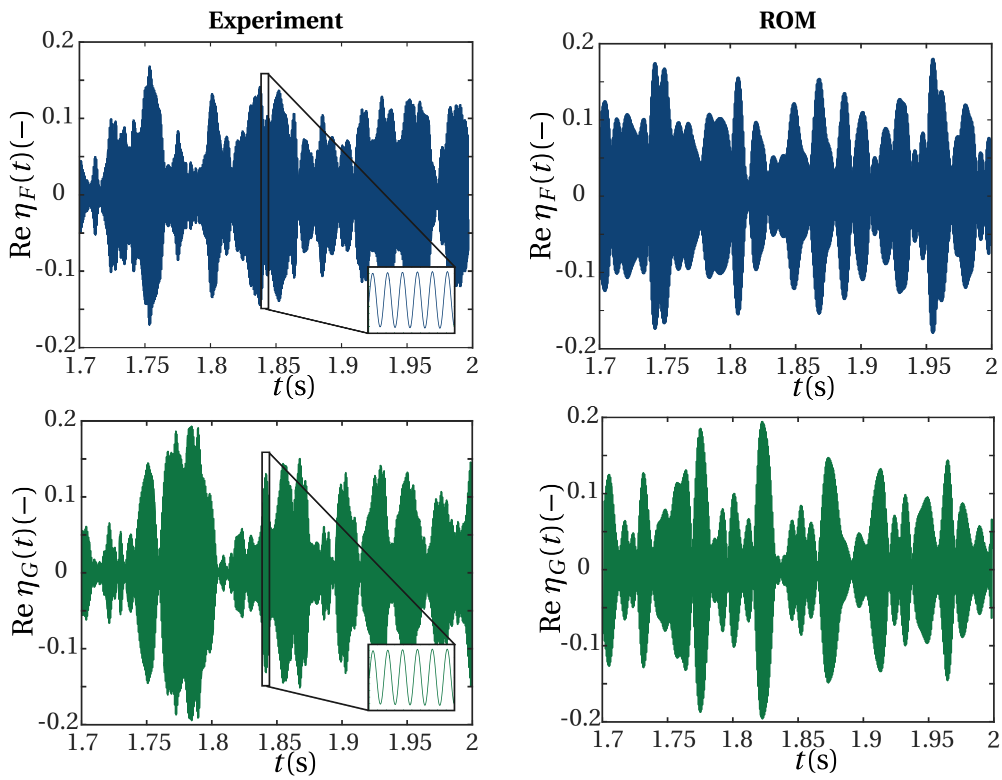

Figure 10.2: Stable operation point for LLC growth rate extraction: temporal oscillations of Fourier coefficients (left column: experimental results, right column: ROM results)

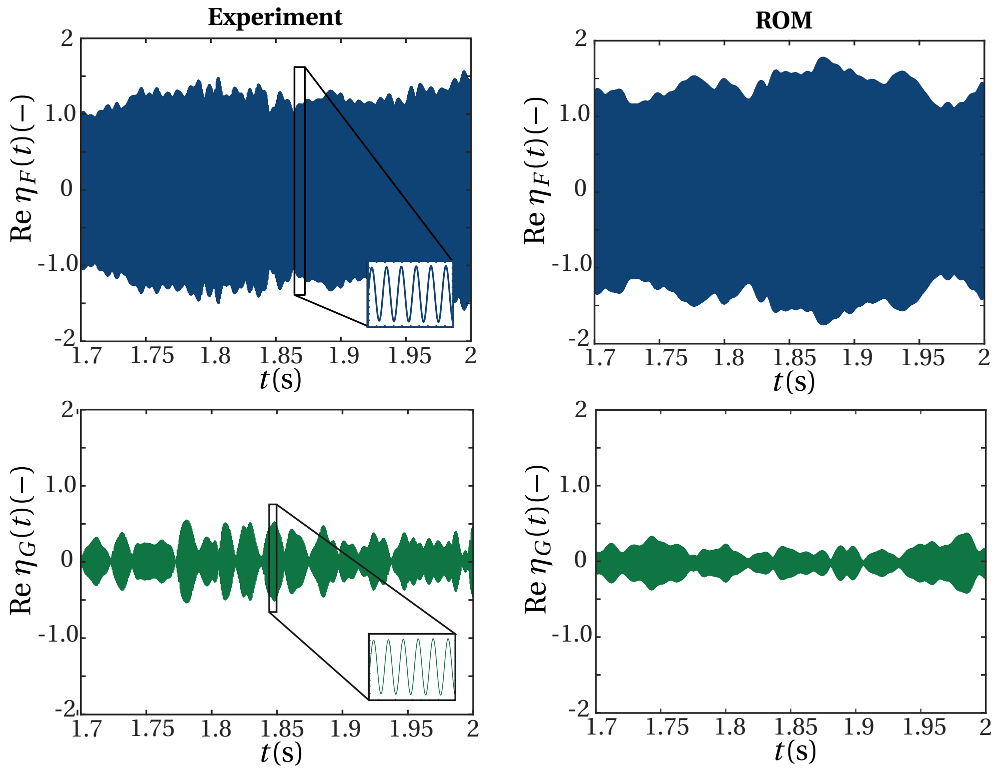

Figure 10.3: Unstable operation point for LLC growth rate extraction: temporal oscillations of Fourier coefficients (left column: experimental results, right column: ROM results)

Details on measurement techniques and originating references are presented in Chap. 3. The length of each time series is 5 s recorded at a time step of $\mathrm{d}t = 1.25 \times 10^{-5}$ s. The amplitude traces $F(t)$ and $G(t)$ of these signals are then obtained using the procedure explained in Sec. 8.1. There are ROM and experimental traces for one stable and one unstable operation point, i.e. in total four sets of amplitude traces $F(t)$ and $G(t)$. The LLC procedure requires the amplitude perturbation traces, which are obtained through Eqns. 10.3-10.4, i.e. $F'(t) = F(t) - \bar{F}$ and $G'(t) = G(t) - \bar{G}$. Then, the auto-correlation functions of these perturbation traces are computed and fitted to the expression given in Eqn. 10.10 and Eqns. 10.19-10.20 to yield the desired growth rates.

Results and performance assessments of the LLC methodology using the above-presented ROM and experimental amplitude traces as test data are discussed in the following subsections. The extracted growth rates are compared to known reference values. For the ROM cases, these reference growth rates are automatically given by the eigenvalues of the system matrix of the corresponding ROM (cf. ROM methodology and derivation in Chap. 7). For the experimental cases, there are no reliable reference growth rate values available at the moment. Thus, a quantitative comparison between growth rate values originating from the linear stability assessment and the LLC extraction is omitted for the experimental data. The reason for this omission is due to the inconsistency found for the linear stability methodology (cf. Sec. 6.2), which implies that respective results may not be correct. Thus, a comparison of the LLC results to potentially incorrect reference results is irrelevant and would be misleading. Nevertheless, the LLC results for the experimental data are assessed in an order of magnitude sense, i.e. rating whether the extracted growth rate values are realistic to yield a first indicator of the method's feasibility for application to measured data. Of course, a quantitative comparison between extracted and definite reference values is required for complete validation, which is left as a future work task.

10.3.1 Stable Case

First, the stable operation point is considered. The LLC fit results are presented in Figs. 10.4 and 10.5 for the ROM and experimental data, respectively. The blue lines represent the auto-correlation functions of the input data, i.e. amplitude perturbation traces $F'(t)$ and $G'(t)$ from the ROM data (Fig. 10.4) and experimental data (Fig. 10.5). The reconstructed functions, i.e. evaluation of the functional expression in Eqns. 10.19-10.20 that include the corresponding extracted growth rate value are plotted in green. The dashed and full lines indicate the respective allocation of the functions to the $\mathrm{T1}_F$ (CCW spinning) and $\mathrm{T1}_G$ (CW spinning) mode constituents. Visually inspecting the fit quality, i.e. assessing how well the reconstructed auto-correlation functions match the input counterparts, yields accurate results for the CCW and CW modes for both, the ROM and experimental case.

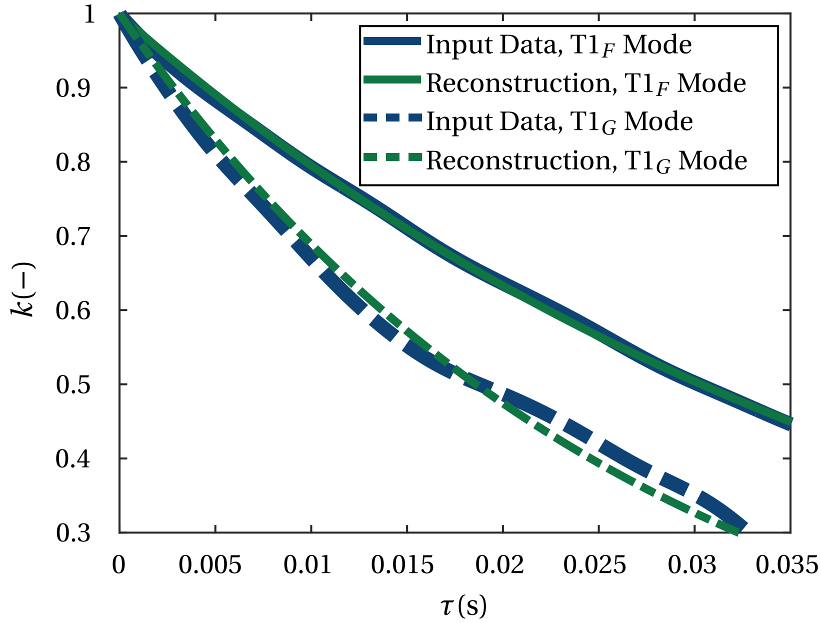

Figure 10.4: Auto-correlation fit results LLC methodology with ROM data – stable operation point

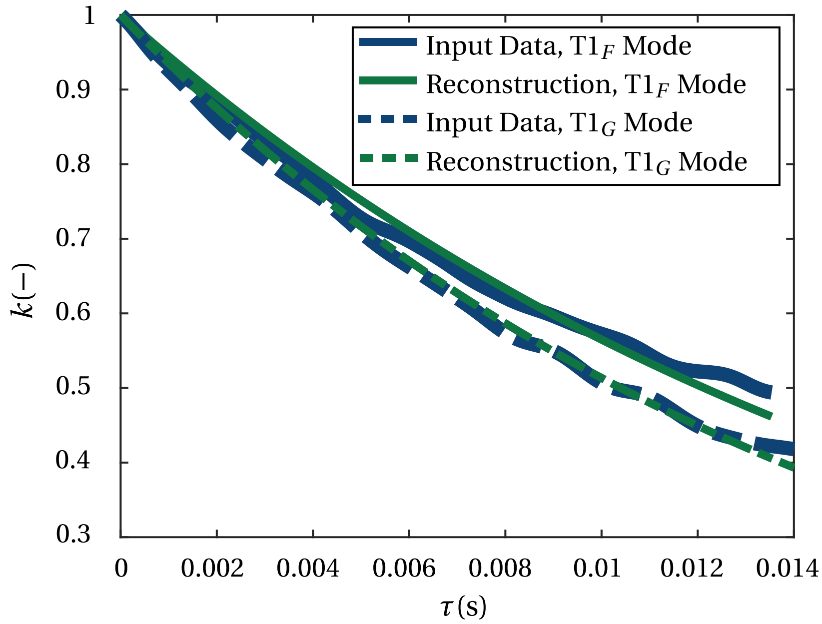

Figure 10.5: Auto-correlation fit results of LLC methodology with experimental data – stable operation point

Table 10.1 presents the extracted growth rates for the ROM and experimental data sets. Specifically, the first two lines provide the growth rates of the $T1_F$ and $T1_G$ mode of the ROM data, which are denoted by $\nu_{F,ROM}$ and $\nu_{G,ROM}$, respectively. As noted before, reference values of the extracted growth rates originating from the system matrices are available for the ROM case, and accurately agree with the extracted values. The extracted growth rates of the experimental data of both modes are given in the last two lines of the table, and are denoted by $\nu_{F,EXP}$ and $\nu_{G,EXP}$. Here, no reference values are available as explained above, while the order of magnitude can be viewed as realistic.

	LLC Extraction Result	Reference Value
$\nu_{F,ROM}$	−11.4 rad/s	−12.7 rad/s
$\nu_{G,ROM}$	−18.7 rad/s	−18.6 rad/s
$\nu_{F,EXP}$	−28.6 rad/s	n/a
$\nu_{G,EXP}$	−33.3 rad/s	n/a

Table 10.1: Growth rate results of LLC methodology – stable operation point

The performance of the LLC methodology for stable cases yields the following observation:

- Successful identification of the ROM reference growth rates.
- Non-degeneracy of the transversal mode pair, i.e. CCW and CW mode exhibit larger and smaller (stable) growth rates, is consistently reproduced from both, the ROM and experimental data traces.
- Same orders of magnitude are found for growth rates retrieved from experimental data as computed by the linear stability assessment in Chap. 6.

Both, the theory to compute growth rates (Chaps. 4-6) and the identification procedure (this chapter) present new developments. The closeness of results (in terms of order of magnitude) establishes confidence to a general correctness of the theory, implementations and employed procedures, although further refinement and validations remain as open tasks for future work.

10.3.2 Unstable Case

The auto-correlation plots of the ROM and experimental data for the unstable operation point is shown in Fig. 10.6 and Fig. 10.7, respectively. Recall that only the mode of the counter-rotating T1 mode pair that constitutes the limit cycle oscillations (in this work the CCW mode $T1_F$) is accessible for the LLC growth rate identification methodology. The blue lines in the two figures represent the auto-correlation of the input data, i.e. the perturbation amplitude trace $F'(t)$, whereas the reconstructed auto-correlation using the extracted growth rate values are plotted by the green lines. The extracted growth rate values are provided in Tab. 10.2. As for the stable results, a reference values are only available for the ROM case as above-discussed.

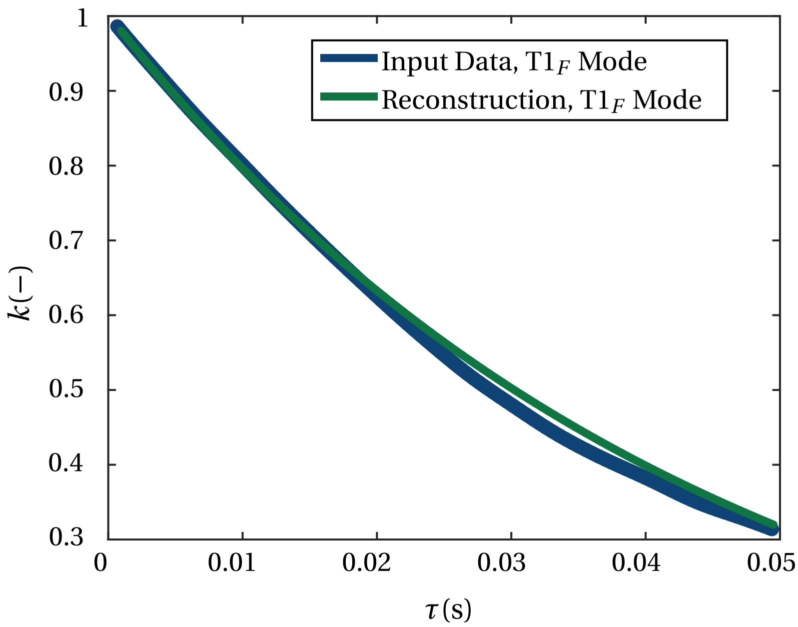

Figure 10.6: Auto-correlation fit results LLC methodology with ROM data – unstable operation point

The LLC applied to the unstable case yields the following observations:

- Underestimation of growth rates from the ROM data, although the fit itself appears as accurate.

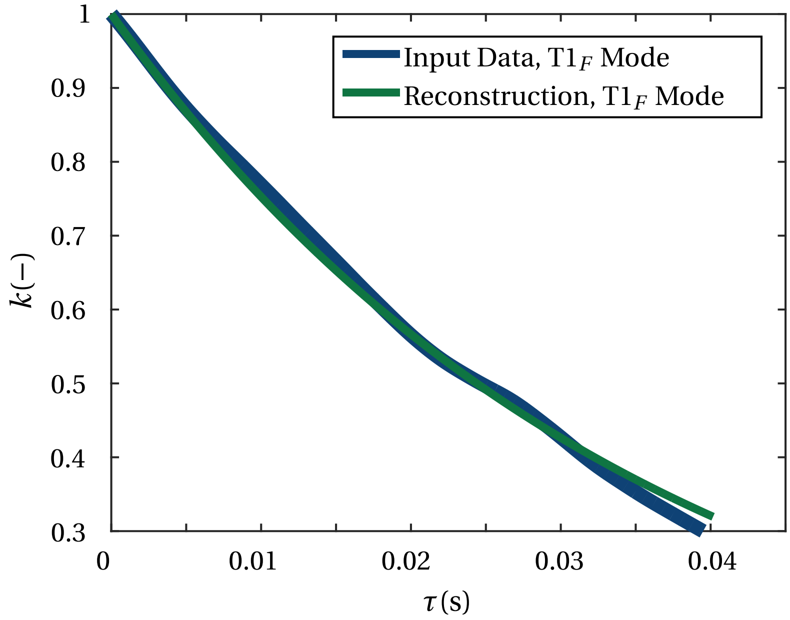

Figure 10.7: Auto-correlation fit results LLC methodology with experimental data – unstable operation point

	LLC Extraction Result	Reference Value
$\nu_{F,ROM}$	11.1 rad/s	16.6 rad/s
$\nu_{G,ROM}$	n/a	8.7 rad/s
$\nu_{F,EXP}$	14.2 rad/s	n/a
$\nu_{G,EXP}$	n/a	n/a

Table 10.2: Growth rate results LLC methodology – unstable operation point

- Accurate fit of the experimental amplitude data to the autocorrelation function, whereas a statement on correctness of the extracted growth rates cannot be made due to the unavailability of reference values as discussed above.

The results of the output-only system identification for the considered unstable cases are dissatisfactory. The reason for this failure is given by the stochastic perturbation strength of the limit cycle amplitude, which does not meet the smallness criteria required by the linearization of the SDE (cf. Eqns. 10.3-10.4). As can be seen in Fig. 8.10, this perturbation is clearly not "small" and is rather of the same order of magnitude as the mean level. In order to verify this explanation, the unstable operation point is re-simulated with a reduced noise strength to yield ROM time series that satisfy the linearization assumption. The respective amplitude traces are shown in Fig. 10.8. The identified growth rate results in $\nu_{F,ROM} = 18.7\,\mathrm{rad/s}$, which reproduces the reference value in Tab. 10.2 quite accurately. For the experimental data, the stochastic perturbation strength cannot be controlled so that a corresponding identification of the growth rate using the LLC is not possible for the given operation point.

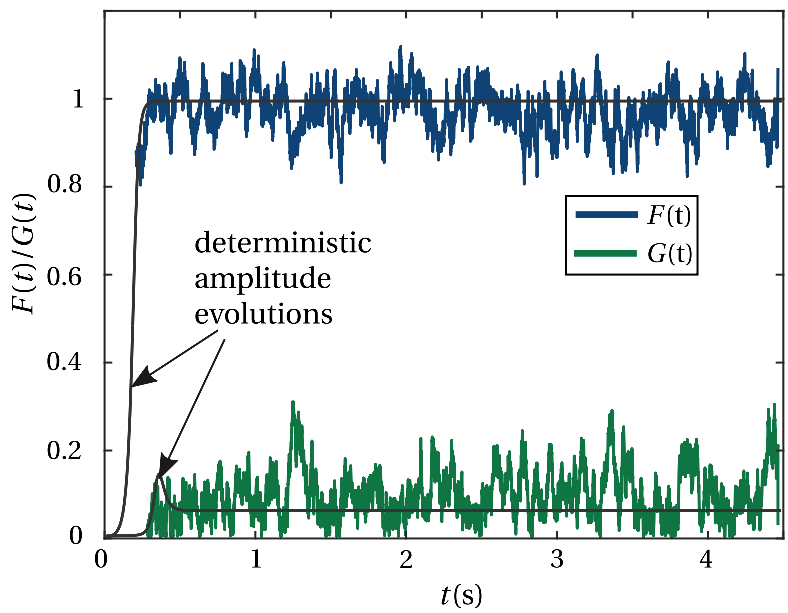

Figure 10.8: Amplitude time trace of ROM simulations with small noise perturbation strength

10.4 Summary and Findings – Growth Rate Identification from Time-Domain Data

The foregoing chapter concerned the development of an output-only system identification methodology to extract thermoacoustic growth rates of transversal modes from time domain data. Specifically, the methodology is comprised of linearizing the SDE – which were derived in the previous chapter – around the steady-state amplitudes. This imposed the constraint that the perturbation of limit cycle amplitude by stochastic noise is small for unstable cases. From this linearized SDE, a solution expression was derived against which measurement data were fitted to yield the desired growth rates. The methodology is applicable to both, linearly stable and unstable operation points. The methodology was tested by applications to synthetic time series generated by ROM simulations (for which target growth rates were known) and experimental data. The main results are as follows:

- Accurate identification of growth rates from stable operation point. Thus, the methodology was found suitable for application to stable operation points.
- The noise strength emerged as sensitive to the identification of growth rates from unstable operation points, i.e. it fails if the noise perturbation of the amplitude is too strong. Consequently, employing the method to unstable operation points requires awareness of the underlying assumptions.

For future work, the execution of test campaigns using different sets of ROM and experimental data with varying levels of growth rates and noise strengths should be considered with the goal to acquire more understanding of practical employment aspects of the LLC methodology in HF systems. In addition to varying the growth rate and noise strength values, the impact of sample size, step sizes and bandpass filter width of the acoustic pressure time series used to carry out the identification should be assessed, too. During the work for this thesis, these parameter emerged to have an impact on the extracted growth rate values, which is also known from LF activities in [107]. Besides the LLC methodology, there are further approaches from the field of LF oscillations, which allow an identification of unstable growth rates without any constraint to stochastic perturbation strength [23,64]. The idea of this approach is to numerically solve an adjoint Fokker-Planck equation that governs the amplitude dynamics and match the results to experimental data using an optimization routine. This allows to identify the growth rate rather independently of the noise intensity, sample sizes, filter width and time steps. A transferal from the 1D (longitudinal modes) [23] to 2D (transversal modes) oscillation was already carried out through the course of a semester thesis written by a Master's student [77], which was initiated and overseen by the author of this thesis. The explicit presentation of the material along with results is omitted here as to maintain a reasonable length of this thesis document. In the student thesis, the Fokker Planck approach for the 2D situation was numerically implemented and verifications test campaigns using synthetic ROM time traces as input data were conducted. First applications of the routine to experimental data from the swirl-stabilized combustor were executed, too. As findings for both – i.e. the ROM and experimental data – the capabilities for identifying the growth rate of two linearly unstable and non-degenerate transversal mode even for increased noise strengths was demonstrated. The computational effort of the numerical optimization routine was quite extensive. Thus, future work tasks are to improve the numerical routines for speed and efficiency (e.g. implementing the approach into a FEM environment such as COMSOL [2] that readily provides robust solver infrastructure. Furthermore, the adjoint Fokker Planck approach should the used to identify the growth rates of the unstable operation points of the linear stability assessment in Chap. 6, which are not accessible by the LLC due to a strong noise impact on the amplitude. These results can then be utilized for further physical interpretation of instability promoting features as well as for cross validation of underlying flame/damping models and system identification methodology itself.

11 Summary and Future Work

This thesis deals with high-frequency (HF) thermoacoustic oscillations in lean and premixed gas turbine combustors. Specifically, a model version of a can type combustor with one swirl-stabilized flame sitting downstream of an area jump in a tube geometry was used as the research benchmark. For such types of system, high-frequency thermoacoustics is characterized by:

- Non-compactness of thermoacoustic interactions, which is characterized by a Helmholtz number that reflects the same order of magnitude between the flame and a quarter of a wavelength.
- Frequencies larger than the cut-on frequency associated with transversal or radial modes of the combustor, which leads to multi-dimensional acoustic modes that constitute the oscillations.
- Dominance of flame driving due to local effects at the heat release zone.

Moreover, for the considered type of swirl-stabilized combustion systems, convective modulation mechanisms can be presumed as rather insignificant in the HF regime due to the zero value of the concerned T1 mode in the mixing tube section of the benchmark system as well as the low-pass characteristics of the encountered flames. The research tasks were of theoretical nature with the explicit focus on modeling and analysis of high-frequency and non-compact thermoacoustic oscillations in gas turbine combustors. Extensive experimental data were used for validation of the theoretical tasks, although the execution of experiments itself were not part of this work. Structure and specific content of the research tasks were generated based on three main research objectives:

- Development of a comprehensive framework for modeling, analysis and numerical computations of HF thermoacoustic phenomena.

- Validation of the framework and generation of theoretical understanding of HF thermoacoustic oscillations.

- Technical applicability of findings and methodologies to industrial gas turbine combustors.

All investigations, model developments, theoretical and numerical analyses were carried out using an experimental swirl-stabilized combustor as a benchmark system. This system can be viewed as a experimental version of a can-type chamber in industrial gas turbines, and exhibits self-sustained thermoacoustic oscillations at the first transversal mode. All criteria (non-compact flames, multidimensional modes, insignificance of convective modulation effects) to label the oscillations as "high-frequency" were satisfied. Moreover, extensive experimental baseline data were readily available to yield optimal conditions for validation of models and results.

Flame modulation comprised the first subject of investigations. Physical mechanisms that cause non-compact heat release rate oscillations (or flame driving) were theoretically assessed and mathematically modeled. Non-compact linear transfer functions for the two dominant driving mechanisms, i.e. heat release modulations due to local acoustic oscillation of fluid density and fluid particle displacement, were derived from first principles. Moreover, a 3D methodology in frequency domain to compute driving rates as a quantification measure for thermoacoustic energy generation of non-compact flames was established. Then, thermoacoustic driving rates for each mechanism (displacement and density) of the first transversal (T1) mode were computed for a set of operation points of the benchmark combustor. Respective result interpretations yielded the following findings that are valid for a T1 mode:

- Experimentally observed unstable operation points were associated with larger driving rates, and vice versa for stable operation points. A correlation between magnitude of driving strength and oscillation amplitude as well as flame's power density was detected.

- Density modulation of the heat release rates for swirl flames was found to be approximately three times stronger than displacement modulation.
- Density modulation distribution was found to exhibit positive driving zones throughout the flame volume. The displacement modulation counterpart reveals both, positive and negative driving zones. From an integral perspective, density modulation always generates acoustic energy while displacement – depending whether the positive or negative zones are larger – either generates or absorbed acoustic energy.
- Specific physical features that promote/inhibit thermoacoustic driving, and thus, the occurrence of an instability were identified. Higher and lower swirl of the mean flow increases and decreases the instability propensity at a given operation point, respectively. In accordance with the Rayleigh integral, flame shapes that are rather concentrated and located towards the centerline lead to less driving than flame shapes that are widespread and settle near the combustor walls.

Future work tasks regarding these driving assessments were identified as:

- Experimental determination of driving rates for validation against computed counterparts and underlying models.
- Investigation of a potential presence of further driving mechanisms.
- Execution of presented driving analysis using other flame and combustors types, e.g. self-ignition systems, to promote the generality of the developed methodology and models.

Damping of transversal modes due to acoustically induced vortex-shedding processes at the mean shear-layer was concerned next. The capabilities of the Linearized Euler Equations (LEE) to capture these processes were theoretically discussed. In order to resolve the vortex-shedding process accurately, the simplification based on the Bloch symmetry was implemented to transform the computational domain from a 3D to a 2D space, which enabled a substantial increase of mesh resolution capabilities. These LEE assessments yielded the following findings:

- Isentropic LEE accurately capture the process of acoustically induced vortex-shedding, although a fine mesh resolution is required.
- Solutions of LEE modes contain both, acoustic and vorticity disturbances.
- The LEE are incapable of capturing the dissipation of vorticity fluctuations. This dissipation is due to turbulent effects, which are not captured by the LEE. Thus, directly retrieving the acoustic damping rates from LEE eigensolutions is not straightforward. Using the LNSE instead of the LEE adds molecular and/or turbulent diffusion terms to the equation through which dissipation of vortical disturbance only cannot be captured, too.

Then, a modeling methodology to quantify only the damping effects on transversal acoustic modes was developed, verified and applied for analyses of the benchmark combustor. The principal idea of the methodology is to model the acoustic energy loss due to vortex-shedding by a momentum absorption term. The absorption strength at the frequency of interest is determined by using reflection coefficients computed via LEE simulations – which describe pure acoustic damping – as a reference. The main findings associated with the damping model are summarized to:

- Successful validation of the methodology using the isothermal configuration of the benchmark combustor as test case.
- Damping rates of the first transversal mode in the reactive configuration for a wide set of operation points were computed.
- Primary dependence of damping strength on the magnitude of the mean flow velocity at the shear-layer was revealed.

The damping investigations yielded the following suggestion for future work:

- Development of a decomposition methodology to separate LEE modes into explicit acoustic and vortical disturbance fields.

- Derivation of a LEE description that allows for direct solutions of acoustic and vortical modes along with corresponding damping rates.
- Investigation of the assumption that vortical damping for transversal modes is equal between isothermal and reactive conditions.
- Derivation of a simple model for computing the acoustic damping rate due to vortex-shedding that is based on mean flow quantities only and is non-mode specific as the presented reflection coefficient method. This method should works for any mode type, to be applicable to industrial combustors that contain multiple – potentially unstable – HF modes.

The combination of the driving and damping considerations led to the linear assessment of the benchmark system. Essentially, the superposition of computed driving and damping rates yielded the thermoacoustic growth rates. The sign of the growth rate indicated the linear stability state of the operation point of concern. Comparing the computed stability states with experimental observation yielded the following findings:

- Same order of magnitudes of computed growth rates were found as occurring in experiments, which indicate that no fundamental flaws exist in the methodology.
- Growth rates of stable operation points emerged as negative, i.e. confirming the experimental observations.
- Growth rates of unstable operation points computed as negative, too, which did not reflect the experimental observations.

The improvement of the system identification methodology regarding the inconsistency of the unstable operation points was assigned to research tasks for the future.

The development of a Reduced Order Modeling (ROM) methodology comprised the central component of the non-linear part of the modeling framework. This methodology produces Reduced Order Models of large-scale

LEE or Helmholtz Equation (HE) systems in state-space form, which allows for fast-pace simulations in time domain. Non-compact flame dynamics could be included by dividing the flame volume into a set of compact sub-regions. Forming a feedback loop for each sub-region using local transfer functions models the overall non-compact thermoacoustic system. Linear, non-linear and stochastic contributions of flame transfer functions can be included. The primary outcomes of the ROM development are given by:

- Theoretical basis of a Model Order Reduction technique to derive ROM of large-scale, 3D LEE/HE for analysis of non-compact thermoacoustic system was established.
- Experimental validation of the ROM's capabilities to describe acoustic behavior of a "gas turbine-like" configuration was achieved using an orifice-tube as test case. The order of the ROM was substantially lower than the large-scale reference system, which was accompanied with an increase of computational efficiency as desired.
- Procedural guidelines to derive and verify a ROM including the non-compact flame modeling feature were generated.

For future work, the capability of including damping devices by means of incorporating respective transfer functions within the ROM framework should be validated. Thereby, the area of applicability of the ROM – e.g. for analysis of different combustor configurations as well as operational scenarios – would be expanded.

The ROM methodology was employed for thermoacoustic time-domain analysis of the swirl-stabilized benchmark combustor. Specifically, the non-compact thermoacoustic dynamics of the first transversal mode for two operation points (1x stable and 1x unstable) were numerically reconstructed, compared against experimental data and respectively interpreted. The following core findings emerged:

- Accurate reproduction of limit cycle and stable mode dynamics including stochastic effects due to turbulent combustion noise. Thus, the suitability of the ROM framework for modeling non-compact thermo-acoustic systems in time-domain was demonstrated.

- Identification of physical features, i.e. limit cycle oscillations of non-degenerate transversal modes that are constituted by the rotating mode that exhibits the larger frequency and growth rate. Thus, the modal rotation direction is in the same direction as the swirling mean flow.
- Stable cases are characterized by standing modes that slowly rotate in direction of the mean flow. The phase speed of this rotation is given by the frequency difference of the two counter-rotating, non-degenerate transversal modes, and is thus, much smaller than the speed of sound. These dynamics are a consequence of the superposition of the two counter-rotating modes that are individually excited by broadband combustion noise.

The non-linear behavior of the flame leading to saturation of driving and accompanied limit cycle dynamics was modeled using a cubic saturation term. Thus, the utilization of more complex model for the non-linear as well as stochastic dynamics of the flame should be considered to increase the generality (e.g. for further flame/combustor types) of the model within future work tasks.

The limit cycle oscillations of two counter-rotating (non-degenerate) transversal modes were analyzed using theoretical approaches from the field of non-linear dynamics. A system of non-linear Stochastic Differential Equation (SDE) that governs the amplitude-phase dynamics of the oscillations was derived using a Krylov-Bogoliubov approach. The SDE included the effects of linear flame driving, non-linear saturation and stochastic forcing due to broadband combustion noise. Executing a fixed point analysis on the deterministic part of the SDE yielded the following findings:

- The only non-linearly stable – and thus physically feasible – solution emerged as rotating modes that spin in the same direction as the mean swirl flow. This finding presents a theoretical confirmation of the numerical results from the ROM analysis chapter.

- The role of combustion noise is of additive nature only, i.e. induces stochastic perturbation of the amplitude-phase dynamics. Theoretically, these perturbation can cause a change of rotation direction of the limit-cycle mode, which is yet to be observed in experiments.

Future work emerging from the theoretical analysis task are formulated as:

- Derivation of an analogous system of SDE without the simplification of small space frequencies, i.e. targeting widely spaced modes.
- Inclusion of more complex saturation and stochastic models for the flame dynamics function.

The system of SDE provided the basis for the development of an output-only system identification methodology to extract linear growth rates from time domain data. The basic idea of such a methodology is to formulate a solution expression of the SDE, which contains the growth rate as an unknown parameter. This expression is then fitted against experimental data to yield the desired growth rate. Specifically, the approach called "Linearized Limit Cycle" was employed. This method linearizes the SDE around the fixed points from which an auto-correlation expression of the amplitude perturbation as the fitting function is derived. The methodology was tested using synthetic ROM data (for which underlying growth rates are known) and measurements of a stable and unstable operation point. This verification test case emerged the following results:

- Applicability to stable cases was found to work correctly.
- Application to the unstable case failed for the ROM and experimental data. The reason was found in the noise level, which lead to a perturbation of the amplitude that violates the "smallness" assumption.
- Re-execution of the unstable case using ROM data with considerable less noise strength yielded successful extractions of the growth rate.

These findings generated the following future work tasks:

- Execution of verification test campaigns using ROM data with different level of growth rates and noise strengths. Moreover, the impact of total sample time and step size along with bandpass filtering width should be assessed, too.
- Continuance of more advanced identification routines that are not constrained by an assumption of low noise intensity. These routines are based in solving a numerical optimization problem using the adjoint Fokker Planck equation, and were already implemented and tested in the course of this thesis work.
- Identification of growth rates of the operation points concerned for the stability analysis of the benchmark combustor. The extracted growth rates should then be compared to the (improved) analyses results for cross validation of underlying models and system identification methods.

The development of the output-only system identification methodology presented the last component of the modeling and analysis framework for HF oscillations, and concluded this thesis.

A Assessment of Frequency Dependence of Convective Driving Mechanisms

The impact of convective modulation effects for increasing frequencies is shown with the help of the generic combustor schematic shown in Fig. 1.1 presented in Chap. 1. For simplicity, planar traveling acoustic waves propagating from the burner inlet to the chamber outlet are concerned. Possible reflections at area and temperature jumps are neglected. The acoustic pressure and velocity of a traveling wave are related through the momentum equation, which gives

$$\hat{p} = \bar{\rho} c \hat{u}, \tag{A.1}$$

where $\bar{\rho}$ and c is the fluid density and speed of sound, respectively. It is assumed that the wave modulates the equivalence ratio at the injector as explained in Sec. 1.2. The resulting heat release oscillations are given by [121, 138]

$$\frac{\hat{q}_\phi}{\bar{q}} = F_\phi \frac{\hat{\phi}}{\bar{\phi}} \exp(-\frac{\omega^2 \sigma^2}{2}), \tag{A.2}$$

where $\hat{\phi}$, $\bar{\phi}$ and $\bar{q}$ are mean equivalence ratio, fluctuating equivalence ratio and mean heat release rate, respectively. The function F_ϕ relates the conversion of equivalence ratio into heat release fluctuations. It contains information regarding the transport of equivalent ratio fluctuation via a time delay description from the injector to the flame. The quantity σ denotes the standard deviation of the time delays accounting for a spatial extent of the flame shape and a corresponding distribution of delay times [121, 138]. The equivalence ratio fluctuations are caused by air velocity oscillations at the injector, which gives

$$\frac{\hat{q}_\phi}{\bar{q}} = F_u \frac{\hat{u}}{\bar{u}} \exp(-\frac{\omega^2 \sigma^2}{2}), \tag{A.3}$$

where F_u is the flame transfer function that describes the conversion of velocity oscillations at the injector into heat release oscillations at the flame. At the same time, mass flux fluctuation at the flame front, which correspond to the dominant flame modulation mechanism "flame deformation " of the T1 mode (cf. Chap. 4) induce oscillations of the heat release rate, too. The respective flame transfer function reads

$$\frac{\hat{q}_\rho}{\bar{q}} = \frac{\hat{p}}{\gamma \bar{p}}, \tag{A.4}$$

where γ is the ratio of specific heats and $\bar{p}$ is the mean pressure. Substituting the acoustic pressure into Eqn. A.4 by Eqn. A.1 yields a dependency on the mean Mach number Ma, i.e.

$$\frac{\hat{q}_\rho}{\bar{q}} = \frac{\hat{u}}{\bar{u}} Ma, \tag{A.5}$$

which induces the velocity ratio $\frac{\hat{u}}{\bar{u}}$ as independent variable into the expression. The purpose of this velocity ratio is to establish comparability to the equivalence ratio expression in Eqn. A.3. In order to assess the relative significance between both modulation types, the transfer functions need to be manipulated to allow an order of magnitude comparison. This is achieved by dividing both expressions in Eqns. A.3 and A.5 by the velocity ratio $\frac{\hat{u}}{\bar{u}}$ to eliminate the acoustic dependency. The comparison functions read:

$$C_\phi = \frac{\hat{q}_\phi \bar{u}}{\bar{q} \hat{u}} = F_u \exp(-\frac{\omega^2 \sigma^2}{2}) \tag{A.6}$$

$$C_\rho = \frac{\hat{q}_\rho \bar{u}}{\bar{q} \hat{u}} = Ma \tag{A.7}$$

The convective comparison function C_ϕ presents a low-pass filter [138] while the deformation function C_ρ is frequency independent and constant. Equations A.6 and A.7 directly show that for increasing frequency, convective modulation effects become irrelevant, which explains the increasing dominance of local flame driving mechanisms for increasing frequencies.

Now the question is how to decide at which frequency levels convective modulation becomes insignificant. The answer is given by the low-pass element in Eqn. A.6, i.e. $\exp(-\frac{\omega^2\sigma^2}{2})$, and specifically by the standard deviation of the time delays σ. The quantitative value depends on the convective transport velocity in the mixing/injector parts upstream of the flame, the length of these mixing/injector tubes and the flame length scales – all of which are individual to the concerned combustor configuration. Hence, it cannot be universally stated that convective effects are insignificant for HF oscillations. This is demonstrated by comparing the low-pass behaviour of two different systems, i.e. a swirl-stabilized system with one main burner tube (resembling the A^{2}EV benchmark used in this thesis) and a generic tubular chamber with circumferentially arranged injector tubes instead of one main burner. Simplified schematics of both system along with the key quantities to compute the σ-values are presented in Fig. A.1.

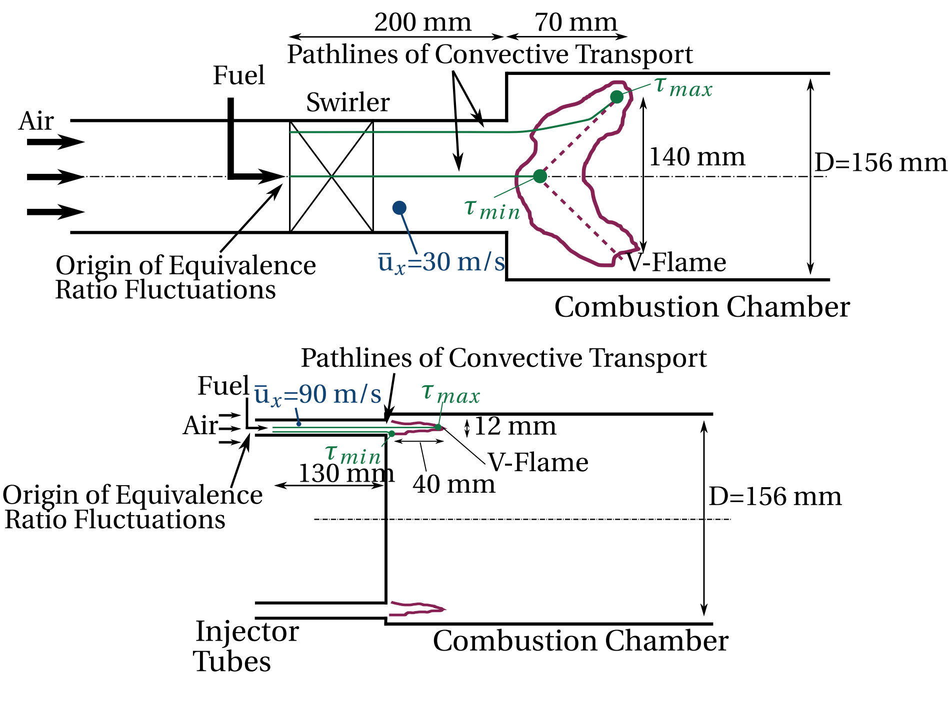

Figure A.1: Schematic of swirl-stabilized system (top) and injector tube configuration (bottom) with key quantities for assessment of low-pass behaviour

The standard deviation of the time delays is approximated by $\sigma = \tau_{max} - \tau_{min}$. Theses maximum and minimum time delays are computed by $\tau_{max} = l_{max}/\bar{u}_{max}$ and $\tau_{min} = l_{min}/\bar{u}_{min}$, where the l_{min} and l_{max} denote the lengths of convective traveling paths as indicated in Fig. A.1. The transport velocity is assumed as constant, i.e. $\bar{u}_{max} = \bar{u}_{min}$. Evaluating the standard deviations using the velocity and length values shown in the figure gives for the swirl-stabilized system $\sigma_{SW} = 2.67\,\mathrm{ms}$ and the injector tube system $\sigma_{IT} = 0.4444\,\mathrm{ms}$. Next, the low-pass behaviour is plotted over the frequency and shown in Fig. A.2. For the swirl-stabilized system, convective modulation effects can be disregarded for frequencies larger than 250 Hz. Transferring these results to the to the A^{2}EV – where the the T1 frequencies are around 2000 Hz – 3000 Hz – indicates that the concerned frequency range is certainly outside of the non-zero low-pass region. The only driving effects that remain active are due to local interaction, i.e. deformation and displacement. The low-pass behaviour of the flame in the injector tube configuration starts at higher frequencies, i.e. around 1200 Hz, than for the swirl-stabilized setup. Hence, convective mechanisms are active for higher frequencies. Thus, answering question whether or not convective effects are relevant for HF oscillations requires an individual assessment of the combustor configuration of interest.

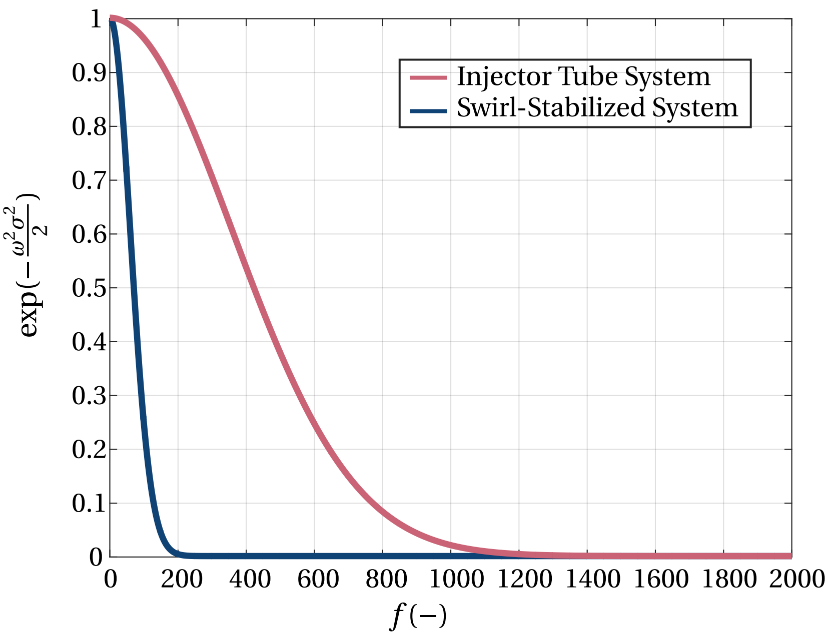

Figure A.2: Low-pass behaviour of the flames in the swirl-stabilized and injector tube configurations

B Effects of a Swirling Mean Flow on Transversal Modes

Chapters 4-6 in the the main document of this dissertation addressed linear flame driving, vortical damping and linear stability assessments of transversal oscillations in gas turbine combustors, all contained one central assumption: The split of eigenfrequencies, i.e. loss of degeneracy [10, 21], associated with transversal mode pairs in swirling mean flow environments was neglected. This negligence is justified by the smallness of this split and the implication that results, interpretations and findings of the respective chapters are not impacted. However, this non-degeneracy of the transversal mode pairs turned out as a crucial feature that affects limit cycle oscillations concerned in Chaps. 7-9.

In this appendix, the physical origin of the loss of degeneracy in transversal systems is investigated, which is found in the linear regime. The results contribute towards increasing the theoretical understanding of HF thermoacoustics as well as consolidates the linear analysis framework's capability to capture all relevant physics correctly. Particularly, the specific objectives of this appendix seek to

- Investigate interactions between transversal modes and swirling mean flows.
- Demonstrate the non-compact linear analysis framework's capabilities for reproduction of real system features.
- Generate theoretical understanding of transversal modes in swirling mean flows, and

B.1 Isothermal Test Case

The isothermal nozzle configuration as used for the damping modeling approach presented in Chap. 3 is used as investigation benchmark. Due to the absence of combustion/thermoacoustics, this configuration yields ideal conditions to investigate interactions between swirling mean flow and transversal modes that cause the loss of degeneracy. The experimental setup is equipped with two adjacent compression drivers mounted to the nozzle tube, which are used to excite transversal system modes at discrete frequencies (cf. Chap. 3 for details and references on setup, operational aspects and measurements). The same operation point ($\bar{\dot{m}} = 0.12\,\mathrm{kg/s}, \bar{T}_{in} = 293.15\,\mathrm{K}, \bar{p} = p_{atm}$) as for the validation of the damping modeling approach in Sec. 5.4 is used. All relevant mean flow effects that induce the loss of degeneracy of transversal modes are implicitly captured by the LEE in frequency domain, which are given by Eqns. 2.18 -2.19. Hence, LEE eigenmodes of T1 modes are computed to assess the observed non-degeneracy. In order to produce the numerical solution, the same setup (fine mesh configuration in Fig. 5.8, Bloch symmetry, boundary conditions, mean flow field) as used for the LEE simulations in Sec. 5.4. The damping rates were obtained through the quantification methodology presented in Chap 5, where the reflection coefficient was matched at the respective CCW and CW frequencies.

B.2 Loss of Degeneracy of Transversal Modes

The loss of degeneracy is characterized by the occurrence of two distinct peaks around a first transversal mode in the Fourier spectrum. For the concerned isothermal nozzle configuration, these two peaks are revealed in the pressure spectrum shown in Fig. B.1. The underlying time series to compute this spectrum were obtained as follows: First, acoustic pressure time traces are recorded at the faceplate for a set of excitation frequencies. External excitation of the system occurs via compression drivers (cf. Fig. 3.3), where the respective excitation signals are 180-degree phase shifted in order to predominantly excite first transversal mode shapes. Second, the time signals for each excitation frequency are added, which is in accordance with Fourier's theory [84]. Third, this total time series is Fourier transformed to yield the amplitude spectrum given in Fig. B.1. Note that the peaks the amplitude spectrum belong to the T1L1 mode (cf. Fig. 5.9) of the chamber, which is also the mode of concern for the subsequent discussion. The reasons for using the T1L1 instead of the T1 mode is that the experimental response of the isothermal system to the external excitation was stronger than for the T1 mode, which yielded clearer experimental results.

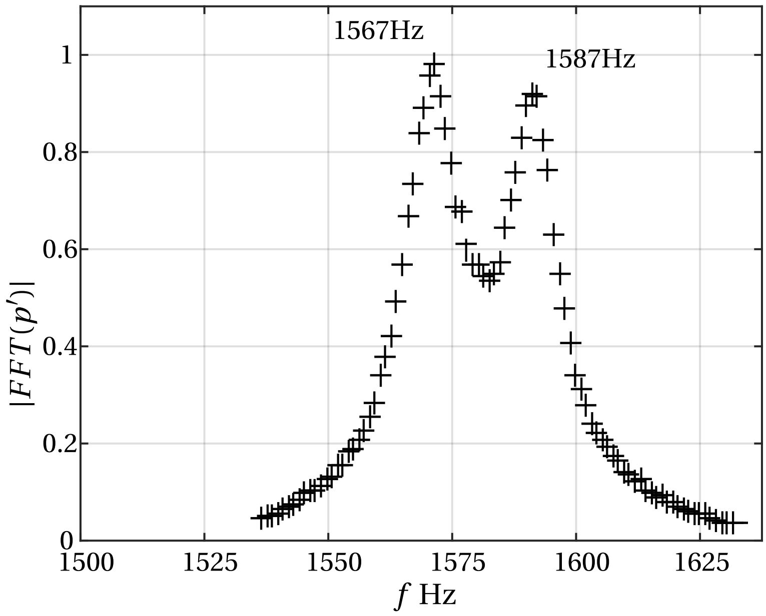

Figure B.1: Measured pressure spectrum reflecting two peaks that indicate non-degeneracy of the T1L1 mode pair

The LEE simulations reproduce both eigenfrequencies as is indicated in the figure, too. Furthermore, it is revealed that each eigenfrequency is associated with a rotating eigenmode. More specifically, the higher and lower frequencies ($\omega_F \neq \omega_G$) are associated with a counter-clockwise (CCW, denoted with $T1_F$) and clockwise (CW, denoted with $T1_G$) running mode in and against the mean-swirl direction, respectively. Hence, as revealed by the LEE eigensolutions, the non-degenerate situation is characterized by two counter-rotating modes of deviating frequencies, whereas the degenerate transversal modes emerge as standing modes (denoted by A and B) that exhibit equal frequencies ($\omega_A =$

ω_B). Note that the degenerate case can also be described by two counter-rotating modes of the same frequency. However, the clarity of interpretations and explanations in this thesis, degenerate and non-degenerate circumstances are described by standing and counter-rotating mode pairs, respectively. Generally, a loss of degeneracy implies a loss of symmetry [21], which is for swirling flows induced due to one dominant direction of the azimuthal mean velocity. Figure B.2 illustrates departure of degeneracy from standing modes (e.g. occurring in a combustor with a jet flow) to non-degenerate counter-rotating modes (e.g. occurring in a combustors with a swirl flow).

Quantitatively, the difference between oscillation frequencies emerges as $\Delta\omega \approx \omega_F - \omega_G = 20.5 \cdot 2\pi \ (rad/s)$, which is retrieved from both, the spectrum in Fig. B.1 and the LEE eigenfrequency results. Additionally, the individual frequency values of the CW and CCW rotation are accurately reproduced (cf. Table B.1). Relative errors between numerically computed frequency difference and respective frequency values and experimental counterparts remain below 5%. Furthermore, measured and computed damping rates (cf. Table B.1) reveal a deviation between the CCW and CW rotating mode as for the oscillation frequencies, too. Specifically, the damping rates of the CW (against mean swirl) and CCW (with mean swirl) exhibit smaller and larger relative values, respectively, i.e. $\alpha_G < \alpha_F$. This deviation of damping is confirmed using the reflection coefficient associated with transversal modes in Fig. 5.13, which reveals a slightly lower and higher reflection coefficient, i.e. larger and weaker damping), for lower and higher frequencies, respectively. Notice that the two measured damping rates were identified using method of fitting the envelope of the decaying pressure signal that results of a sudden switch off of the excitation signal. Details on the the fitting method is given in [159, 169].

	Experiment	Simulation	Direction
ω_F (rad/s)	$1587 \cdot 2\pi$	$1573 \cdot 2\pi$	CCW
ω_G (rad/s)	$1567 \cdot 2\pi$	$1553 \cdot 2\pi$	CW
α_F (rad/s)	-23.5	-23	CCW
α_G (rad/s)	-28.0	-25	CW

Table B.1: Eigenfrequencies and damping rates

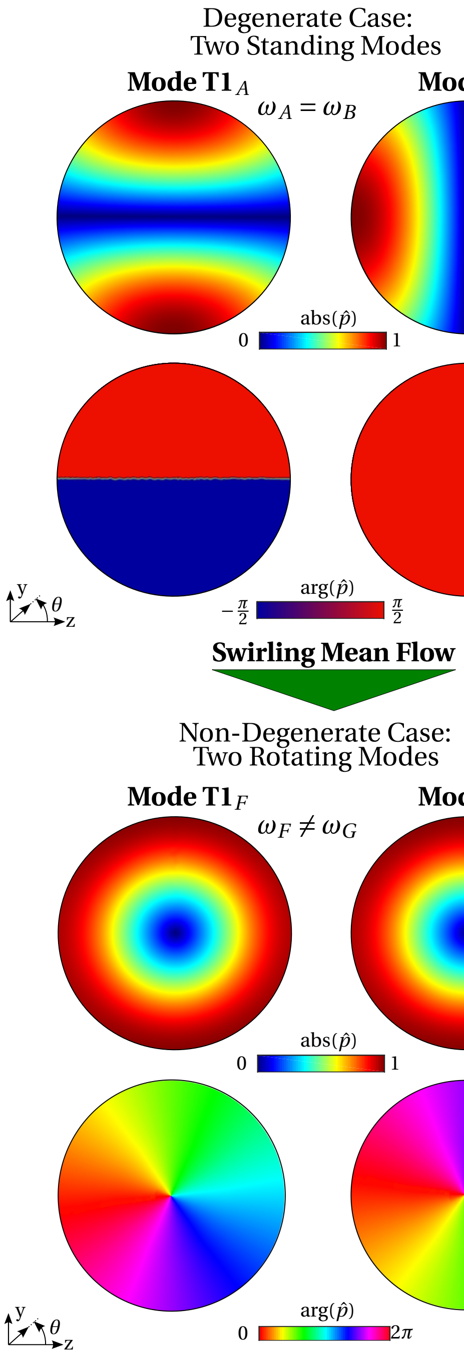

Figure B.2: Schematic: departure from degeneracy (two standing modes T1$_A$ and T1$_B$, orthogonal to each other, equal frequencies) into non-degeneracy (two counter-rotating modes T1$_F$ and T1$_G$, deviating frequencies) due to swirling mean flow

B.3 Physical Origin of Non-Degeneracy

The previous section identified distinct features of non-degenerate transversal modes in swirling mean flow environments. Also, LEE eigenmodes are revealed to capture the loss of degeneracy, and accurately reconstructed the experimental observations. The root cause of the non-degeneracy, i.e. the physical origins of the deviations of damping and growth rates, is addressed in this section.

B.3.1 Growth and Damping Rate Deviation

The physical origin of the deviation of CCW and CW modes' damping rates is discussed using the reflection coefficient results given in Fig. 5.12. Specifically, the reflection coefficient increases with increasing frequencies. The reflection coefficient at the eigenfrequencies with which the damping rates shown in Tab. B.1 are determined valuate to 0.96 and 0.965 for the CW ($b = 1$) and CCW ($b = -1$) Bloch mode, respectively. As a possible interpretation, the CCW mode can be thought to experience less resistance than the CW due to the co- and counter-rotation with respect to the mean flow swirl. Associated interactions between acoustics and shear zones, i.e. vortex-shedding, are amplified and attenuated, which leads to respectively more and less damping due to vortex shedding.

For reactive cases of the benchmark system, thermoacoustic flame driving acts quantitatively equal onto both modes, i.e. $\beta_F = \beta_G$. This equality is due to the frequency independence of the deformation source term in Eqn. 4.25, and the negligibility of the frequency dependence of the displacement source term in Eqn. 4.24 over the split range $\Delta\omega$. Writing the growth rates as

$$\nu_F = \beta_F + \alpha_F, \tag{B.1}$$

$$\nu_G = \beta_G + \alpha_G, \tag{B.2}$$

reveals the impact of the of non-degeneracy, i.e. a smaller acoustic damping rate leads to a larger growth rate, and vice versa. For the benchmark case in this work the growth rate of the CCW mode is larger than the CW mode, i.e. $\nu_F > \nu_G$ because of $\alpha_F < \alpha_G$.

B.3.2 Frequency Gap

The reason for the frequency gap intuitively connects to interaction effects between the swirling mean flow and acoustics fluctuations. It seems apparent that the azimuthal component of the mean flow vector induces this loss in degeneracy analogously as shown in [10]. This reference concerns an annular system, where a constant azimuthal mean flow induces a frequency difference – and thus a loss in degeneracy – into the azimuthal mode pairs. In order to assess the basic mechanisms governing the interactions between azimuthal mean flow and transversal acoustics the swirling 3D system is approximated by a 2D circular domain as is illustrated in Fig. B.3. The swirling mean flow is modeled via a solid body rotation, which implies a linear variation of the azimuthal mean velocity component while the radial mean velocity is zero as indicated in the schematic. All other mean quantities remain constant.

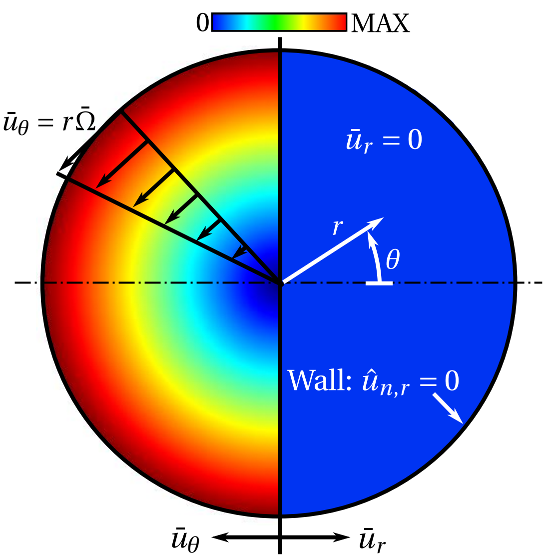

Figure B.3: 2D domain with solid body rotating mean flow

The corresponding LEE system in frequency domain governing the simplistic

2D model is retrieved from Eqns. 2.18-2.19, and reads in cylindrical coordinates

$$\bar{\rho} i\omega \hat{u}_{n,r} + \bar{\rho}\bar{\Omega}\frac{\partial \hat{u}_{n,r}}{\partial \theta} - \overbrace{(2\bar{\rho}\bar{\Omega}\hat{u}_{n,\theta})}^{\text{Coriolis}-r} \cdot s_{cor} + \frac{\partial \hat{p}_n}{\partial r} = 0, \tag{B.3}$$

$$\bar{\rho} i\omega \hat{u}_{n,\theta} + \bar{\rho}\bar{\Omega}\frac{\partial \hat{u}_{n,\theta}}{\partial \theta} + \overbrace{(2\bar{\rho}\bar{\Omega}\hat{u}_{n,r})}^{\text{Coriolis}-\theta} \cdot s_{cor} + \frac{1}{r}\frac{\partial \hat{p}_n}{\partial \theta} = 0, \tag{B.4}$$

$$i\omega \hat{p}_n + \bar{\Omega}\frac{\partial \hat{p}_n}{\partial \theta} + \gamma \bar{p}\left(\frac{\hat{u}_{n,r}}{r} + \frac{\partial \hat{u}_{n,r}}{\partial r} + \frac{1}{r}\frac{\partial \hat{u}_{n,\theta}}{\partial \theta}\right) = 0, \tag{B.5}$$

where $\bar{\Omega}$ denotes the constant angular mean flow velocity, while $\hat{u}_r$, $\hat{u}_\theta$ present the acoustic velocity mode shapes in radial r and azimuthal θ direction, respectively. The switch parameter s_{cor} in Eqns. B.3-B.4 is used to quantify the relative contribution of the convective and Coriolis terms on the transversal modes' eigensolutions. The resulting eigenfrequency differences (normalized with experimental value) from simulations of the 2D system for $s_{cor} = 1$ and $s_{cor} = 0$ are drawn in Fig. B.4. The same figure hosts the gaps from the measurements, and the corresponding 3D LEE simulations the swirling isothermal combustor configuration.

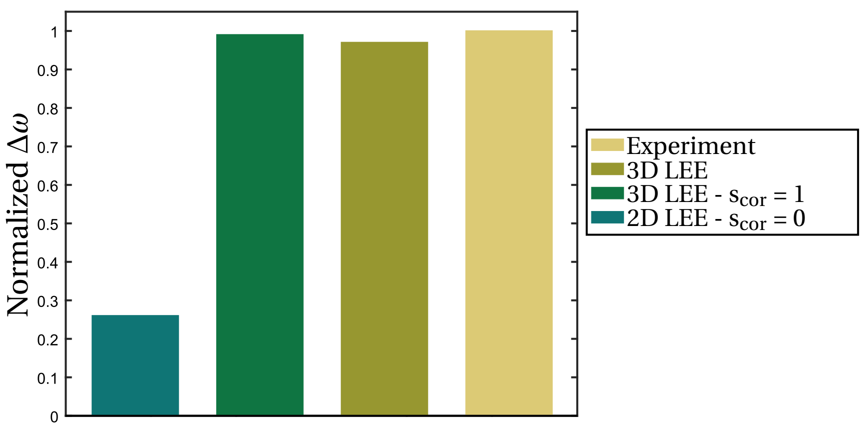

Figure B.4: Eigenfrequency differences

Comparing the results for $s_{cor} = 1$ and $s_{cor} = 0$ identifies the Coriolis effect as the dominant mechanism that quantitatively causes the observed frequency differences. The convective case ($s_{cor} = 0$) only reproduces the analytical counterpart results as expected. Thus, only considering convective effects leads to an underestimation of the frequency difference in combustors with non-degenerate transversal modes. This circumstance emphasizes one major difference between azimuthal (annular cross section) and transversal (circular cross section) acoustic oscillations: The Coriolis force presents a relevant, non-negligible physical mechanism in transversal thermoacoustic systems with swirling mean flows. The occurring physics can be thought of an acceleration and deceleration of the counter rotating modes induced by the Coriolis force, which causes an in- and decrease of the associated wave numbers (and thus oscillation frequencies), respectively.

B.4 Summary and Findings – Mean Flow Interactions

In the previous sections, the loss of degeneracy of transversal modes that occurs in swirl-type combustion chambers was investigated. This non-degeneracy physically results in two counter-rotating transversal eigenmode pairs with deviating oscillation frequencies, damping rates and (in for reactive, thermoacoustic cases) growth rates. Then, the physical origin of the non-degeneracy was explored using an aeroacoustic test case of a swirl stabilized burner. Experimental and numerical investigations generated the following findings:

- Physical origin of the eigenfrequency gap is governed by Coriolis effects due to the swirling mean flow.
- Rotating modes in and against the mean swirl direction exhibit higher and lower rotational speeds, i.e. eigenfrequencies, respectively.
- Physical origin of the growth rate gap is due to unequal damping of the constituting rotating modes, while flame driving acts equally on both modes.
- Rotating modes in and against the mean swirl direction experience attenuated and amplified vortex shedding, which translates into a smaller and higher damping rate, respectively.

Overall, new theoretical insight into physical mechanisms of transversal modes for HF thermoacoustics oscillations was generated. The successful numerical reproduction supports the applicability of the LEE methodology to capture the mean flow interaction processes that induce the non-degenerate eigenfrequencies. Finally, the discussion of mean flow effects on linear eigenmodes in this appendix presents the last component – after driving, damping and stability investigation in Chaps. 4-6 – of the linear considerations of this thesis.

C Evaluation of $\mathbf{W_r E^{-1}}$

This appendix presents a procedure to determine the expression $\mathbf{W_r E^{-1}}$ needed for the MOR in Chap. 7 without carrying out the computationally extensive inversion operation of the descriptor matrix $\mathbf{E}$. This procedure starts with the right and left generalized eigenvalue problem, i.e.

$$\mathbf{A} = \boldsymbol{E V \Lambda W}, \tag{C.1}$$

$$\mathbf{A} = \boldsymbol{V \Lambda W E}, \tag{C.2}$$

where $\boldsymbol{V}$, $\boldsymbol{W}$, $\boldsymbol{\Lambda}$ and $\boldsymbol{A}$ denotes the left eigenvector matrix, right eigenvector matrix, eigenvalue matrix and system matrix of size N, respectively. The dot product of the left and right eigenvector matrix yields the unity matrix, i.e.

$$\boldsymbol{VW} = \boldsymbol{WV} = \boldsymbol{I}. \tag{C.3}$$

Next, Eqns. C.1-C.2 are respectively pre- and post-multiplied with $\boldsymbol{V}$ and $\boldsymbol{W}$ to give under consideration of Eqn. C.3

$$\boldsymbol{WAV} = \boldsymbol{WEV\Lambda}, \tag{C.4}$$

$$\boldsymbol{WAV} = \boldsymbol{\Lambda WEV}, \tag{C.5}$$

to give

$$\boldsymbol{WEV\Lambda} = \boldsymbol{\Lambda WEV}. \tag{C.6}$$

Recall that $\boldsymbol{\Lambda}$ is a diagonal matrix. Thus, satisfying Eqn. C.6 requires $\boldsymbol{K} = \boldsymbol{WEV}$ to be a diagonal matrix, too. Next, Eqn. C.6 is inverted, i.e.

$$\boldsymbol{K^{-1}} = \boldsymbol{V^{-1} E^{-1} W^{-1}}. \tag{C.7}$$

Post-multiplying Eqn. C.7 with $\boldsymbol{W}$ gives

$$\boldsymbol{WE^{-1}} = \boldsymbol{K^{-1} W}, \tag{C.8}$$

which furthermore transforms into the desired expression by utilizing the eigenvectors that define the subspace of the MOR, i.e.

$$\boldsymbol{W_r E^{-1}} = \boldsymbol{K_r^{-1} W_r}, \tag{C.9}$$

The remaining task is to evaluate $\boldsymbol{K_r^{-1}}$, which requires to invert the reduced diagonal matrix given by

$$\boldsymbol{K_r} = \boldsymbol{W_r E V_r}, \tag{C.10}$$

by taking the reciprocal of each entry.

D Illustration of Beating Frequency in Fourier Spectrum

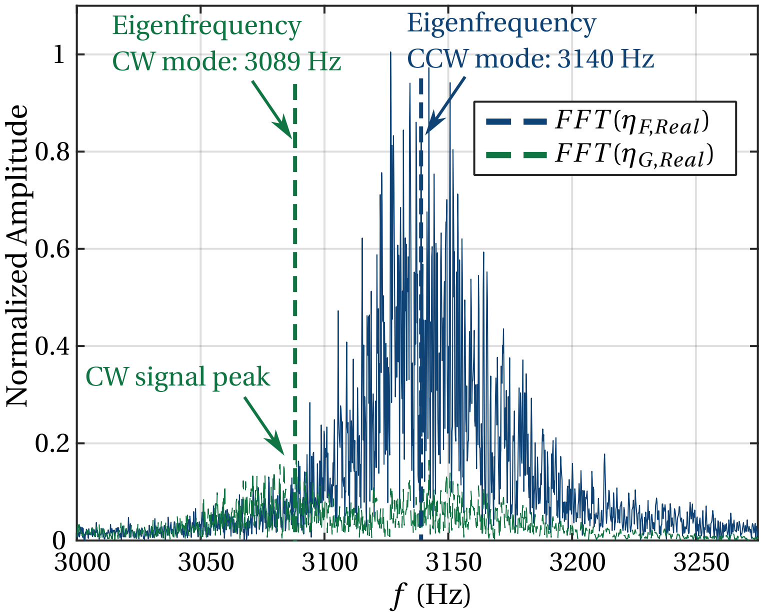

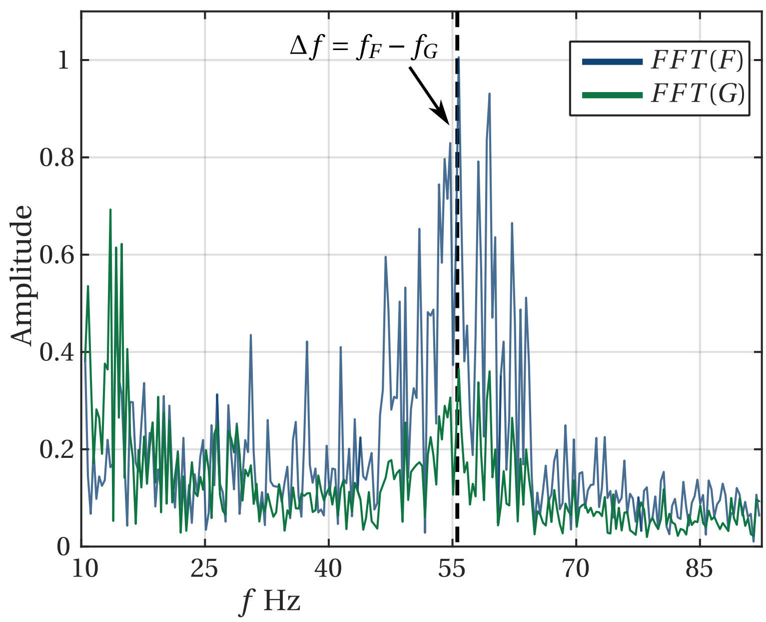

Figure D.1: Fourier spectra of experimental data (unstable case) – top (previous page): oscillating mode signals, bottom (this page): slowly varying amplitudes

E Eigenvalue of Standing Mode Fixed Point

$$\lambda_1 = -\frac{(\nu_{n,a,F}+\nu_{n,a,G})}{3} - \sqrt{\frac{62\nu_{n,a,F}\nu_{n,a,G}-23(\nu^2_{n,a,F}+\nu^2_{n,a,G})}{9}} \tag{E.1}$$

$$\lambda_2 = -\sqrt{\frac{62\nu_{n,a,F}\nu_{n,a,G}-23(\nu^2_{n,a,F}+\nu^2_{n,a,G})}{9}} \tag{E.2}$$

Previous Publications

Significant parts of this thesis were already published by the author in journal and conference papers [15–17, 63, 69–76, 129, 130, 145, 157]. All these publications are registered according to the valid doctoral regulations. However, not all of them are quoted explicitly everywhere. Whether these personal prior printed publications were referenced depends on maintaining comprehensibility and providing all necessary context.

Supervised Student Theses

Associated with this Ph.D. thesis, a number of student theses were supervised by the author of the present work. These theses were prepared at the Lehrstuhl für Thermodynamik, Technische Universität München in the years 2014 to 2017 under the close supervision of the present author. Parts of these supervised theses may be incorporated into the present thesis. The author would like to express his sincere gratitude to all formerly supervised students for their commitment and support of this research project.

Name	Title, thesis type, submission date
Pedro Romero	3D Low-Order Modeling and Analysis of a Thermoacoustically Non-Compact Experimental Gas Turbine Combustor, Master's thesis, April 30th 2015
Klaus Hammer	Modellierung von nicht kompakten, akustischen Randbedingungen in Modellen reduzierter Ordnung, Semester thesis, August 1st 2015
Tobias Bieniek	Numerische Untersuchung des Strömungs- und Verbrennungsverhaltens eines aerodynamisch stabilisierten Vormischbrenners, Bachelor's thesis, October 1st 2015
Klaus Hammer	Theoretical and Analytical Investigations of Nonlinear, Transversal, High-Frequency Thermoacoustic Oscillations in Gas Turbine Combustors, Master's thesis, April 30th 2016
Thomas Hofmeister	Modeling of Acoustic Damping Induced by Periodic Vortex Shedding in Noncompact Thermoacoustic Systems, Master's thesis, April 30th 2017
Daniel Jäger	Analytical Modeling and System Identification of Transversal Thermoacoustic Oscillations via Stochastic Differential Equations, Semester thesis, September 29th 2017

Bibliography

[1] *ANSYS. General documentation. Fluent, Release 13.*

[2] *Introduction to COMSOL Multiphysics. VERSION 4.3a.*

[3] M. Abom. Measurement of the Scattering-matrix of Acoustical Two-Port. *Mechanical System and Signal Processing*, 5:89–3104, 1991.

[4] M. Abom. A Note on the Experimental Determination of Acoustical Two-Port Matrices. *Journal of Sound and Vibration*, 155(1):185–188, 1992.

[5] International Energy Agency. *World Energy Outlook 2016.* 2016.

[6] Lars Valerian Ahlfors. *Complex analysis: An introduction to the theory of analytic functions of one complex variable.* McGraw-Hill, 1966.

[7] N. Ananthkrishan. Reduced-Order Modeling and Dynamics of Nonlinear Acoustic Waves in a Combustion Chamber. *Combustion Science and Technology*, 177:2:221–248, 2006.

[8] A. C. Antoulas. *Approximation of Large-Scale Dynamical Systems.* Society for Industrial and Applied Mathematics, 2005.

[9] R. Balachandran, A.P. Dowling, and E. Mastorakos. Non-linear Response of Turbulent Premixed Flames to Imposed Inlet Velocity Oscillations of Two Frequencies. *Flow, Turbulence and Combustion*, 80(4):455, May 2008.

[10] M. Bauerheim, M. Cazalens, and T. Poinsot. A theoretical Study of Mean Azimuthal Flow and Asymmetry Effects on Thermo-acoustic Modes in

Annular Combustors. *Proceedings of the Combustion Institute*, 35:3219–3227, 2015.

[11] D.W. Bechert. Sound Absorption Caused by Vorticity Shedding, Demonstrated with a Jet Flow. *Journal of Sound and Vibration*, 70(3):389–405, 1980.

[12] B. D. Bellows, M. K. Bobba, A. Forte, J. M. Seitzmann, and T. Lieuwen. Flame Transfer Function Saturation Mechanisms in a Swirl-Stabilized Combustor. *Proceedings of the Combustion Institute*, 31:3181–3188, 2007.

[13] V. Bellucci, B. Schuermans, D. Nowak, P. Flohr, and C. O. Paschereit. Thermoacoustic Modeling of a Gas Turbine Combustor Equipped With Acoustic Dampers. *Journal of Turbomachinery*, 127:372–379, 2005.

[14] P. Benner. Model Reduction for Linear Dynamical Systems. *Summer School on Numerical Linear Algebra for Dynamical and High-Dimensional Problems, Trogir, Croatia, October 10-15*, 2011.

[15] F. Berger, T. Hummel, M. Hertweck, B. Schuermans, and T. Sattelmayer. High-Frequency Thermoacoustic Modulation Mechanisms in Swirl-Stabilized Gas Turbine Combustors, Part I: Experimental Investigation of Local Flame Response. *Journal of Engineering for Gas Turbines and Power*, 139(7):071501–9, 2017.

[16] F. Berger, T. Hummel, P. Romero, B. Schuermans, and T. Sattelmayer. A Novel Reheat Combustor Experiment for the Analysis of High-Frequency Flame Dynamics. *ASME Turbo Expo 2018 GT2018-77101, June 11-15, Oslo, Norway*, 2018.

[17] F. Berger, T. Hummel, B. Schuermans, and T. Sattelmayer. Pulsation-Amplitude-Dependent Flame Dynamics of High-Frequency Thermoacoustic Oscillations in Lean-Premixed Gas Turbine Combustors. *Journal of Engineering for Gas Turbines and Power*, 140(4):041507–10, 2017.

[18] F. Berger, J. Kaufmann, B. Schuermans, and T. Sattelmayer. Identification of Flame Displacement from High Frequency Thermoacoustic

Pulsations in Gas Turbine Combustors. *24th International Congress on Sound and Vibration, July 23 - 27, London, England*, 2017.

[19] R. S. Blumenthal. A Systems View on Non-Normal Transient Growth in Thermoacoustics. *Doctoral Thesis, Lehrstuhl f. Thermodynamik, Technische Universität München*, 2015.

[20] M. R. Bothien, J. P. Moeck, A. Lacarelle, and C. O. Paschereit. Time Domain Modelling and Stability Analysis of Complex Thermoacoustic Systems. *Proceedings of the Institution of Mechanical Engineers, Part A: Journal of Power and Energy*, 221(5):657–668, 2007.

[21] M. R. Bothien, N. Noiray, and B. Schuermans. Analysis of Azimuthal Thermoacoustic Modes in Annular Gas Turbine Combustion Chambers. *Journal of Engineering for Gas Turbines and Power*, 137(6):061505, 2015.

[22] E. Boujo, A.D. Denisov, B. Schuermans, and N. Noiray. Quantifying Acoustic Damping using Flame Chemiluminescence. *Journal of Fluid Mechanics*, 808:245–257, 2016.

[23] E. Boujo and N. Noiray. Robust Identification of Harmonic Oscillator Parameters using the Adjoint Fokker-Planck Equation. *Proceedings of the Royal Society A*, 473(2200), 04 2017.

[24] J. Bourgouin, D. Durox, J. P. Moeck, T. Schuller, and S. Candel. Self-Sustained Instabilities in an Annular Combustor Coupled by Azimuthal and Longitudinal Acoustic Modes. *ASME GT2013-95010, June 3-7, San Antonio, Texas, USA*, 2013.

[25] M.J. Brear, F. Nicoud, M. Talei, A. Giauque, and E.R. Hawkes. Disturbance Energy Transport and Sound Production in Gaseous Combustion. *Journal of Fluid Mechanics*, 707:53–73, 2012.

[26] V. S. Burnley and F. E.C. Culick. Influence of Random Excitations on Acoustic Instabilities in Combustion Chambers. *AIAA Journal*, 38-8:1403–1410, 2000.

[27] S. M. Camporeale, B. Fortunato, and G. Campa. A Finite Element Method for Three-Dimensional Analysis of Thermo-acoustic Combustion Instability. *Journal of Engineering for Gas Turbines and Power*, 133(1):011506, 2010.

[28] S. Candel. Combustion Dynamics and Control: Progress and Challenges. *Proceedings of the Combustion Institute*, 29:1–28, 2002.

[29] L.S. Chen, S. Bomberg, and W. Polifke. Propagation and Generation of Acoustic and Entropy Waves Across a Moving Flame Front. *Combustion and Flame*, 166:170 – 180, 2016.

[30] B. Cosic, J. P. Moeck, and C. O. Paschereit. Open-Loop Control of Combustion Instabilities and the Role of the Flame Response to Two-Frequency Forcing. *Journal of Engineering for Gas Turbines and Power*, 134:061502, 06 2012.

[31] F.E.C. Culick. *Unsteady Motions in Combustion Chambers for Propulsion Systems*. Number AC/323(AVT-039)TP/103 in RTO AGARDograph AG-AVT-039, 2006.

[32] F.E.C. Culick. Spatial Averaging Combined with a Perturbation/Iteration Procedure. *International Journal of Spray and Combustion Dynamics*, 4(3):185–246, 2012.

[33] L. Cveticanin. Approximate analytical solutions to a class of non-linear equations with complex functions. *Journal of Sound and Vibration*, 157(2):289–302, 1992.

[34] M. de Groot, W. Crijns-Graus, and R. Harmsen. The Effects of Variable Renewable Electricity on Energy Efficiency and Full Load hours of Fossil-fired Power Plants in the European Union. *Energy*, 138:575 – 589, 2017.

[35] A. P. Dowling. The Calculation of Thermoacoustic Oscillations. *Journal of Sound and Vibration*, 180(4):557–581, 1995.

[36] A. P. Dowling. Nonlinear Self-Excited Oscillations of a Ducted Flame. *Journal of Fluid Mechanics*, 346:271–290, 1997.

[37] A. P. Dowling. The Challenges of Lean Premixed Combustion. *Proceedings of the International Gas Turbine Congress, Nov 2-7,, Tokyo, Japan*, IGTC2003Tokyo KS-5, 2003.

[38] A. P. Dowling and Y. Mahmoudi. Combustion Noise. *Proceedings of the Combustion Institute*, 35:65–100, 2015.

[39] S. Ducruix, T. Schuller, D. Durox, and S. Candel. Combustion Dynamics and Instabilities: Elementary Coupling and Driving Mechanisms. *Journal of Propulsion and Power*, 19(5):722–734, 2003.

[40] I. D. J. Dupere and A. P. Dowling. Absorption of Sound near Abrupt Area Expansions. *AIAA JOURNAL*, 38(2):193–202, 2000.

[41] Thomas Emmert, Stefan Jaensch, Carlo Sovardi, and Wolfgang Polifke. taX - a Flexible Tool for Low-Order Duct Acoustic Simulation in Time and Frequency Domain. *Forum Acusticum Krakow, Poland, September 7-12*, 2014.

[42] S. Evesque and W. Polifke. Spinning and Azimuthally Standing Acoustic Modes in Annular Combustors. *9th AIAA/CEAS Aeroacoustics Conference, Conference, May 12-14 , Hilton Head, SC, USA*, 2003.

[43] J. H. Ferziger and M. Peric. *Computational Methods for Fluid Dynamics.* Springer, Berlin, Germany, 2002.

[44] J. Fish and T. Belytschko. *A First Course in Finite Elements.* John Wiley & Sons, West Sussex, England, 2007.

[45] S. Föller and W. Polifke. Identification of Aero-Acoustic Scattering Matrices from Large Eddy Simulation. Application to a Sudden Area Expansion of a Duct. *Journal of Sound and Vibration*, 331:3096–3113, 2012.

[46] R. Friedrich, J. Peinke, M. Sahimi, and M. R. R. Tabar. Approaching Complexity by Stochastic Methods: From Biological Systems to Turbulence. *Physics Reports*, 506:87–162, 2011.

[47] R. Friedrich, S. Siegert, J. Peinke, St. Lueck, M. Siefert, M. Lindemann, J. Raethjen, G. Deuschl, and G. Pfister. Extracting model equations from experimental data. *Physics Letters A*, 271:217–222, 2000.

[48] Crispin Gardiner. *Stochastic Methods.* Springer, Berlin, 2009.

[49] A.M.G. Gentemann, A. Fischer, S. Evesque, and W. Polifke. Acoustic Transfer Matrix Reconstruction and Analysis for Ducts with Sudden Change of Area. *9th AIAA/CEAS Aeroacoustics Conference and Exhibit, 12-14 May 2003, Hilton Head, South Carolina, USA*, 05 2003.

[50] A. Ghani, T. Poinsot, L. Gicquel, and G. Staffelbach. LES of Longitudinal and Transverse Self-Excited Combustion Instabilities in a Bluff-Body Stabilized Turbulent Premixed Flame. *Combustion and Flame*, 162-11:4075–4083, 2015. DOI 10.1007/s11071-008-9402-y.

[51] G. Ghirardo, M. P. Juniper, and J.P. Moeck. Weakly Nonlinear Analysis of Thermoacoustic Instabilities in Annular Combustors. *Journal of Fluid Mechanics*, 805:52–87, 2016.

[52] J. Gikadi. Prediction of Acoustic Modes in Combustors using Linearized Navier-Stokes Equations in Frequency Space. *Doctoral Thesis, Lehrstuhl f. Thermodynamik, Technische Universität München*, 2013.

[53] J. Gikadi, S. Föller, and T. Sattelmayer. Impact of Turbulence on the Prediction of Linear Acoustic Interactions: Acoustic Response of a Turbulent Shear Layer. *Journal of Sound and Vibration*, 333:6548–6559, 2014.

[54] J. Gikadi, M. Schulze, S. Föller, J. Schwing, and T. Sattelmayer. Linearized Navier-Stokes and Euler Equations for the Determination of the Acoustic Scattering Behaviour of and Area Expansion. *18th AIAA/CEAS Conference, AIAA 2012-2292,Colorado Springs, CO, USA*, 2012.

[55] J. Gikadi, W. Ullrich, T. Sattelmayer, and F. Turrini. Prediction of the Acoustic Losses of a Swirl Atomizer Nozzle under Non-Reactive Conditions. *ASME GT2013-95449, June 3-7, San Antonio, Texas, USA*, 2013.

[56] M.A. Gonzalez-Salazar, T. Kirsten, and L. Prchlik. Review of the Operational Flexibility and Emissions of Gas- and Coal-fired Power Plants in a Future with Growing Renewables. *Renewable and Sustainable Energy Reviews*, 82:1497 – 1513, 2018.

[57] F. Grimm, J.-M. Lourier, O. Lammel, B. Noll, and M. Aigner. A Selective Fast Fourier Filtering Approach Applied to High Frequency Thermoacoustic Instability Analysis. *ASME Turbo Expo 2017 GT2017-63234, June 26-30, Charlotte, USA*, 2017.

[58] S. Groening, D. Suslov, M. Oschwald, and T. Sattelmayer. Stability Behaviour of a Cylindrical Rocket Engine Combustion Chamber Operated with Liquid Hydrogen and Liquid Oxygen. *5th European Conference for Aeronautics and Space Sciences (EUCASS), July 1-5, 2013, Munich, Germany*, 2013.

[59] L. Hakim, A. Ruiz, T. Schmitt, M. Boileau, G. Staffelbach, S. Ducruix, C. Benedicte, and S. Candel. Large Eddy Simulations of Multiple Transcritical Coaxial Flames Submitted to a High-Frequency Transverse Acoustic Modulation. *Proceedings of the Combustion Institute*, pages –, 01 2014.

[60] J. Hardi, M. Oschwald, S. Webster, S. Groening, S. Beinke, W. Armbruster, N. Blanco, D. Suslov, and B. Knapp. High frequency combustion instabilities in liquid propellant rocket engines: research programme at DLR Lampoldshausen. In *Proceedings of the International Symposium on Thermoacoustic Instabilities in Gas Turbines and Rocket Engines: Industry meets Academia*, Garching Forschungszentrum der TUM, Jun 2016. TUM, LS für Thermodynamik / IAS.

[61] J. S. Hardi. Experimental Investigation of High Frequency Combustion Instability in Cryogenic Oxygen-Hydrogen Rocket Engines. *Doctoral Thesis, School of Mechanical Engineering, The University of Adelaide*, 2012.

[62] M. Hertweck. Einfluss der Flammenposition auf transversale hochfrequente akustische Moden in zylindrischen Brennkammern. *Doctoral Thesis, Lehrstuhl f. Thermodynamik, Technische Universität München*, 2016.

[63] M. Hertweck, T. Hummel, F. Berger, and T. Sattelmayer. Impact of the Heat Release Distribution on High-Frequency Transverse Thermo-

acoustic Driving in Premixed Swirl Flames. *International Journal of Spray and Combustion Dynamics*, 9:143–154, 2017.

[64] C. Honisch and R. Friedrich. Estimation of Kramers-Moyal Coefficients at Low Sampling Rates. *Physical Review E*, 83, 2011.

[65] M. Howe. *Mathematical Methods for Mechanical Sciences*. Imperial College Press, London, UK, 2015.

[66] M.S. Howe. The Generation of Sound by Aerodynamic Sources in an Inhomogeneous Steady Flow. *Journal of Fluid Mechanics*, 67(3):597–610, 1975.

[67] M.S. Howe. On the Theory of Unsteady High Reynolds Number Flow Through a Circular Aperture. *Proceedings of the Royal Society A*, 366:205–223, 1979.

[68] M.S. Howe. The Dissipation of Sound at an Edge. *Journal of Sound and Vibration*, 70(3):407–411, 1980.

[69] T. Hummel, F. Berger, M. Hertweck, B. Schuermans, and T. Sattelmayer. High-Frequency Thermoacoustic Modulation Mechanisms in Swirl-Stabilized Gas Turbine Combustors, Part II: Modeling and Analysis. *Journal of Engineering for Gas Turbines and Power*, 139(7):071502–10, 2017.

[70] T. Hummel, F. Berger, B. Schuermans, and T. Sattelmayer. Theory and Modeling of Non-Degenerate Transversal Thermoacoustic Limit Cycle Oscillations. *International Symposium on Thermoacoustic Instabilities in Gas Turbines and Rocket Engines: Industry meets Academia*, GTRE-038, 2016.

[71] T. Hummel, F. Berger, N. Stadlmair, B. Schuermans, and T. Sattelmayer. Extraction of Linear Growth and Damping Rates of High-Frequency Thermoacoustic Oscillations From Time Domain Data. *Journal of Engineering for Gas Turbines and Power*, 140(5):051505–10, 2017.

[72] T. Hummel, K. Hammer, P. Romero, B. Schuermans, and T. Sattelmayer. Low-Order Modeling of Nonlinear Transversal Thermoacoustic Oscillations in Gas Turbine Combustors. *Journal of Engineering for Gas Turbines and Power*, 139(7):071503–11, 2017.

[73] T. Hummel, T. Hofmeister, B. Schuermans, and T. Sattelmayer. Modeling and Quantification of Acoustic Damping Induced by Vortex Shedding in Non-Compact Thermoacoustic Systems. *24th International Congress on Sound and Vibration, July 23 - 27, London, England*, 2017.

[74] T. Hummel, P. Romero, F. Berger, M. Schulze, B. Schuermans, and T. Sattelmayer. Analysis of High-Frequency Thermoacoustic Instabilities in Lean-Premixed Gas Turbine Combustors. *COMSOL Conference, October 12-14, Munich, Germany*, 2016.

[75] T. Hummel, M. Schulze, B. Schuermans, and T.Sattelmayer. Reduced Order Modeling of Transversal and Non-Compact Combustion Dynamics. *22nd International Congress on Sound and Vibration, July 12 - 16, Florence, Italy*, 2015.

[76] T. Hummel, C. Temmler, B. Schuermans, and T. Sattelmayer. Reduced Order Modeling of Aeroacoustic Systems for Stability Analyses of Thermoacoustically Non-Compact Gas Turbine Combustors. *Journal of Engineering for Gas Turbines and Power*, 138(5):051502–11, 2016.

[77] D. Jäger. Analytical Modeling and System Identification of Thermoacoustic Oscillations via Stochastic Differential Equations. *Semster Thesis, Lehrstuhl f. Thermodynamik, Technische Universität München*, 2017.

[78] C.C. Jahnke and F.E.C. Culick. An Application of Dynamical Systems Theory to Nonlinear Combustion Instabilities. *AIAA 31st Aerospace Sciences Meeting & Exhibit, January 11-14, 1993, Reno, NV, USA*, 1993.

[79] R. Kathan. Verlustmechanismen in Raketenbrennkammern. *Doctoral Thesis, Lehrstuhl f. Thermodynamik, Technische Universität München, www.td.mw.tum.de*, 2013.

[80] J.J. Keller. Thermoacoustic Oscillations in Combustion Chambers of Gas Turbines. *AIAA Journal*, 33(12):2280–2287, 1995.

[81] S. Köglmeier, R. Kaess, and T. Sattelmayer. Numerical Investigation on Nonlinear Acoustics in Liquid Rocket Combustion Instability. In *4th European Conference for Aerospace Sciences*, Saint Petersburg, Russia, 2011.

[82] A. Kierkegaard. Frequency Domain Linearized Navier-Stokes Equations Methods for Low Mach Number Internal Aeroacoustics. *Doctoral Thesis, Department of Aeronautical and Vehicle Engineering, Royal Institute of Technology, Stockholm*, 2011.

[83] N. Klarmann, T. Sattelmayer, B. Zoller, W. Geng, and F. Magni. Impact of Flame Stretch and Heat Loss on Heat Release Distributions in Gas Turbines Combustors: Model Comparison and Validation. *ASME GT2016-57625, June 13-17, Seoul, South Korea*, 2016.

[84] E. Kreiyszig. *Advanced Engineering Mathematics*. Wiley, Hoboken, USA, 2007.

[85] N. Krylov and N. Bogoliubov. *Introduction to nonlinear mechanics*. Princeton University Press., 1949.

[86] S.J. Lade. Finite sampling interval effects in Kramers–Moyal analysis. *Physics Letters A*, 373:3705–3709, 2009. DOI 10.1007/s11071-008-9402-y.

[87] D. Laera, T. Schuller, K. Prieur, D. Durox, S. M. Camporeale, and S. Candel. Flame Describing Function Analysis of Spinning and Standing Modes in an Annular Combustor and Comparison with Experiments. *Combustion and Flame*, 184:136 – 152, 2017.

[88] M. Lax. Classical Noise. V. Noise in Self-Sustained Oscillators. *Pys. Rev.*, 160(2):290–307, 1967.

[89] A. H. Lefebvre and D. R. Ballal. *Gas Turbine Combustion*. CRC Press, 1998.

[90] T. Lieuwen. Nonlinear Modeling of Unstable Gas Turbine Combustor Dynamics Using Experimental Data. *36th AIAA/AME/SAE/ASEE Joint Propulsion Conference and Exhibit, July 16-19, Huntsville, AL, USA*, 2000.

[91] T. Lieuwen. Experimental Investigation of Limit-Cycle Oscillations in an Unstable Gas Turbine Combustor. *Journal of Propulsion and Power*, 18(1):61–67, 2002.

[92] T. Lieuwen. Introduction: Combustion Dynamics in Lean-Premixed Prevaporized (LPP) Gas Turbines. *Journal of Propulsion and Power*, 19(5):721, 2003.

[93] T. Lieuwen. Modeling Premixed Combustion–Acoustic Wave Interactions: A Review. *Journal of Propulsion and Power*, 19-05, 2003.

[94] T. Lieuwen. Statistical Characteristics of Pressure Oscillations in a Premixed Combustor. *Journal of Sound and Vibration*, 260:3–17, 2003.

[95] T. Lieuwen. Online Combustor Stability Margin Assessment Using Dynamic Pressure Data. *Journal of Engineering for Gas Turbines and Power*, 127(3):478, 2005.

[96] T. Lieuwen. *Unsteady Combustor Physics*. Cambridge University Press, 2012.

[97] T. Lieuwen and Y. Neumeier. Nonlinear Pressure-Heat Release Transfer Function Measurements in a Premixed Combustor. *Proceedings of the Combustion Institute*, 29:99–105, 2002.

[98] T. Lieuwen and B. T. Zinn. Theoretical Investigations of Combustion Instability Mechanisms in Lean Premixed Gas Turbines. *36th Aerospace Sciences Meeting & Exhibit, January 12-15, 1998, Reno, NV, USA*, 1998.

[99] Gamal M. Mahmoud. Approximate solutions of a class of complex nonlinear dynamical systems. *Physics Letters A*, 253:211–222, 1998.

[100] C. Mayer. Konzept zur vorgemischten Verbrennung wasserstoffhaltiger Brennstoffe in Gasturbinen. *Doctoral Thesis, Lehrstuhl f. Thermodynamik, Technische Universität München*, 2012.

[101] K. R. McManus, T. Poinsot, and S.M. Candel. A Review of Active Control of Combustion Instabilities. *Proceedings of the Combustion Institute*, 19:1–19, 1993.

[102] G.A. Mensah, G. Campa, and J. P. Moeck. Efficient Computation of Thermoacoustic Modes in Industrial Annular Combustion Chambers Based on Bloch-Wave Theory. *Journal of Engineering for Gas Turbines and Power*, 138(8):081502, 2016.

[103] A. Michalke. On Spatially Growing Disturbances in an Inviscid Shear Layer. *Journal of Fluid Mechanics*, 23(3):521–544, 1965.

[104] J. P. Moeck and C.O. Paschereit. Nonlinear Interactions of Multiple Linearly Unstable Thermoacoustic Modes. *International Journal of Spray and Combustion Dynamics*, 4(1):1–28, 2012.

[105] M. K. Myers. Transport of Energy by Disturbances in Arbitrary Steady Flows. *Journal of Fluid Mechanics*, 226:383–400, 1991.

[106] F. Nicoud, L. Benoit, C. Sensiau, and T. Poinsot. Acoustic Modes in Combustors with Complex Impedances and Multidimensional Active Flames. *AIAA Jounral*, 45-02:426–441, 2007.

[107] N. Noiray. Linear Growth Rate Estimation From Dynamics and Statistics of Acoustic Signal Envelope in Turbulent Combustors. *Journal of Engineering for Gas Turbines and Power*, 139(4):041503–11, 2016.

[108] N. Noiray, M. R. Bothien, and B. Schuermans. Investigation of azimuthal staging concepts in annular gas turbines. *Combustion Theory and Modelling*, 15:5:585–606, 2011.

[109] N. Noiray and A. Denisov. A Method to Identify Thermoacoustic Growth Rates in Combustion Chambers from Dynamic Pressure Time Series. *Proceedings of the Combustion Institute*, 36(3):3843–3850, 07 2017.

[110] N. Noiray, D. Durox, T. Schuller, and S. Candel. A Unified Framework for Nonlinear Combustion Instability Analysis based on the Flame Describing Function. *Journal of Fluid Mechanics*, 615:139–167, 2008.

[111] N. Noiray and B. Schuermans. Theoretical and Experimental Investigations on Damper Performance for Suppression of Thermoacoustic Oscillations. *Journal of Sound and Vibration*, 331:2753–2763, 2012.

[112] N. Noiray and B. Schuermans. Deterministic Quantities Characterizing Noise Driven Hopf Bifurcations in Gas Turbine Combustion Chambers. *International Journal of Non-Linear Mechanics*, 50:152–163, 2013.

[113] N. Noiray and B. Schuermans. On the Dynamic Nature of Azimuthal Thermoacoustic Modes in Annular Gas Turbine Combustion Chambers. *Proceedings of the Royal Society A*, 469, 2013.

[114] Jacqueline O'Connor, Vishal Acharya, and Timothy Lieuwen. Transverse Combustion Instabilities: Acoustic, Fluid Mechanic, and Flame Process. *Progress in Energy and Combustion Sciences*, 49:1–39, 2015.

[115] German Federal Ministry of Education and Research. Energy and economy - german energy transition. *https://www.bmbf.de/en/german-energy-transition-2319.html*, 2018. Zugriff am 28.23.2018.

[116] Intergovernmental Panel on Climate Change. *Climate Change 2013 – The Physical Science Basis: Working Group I Contribution to the Fifth Assessment Report of the Intergovernmental Panel on Climate Change.* Cambridge University Press, 2014.

[117] Americal Physical Society Panel on Public Affairs. *Integrating Renewable Electricity on the Grid.* APS Physics, 2011.

[118] C. O. Paschereit, B. Schuermans, W. Polifke, and O. Mattson. Measurement of Transfer Matrices and Source Terms of Premixed Flames. *Journal of Engineering for Gas Turbines and Power*, 2002.

[119] J. E. Pieringer. Simulation selbsterregter Verbrennungsschwingungen in Raketenschubkammern im Zeitbereich. *Doctoral Thesis, Lehrstuhl f. Thermodynamik, Technische Universität München*, 2008.

[120] T. Poinsot and D. Veynante. *Theoretical and Numerical Combustion.* R.T. Edwards, Philadelphia, USA, 2005.

[121] W. Polifke. Combustion Instabilities. *VKI Lecture Series*, 2004.

[122] W. Polifke. Black-Box System Identification for Reduced Order Model Construction. *Annals of Nuclear Energy*, 67:109–128, 2014.

[123] S. B. Pope. *Turbulent Flows.* Cambridge University Press, 2000.

[124] P. Rao and P. Morris. Use of Finite Element Methods in Frequency Domain Aeroacoustics. *AIAA Journal*, 44(7):1643–1652, 2006.

[125] J.W.S. Rayleigh. The Theory of Sound. *Dover Publications,New York*, 1-2, 1945.

[126] F. Richecoeur, S. Ducruix, P. Scouflaire, and S. Candel. Experimental Investigation of High-Frequency Combustion Instabilities in Liquid Rocket Engine. *Acta Astronautica*, 62(1):18–27, 2008.

[127] S.W. Rienstra and A. Hirschberg. *An Introduction to Acoustics.* 2016.

[128] J.B. Roberts and P-T. D. Spanos. Invited Review No. 1 Stochastic Averaging: An Approximate Method of Solving Random Vibration Problems. *International Journal of Non-Linear Mechanics*, 21(2):111–134, 1986.

[129] P. Romero, F. Berger, T. Hummel, B. Schuermans, and T. Sattelmayer. Numerical Design of a Novel Reheat Combustor Experiment for the Analysis of High-Frequency Flame Dynamics. *ASME Turbo Expo 2018 GT2018-77034, June 11-15, Oslo, Norway*, 2018.

[130] P. Romero, T. Hummel, B. Schuermans, and T. Sattelmayer. Damping due to Acoustic Boundary Layer in High-Frequency Transverse Modes. *24th International Congress on Sound and Vibration,July 23 - 27, London, England*, 2017.

[131] J. Sangl. Erhöhung der Brennstoffflexibilität von Vormischbrennern durch Beeinflussung der Wirbeldynamik. *Doctoral Thesis, Lehrstuhl f. Thermodynamik, Technische Universität München*, 2011.

[132] T. Sattelmayer. Influence of the Combustor Aerodynamics on Combustion Instabilities from Equivalence Ratio Fluctuations. *ASME GT2000-0082, May 8-11, Munich, Germany*, 2000.

[133] T. Sattelmayer. *Grundlagen der Verbrennung in stationären Gasturbinen*, chapter 9 in: Stationäre Gasturbinen, 2. neu bearbeitete Auflage, pages 397–452. Springer Verlag, 2010.

[134] T. Sattelmayer, M. Schmid, and M. Schulze. Interaction of combustion with transverse velocity fluctuations in liquid rocket engines. *Journal of Propulsion and Power*, (Volume 31, Issue 4):1137–1147, Aug 2015.

[135] S. Schimek, B Cosic, J.P. Moeck, S. Terhaar, and C.O. Paschereit. Amplitude-Dependent Flow Field and Flame Response to Axial and Tangential Velocity Fluctuations. *Journal of Engineering for Gas Turbines and Power*, 137(8):081501, 2015.

[136] M. Schmid. Thermoakustische Kopplungsmechanismen in Flüssigkeitsraketentriebwerken. *Doctoral Thesis, Lehrstuhl f. Thermodynamik, Technische Universität München, www.td.mw.tum.de*, 2014.

[137] B. Schuermans. Modeling and Control of Thermoacoustic Instabilities. *Doctoral Thesis, École Polytechnique Fédérale de Lausanne, http://infoscience.epfl.ch/record/33275*, 2003.

[138] B. Schuermans, V. Bellucci, F. Guethe, F. Meili, P. Flohr, and C.O. Paschereit. A Detailed Analysis of Thermoacoustic Interaction Mechanisms in a Turbulent Premixed Flame. *ASME GT2004-53831, June 14-17, Vienna, Austria*, 2004.

[139] B. Schuermans, V. Bellucci, and C.O. Paschereit. Thermoacoustic Modeling and Control of Multi Burner Combustion Systems. *ASME GT2003-38688, June 16-19, Atlanta, GA, USA*, 2003.

[140] B. Schuermans, M. R. Bothien, M. Maurer, and B. Bunkute. Combined Acoustic Damping-Cooling System for Operational Flexibility of GT26/24 Reheat Combustors. *ASME GT2015-42287, June 15-19, Montreal, Canada*, 2015.

[141] B. Schuermans, F. Guethe, and W. Mohr. Optical Transfer Function Measurements for Technically Premixed Flames. *Journal of Engineering for Gas Turbines and Power*, 132(8):081501, 2010.

[142] B. Schuermans, H. Luebcke, D. Bajusz, and P. Flohr. Thermoacoustic Analysis of Gas Turbine Combustion Systems using Unsteady CFD. *ASME GT2005-68393, June 6-9, Reno-Tahoe, NV, USA*, 2005.

[143] Bruno Schuermans, Christian Oliver Paschereit, and Peter Monkewitz. Non-linear Combustion Instabilities in Annular Gas-Turbine Combustors. *44th AIAA Aerospace Science Meeting and Exhibit, January 9-12, Reno, NV, USA*, 2006.

[144] M. Schulze. Linear Stability Assessment of Cryogenic Rocket Engines. *Doctoral Thesis, Lehrstuhl f. Thermodynamik, Technische Universität München*, 2016.

[145] M. Schulze, T. Hummel, N.Klarmann, F. Berger, B. Schuermans, and T. Sattelmayer. Linearized Euler Equations for the Prediction of Linear High-Frequency Stability in Gas Turbine Combustors. *Journal of Engineering for Gas Turbines and Power*, 139(3):031510–031, 2016.

[146] M. Schulze and T. Sattelmayer. Linear Stability Assessment of a Cryogenic Rocket Engine. *International Journal of Spray and Combustion Dynamics*, 9-4:277–298, 2017.

[147] M. Schulze, M. Wagner, and T. Sattelmayer. Acoustic Scattering Properties of Perforated Plates and Orifices with Stratified Flow-Hf-8 Test Case. *Proceedings of the 3rd REST Modelling Workshop, March 27/28, Vernon*, 2013.

[148] J. Schwing. Über die Interaktion von transversalen akustischen Moden, Strömung und drallstabilisierter Flamme in zylindrischen Flammenrohren. *Doctoral Thesis, Lehrstuhl f. Thermodynamik, Technische Universität München*, 2013.

[149] J. Schwing, F. Grimm, and T. Sattelmayer. A Model for Thermo-acoustic Feedback of Transverse Acoustic Modes and Periodic Oscillations in Flame Positions in Cylindircal Flame Tubes. *ASME GT2012-68775, June 11-15, Copenhagen, Denmark*, 2012.

[150] J. Schwing and T. Sattelmayer. High-Frequency Instabilities in Cylindrical Flame Tubes: Feedback Mechanism and Damping. *ASME GT2013-94064, June 3-7, San Antonio, Texas, USA*, 2013.

[151] J. Schwing, T. Sattelmayer, and N. Noiray. Interaction of Vortex Shedding and Transverse High-Frequency Pressure Oscillations in a Tubular Combustion Chamber. *ASME GT2011-45246, June 6-10, Vancouver, British Columbia, Canada*, 2011.

[152] V. Seidel. Numerische und experimentelle Untersuchungen der Aerodynamik und Verbrennungsstabilität eines Vormischbrenners. *Doctoral Thesis, Lehrstuhl f. Thermodynamik, Technische Universität München*, 2014.

[153] L. Selle, G. Lartigue, T. Poinsot, R. Koch, K.-U. Schildmacher, W. Krebs, B. Prade, P. Kaufmann, and D. Veynante. Compressible Large Eddy Simulation of Turbulent Combustion in Complex Geometry on Unstructured Meshes. *Combustion and Flame*, 137:489–505, 2004.

[154] J.C. Sisco, Y.C. Yu, V. Sankaran, and W.E. Anderson. Examination of Mode Shapes in an Unstable Model Combustor. *Journal of Sound and Vibration*, 330:61–74, 2010.

[155] M. Sliphorst, S. Groening, and M. Oschwald. Theoretical and Experimental Identification of Acoustic Spinning Mode in a Cylindrical Combustor. *Journal of Propulsion and Power*, 27:182–189, 2011.

[156] P-T. D. Spanos. Stochastic Analysis of Oscillators with Non-Linear Damping. *International Journal of Non-Linear Mechanics*, 13:249–259, 1978.

[157] N. Stadlmair, T. Hummel, and T. Sattelmayer. Thermoacoustic Damping Rate Determination from Combustion Noise Using Bayesian Statistics. *Journal of Engineering for Gas Turbines and Power*, 2018. Accepted for publication.

[158] N. Stadlmair, P. Mohammadzadeh-Keleshtery, M. Zahn, and T. Sattelmayer. Impact of Water Injection on Thermoacoustic Modes in a Lean Premixed Combustor under Atmospheric Conditions. *ASME Turbo Expo 2017, GT2017-63342, June 26-30, Charlotte, USA*, Jun 2017.

[159] N. Stadlmair, M. Wagner, C. Hirsch, and T. Sattelmayer. Experimentally Determining the Acoustic Damping Rates of a Combustor with a Swirl-Stabilized Lean Premixed Flame. *ASME Turbo Expo 2015 GT2015-42683, June 15-19, Montreal, Canada*, 2015.

[160] S.H. Strogatz. *Nonlinear Dynamics And Chaos*. Studies in nonlinearity. Westview Press, Boulder, Colorado, USA, 2001.

[161] P. Stuttaford, H. Rizkalla, K. Oumejjoud, N. Demougeot, J. Bosnoian, F. Hernandez, M. Yaquinto, A. P. Mohammad, D. Terrell, and R. Weller. FlameSheet^{TM} Combustor Engine and Rig Validation for Operational and Fuel Flexibility with Low Emissions. *ASME Turbo Expo 2016 GT2016-56696, June 13-17, Seoul, South Korea*, 2016.

[162] G. W. Swift. *Thermoacoustics A Unifying Perspective for Some Engines and Refrigerators*. Springer, Cham, Switzerland, 2017.

[163] J. C. Tannehill, D. A. Anderson, and R. H. Pletcher. *Computational Fluid Dynamics*. Taylor & Francis, Philadelphia, USA, 1997.

[164] W. Ullrich, C. Hirsch, T. Sattelmayer, K. Lackhove, A. Sadiki, A. Fischer, and M. Staufer. Combustion Noise Prediction Using Linearized Navier–Stokes Equations and Large-Eddy Simulation Sources. *Journal of Propulsion and Power*, 34-1:198–212, 2018.

[165] W. Ullrich and T. Sattelmayer. Transfer Functions of Acoustic, Entropy and Vorticity Waves in an Annular Model Combustor and Nozzle for the Prediction of the Ratio Between Indirect and Direct Combustion Noise. *21st AIAA/CEAS Aeroacoustics Conference, 22-26 June, Dallas, USA*, 2015.

[166] W. C. Ullrich, J. Gikadi, C. Jörg, and T. Sattelmayer. Acoustic-entropy coupling behavior and acoustic scattering properties of a Laval nozzle. *20th AIAA/CEAS Aeroacoustics Conference, Conference, June 16-20 , Atlanta, GA, USA*, 2014.

[167] A. Urbano, Q. Douasbin, L. Selle, G. Staffelbach, B. Cuenot, T. Schmitt, S. Ducruix, and S. Candel. Study of Flame Response to Transverse Acoustic Modes from the LES of a 42-Injector Rocket Engine. *Proceedings of the Combustion Institute*, 2016.

[168] A. Urbano and L. Selle. Driving and Damping Mechanisms for Transverse Combustion Instabilities in Liquid Rocket Engines. *Journal of Fluid Mechanics*, 820 (R2):1–12, 2017.

[169] M. Wagner, C. Joerg, and T. Sattelmayer. Comparisions of the Accuracy of Time-Domani Measurement Methods for Combustor Damping. *ASME Turbo Expo 2013 GT2013-94844, June 03-07, San Antonio, USA*, 2013.

[170] D. Wassmer, B. Schuermans, C. O. Paschereit, and J. P. Moeck. Measurement and Modeling of the Generation and the Transport of Entropy Waves in a Model Gas Turbine Combustor. *International Journal of Spray and Combustion Dynamics*, 9-4:299–309, 2017.

[171] C. D. Wilcox. *Turbulence Modeling for CFD (3rd Edition)*. DCW Industries, La Canada, CA,USA, 01 2006.

[172] P. Wolf, G. Staffelbach, L. Y.M. Gicquel, J. Müller, and T. Poinsot. Acoustic and Large Eddy Simulation Studies of Azimuthal Modes in Annular Combustion Chambers. *Combustion and Flame*, 159:3398–3413, 2012.

[173] N. A. Worth and J. R. Dawson. Modal Dynamics of Self-Excited Azimuthal Instabilities in an Annular Combustion Chamber. *Combustion and Flame*, 160(11):2476 – 2489, 2013.

[174] V. Yang and F. E.C. Culick. On the Existence and Stability of Limit Cycles for Transverse Acoustic Oscillations in a Cylindrical Combustion Chamber. 1: Standing Modes. *Combustion Science and Technology*, 72:1-3:37–65, 1990.

[175] V. Yang, S. Kim, and F. E.C. Culick. Third-Order Nonlinear Acoustic Instabilities in Combustion Chambers, Part II: Transverse Modes. *AIAA 26th Aerospace Sciences Meeting*, 1988.

[176] M. Zahn, M. Betz, M. Schulze, C. Hirsch, and T. Sattelmayer. Predicting the Influence of Damping Devices on the Stability Margin of an Annular Combustor. *ASME Turbo Expo 2017 GT2017-64238, June 26-30, Charlotte, USA*, Jun 2017.

[177] M. Zahn, M. Schulze, M. Wagner, C. Hirsch, and T. Sattelmayer. Frequency Domain Predictions of the Acoustic Reflection Coefficient of a Combustor Exit Nozzle with Linearized Navier-Stokes Equations. *24th International Congress on Sound and Vibration, July 23 - 27, London, England*, 2017.

[178] M. Zellhuber. High Frequency Response of Auto-Ignition and Heat Release to Acoustic Perturbations. *Doctoral Thesis, Lehrstuhl f. Thermodynamik, Technische Universität München*, 2013.

[179] M. Zellhuber, J. Schwing, B. Schuermans, T. Sattelmayer, and W. Polifke. Experimental and Numerical Investigations of Thermoacoustic Sources Related to High-Frequency Instabilities. *International Journal of Spray and Combustion Dynamics*, 6:1–34, 2014.